In compliance with the
Canadian Privacy Legislation
some supporting forms
may have been removed from
this dissertation.

While these forms may be included
in the document page count,
their removal does not represent
any loss of content from the dissertation.

UNIVERSITY OF ALBERTA

Studies of Noise and Polarization Performance of the Antennas of the DRAO Synthesis Telescope

By

Teresia Cheuk Wa Ng ©

A thesis submitted to the Faculty of Graduate Studies and Research in partial fulfillment of the requirements for the degree of Master of Science.

DEPARTMENT OF ELECTRICAL AND COMPUTER ENGINEERING

Edmonton, Alberta
Fall 2003

National Library of Canada
Acquisitions and Bibliographic Services
395 Wellington Street
Ottawa ON K1A 0N4
Canada

Bibliothèque nationale du Canada
Acquisisitons et services bibliographiques
395, rue Wellington
Ottawa ON K1A 0N4
Canada

Your file Votre référence
ISBN: 0-612-87850-3
Our file Notre référence
ISBN: 0-612-87850-3

The author has granted a non-exclusive licence allowing the National Library of Canada to reproduce, loan, distribute or sell copies of this thesis in microform, paper or electronic formats.

The author retains ownership of the copyright in this thesis. Neither the thesis nor substantial extracts from it may be printed or otherwise reproduced without the author's permission.

L'auteur a accordé une licence non exclusive permettant à la Bibliothèque nationale du Canada de reproduire, prêter, distribuer ou vendre des copies de cette thèse sous la forme de microfiche/film, de reproduction sur papier ou sur format électronique.

L'auteur conserve la propriété du droit d'auteur qui protège cette thèse. Ni la thèse ni des extraits substantiels de celle-ci ne doivent être imprimés ou aturement reproduits sans son autorisation.

Canadä

University of Alberta

Library Release Form

Name of Author: Teresia Cheuk Wa Ng

Title of Thesis: Studies of Noise and Polarization Performance of the Antennas of the DRAO Synthesis Telescope

Degree: Master of Science

Year this Degree Granted: 2003

Permission is hereby granted to the University of Alberta Library to reproduce single copies of this thesis and to lend or sell such copies for private, scholarly or scientific research purposes only.

The author reserves all other publication and other rights in association with the copyright in the thesis, and except as here before provided, neither the thesis nor any substantial portion thereof may printed or otherwise reproduced in any material form whatever without the author's prior written permission.

Date: Sept 25, 2003

University of Alberta

Faculty of Graduate Studies and Research

The undersigned certify that they have read, and recommend to the Faculty of Graduate Studies and Research for acceptance, a thesis entitled *Studies of Noise and Polarization Performance of the Antennas of the DRAO Synthesis Telescope* by *Teresia Cheuk Wa Ng* is partial fulfillment of the requirements for the degree of *Master of Science*.

Dr. T. L. Landecker (Co-Supervisor)

Dr. D. Routledge (Co-Supervisor)

Dr. J. McMullin

Dr. A. Peterson

Date: Sept. 23, 2003

Abstract

This thesis covers two topics related to the performance of the Synthesis Telescope at the Dominion Radio Astrophysical Observatory (DRAO). First, the sources of ground noise (mesh leakage, spillover and strut scattering noise) which contribute to the antenna temperature and methods to reduce these noise contributions were studied. By combining the results from the experiments performed and antenna modifications suggested here, the antenna temperature can be reduced from 14 K to 8 K. The second topic is an investigation of instrumental polarization across the field of view of a radio telescope antenna. The antenna components that have significant effect on instrumental polarization are the reflector curvature, feed cross polarization, reflector surface roughness and the struts (different strut arrangements, sizes and cross-sectional shapes have different impacts on instrumental polarization). This study showed that feed cross polarization is the most significant source of instrumental polarization, followed by strut properties, reflector curvature and reflector surface roughness.

Acknowledgement

I would like to express my gratitude to my supervisors Dr. Tom Landecker of the Dominion Radio Astrophysical Observatory and Dr. Dave Routledge of the University of Alberta for their encouragement, guidance and helpful suggestions through my graduate studies. I would also like to thank the staff of the Dominion Radio Astrophysical Observatory, especially Dave del Rizzo, Andrew Gray, Richard Hellyer, Ev Sheehan and Bruce Veidt, for their assistance.

Contents

Chapter 1 Introduction 1
1.1 History of Radio Astronomy 1
1.2 Modern Radio Telescopes 2
1.3 Reflector Antenna 3
1.3.1 Feed Systems 4
1.4 Antenna Analysis Methods 5
1.4.1 Method of Moments 6
1.4.2 Transmission Line Matrix Method 6
1.4.3 Geometrical Optics and Geometrical Theory of Diffraction 7
1.4.4 Physical Optics and Physical Theory of Diffraction 7
1.5 Aperture Synthesis 8
1.6 Radio Emission 13
1.7 Wave Polarization 15
1.8 The DRAO Synthesis Telescope 16
1.8.1 The Array 17
1.8.2 The Antennas 18
1.8.3 Receiver 19
1.8.4 C21 Correlator 20
1.8.5 Canadian Galactic Plane Survey 22
1.9 Topics of Thesis 23

Chapter 2 Ground Noise **25**
2.1 Introduction 25
2.2 Theory of Antenna Temperature 26
2.2.1 The Antenna Temperature of the Synthesis Telescope 29
2.3 Celestial Coordinate System 31
2.4 Actual Measurements 35
2.4.1 Calculation of System Temperature 35
2.4.2 Data Processing 38
2.5 Mesh Leakage 40
2.5.1 Theoretical Calculation 42
2.5.2 Experimental results 44
2.6 Spillover 47
2.6.1 Theoretical Calculation 50
2.6.2 Considerations for Mesh Fence Design 58
2.6.3 Using Ground Mesh to Reduce Spillover Noise of Antenna 6 63
2.6.4 Modification of Antenna 1 to Reduce Spillover Noise 68
2.6.4.1 Design 69
2.6.5 Modification of Antenna 7 to Reduce Spillover Noise 81
2.6.5.1 Design 81
2.6.5.2 Result 85
2.6.6 Proposed Fence design for Antenna 5 88

2.6.7 Proposed Fence Design for the Moveable Antennas 90
2.7 Strut Scattering 94
2.7.1 Induced Field Ratio and Scattering Pattern 95
2.7.1.1 Micro-Stripes simulation 96
2.7.1.2 *IFR* calculation 99
2.7.1.3 Scattering Pattern 105
2.7.2 Calculation of Antenna Noise due to Strut Scattering 107
2.7.3 Modification of Strut Cross Sectional Shape 119
2.8 Diffraction around Rim 122
2.9 Conclusion 126

Chapter 3 Instrumental Polarization 130
3.1 Introduction 130
3.2 Stokes Parameters 131
3.3 Simulation Procedures 133
3.3.1 GRASP8 135
3.3.1.1 Antenna modeling 136
3.3.1.2 Simulation 138
3.3.2 Stokes Parameter Computation 142
3.3.3 Plotting with MADR and PLOT 143
3.3.4 Verification of the Simulation Procedure 143
3.4 Study of Instrumental Polarization 148
3.4.1 Reflector curvature 148
3.4.2 Feed Cross Polarization 152
3.4.3 Surface Roughness 155
3.4.4 Different Strut Configurations 161
3.4.5 Different Strut Diameters 166
3.4.6 Different Strut Cross-sectional Shapes 167
3.5 Stokes Parameter Plots for the Synthesis Telescope 172
3.6 Conclusion 174

Chapter 4 Conclusion 176

Appendix A. Defining the Coordinates of a Point in a Rotated Coordinate System 178

Reference 181

List of Tables

Table 2.1 Initial noise contribution attributable to radiation from the ground. These values are calculated using the techniques developed in this thesis 31
Table 2.2 The level of injected noise for each of the seven antennas. [Del Rizzo, 2003] 36
Table 2.3 Initial noise contribution attributable to radiation from the ground. 128
Table 2.4 Predicted noise levels after antenna modification as suggested above..... 129
Table 3.1 Physical characteristics of Antenna 3 136

List of Figures

Figure 1.1 The basic components of a superheterodyne receiver. [Burke and Graham-Smith, 2002] 3
Figure 1.2 A paraboloidal reflector. Plane waves reflected off the reflector are collected at point P. [Burke and Graham-Smith., 2002] 4
Figure 1.3 The geometry of a (from left to right) Cassegrain, Gregorian and offset Cassegrain systems. [Rohlfs and Wilson, 2000] 5
Figure 1.4 A simple two-element interferometer 10
Figure 1.5 The polarization ellipse of a general elliptically polarized wave. 16
Figure 1.6 The array configuration. The separation between antennas is shown in terms of baseline increment L = 4.286 m. The variable s varies from 3L to 14L as antennas 2, 3 and 4 are moved [Landecker et al. 2000]. 17
Figure 1.7 The continuum and spectroscopy bands near 1420 MHz. S is the HI band and A, B, C and D are the continuum bands [Landecker, private communication, 2001]. 20
Figure 1.8 Model of a correlation interferometer 21
Figure 2.1 Antenna and spherical coordinate system 27
Figure 2.2 Contributions to antenna temperature for the Synthesis Telescope Antenna 7 (Diagram adapted from Anderson et al., 1991 with new values for the contributions to antenna temperature derived in this thesis) 30
Figure 2.3 The horizon coordinate system [Kraus, 1986] 32
Figure 2.4 The equatorial coordinate system [Kraus, 1986] 33
Figure 2.5 Structure of the system temperature files 38
Figure 2.6 The feed pattern is defined with respect to the feed coordinate system with x'-, y'- and z'-axes. 41
Figure 2.7 Geometry of the reflector with the central portion covered. 43
Figure 2.8 Reduction in noise from mesh leakage resulting from covering the central area of the reflector to radius r meters with solid metal. The circles shows experimentally determined values. 44
Figure 2.9 The system noise temperature of Antenna 7 of the DRAO Synthesis Telescope as a function of altitude. The gray line shows the noise temperature measured before the reflector was shielded. The thinner black line shows the noise temperature measured after a 1.4 m radius of a 9-m reflector was covered with aluminum tape. The thicker black line shows the noise temperature measured after 2.1 m radius was covered 45
Figure 2.10 Antenna 7 of the Synthesis Telescope at DRAO. Aluminum tape covers the central 2.1 m radius of the reflector. 46
Figure 2.11 Spillover region when the antenna is pointing at zenith 48
Figure 2.12 Reducing spillover noise by attaching cylindrical fence (shroud) to the rim of the antenna [Anderson, 1989] 49
Figure 2.13 Spillover reduction by using ground mesh and a fence with slanting angle θs 50
Figure 2.14 Flowchart for the brightness temperature calculation procedure within the program Spillover.c 52

Figure 2.15 The effective temperature of the ground at 1420 MHz as a function of angle of incidence. [Anderson, 1989] 53
Figure 2.16 Coordinate systems B, B' and P are defined with respect to the antenna for the computation of spillover lobe on the ground. Also shown is the location of spillover on the ground using ray tracing. 54
Figure 2.17 Calculated spillover noise as a function of antenna pointing, expressed as zenith angle (0° at the center of the plot) and azimuth. 57
Figure 2.18 Antenna pointing zenith angle and azimuth for declination equals to 90° (dot at zenith angle = 41°) 80°, 70°, 60°, 50°, 40°, 30°, and 18° (largest curve)..... 59
Figure 2.19 Geometries for solving the maximum height of the fence. 60
Figure 2.20 Geometry for solving the maximum slanting angle of the fence. 62
Figure 2.21 Square areas of mesh with side s (s = 4 m, 6 m, 10 m, 20 m, 30 m, 40 m, and 50 m) are placed on the ground around the antenna. The antenna is located in the center of the mesh area. The resultant spillover noise is plotted versus the antenna zenith angle..... 63
Figure 2.22 Location of mesh around Antenna 6. The shaded areas indicate the location of the ground screen. 65
Figure 2.23 Expected spillover noise reduction. The four darker curves on the plot indicate the path of antenna pointing for the four observations (pointing declinations are indicated on the plot) used to compare the change in antenna temperature after the installation of the ground mesh..... 66
Figure 2.24 Antenna noise comparison. Dotted line indicates positive azimuth angles and solid line indicates negative azimuth angles. The black line is the average antenna temperature for observations at declination 43° 16' 42.9", collected before the installation of the ground mesh. The gray line shows the antenna temperature (observing at declination 42° 10' 46.1") when the ground mesh was present. 67
Figure 2.25 Antenna noise comparison. The data for the black line (declination = 68° 49' 13.1") was collected before the installation of the mesh and the data for the gray line (declination = 69° 41' 16.7") was collected after. 68
Figure 2.26 A fence 25 m long and 4.57 m wide on the North side of Antenna 1.. 70
Figure 2.27 The predicted spillover noise reduction for a fence built to the North of the antenna. The thicker curve, the pointing path for 18° declination, indicates the observation limit of the Synthesis Telescope. The telescope is only used to observe sources with pointings above this curve. 71
Figure 2.28 A 25 m long and 5.49 m wide fence to the West of Antenna 1..... 72
Figure 2.29 The expected spillover noise reduction after building the West fence..... 72
Figure 2.30 Final design of the mesh fences around Antenna 1..... 73
Figure 2.31 Antenna 1: predicted spillover noise reduction with both fences..... 74
Figure 2.32 Mesh fences built around Antenna 1 to reduce spillover noise..... 75
Figure 2.33 The dimensions for the actual mesh fence around Antenna 1 76
Figure 2.34 The expected spillover noise reduction when the west fence was built..... 78
Figure 2.35 The expected spillover noise reduction upon the completion of the entire fence design. 78
Figure 2.36 The measured antenna temperature for Antenna 1 when observing a source at 38° declination. The black line indicates the measured antenna

temperature before any fence was built around the antenna; the dotted black line is temperature after the west fence was built; and the gray line is the antenna temperature when the entire fence was completed. 79
Figure 2.37 The measured antenna temperature for Antenna 1 when observing a source at 67° declination. Noise reduction comparisons for no mesh fence (black line), the west fence (dotted black line) and the entire design (gray line) 79
Figure 2.38 The calculated spillover and strut scattering noise reduction for the actual fence design. 80
Figure 2.39 Final design of Antenna 7 ground screen and mesh fence 83
Figure 2.40 Plot of predicted direct spillover and strut scattering noise reduction for Antenna 7. The thick curves is the pointing path for 18° declination, the observation limit. 85
Figure 2.41 Mesh fence built around Antenna 7 86
Figure 2.42 The measured antenna temperature for Antenna 7 when observing at 38° declination. Black line is the system temperature without the mesh fence and gray line is with the mesh fence. 86
Figure 2.43 The measured antenna temperature for Antenna 1 when observing at 38° declination. The black line and the gray line show the antenna temperature before and after construction of the Antenna 7 fence, respectively. The 2 K increase is due to the change in the ground temperature. 87
Figure 2.44 Final design of the mesh fence and ground screen for Antenna 5 89
Figure 2.45 The expected spillover and strut scattering noise reduction for Antenna 5 90
Figure 2.46 Ground mesh and mesh fence design for the movable antennas. 91
Figure 2.47 Expected spillover and strut scattering noise reduction for an antenna with three circular feedlegs (Antennas 2 and 4). 92
Figure 2.48 Expected spillover and strut scattering noise reduction of an antenna with three triangular struts (Antenna 3). 93
Figure 2.49 Expected spillover and strut scattering noise reduction of Antenna 1 (Compare with Figure 2.38) 93
Figure 2.50 The three types of cylinder considered in the *IFR* calculation 96
Figure 2.51 Micro-Stripes simulation for IFR_E calculation. The gray planar structure represents a plane wave which is propagating upwards (in the x direction) towards the cylinder. The cone shaped structure indicates the polarization of the wave. The plane wave is polarized parallel to the cylinder axis. 98
Figure 2.52 Micro-Stripes simulation for IFR_H calculation. The plane wave is polarized perpendicular to the cylinder axis. 98
Figure 2.53 Output of the Micro-Stripes simulation for a 1" circular cylinder immersed in a plane wave polarized parallel to the cylinder axis. The frequency, directivity and total scattered power of the scattered field are shown at the foot of the plot on the left. The black line on the plot is the -3 dB contour. f_s is the angle around the scattering pattern with $f_s = 0°$ pointing towards the forward direction. 99
Figure 2.54 Comparison of $|IFR|$ for circular cylinders calculated using the Micro-Strips simulation (black lines) and the method of moments (dotted lines) [Rusch, 1978]. 102

Figure 2.55 *IFR* magnitude for circular (circle marker), triangular (triangle marker) and teardrop shaped (diamond marker) cylinders. $|IFR_E|$ is greater than 1.0 and $|IFR_H|$ is less than 1.0. 103
Figure 2.56 *IFR* magnitude for a dielectric, circular cylinder. Black line represents IFR_E and dotted line represents IFR_H. 104
Figure 2.57 Scattering pattern of 3" struts with circular (black), triangular (dotted black) and teardrop shape (gray) cross sections at 1.42 GHz 106
Figure 2.58 Scattering pattern of 6" struts with circular (black), triangular (dotted black) and teardrop shape (gray) cross sections at 1.42 GHz 106
Figure 2.59 Geometry of the scatter cone of a feed support strut in a symmetrical paraboloidal antenna. 108
Figure 2.60 If the width of the triangular strut is large with respect to wavelength, scattered energy is concentrated in the two directions determined by specular reflection from the sides of the strut. 111
Figure 2.61 Coordinate systems B, B', P, P' and S are defined with respect to the antenna for the computation of scatter cone sidelobes on the ground. 113
Figure 2.62 Predicted strut scattering noise for an antenna with four 3" circular metal struts 115
Figure 2.63 Predicted strut scattering noise for an antenna with three 6" circular metal struts 116
Figure 2.64 Predicted strut scattering noise for antenna with three 6" triangular metal struts 116
Figure 2.65 Predicted strut scattering noise for antenna with three 6" circular dielectric struts 117
Figure 2.66 Antenna temperature measured before and after the strut cross sections of Antenna 3 were changed from circular to teardrop shape [Robitaille, 1997]..... 118
Figure 2.67 Predicted strut scattering noise for an antenna with four 3" triangular struts. (Compare to Figure 2.62) 120
Figure 2.68 The system noise temperature of Antenna 7 of the DRAO Synthesis Telescope as a function of altitude. The gray line shows the noise temperature measured when the feed-support struts have circular cross sections. The black line shows the noise temperature measured after the struts were modified to have triangular cross sections. 121
Figure 2.69 A plane wave illuminating a conducting half-plane from above and the resultant power density pattern below the plane. [Kraus, 1984] 123
Figure 2.70 A flanged parabolic reflector. The flange forms a right angle with the reflector surface [Bucci et al., 1985]. 124
Figure 2.71 Radiation pattern of a parabolic dish with corrugated right-angled flange (solid lines) and unflanged (dotted lines) [Bucci et al., 1985]. Angle 180 is in the direction of the antenna bore sight and angle 0 behind the reflector. 125
Figure 2.72 Side view of a paraboloidal reflector. This figure shows the elliptical edge (dotted line) and the blended rolled edge (solid line). Point e is the junction of the reflector and the rolled edge [Gupta et al., 1990]. 126
Figure 3.1 The IAU coordinate system with the z-axis pointing out of the page [Hamaker et al. 1996] 133
Figure 3.2 The simulation procedure for the study of instrumental polarization 134

Figure 3.3 Geometrical plot of Antenna 3 with the antenna coordinate system..... 137
Figure 3.4 The feed radiation pattern in the E- (black), D- (gray) and H- (light gray) planes. The co-polar pattern is plotted with solid lines and the cross-polar pattern in the D-plane is plotted with a dotted line..... 138
Figure 3.5 Spherical wave scattering: 1) feed illuminates the struts, 2) the feed and the induced current on the struts illuminate the reflector and 3) current induced on the reflector in turn illuminates the struts 141
Figure 3.6 Q/I plot for the prototype antenna. 144
Figure 3.7 U/I plot for the prototype antenna. 145
Figure 3.8 Legend for the Stokes parameter contour plots. 145
Figure 3.9 Q/I plot for the experimental data. [Peracaula, 1999] 146
Figure 3.10 U/I plot for the experimental data. [Peracaula, 1999] 147
Figure 3.11 Q/I contour plot for a perfectly linear feed illuminating a paraboloidal reflector with no struts. 150
Figure 3.12 U/I contour plot for a perfectly linear feed illuminating a paraboloidal reflector with no struts. 150
Figure 3.13 A feed with perfect linear polarization, after reflection, produces the field lines shown by the dashed lines. This distorted field contains cross-polarized components, strongest on lines at 45o to the feed polarization. [Christiansen and Högbom, 1985] 151
Figure 3.14 Plot of Stokes parameter I (black) and the absolute value of Q (gray) through the u-axis. 152
Figure 3.15 Q/I contour plot for the actual feed illuminating a paraboloidal reflector (no struts). 154
Figure 3.16 U/I contour plot for the actual feed illuminating a paraboloidal reflector (no struts) 154
Figure 3.17 Q/I plot for the actual feed illuminating a reflector with surface roughness (no struts). 156
Figure 3.18 U/I plot for the actual feed illuminating a reflector with surface roughness (no struts). 156
Figure 3.19 Gain-loss factor as a function of surface roughness as calculated by GRASP8 (black), and using equation 3.4.1 (gray) and the Ruze relation (light gray). 158
Figure 3.20 Stokes I through u-axis for the case of a perfect reflector (no struts) with no surface roughness (thin gray) is compared with an imperfect reflector having rms roughness of p (black), 2p (dotted black), 3p (gray) and 4p (dotted gray). p = 0.005 m. The vertical lines indicate the extent of the main beam 158
Figure 3.21 V/I plot for the actual feed illuminating a reflector with surface roughness of 0.005 m rms (no struts)..... 160
Figure 3.22 V/I plot for the actual feed illuminating a reflector with no surface roughness (no struts). 160
Figure 3.23 V/I plot through u-axis for rms surface error of p = 0.005 m (black), 2p (dotted black), 3p (gray) and 4p (dotted gray). The two vertical lines indicate the extent of the main beam. 161

Figure 3.24 Strut positions for the three-strut configuration (left) and four-strut configuration (right). Both diagrams are positioned relative to the Stokes parameter contour plots 162
Figure 3.25 Q/I plot for the three-strut configuration 163
Figure 3.26 U/I plot for the three-strut configuration 163
Figure 3.27 V/I plot for the three-strut configuration 164
Figure 3.28 Q/I plot for the four-strut configuration 164
Figure 3.29 U/I plot for the four-strut configuration 165
Figure 3.30 V/I plot for the four-strut configuration 165
Figure 3.31 Q/I plot through u-axis. Solid black line represents no struts, dotted black line - 3" struts, solid gray line - 6" struts, dotted gray line - 9" struts (strut diameter is used in each case). The vertical lines indicate the extent of the main beam. 167
Figure 3.32 Scattered field from a square cylinder with sides s = 0.89λ calculated by MoM, PO+PTD and PO [Pontoppidan, 2000]. 169
Figure 3.33 Q/I plot for an antenna with three triangular struts 170
Figure 3.34 U/I plot for an antenna with three triangular struts 171
Figure 3.35 V/I plot for an antenna with three triangular struts 171
Figure 3.36 Q/I plot for the actual feed illuminating a rough reflector with three 6" circular struts 173
Figure 3.37 U/I plot for the actual feed illuminating a rough reflector with three 6" circular struts 173
Figure 3.38 V/I plot for the actual feed illuminating a rough reflector with three 6" circular struts 174

Chapter 1 Introduction

This chapter will present a brief history of radio astronomy, basic principles of radio telescopes, antenna analysis methods, aperture synthesis techniques, mechanisms of radio emission and polarization theory. The Synthesis Telescope at the Dominion Radio Astrophysical Observatory (DRAO) and the Canadian Galactic Plane Survey (CGPS) will also be described.

1.1 History of Radio Astronomy

The field of radio astronomy began in the early 1930's when Karl Jansky detected cosmic radio noise from the disk of the Milky Way Galaxy while he was working as a radio engineer at the Bell Telephone Laboratories. In 1931, Jansky was studying the direction of arrival of radio frequency interference. This information would enable the design of an antenna system that would have a minimal response in the direction of interference. To study this problem, Jansky built a vertically polarized unidirectional beam antenna that could rotate in azimuth. The antenna, operated at a wavelength of 14.6 m, was connected to a sensitive receiver and the antenna's output was written on a strip-chart recorder.

With this antenna, Jansky was able to identify three groups of natural interference: static from local thunderstorms, static from distant thunderstorms and "a steady hiss type static of unknown origin" [Kraus, 1986]. He noticed that the direction of this "steady hiss" changes throughout the day and goes through almost a complete circle in approximately 24 hours. In 1933, Jansky concluded in the paper "Electrical Disturbances Apparently of Extraterrestrial Origin" that this unknown interference must come from sources outside the solar system [Kraus, 1986]. This discovery marked the birth of Radio Astronomy.

In 1937, Grote Reber constructed the first radio telescope, a 9.5 m parabolic-reflector antenna. He found strong radio emissions along the plane of the Milky Way. In 1944, Reber published the first radio frequency maps [Kraus, 1986]. After Word War II, radio astronomy developed rapidly. Astronomers began to build telescopes with larger apertures. Increasing the size of the telescope aperture increases the energy-collecting area (effective area) and the power received, thus greater sensitivity can be achieved. Also, larger apertures have narrower antenna beams (higher angular resolution) and allow fine structures to be studied. Angular resolution is the smallest angular separation which two point sources can have in order to be recognized as separate objects.

However, the strength of construction materials limited the size of radio telescopes. The largest fully steerable radio telescopes are the 100 m parabolic reflector at Effelsberg near Bonn, West Germany and the 100 m Green Bank Telescope at the National Radio Astronomy Observatory in West Virginia, USA. The largest antenna is the 305 m Arecibo dish in Puerto Rico. Its reflector is constructed in a bowl-shaped depression in the ground and beam steering is achieved by moving the feed which is suspended above the reflector [Kraus, 1986]. The technique of aperture synthesis solved the problem of aperture size limitation by gathering the measurements made by two or more smaller antennas to synthesize a very large aperture (see section 1.5).

1.2 Modern Radio Telescopes

Radio telescope antennas are grouped into two general categories: filled-aperture or unfilled-aperture telescopes. The paraboloidal reflector antenna is the most familiar type of filled aperture telescope and the unfilled aperture applies the techniques of aperture synthesis. In both types of telescopes, the signal from the antenna is amplified by a receiver such as the superheterodyne receiver as shown in Figure 1.1. First, the signal is amplified by a low noise amplifier with a gain in the order of 10 to 30 dB [Kraus, 1986]. The next stage is the mixer or frequency converter which shifts the signal from the initial frequency band v_i to the intermediate frequency v_{if} by mixing the received signal with a local oscillator signal v_{lo}. The intermediate frequency signal is further

amplified with a gain in the order of 60 to 90 dB [Kraus, 1986]. The results are processed and analyzed by computers.

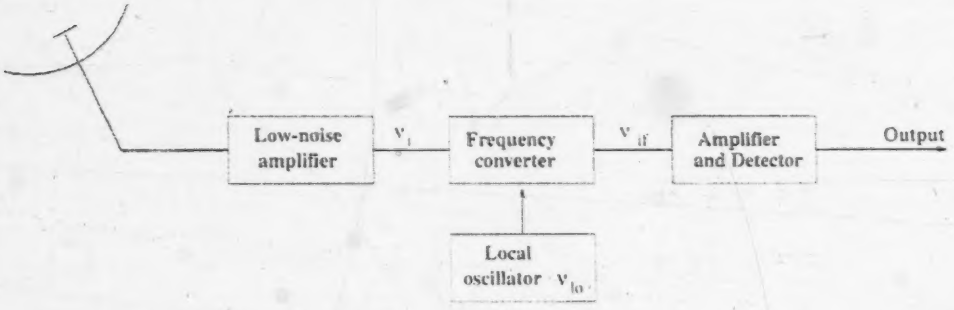

Figure 1.1 The basic components of a superheterodyne receiver. [Burke and Graham-Smith, 2002]

1.3 Reflector Antenna

The paraboloidal reflector antenna is the most widely used type of filled aperture radio telescope. The basic principle of the parabolic reflector antenna can be understood using ray tracing or geometric optics GO (Figure 1.2); the incoming plane waves reflected off the reflector reach the focal point P in phase. The feed, usually a horn antenna, is placed at point P to capture the signal collected by the reflector. This type of antenna is called a prime focus parabolic reflector antenna since the feed is placed at the focal point. It is rotationally symmetric and is entirely defined by its diameter D and its focal length F.

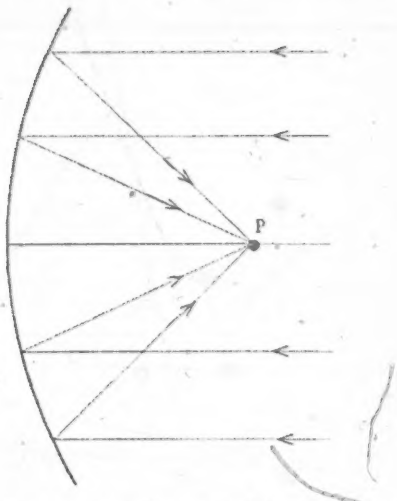

Figure 1.2 A paraboloidal reflector. Plane waves reflected off the reflector are collected at point P. [Burke and Graham-Smith., 2002]

1.3.1 Feed Systems

A disadvantage of focus-fed reflector antennas with large aperture is that the equipment at the prime focus is heavy and difficulties are encountered when constructing the feed supporting structures. A solution is to use a dual-reflector system such as the Cassegrain and the Gregorian systems (Figure 1.3). In a Cassegrain system, a convex hyperbolic reflector (sub-reflector) is placed in front of the prime focus to transfer the converging rays to a secondary focus located close to the vertex of the primary reflector. The Gregorian reflector has a concave elliptic sub-reflector. Its sub-reflector is positioned behind the prime focus in the diverging beam. Another advantage of the dual-reflector system is that spillover (in terms of transmitting, spillover is the radiation from the feed that is not intercepted by the reflector) toward the ground can be reduced since the feed is directed toward the sky.

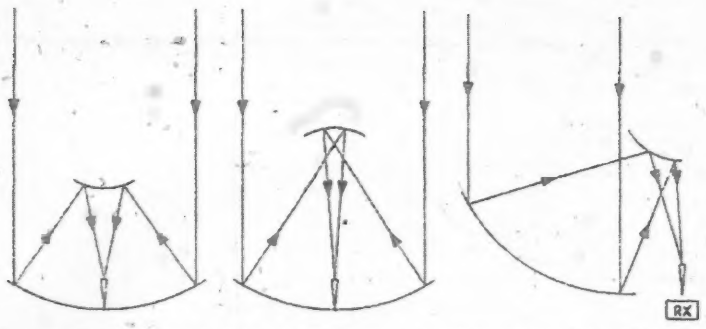

Figure 1.3 The geometry of a (from left to right) Cassegrain, Gregorian and offset Cassegrain systems. [Rohlfs and Wilson, 2000]

The drawback of the prime focus and secondary focus arrangements is that part of the aperture is blocked by the feed or the sub-reflector and their supportive structures. To avoid this problem, an offset-feed reflector is used. The offset reflector is actually a section of a larger axisymmetric paraboloidal reflector. The feed is still located at the focal point of the paraboloid, but is pointed toward the center of the offset reflector. With an offset Cassegrain system (Figure 1.3), the feed is placed beside the reflector and a convex reflector is positioned in front of the focus point to reflect radiation towards the feed. The cost of the offset design is beam squinting (the peak response of the two circularly polarized beams point in slightly different directions) which is accompanied by gain loss, and a more complex construction.

1.4 Antenna Analysis Methods

The analysis of the radiation characteristics of reflector antennas requires extensive calculations. Electromagnetic simulators using various antenna modeling techniques such as method of moments (MoM), transmission line matrix method (TLM), geometrical optics (GO), geometrical theory of diffraction (GTD), physical optics (PO), physical theory of diffraction (PTD) or combinations of these techniques have become increasingly important in the study of antenna designs.

1.4.1 Method of Moments

The field scattered by the antenna can be expressed as an integral of the unknown surface currents on the structure. MoM (also known as the integral-equation method) is a solution procedure for approximating an integral equation with a system of simultaneous linear algebraic equations in terms of the unknown currents. The algebraic equations have the general form [Stutzman and Thiele, 1998]

$$[Z_{mn}][I_n] = [V_m] \tag{1.4.1}$$

The elements in the impedance matrix $[Z_{mn}]$ are calculated using the integral equations constructed by solving the electromagnetic radiation problem of the antenna under test. $[I_n]$ is the unknown current coefficients and $[V_m]$ is the excitation data vector. The antenna is excited by a continuous voltage source at a constant operating frequency. In equation (1.4.1), $[Z_{mn}]$ and $[V_m]$ are known and $[I_n]$ can be solved by matrix inversion. Once $[I_n]$ is found, the current distribution is known in discrete form and the radiation pattern can be determined.

MoM is a theoretically exact method, which is useful for the analysis of structures that are smaller than a few tens of wavelengths. The main drawback of this method is the large computational resources required. The number of unknowns N increases with the dimension of the antenna structure; the computer storage requirement is proportional to N^2 and the time to invert the NxN matrix is proportional to N^3 [Veidt, 1998].

1.4.2 Transmission Line Matrix Method

TLM is based on a fictitious network of transmission lines connecting a grid of nodes in the problem space. Electric and magnetic fields are modeled as voltage and current pulses which travel along the transmission lines and are scattered by the nodes into other lines. Material properties are modeled by the impedance of the transmission lines and the scattering parameters of the nodes. TLM is a time domain method; the

simulation commences by applying a stimulus to a node or group of nodes, and observing how that stimulus propagates through the structure, reflecting off nodes and transmitting to other nodes through the transmission lines. The TLM method solves a scattering problem by using absorbing boundary conditions (ABC) where the outer boundary of the computation space absorbs all waves striking it. Therefore, there is no reflection and the problem space appears to be infinite. The time domain results are converted to frequency domain through a Fourier transform. [Veidt, 1998]

1.4.3 Geometrical Optics and Geometrical Theory of Diffraction

GO uses a ray method which traces the flow of energy and assumes the path of the electromagnetic radiation can be described using only reflection and refraction. The amplitude of the rays decreases as the distance from the source increases. In the far field, the amplitude is inversely proportional to the distance from the source. GO is exact only in the limit of zero wavelength, but is useful for analyzing large structures such as a reflector antenna that is larger than tens of wavelengths in extent. Also, this method does not give good results close to the physical boundaries, thus GTD is often combined with GO to give a more accurate approximation.

GTD considers diffracted rays which are produced when a ray strikes an edge or vertex. These rays account for the nonzero field in the shadow region and modify the GO field in the illuminated region. The magnitude of the diffracted ray is proportional to the product of the incident ray at the point of diffraction and a diffraction coefficient. The diffraction coefficient is determined from the solution of a canonical problem such as wedge diffraction and is dependent on the type of discontinuity, the incident angle and the position of the observation point [Trikha, 1991].

1.4.4 Physical Optics and Physical Theory of Diffraction

PO can accurately compute the radiated field of a system with dimensions in the order of a wavelength. It is an approximation that relates the surface current on a

conductor with the incident electromagnetic field. The surface current at a specific point on a curved, perfectly conducting scatterer is assumed to be the same as the surface current on an infinite planar surface which is tangent to the scattering surface. Thus, the induced electric current at any point is given by [Pontoppidan, 2000]

$$\bar{J}^e = \begin{cases} 2\hat{n} \times \bar{H}^i & \textit{illuminated} \\ 0 & \textit{otherwise} \end{cases} \tag{1.4.2}$$

where $\bar{J}^e$ is the induced electric current, $\hat{n}$ is the unit vector normal to the surface and pointing outward, and $\bar{H}^i$ is the incident magnetic field. For the case of scattering off an infinite, flat and perfectly conducting surface, the tangential component of the scattered magnetic field is in phase with and equal in magnitude to that of the incident field. Thus, the factor of 2 in equation (1.4.2) indicates the summation of the incident and the scattered field.

The behaviour of the surface current close to the edges of the scatterer is modeled using PTD. PTD tackles the same canonical problems as GTD, but it estimates the surface current introduced by the discontinuity rather than the diffracted ray field contribution. The PTD expression is derived from the canonical problem of a plane wave illuminating an infinite, uniform wedge with a specified wedge angle. The PO and PTD contributions are summed vectorially to give an accurate approximation to the surface current close to the edge of the scatterer [Pontoppidan, 2000].

1.5 Aperture Synthesis

The most basic form of aperture synthesis can be thought of as a method to synthesize the information gathering ability of a large aperture by measuring with two small antennas. Aperture synthesis uses the principle of interferometry. One of the antennas remains stationary to provide a phase reference while the other is moved to all positions within the large aperture. The source is assumed not to change with time, and

the data collected as the second antenna samples the entire aperture are added in phase and an image is formed.

Two or more antennas separated by a baseline B are electronically linked to form an interferometer. Consider a two-element radio interferometer observing a point source of frequency ω (Figure 1.4). The signals received by the two antennas are cross-correlated (or multiplied and then time averaged using an integrator) [Burke and Graham-Smith, 2000].

$$R(\tau) = < V_1(t) V_2(t-\tau) > \tag{1.5.1}$$

where V_1 and V_2 are the responses of antennas 1 and 2, τ is the time delay of the second response and < > denotes time average. Taking antenna 1 as the reference antenna, the signal at the second antenna is delayed by the geometric time delay τ_g. As the Earth rotates and hence the source is moved across the sky, the two received signals will alternately reinforce and oppose each other as the phase difference between the source and the antennas changes. The alternately constructive and destructive interference of the signals from the two antennas produces interference fringes. These fine structures are introduced into the primary beam to increase the resolution.

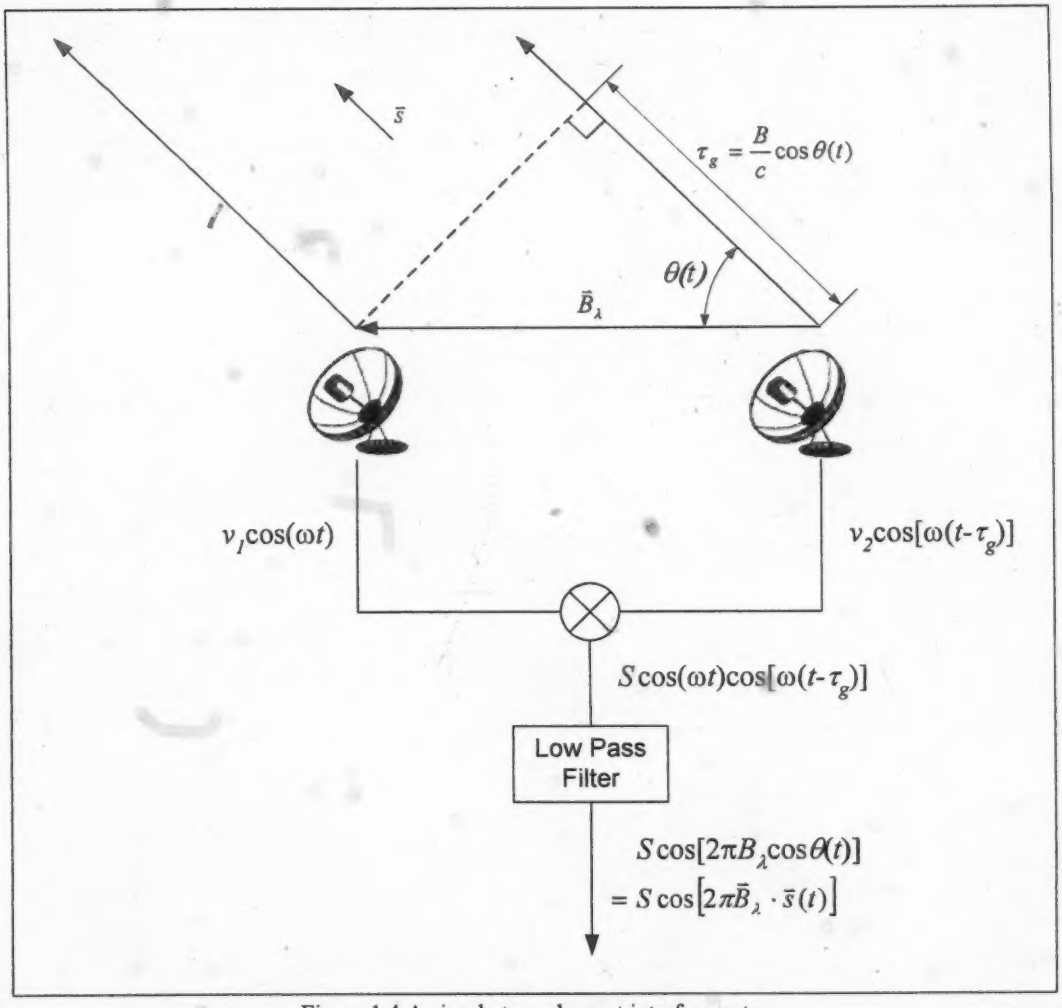

Figure 1.4 A simple two-element interferometer

The output of the cross-correlator, having dimension of power, is proportional to the source flux density S. The phase difference $2\pi B_\lambda\cos\theta$ (B_λ is the length of the baseline in terms of wavelength) can be written as the dot product of the baseline vector $\vec{B}_\lambda$ (from the second antenna to the reference antenna) and the direction to the source given by the unit vector $\vec{s}$. Thus the interferometry response to a point source is

$$R(t) = S\cos\left[2\pi\vec{B}_\lambda\cdot\vec{s}(t)\right] \tag{1.5.2}$$

Radio telescopes operate over a finite bandwidth Δf. However, if the bandwidth is greater than $1/\tau_g$, the correlation between the two signals is lost and fringes disappear. This can be solved by inserting an instrumental time delay τ_i in the antenna 1 signal path to compensate for the geometric time delay in the signal. τ_i is chosen to be approximately equal to τ_g.

Consider an extended source: the response of a two-element interferometer can be obtained by considering the source to be a collection of point sources. Let $\vec{s}_o$ be in the direction of the phase center so that any point on the source can be denoted by $\vec{s}_o + \vec{\sigma}$. Then the cross-correlation output for an extended source is the response to a point source integrated over the source [Fomalont and Wright, 1974].

$$R(t) = \int I(\sigma)\cos\left[2\pi\vec{B}\cdot(\vec{s}_o(t)+\vec{\sigma})\right]d\sigma \tag{1.5.3}$$

I(σ) is the brightness distribution of the source and the flux density of the source is equal to the integral of brightness over the extent of the source $S = \int I(\sigma)d\sigma$. $R(t)$ is now stated in terms of the projected spacing $\vec{b} = \vec{B} - (\vec{s}\cdot\vec{B})\vec{s}$ of the physical baseline $\vec{B}$ as viewed from the source. $\vec{b}$ is a useful quantity in aperture synthesis (see below). Since $\vec{\sigma}$ is almost perpendicular to $\vec{s}$, equation (1.5.3) can be approximated by [Fomalont and Wright, 1974]

$$R(t) = \int I(\sigma)\cos\left[2\pi(\vec{B}\cdot\vec{s}_o(t)+\vec{b}\cdot\vec{\sigma})\right]d\sigma \tag{1.5.4}$$

(1.5.4) can be expanded and rewritten in complex form.

$$R(t) = e^{j2\pi\vec{B}\cdot\vec{s}(t)}\int I(\sigma)e^{j2\pi\vec{b}\cdot\vec{\sigma}}d\sigma \tag{1.5.5}$$

$$R(t) = Ve^{j2\pi\vec{B}\cdot\vec{s}(t)} \tag{1.5.6}$$

where

$$V = \int I(\sigma) e^{j2\pi \vec{b}\cdot\vec{\sigma}} d\sigma \tag{1.5.7}$$

V, called the complex visibility function, is a complex number with magnitude proportional to the source brightness and argument equal to the phase shift in the fringe pattern relative to that of a point source at the phase center. According to (1.5.7), the visibility function is the Fourier transform of the source brightness. The brightness distribution can be obtained by taking the inverse Fourier transform of the visibility function which would result from observing with all possible projected baselines.

$$I(\vec{\sigma}) = \int_{-\infty}^{\infty} V(\vec{b}) e^{-j2\pi \vec{b}\cdot\vec{\sigma}} d\vec{b} \tag{1.5.8}$$

The projected baseline is usually specified in a right-handed coordinate system (the uv plane) which is a plane perpendicular to the unit vector $\vec{s}_o$. The u and the v axes are projected towards the East and North, respectively. A single interferometer observation evaluates the Fourier transform of the source brightness distribution for a particular value of spatial frequency, which is represented as a single point in the u-v plane. The goal of aperture synthesis is to use many interferometer pairs with different projected baseline lengths and orientations to fully sample all the points in the uv plane.

The sampling of the aperture can be achieved by making use of the Earth's rotation. Due to the rotation of the Earth, the projected baseline changes as the antennas track a source in the sky. As viewed from the radio source, an interferometer pair traces out an elliptical ring in the u-v plane over a period of 24 hours. Since V(u, v) is an even function, a 12-hour observation provides the visibility function on one side of the ellipse and the values for the other half of the ellipse can be deduced using $V^*(-\vec{b}) = V(\vec{b})$. The maximum projected baseline is set by the maximum separation between the antennas. The maximum possible separation between the sampling points in the u-v plane is determined by the Nyquist sampling theorem. Consider the one-dimensional case; if the brightness distribution B(ξ) is nonzero only within an interval of width ξ_w, then B(ξ) is

fully specified by sampling the visibility function with separations $\Delta u = 1/\xi_w$. This Nyquist sampling theorem also applies to the spacing of grid points in the two-dimensional u-v plane. In a multi-element array with N antennas, the number of instantaneous baselines is $N(N\text{-}1)/2$. A few movements of the antennas can achieve full sampling of the u-v plane within the area bounded by the maximum dimensions set by B_λ, the latitude, declination of the source, and orientation of the baseline on the ground.

1.6 Radio Emission

Electromagnetic radiation is generated by either thermal or non-thermal mechanisms. Thermal emission is derived from the heat energy of the emitting object while non-thermal emission is not temperature dependent. Processes of thermal radiation include blackbody radiation, free-free emission in an ionized gas and spectral line emission. Non-thermal emission includes synchrotron radiation and amplified emission due to insterstellar masers.

All objects at temperature above absolute zero radiate energy in the form of electromagnetic waves. This form of radiation is denoted as blackbody radiation if the emitter is optically thick. A blackbody is a hypothetical object that absorbs all radiation falling upon it at all wavelengths (perfect absorber). It is also a perfect radiator. The brightness, or the energy received per unit area per unit solid angle for a particular frequency bandwidth, of the blackbody radiation is characterized by Planck's radiation law [Kraus, 1984].

$$B = \frac{2hf^3}{c^2}\frac{1}{e^{hf/kT}-1} \tag{1.6.1}$$

where

h = Planck's constant, 6.63×10^{-34} J s

f = frequency, Hz

c = velocity of light, 3.00×10^{8} m s^{-1}

T = temperature, K

Brightness here is frequency and temperature dependent. Objects at lower temperatures emit more radiation at longer wavelengths. Thus, measuring the brightness of an astronomical object at several frequencies can determine its temperature.

Free-free or bremsstrahlung radiation is thermal radio emission which involves the interaction of free electrons and protons in clouds of ionized hydrogen (HII regions). This process is called free-free emission because an electron is unbound before and after an interaction with a proton. The electron is accelerated when it is deflected in passing near a proton, and a charged particle undergoing an acceleration radiates electromagnetic energy. Since the free-free emission is the combination of many independent electron-proton interactions the frequency spectrum is continuous. At low frequency, the brightness varies as the square of the frequency. At sufficiently high frequency, the brightness spectrum bends over to become approximately constant. A source of free-free radio emission is ionized gas near star forming regions.

The third type of thermal emission is spectral line emission from atoms and molecules. This process involves the electron changing states within the atom and emitting a photon of energy at a wavelength characteristic of that atom. An important spectral line is the 21-cm neutral hydrogen (HI) line. In its ground state, the electron and proton of a neutral hydrogen atom spin in opposite directions. When the atom is excited, the spin of the electron flips to align with the spin of the proton. As the atom returns to its ground state, it emits a photon with a wavelength of 21.1 cm. Since the emission is highly monochromatic, accurate velocity measurement can be made by mapping spectral lines and considering the Doppler shift. Also, since hydrogen is a major constituent of the interstellar medium, the 21-cm line provides a means of mapping the galaxy.

Non-thermal emission does not have a spectrum that resembles the characteristic curve of blackbody radiation. Synchrotron radiation is the most common form of non-thermal emission. Synchrotron emission arises when cosmic-ray electrons, traveling at

$\vec{v}$ close to the speed of light, encounter magnetic fields ($\vec{B}$). These particles experience the Lorentz ($\vec{v}x\vec{B}$) force, which causes them to accelerate around a helical path and radiate away some of their energy in the form of radio waves. The frequency of the radiation is dependent on the initial speed of the electrons and the strength of the magnetic field. The intensity of synchrotron radiation increases at longer wavelength. This process produces partially linearly polarized radiation with $\vec{E}$ perpendicular to the magnetic field. Supernova remnants are strong sources of synchrotron emission.

Another form of non-thermal emission comes from "microwave amplification by simulated emission of radiation" or masers. Maser action occurs when a cloud of molecules encounters an intense radiation field and a large portion of the molecules is energized to their excited state. As a result, some molecular line emission can be greatly and coherently amplified when the molecules return to the lower energy level.

1.7 Wave Polarization

Polarization is a quantity describing the orientation of the electric field in an electromagnetic wave as the wave travels in space. A linearly polarized electromagnetic wave has a transverse electric field with constant orientation, and the magnitude of the field at a fixed point in space varies sinusoidally with time. A circularly polarized wave has a transverse electric field of constant magnitude, with an orientation that changes uniformly with time, making one revolution per wave period. An elliptically polarized wave is the general form; it may be thought of as the superposition of a linearly and a circularly polarized wave.

The properties of the polarized wave with respect to a reference coordinate system (x, y) are defined by the parameters of the polarization ellipse, E_a, E_b and ψ (Figure 1.5). E_a and E_b are the semi-major and semi-minor axes of the ellipse and ψ is the tilt angle of the major axis. $E_b = 0$ for a linearly polarized wave and $E_a = E_b$ for a circularly polarized wave.

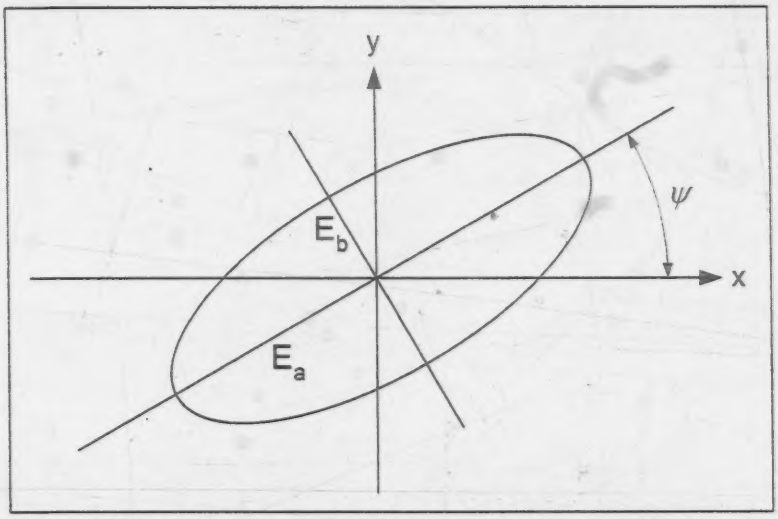

Figure 1.5 The polarization ellipse of a general elliptically polarized wave.

A wave is polarized if a lasting phase and amplitude relation exists between its two orthogonal components. If the duration of this relation is short compared to the wave period then the time averaged polarization will be zero and the wave is randomly polarized or unpolarized. A partially polarized wave consists of both polarized and unpolarized components. A useful set of variables that describes a partially polarized wave is the Stokes parameters. The Stokes parameters are explained in Section 3.2.

1.8 The DRAO Synthesis Telescope

The DRAO Synthesis Radio Telescope [Landecker et al. 2000] is designed to map atomic hydrogen emission using 256 spectral channels centered on the 21 cm HI spectral line, and simultaneously, continuum emission in the two bands centered at 408 MHz (74 cm) and at 1420 MHz (21 cm). It also performs polarization imaging of the continuum emission at 1420 MHz. The Synthesis Telescope achieves arcminute angular resolution over a wide field of view of 2.65° at 1420 MHz. This feature allows the mapping of large structures in the interstellar medium. Linearly polarized emission is detected by receiving both hands of circular polarization. The correlator forms cross-correlations of

all combinations of left- and right-hand circular polarization and from these the four Stokes parameters are calculated and converted to images.

1.8.1 The Array

The Synthesis Telescope consists of seven 9-meter dishes on an east-west baseline of 600 m. Figure 1.6 shows the telescope configuration. Antennas 2, 3 and 4 are mounted on motorized platforms that ride on a precision rail track. The baseline increment is L = 4.286 m, about half an antenna diameter. However, due to antenna shadowing and risk of mechanical interference, the minimum usable baseline is limited to $3L$ = 12.86 m. The maximum baseline of $144L$ = 617.18 m is between the two stationary elements on either end of the array. This allows full representation of images of size 1 arcmin to 40 arcmin at 1420 MHz.

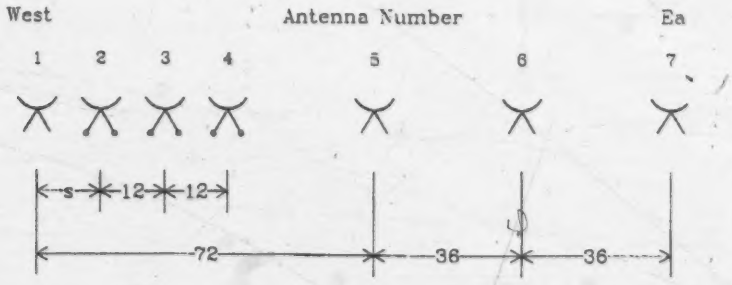

Figure 1.6 The array configuration. The separation between antennas is shown in terms of baseline increment L = 4.286 m. The variable s varies from 3L to 14L as antennas 2, 3 and 4 are moved [Landecker et al. 2000].

With the seven antennas, the number of instantaneous baselines is 21. Complete coverage of baselines from $3L$ to $144L$ is acquired with twelve settings of the movable antennas. The strategy for achieving these twelve settings is to keep the separation between antennas 2, 3 and 4 at $12L$ while changing the separation between 1 and 2 from $3L$ to $14L$. For each of the element settings, the Synthesis Telescope tracks the object for 12 sidereal hours to obtain full hour-angle coverage. Therefore, a complete survey or an observation set requires a time of 12 x 12 hours. This process fully samples the available

baselines and synthesizes an aperture 600 m in diameter. Normally, the Synthesis Telescope completes seven different 12-hour observations back-to-back leaving approximately 8 hours for maintenance and for moving the antennas in a 4-day cycle. This cycle is repeated 12 times to obtain all the possible baselines for the 7 fields.

1.8.2 The Antennas

The antennas used in the Synthesis Telescope are mounted equatorially with paraboloidal reflectors. The seven antennas are not identical. The main difference is in the size of the reflectors. The antennas at either end of the array have a diameter of D = 9.14 m and focal length f = 3.81 m, while the others have D = 8.53 m and f = 3.66 m. In addition, the antennas have different numbers and shapes of feed-supporting struts. The mesh size also varies among the antennas. Table 1 summarizes the physical structures of the individual antennas.

Antenna	Reflector Diameter	Focal Length	Mesh Size	# of Struts	Strut Diameter	Strut Cross-section	Strut material
1	9.144 m	3.810 m	0.625"	4	3"	Circular	metal
2	8.534 m	3.658 m	0.625"	3	6"	Circular	fibreglass
3	8.534 m	3.658 m	0.375"	3	6"	Circular	metal
4	8.534 m	3.658 m	0.375"	3	6"	Circular	fibreglass
5	8.534 m	3.658 m	0.375"	3	6"	Triangular	metal
6	8.534 m	3.658 m	0.375"	3	6"	Triangular	metal
7	9.144 m	3.810 m	0.625"	4	3"	Circular	metal

Table 1. Physical Characteristics of the antennas used in the DRAO Synthesis Telescope [Landecker, private communication, 2001]

At each antenna, signals are collected by a dual-frequency feed mounted at the focus. At 1420 MHz, a multi-mode feed provides a flat topped illumination pattern, yielding an aperture efficiency η_A = 0.55 and an edge illumination of the reflector of –16 dB [Landecker et al. 2000]. At each antenna feed, a small modulated noise signal is injected. This noise is demodulated from the signal at the correlator to provide a continuous measurement of system gain and system temperature. The feed consists of

two linear probes which receive two orthogonal signals E_x and E_y. These signals pass through a "quarter-wave plate" which is a waveguide section consisting of a cascade of three capacitive pins oriented 45° to the polarization direction of the linearly polarized incident waves [Simmons, 1952]. The linearly polarized wave has components parallel and perpendicular (x' and y') to the capacitive pins. As the incident wave passes through the quarter wave plate, the component parallel to the pins (x') is delayed by 90°. The waveguide introduces a phase difference of 90° between the x' and y' components. Right-hand circular polarization (RHCP) and in a similar fashion left-hand circular polarization (LHCP) are formed by combining the original and the phase-shifted signals.

$$LHCP = E_{x'} + jE_{y'} \qquad (1.8.1)$$

$$RHCP = E_{y'} + jE_{x'} \qquad (1.8.2)$$

1.8.3 Receiver

The received LHCP and RHCP signals are amplified by an uncooled 3-stage high electron mobility transistor (HEMT) amplifier at each Synthesis Telescope antenna. The receiver noise temperature is approximately 35 K. At the time this thesis was written, a project to design a new, single stage, low noise amplifier (LNA) to reduce receiver noise by 15 K was also in progress. This project matches the LNA directly to the antenna instead of connecting it by coaxial cable, thereby eliminating the connection loss [Garcia, 2002].

After amplifying the received signal, it is converted to an intermediate frequency band of 12.5 – 47.5 MHz (Figure 1.7) by the first local oscillator (LO). The LO signal for each antenna is modulated by a switching pattern defined by the 8-step orthogonal Walsh function to reduce cross talk between receiver channels [Landecker et al., 2000]. The switching pattern has 2 Walsh cycles in the telescope visibility-averaging time of 90 s.

At 1420 MHz, the total reception bandwidth is 35 MHz centered on the HI spectroscopy band. Since the total continuum bandwidth is too wide to permit mapping of the entire field of view without bandwidth smearing, the 30 MHz continuum band is divided into four 7.5 MHz sub-bands (A, B, C and D in Figure 1.7) distributed on either side of the HI band (Figure 1.7). The four continuum bands are defined by IF bandpass filters and are converted to baseband using second local oscillators. A quadrature replica of each band is created using a phase-shifted second LO. The continuum baseband signals (both in-phase and quadrature-phase) are then digitized and processed by the correlators (C21 Correctors) [Landecker et al., 2000].

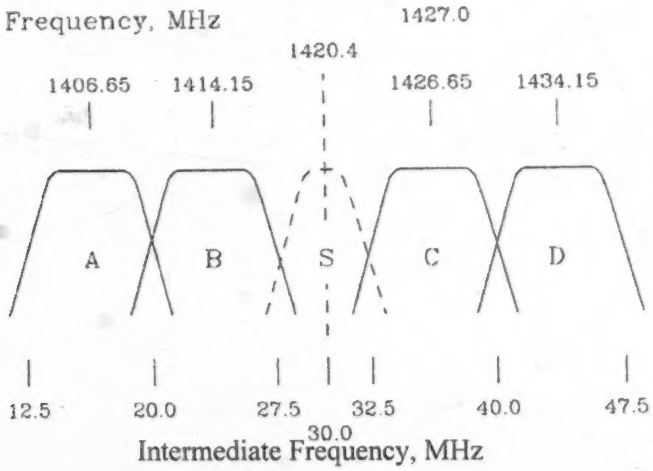

Figure 1.7 The continuum and spectroscopy bands near 1420 MHz. S is the HI band and A, B, C and D are the continuum bands [Landecker, private communication, 2001].

1.8.4 C21 Correlator

The correlator is a circuit that performs the multiplication and averaging of the signals in a modern interferometer. At DRAO, the 1420 MHz continuum digital correlator system C21 [Landecker et al. 2000] is responsible for calculating products of all antenna pairs and forming the four Stokes parameters for polarization analysis. Figure 1.8 is a simple model of a correlation interferometer.

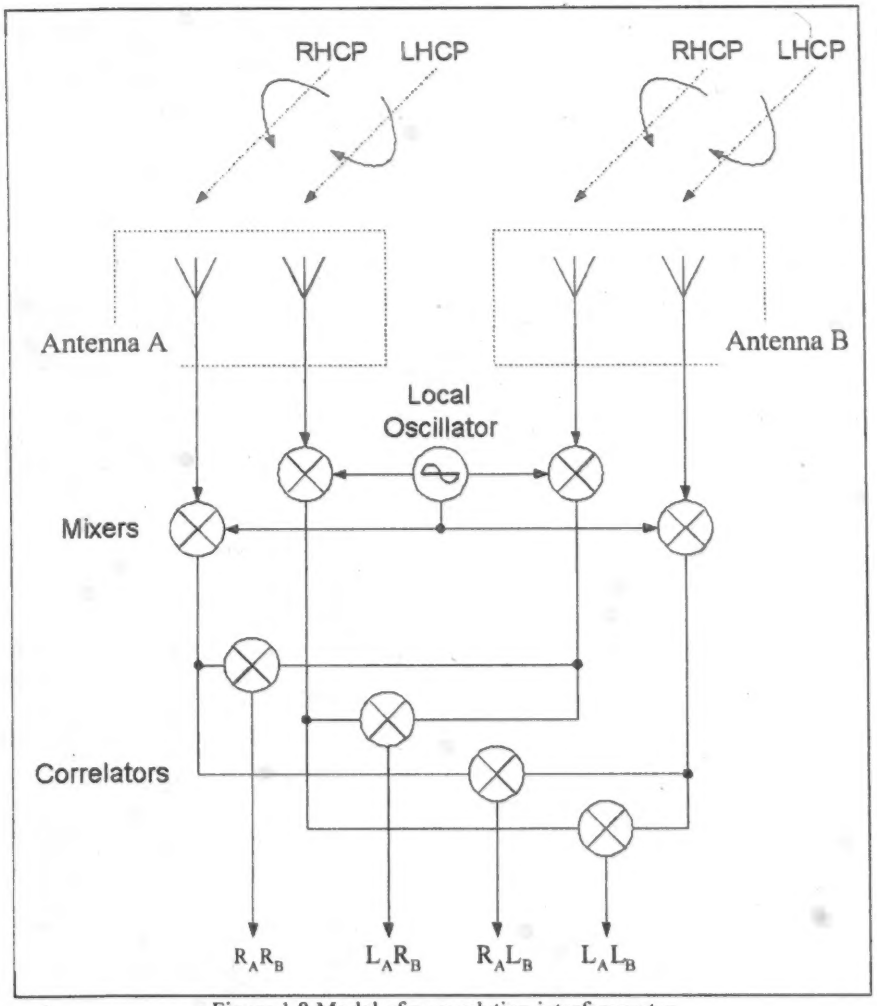

Figure 1.8 Model of a correlation interferometer

The input signals from each of the four sub-bands are digitized using 4-bit monolithic flash converters (AD 9688) running at 20 MHz, a frequency slightly faster than the Nyquist sampling rate for the 7.5 MHz bandwidth. The 4-bit analog-to-digital converter has 16 possible output levels, but only 14 are used to represent the in-phase and quadrature-phase signals. The other two A/D output levels, 0000 and 1111, are reserved for control purposes. With the fourteen-level representation of the input signals and moderate over-sampling, the C21 correlator achieves a very high correlator efficiency (η_c = 0.985) [Landecker et al., 2000].

After digitizing the input signals, each correlator module multiples two 4-bit inputs and the output is an 8-bit number. The product is accumulated for 5.6 seconds. The occurrence of 0000 at either input causes accumulation to stop and the output is read by the system microprocessor. The occurrence of 1111 on either one of the inputs causes the multiplier to produce an 8-bit output corresponding to the square of the 4-bit input on the other input channel. This output corresponds to the power of the input signal [Landecker et al, 2000]. After the correlator computes the products of all the antenna pairs, the sums and differences of the output signals are taken to form the Stokes Parameters [Gray, 1998] (see section 3.2).

$$2I = R_A R_B + L_A L_B \tag{1.8.3}$$

$$j2Q = R_A L_B - L_A R_B \tag{1.8.4}$$

$$2U = R_A L_B + L_A R_B \tag{1.8.5}$$

$$2V = R_A R_B - L_A L_B \tag{1.8.6}$$

1.8.5 Canadian Galactic Plane Survey

The principal project of the DRAO Synthesis Telescope is the Canadian Galactic Plane Survey (CGPS), a project to create mosaicked images of atomic hydrogen line and polarized emission of the Milky Way galaxy at 1420 MHz. The CGPS is a high resolution multi-wavelength study of the interstellar medium (ISM) carried out by DRAO in collaboration with several universities and observatories. The DRAO Synthesis Telescope is contributing data on the 21 cm continuum in Stokes I, Q and U, 74 cm Stokes I continuum and 21 cm HI spectral line with 256 channels. This survey is a major initiative to gain understanding of the states and physical processes within the ISM through the study of dust grains, molecular gas, atomic gas, ionized gas and relativistic plasmas. The first phase of the CGPS, begun in 1995 and completed in 2000, covered the Galactic plane in longitude (l) from 74.2° to 147.3° and latitude (b) from –3.6° to +5.6°. The second phase of observation CGPS 2 is now in progress. CGPS 2 will extend the

observation limits to cover longitude 64° to 175°. Observation of the plane $100° < l < 117°$ will extend to 17.5° latitude [Knee, 2003].

The CGPS has inspired the International Galactic Plane Survey (IGPS), a joint effort to image nearly the entire Galactic plane. The centimeter-wavelength surveys of the IGPS will incorporate the first and second phase of the CGPS, the Southern Galactic Plane Survey by the Australia Telescope and the VLA Galactic Plane Survey. The IGPS will also include millimeter-wavelength and infrared surveys.

1.9 Topics of Thesis

After a brief description of the Synthesis Telescope, this thesis details a project to improve the performance of the telescope by improving its sensitivity and minimizing instrumental polarization. There are two sub-sections in this project: examination of methods to reduce ground noise and a study of instrumental polarization across the field of view of the telescope.

The second chapter focuses on the improvement of the telescope sensitivity by reducing antenna noise from the ground. There are four main contributors to ground noise:

- mesh leakage – ground noise that leaks through the reflector mesh
- direct spillover - ground radiation entering the feed from the region not blocked by the reflector
- strut scattering - noise entering the feed after being scattered by the feed legs
- rim diffraction - diffraction of ground noise around the reflector rim into the feed

The sources of ground noise and methods to reduce each noise contribution were examined. Then, experimental modifications of the Synthesis Telescope antennas were carried out to evaluate the effectiveness of the noise reduction methods. In addition, suggestions to modify the antennas to achieve a better noise performance were presented.

The third chapter is a study of the instrumental polarization across the field of view of a paraboloidal antenna. Instrumental polarization hinders the ability of a telescope to determine the polarization state of a celestial source or the distribution of polarization across an extended source. An antenna modeling software package GRASP8 was used to compute the instrumental polarization numerically. An assessment of the role of each antenna component in creating instrumental polarization is discussed in detail. This knowledge will assist in the modification of the Synthesis Telescope to achieve better polarization performance. In addition, the quantitative results can be used for telescope calibration and correction of the Stokes parameter images.

Chapter 2 Ground Noise

2.1 Introduction

The goal of this section of the project is to reduce the current level of ground noise from 14.3 K to 8 K. By combining the results of this project concerning ground noise reduction with another project concerning receiver noise reduction, the total system temperature is expected to be halved and the sensitivity of the Synthesis Telescope at 1420 MHZ doubled.

Thermal emission from the ground, or ground noise, adds to the system temperature and degrades the sensitivity of the telescope. The sensitivity is a measure of the weakest signal that can be distinguished from the random fluctuations at the output of the receiving system which are caused by noise inherent in the receiving system, represented by the system noise T_{sys}. The minimum detectable signal is directly related to T_{sys}. The primary sources of system noise are the receiver and the antenna. The receiver noise is due to the thermal energy in the receiver electronics. Losses in the transmission line between the antenna and the receiver also contribute to the total receiver noise. Antenna noise includes noise due to ground radiation, thermal emission from the atmosphere, and background radio emission from the Galaxy and the signal from the radio source.

In this chapter, the sources of ground noise and methods to reduce this noise by modifying the antenna will be studied in detail. The four contributors of ground noise are (1) leakage through mesh, (2) direct spillover, (3) strut scattering and (4) diffraction around the reflector rim. The levels of noise contributed by each factor and the noise reduction achievable by each antenna modification were predicted theoretically based on the method of ray tracing. Then, actual modifications of the Synthesis Telescope antenna were made. The measured results were compared to the theoretical calculations and were used to evaluate the effectiveness of each noise reduction method.

2.2 Theory of Antenna Temperature

Antenna temperature is defined as the temperature of a fictitious resistor which delivers thermal power per unit bandwidth equal to that delivered by the antenna [Kraus, 1986]. It is an effective temperature and not the physical temperature of the antenna structure. First consider a resistor of resistance R at temperature T; the thermal noise power per unit bandwidth available at the terminals is given by the Nyquist equation.

$$w = kT \tag{2.2.1}$$

where

w = spectral power, W Hz^{-1}

k = Boltzmann's constant, 1.38 x 10^{-23} J K^{-1}

T = absolute temperature of the resistor, K

If the resistor is replaced by a lossless matched antenna of radiation resistance R, the impedance presented at the terminals is unchanged. The thermal radiation picked up by the antenna in an enclosure of absorbing walls at temperature T would be the same as the power delivered by the resistor. Consider an antenna pointing towards the sky as shown in Figure 2.1. The power per unit bandwidth received by the antenna is [Kraus, 1986]

$$w = \frac{1}{2} A_e \iint B(\theta,\phi) P_n(\theta,\phi) d\Omega \tag{2.2.2}$$

where

w = received spectral power, W Hz^{-1}

A_e = effective aperture of the antenna, m^2

$B(\theta,\phi)$ = brightness of the sky, W m^{-2} Hz^{-1} rad^{-2}

$P_n(\theta,\phi)$ = normalized power pattern of the antenna, P(0, 0) = 1

$d\Omega$ = infinitesimal solid angle of the sky (= $\sin\theta \, d\theta \, d\phi$), rad^2

This equation can be thought of as a convolution of the antenna response with the brightness of its environment. If the source is randomly polarized, which is true in the case of thermal ground noise, and the antenna responds to only one polarization

component, then only half of the incident power will be received. Therefore, the factor 1/2 is introduced in (2.2.2).

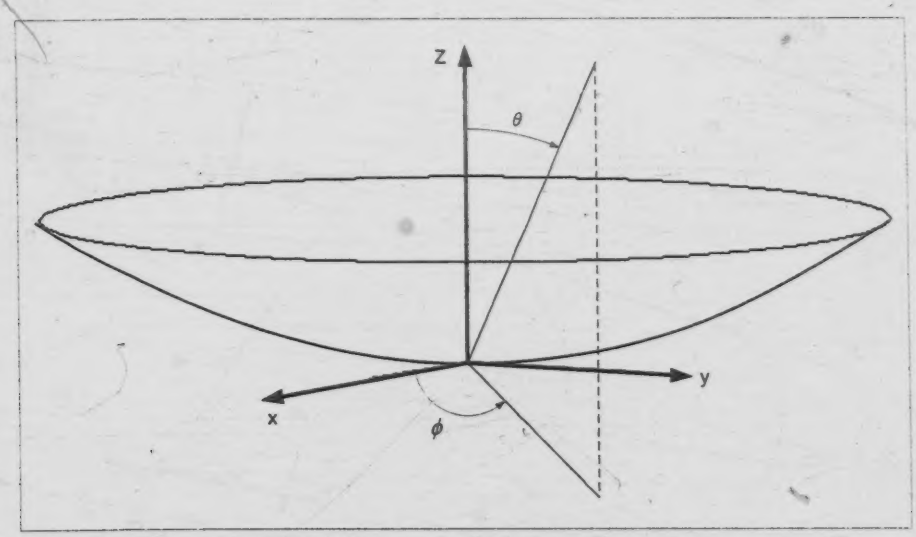

Figure 2.1 Antenna and spherical coordinate system

Brightness, or intensity of radiation, is characterized by the radiation emitted by a blackbody at temperature T at frequency f. A blackbody is a fictitious object that absorbs all the radiation falling on it. It is also a perfect emitter of radiation. The brightness of the radiation from a black body is given by Planck's radiation law (1.6.1). At radio frequencies, the product hf is very small compared to kT ($hf << kT$); the exponential term in (1.6.1) can be approximated by the first two terms in the Taylor series expansion:

$$B = \frac{2kT}{\lambda^2} \tag{2.2.3}$$

where λ is the wavelength of the radiation. This relation is known as the Rayleigh-Jeans law, valid for approximating brightness in the radio region of the electromagnetic spectrum.

If the antenna is placed inside a blackbody enclosure at temperature T, then the brightness will be constant in all directions. Inserting the constant brightness into (2.2.2), the power equation becomes

$$w = \frac{kT}{\lambda^2} A_e \Omega_A \tag{2.2.4}$$

The solid angle of the antenna, Ω_A, is a measure of the antenna's ability to concentrate radiation when transmitting, or to select radiation directionally when receiving. It is given by the integral of the normalized power pattern over a sphere.

$$\Omega_A = \iint_{4\pi} P_n(\theta,\phi) d\Omega \tag{2.2.5}$$

Substituting $A_e \Omega_A = \lambda^2$ into (2.2.4), the equation becomes $w = kT$, which is the same expression as the noise power from the resistor. Therefore, the antenna temperature can be found by inserting (2.2.3) into (2.2.2) and then equating that to (2.2.1):

$$T_A = \frac{A_e}{\lambda^2} \iint T_s(\theta,\phi) P_n(\theta,\phi) d\Omega \tag{2.2.6}$$

or

$$T_A = \frac{1}{\Omega_A} \iint T_s(\theta,\phi) P_n(\theta,\phi) d\Omega \tag{2.2.7}$$

where $T_s(\theta, \phi)$ is the temperature of the environment around the antenna. The evaluation of antenna temperature requires the knowledge of the radiation pattern of the antenna and the brightness temperature distribution in the environment of the antenna.

2.2.1 The Antenna Temperature of the Synthesis Telescope

At 1420 MHz, the antenna noise level before performing any antenna modification was estimated to be 20.2 K [Landecker, private communication, 2001] when the antenna is directed towards the zenith. The total noise is calculated by taking the geometric mean among the seven antennas. The two sources of T_A are noise from the sky and thermal radiation from the ground.

Contributions to antenna temperature arising from the sky cannot be eliminated. Noise accompanying atmospheric attenuation at 1420 MHz contributes approximately 2.0 K [Anderson et al., 1991] when the antenna is pointing at the zenith. This noise is proportional to the secant of the zenith angle. Thus, its effect is very significant at large zenith angles. The combination of cosmic microwave background radiation with galactic emission contributes approximately 3.7 K (when not tuned to the HI line). Together, the sky contributions account for 5.7 K of the total antenna temperature at the zenith.

Using (2.2.7), the ground noise contributions to antenna temperature can be calculated. There are four mechanisms by which ground radiation enters the antenna. (1) Mesh leakage - the ground radiation leaks through the reflector mesh and enters the feed as a source of ground noise. (2) Spillover contribution – the spillover region is between the edge of the reflector (as seen from the feed) and the horizon. Ground radiation in this region is not blocked by the reflector, and therefore enters the feed directly. (3) Strut scattering - ground radiation enters the feed after being scattered from the feed support struts. Radiation may be scattered from the struts onto the reflector and then into the feed (plane wave scattering), or it may enter the feed directly after scattering from the struts (spherical scattering). (4) Diffraction at rim - ground radiation diffracts around the rim of the reflector into the feed. Figure 2.2 illustrates the contributions to antenna temperature for Antenna 7 (far east antenna) of the Synthesis Telescope. The values for each of the ground noise contributions were calculated theoretically based on the method of ray tracing using the techniques developed in this thesis. The computation approaches are discussed in detail in the following sections. As a result of different construction, each of the seven antennas receives a different level of ground noise. Table 2.1

summarizes the initial level of ground noise for each antenna. The geometric mean of the seven antenna totals is 14.3 K. Adding the sky contribution of 5.7 K, gives a total antenna contribution to system noise of 20.0 K, agreeing closely with previous estimation [Landecker, private communication, 2001]. This is a significant quantity because the contribution from the source in the main beam is usually less than 10 K except in HI-line observation.

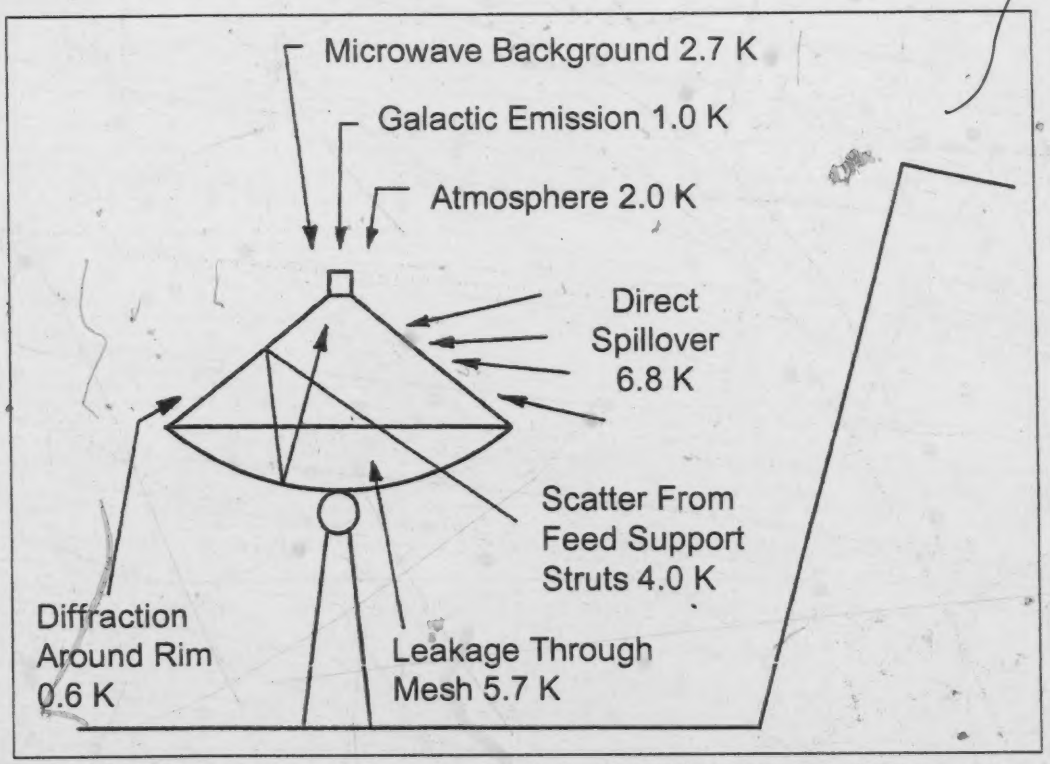

Figure 2.2 Contributions to antenna temperature for the Synthesis Telescope Antenna 7 (Diagram adapted from Anderson et al., 1991 with new values for the contributions to antenna temperature derived in this thesis)

Antenna	Mesh Leakage (K)	Direct Spillover (K)	Strut Scattering (K)	Diffraction at rim (K)	Total (K)
1	5.7	6.8	4.0	0.60	17.1
2	5.7	6.8	4.5	0.60	17.6
3	1.4	6.8	5.9	0.60	14.7
4	1.4	6.8	4.5	0.60	13.3
5	1.4	6.8	2.3	0.60	11.1
6	1.4	6.8	2.3	0.60	11.1
7	5.7	6.8	4.0	0.60	17.2

Table 2.1 Initial noise contribution attributable to radiation from the ground. These values are calculated using the techniques developed in this thesis

In the following sections, the four ground noise contributions, leakage through mesh, direct spillover, strut scattering, and edge diffraction, and the approaches to reduce these contributions will be discussed in detail. First, each of the ground noise contributions will be examined theoretically by applying equation (2.2.7). The theoretical model will be used to predict the expected noise reduction when the antenna is modified. Then, the method and results of the actual antenna modification experiments carried out to verify the prediction will be presented.

2.3 Celestial Coordinate System

The two most frequently used coordinate systems for defining the position of celestial objects are the horizon system and the equatorial system [Kraus, 1986]. In both systems, objects are located by the intersection of a great circle perpendicular to the plane of reference and a small circle parallel to the plane of reference on the celestial sphere. The celestial sphere is an imaginary sphere of infinite radius with the earth at its center. The difference between the two systems is the plane of reference. The horizon system is based on a plane parallel to the observer's horizon and the equatorial system is based on a plane through the earth's equator.

In the horizon system, the position of an object on the celestial sphere is described relative to an observer's horizon and the meridian which is the great circle through the north and south point and the zenith (Figure 2.3). The poles of this system are the zenith

(vertically above the observer) and the nadir (opposite the zenith). The coordinates of an object are given by altitude (a) and azimuth (A), thus this system is also known as the alt-az system. Altitude is measured upward from the horizon along the object circle, the great circle through the object and the zenith, to the object. Zenith angle is similar to altitude, but it is measured downward from the zenith to the object. The sum of altitude and zenith angle is 90°. Azimuth is the horizontal angle measured along the horizon from the north clockwise to the object circle.

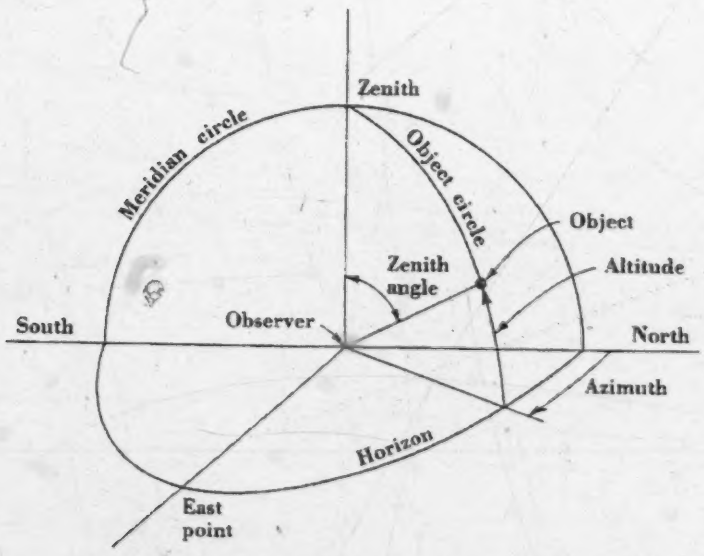

Figure 2.3 The horizon coordinate system [Kraus, 1986]

The horizon system is a local coordinate system; two observers at different points on the earth's surface will measure different altitudes and azimuths for the same object at the same time. In addition, the alt-az coordinates of a celestial object change continuously during the day because of the earth's rotation. Thus, this system is less convenient for defining the position of a celestial object than the equatorial coordinate system which defines fixed coordinates for objects.

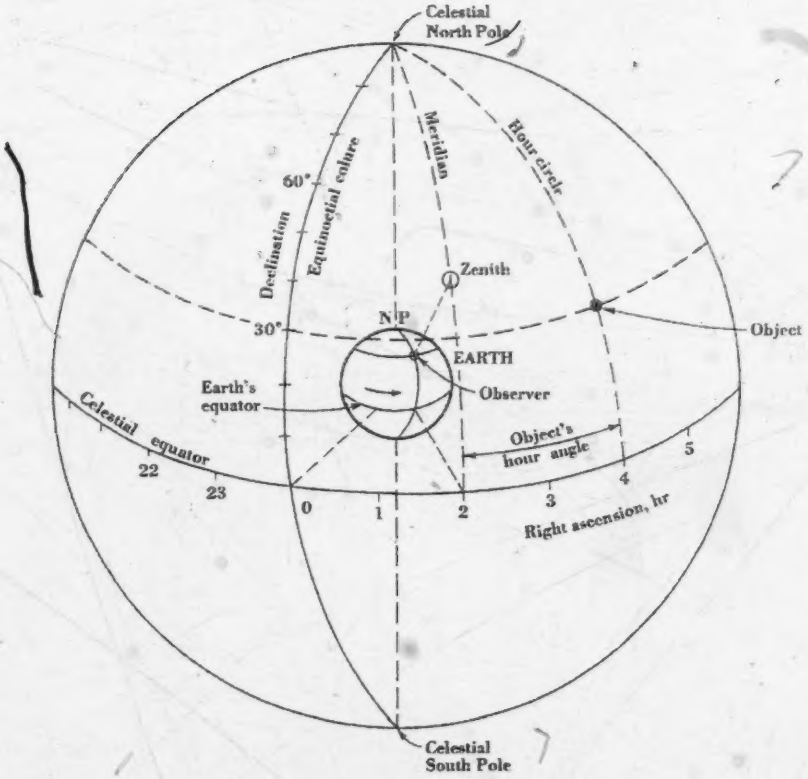

Figure 2.4 The equatorial coordinate system [Kraus, 1986]

The earth's equator is the plane of reference in the equatorial coordinate system. The north and south celestial poles are determined by projecting the rotation axis of the earth to intersect the celestial sphere (Figure 2.4). The great circle that intersects the earth's equator is the celestial equator. The great circle which passes through the celestial poles and the observer's zenith is the meridian circle and the great circle which passes through the celestial poles and the object is the hour circle. The coordinates of a celestial object are given in right ascension (α) and declination (δ). Right ascension is usually measured along the celestial equator from the reference direction, the vernal equinox, which is the intersection of the equinoctial colure with the celestial equator, to the object's hour circle. The equinoctial colure is the great circle through the celestial poles and the vernal equinox (the vernal equinox is the point at which the sun crosses the celestial equator in March). Right ascension is usually measured in units of time, hours, minutes and seconds, rather than degrees of arc. Since a 360° rotation by the earth

corresponds to 24 hours sidereal time, then 1 hour equals 15^{o} of arc. The angular distance between the hour circle and the observer's meridian is called the hour angle (*HA*). The relation between the hour angle and the right ascension of an object is given by

$$HA = \alpha_{meridian} - \alpha_{object} \tag{2.3.1}$$

Due to the rotation of the earth, hour angle increases uniformly with time. Diurnal motion of a star is along its parallel of declination in the course of a day. Declination is measured along the object's hour circle from the celestial equator to the object. This angle is expressed in degrees, minutes and seconds and is positive if the object is north of the celestial equator and negative if south.

The antennas used in the Synthesis Telescope are equatorially mounted. They are driven around two perpendicular arcs, one of which is parallel to the Earth's axis. Since the antenna temperature is affected by the antenna's surrounding and the pointing direction, it is a function of altitude and azimuth. However, observations are recorded in declinations and hour angles. Therefore, converting the antenna pointing from equatorial coordinates to horizon coordinates is necessary for the study of antenna temperature. Transformation equations from the equatorial system to the horizon system are [Lang, 1980].

$$\sin a = \sin\delta \sin\phi + \cos\delta \cos HA \cos\phi \tag{2.3.2}$$

$$\sin A = \frac{-\cos\delta \sin HA}{\cos a} \tag{2.3.3}$$

$$\cos A = \frac{\sin\delta \cos\phi - \cos\delta \cos HA \sin\phi}{\cos a} \tag{2.3.4}$$

where

a = altitude

A = azimuth

δ = declination

HA = hour angle

ϕ = observer's latitude. At DRAO, the latitude is 49.32°

2.4 Actual Measurements

The Synthesis Telescope has a gain monitor that spans the entire signal path, from antenna feed to correlator output. Small modulated noise signals are injected into each antenna feed, and are demodulated from autocorrelation outputs to give continuous measurements of system gain and system temperature [Landecker et al, 2000]. The measured system temperature was used throughout this part of the project to record the system temperature before and after each experimental modification was performed on the Synthesis Telescope antennas. The Synthesis Telescope noise measurement system is able to detect 0.5 K changes accurately. This information was used to evaluate the effectiveness of each modification.

2.4.1 Calculation of System Temperature

The absolute system temperatures (T_{sys}) of each individual antenna are recorded as the Synthesis Telescope completes 12-hour observations. Values for T_{sys} are calculated using a software routine **demod_noise_proc** [DRAO software] by comparing the ratio between the reference noise source T_a and the temperature detected by each antenna during the observation. The computation of T_{sys} requires two antenna parameters, a gain calibration factor g_a and the level of injected noise T_a, for each individual antenna. The gain calibration factor g_a converts the measured power density (W/m^2) to antenna temperature (K).

$$g_a = \frac{\eta_A A_P}{2k} \tag{2.4.1}$$

where the subscript a denotes a solution for each of the 7 antennas, A_P is the physical area of the reflector, $A_P = \frac{\pi D^2}{4}$ and η_A is the aperture efficiency which is assumed to be 0.55 for all Synthesis Telescope antennas at 1420 MHz.

Noise sources of approximately 1 K are injected into the signal path at the focus box before the first amplifier of each antenna. The exact level of this noise source was measured by Walter Wyslouzil in 1996. The measured values of noise level (T_a) for each individual antenna are listed in Table 2.2.

Antenna a	T_a K
1	0.90
2	1.02
3	0.92
4	0.77
5	1.13
6	1.14
7	0.91

Table 2.2 The level of injected noise for each of the seven antennas. [Del Rizzo, 2003]

The noise sources for all the antennas are switched on and off according to the 8-step, 45s long Walsh cycle of Antenna 5 [see Chapter 1]. The raw data are autocorrelated or squared, linearized and then processed by **demod_noise_proc**. The first step in the calculation of T_{sys} is to determine the value of system gain (G). In **demod_noise_proc**, the autocorrelation data are demodulated by the Walsh cycle and then averaged over 90s (2 Walsh cycles). The result is a value for the average noise amplitude $N_{a,P}$ [Del Rizzo, 2003] for each of the 7 antennas and the 2 polarizations (L and R) denoted by subscripts a and P respectively.

$$N_{a,P} = \frac{\sum_{2W} A_{a,P} \cdot W_5}{n_W} \tag{2.4.2}$$

where

$A_{a,P}$ = the 8 consecutive linearized autocorrelated samples that comprise one Walsh cycle

W_5 = Walsh cycle of Antenna 5

n_W = number of samples in one Walsh cycle = 8

Despite averaging over 2 Walsh cycles, the calculation of $N_{a,P}$ requires a division by the length of only one Walsh cycle, because, after demodulating the raw data, $N_{a,P}$ is non-zero only when the W_5 is "on", which is half of the cycle length. The values of system gain for each Synthesis Telescope antenna $G_{a,P}$ [Del Rizzo, 2003] are calculated for each 90 s interval using the gain calibration factor g_a and noise level T_a.

$$G_{a,P} = \sqrt{\frac{N_{a,P} g_a}{2T_a}} \tag{2.4.3}$$

The next step is to average the raw linearized autocorrelation data over two Walsh cycles for each antenna and for each polarization.

$$R_{a,P} = \frac{\sum_{2W} A_{a,P}}{2n_W} \tag{2.4.4}$$

Then, T_{sys} [Del Rizzo, 2003] is obtained by dividing the 90s integration of the autocorrelation sample by the gain value $G_{a,P}$, over the same integration period.

$$T_{sys_{a,P}} = \frac{R_{a,P}}{G_{a,P}} \tag{2.4.5}$$

Values for T_{sys} calculated using **demod_noise_proc** are output in files named *timestamp*.TSYS_C21*F*. The label *timestamp* refers to the start time of the observation and has the format DDMMYY_HHMM. Four system temperature files are created for each observation. *F* represents the four observation bands A through D [see Chapter 1]. These files contain binary values of T_{sys}.

2.4.2 Data Processing

Each system temperature file contains the noise temperature values of the four channels for each of the seven antennas as a function of time. For each antenna, the system temperatures of the in-phase and quadrature signals for both right-hand circular polarization (RHCP) and left-hand circular polarization (LHCP) are collected. These data represent the four channels, in-phase RHCP, quadrature RHCP, in-phase LHCP and quadrature LHCP, and the channels A to D are numbered from 1 to 4 respectively. Within each channel, there are 8 system temperature values representing the 7 Synthesis Telescope antennas and an empty slot that contains zero. These sets of 32 numbers are recorded into the file in 90-second intervals during the observation (Figure 2.5).

$$
\begin{array}{ll}
t=0 & \left[\begin{array}{lll}
channel\ 1: & in-phaseRHCP & \{antenna1-8 \\
channel\ 2: & quadRHCP & \{antenna1-8 \\
channel\ 3: & in-phaseLHCP & \{antenna1-8 \\
channel\ 4: & quadLHCP & \{antenna1-8
\end{array}\right. \\
t=1 & \\
t=2 & \\
\vdots & \\
\vdots &
\end{array}
$$

Figure 2.5 Structure of the system temperature files

A C program, **Time.c**, was written to select a set of observation data representing a specific antenna and a specific channel from the system temperature files and to determine the antenna zenith angle and azimuth at each time interval. In addition, a simple filter was implemented to eliminate unwanted interference spikes. When the

antenna and channel number were entered, the program selected the set of observation data by storing the noise temperature values into an array if the following Boolean function was true.

$$x\%32 == (channel - 1) * 8 + (antenna - 1) \qquad (2.4.6)$$

Here x is the data counter; it labels the first T_{sys} value in the file as number zero and increments as the program reads from the binary file. The "==" symbol means "equivalent to" in C programming code and the "%" sign represents the modulus operator which yields the remainder of an integer division.

The next step was the interference filter implementation. Interference introduces sharp spikes in the noise temperature. Therefore, any data value that differs from the average of its previous and following values by more than 0.5 K was discarded. This filter limit is valid because the noise temperature cannot change as much as 0.5 K in the 90 second interval and interference spikes are usually in the order of several Kelvins. The antenna pointing altitude was computed using equation (2.3.2) and then subtracted from 90° to obtain the zenith angle. The azimuth angle was computed using (2.3.3) and (2.3.4). The declination and starting hour angle are given in the observation schedule. Hour angle in seconds at each time interval was calculated as follows:

$$HA = HA_start + time * 90 \qquad (2.4.7)$$

where time is an integer numbering the time interval. Finally, **Time.c** outputs an ASCII file with 3 columns of data: zenith angle, azimuth and noise temperature.

This program was used throughout the project to keep track of the change in the system noise temperature of the Synthesis Telescope as experimental modifications of the antennas were made. The data from before and after the modification were compared to determine the effectiveness of the modification. To be consistent, the system temperatures of channel 1 of band A were used in all the comparisons.

2.5 Mesh Leakage

There are two types of mesh used for the antenna reflectors of the Synthesis Telescope. The coarse mesh used on Antenna 1, 2 and 7 has openings of 15.875 mm (0.625"). The fine mesh used on Antenna 3, 4, 5 and 6 has openings of 9.525 mm (0.375"). Leakage through the mesh can be estimated using the nomograph of Mumford [1961]. At 1420 MHz, the transmission powers of the coarse and fine mesh are -17 dB and -23 dB respectively. Attenuation factors, α, of $10^{17/10} = 50$ and $10^{23/10} = 200$ were computed for the two types of mesh. Assuming a ground temperature of 300 K[1] and the antenna to be pointing at the zenith, the noise due to leakage through the mesh was calculated by integrating the antenna temperature formula (2.2.7) from the center of the reflector to the edge and then dividing it by the attenuation factor.

$$T_{mesh} = \frac{1}{\alpha}\frac{300}{\Omega_F}\int_{0^\circ}^{360^\circ}\int_{0^\circ}^{60^\circ} g(\theta',\phi')\sin\theta' d\theta' d\phi' \qquad (2.5.1)$$

The two coordinate systems illustrated in Figure 2.6 have origins at the vertex of the reflector and at the feed. The x and y axes of the two coordinate systems are pointed in the same direction. For Antennas 1 and 7, the edge of the reflector is 60° from the center of the reflector as seen from the feed. Ω_F, the feed solid angle, was calculated to be 1.20 sr. using (2.2.6). $g(\theta', \phi')$ is the normalized feed pattern and $\theta' = 0^\circ$ is directed down toward the vertex of the reflector as shown in Figure 2.6; note that this is a left-handed coordinate system. The magnitude of the co- and cross-polar patterns of the feed is illustrated in Figure 3.4. Since thermal radiation is randomly polarized, $g(\theta', \phi')$ is obtained by summing the co- and cross- polar components and then normalizing so that the maximum value of $g(\theta', \phi')$ is one. The above equation can be simplified by assuming the feed pattern to be perfectly circular. The integration over ϕ' can be replaced with 2π.

---

[1] 300 K is a rough estimation of the ground temperature. The actual effective temperature of the ground depends on the incident angle at which the radiation strikes the ground, frequency of the radiation and the ground properties. See section 2.6.1 for the calculation of the actual effective temperature.

$$T_{mesh} = \frac{2\pi}{\alpha}\frac{300}{\Omega_F}\int_{0^\circ}^{60^\circ} g(\theta')\sin\theta' d\theta' \qquad (2.5.2)$$

The calculated noise contributions are 5.71 K and 1.43 K for the coarse and fine mesh surfaces respectively. A mesh leakage noise of 1.43 K is tolerable, but a contribution of 5.71 K is too high. An effective way of eliminating the mesh leakage is to cover the reflector with a continuous conductive surface. When the reflector is shielded, the radiation from the ground cannot leak through, and therefore the noise temperature due to mesh leakage is eliminated. Two questions arise here: what material to use to shield the mesh to reduce leakage, and, how much of the reflector surface should be covered?

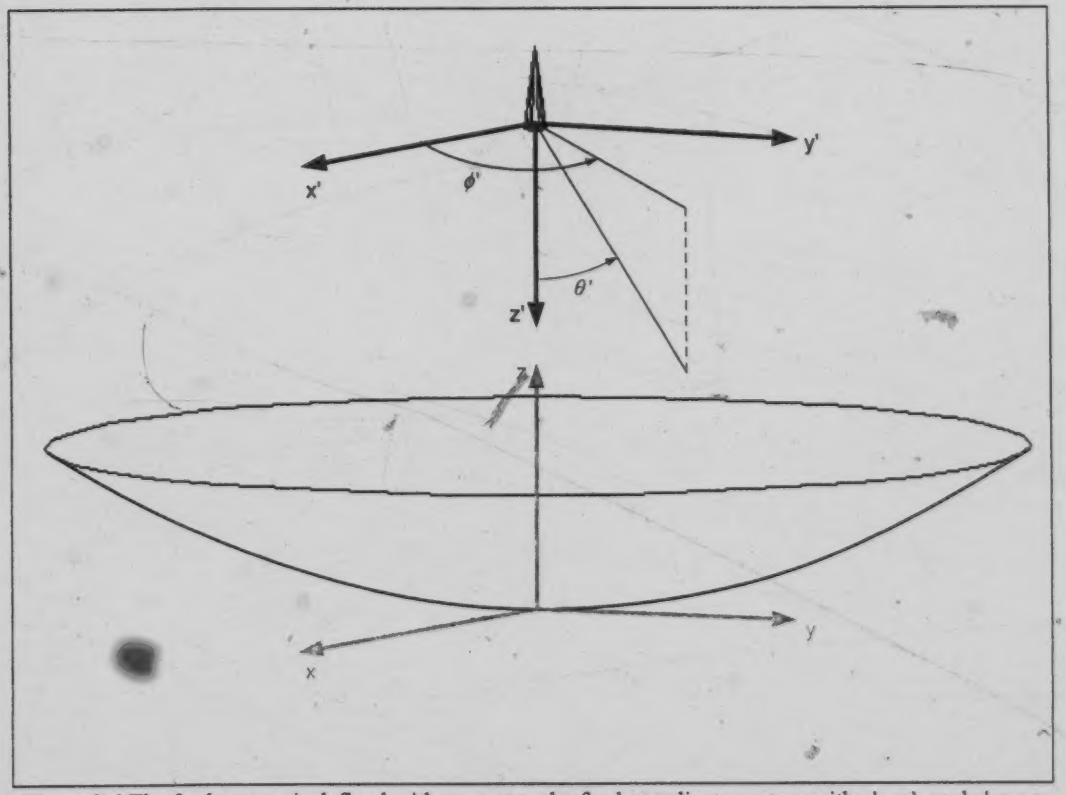

Figure 2.6 The feed pattern is defined with respect to the feed coordinate system with x'-, y'- and z'-axes.

The material used to cover the reflector should be lightweight and must be able to stand exposure to weather. Serious mechanical problems in the antenna steering control system could arise if too much weight is added to the reflector. A self-adhesive, auto body tape manufactured by 3M was chosen to cover the reflector. This aluminum tape is very lightweight. One roll of this tape is able to cover an area of 1.4 m^2 and weighs less than 1.0 kg. It is applied directly onto the reflector mesh. Previously, a piece of this tape was put on the side of the reflector by Tom Landecker. It remained on the dish reasonably well after two years.

The radiation pattern of the feed tapers off sharply towards the edge of the reflector. The noise contribution by leakage through the outer perimeter of the reflector should be smaller than the contribution by the central region. Therefore, it is more rewarding to shield only the center portion of the reflector. The problem of how much of the center of the reflector to shield will be investigated numerically in the next section by calculating the reduction in leakage noise as a function of the radius of the dish covered with solid metal.

2.5.1 Theoretical Calculation

A simple C program, **AntTemp.c** (written by the author), approximated the reduction in noise temperature due to mesh leakage for different radii, measured from the center, of the reflector covered with solid metal. Antenna 7 was considered in the program. It has coarse mesh and the attenuation factor is equal to 50. The ground was assumed to be a blackbody at a temperature of 300 K. This program integrated the antenna temperature equation (2.5.2) numerically.

$$T_{mesh} = \frac{2\pi}{\alpha}\frac{300}{\Omega_F}\sum_{n_{\theta'}=0^\circ}^{\theta_{solid}} f(n_{\theta'})\sin(n_{\theta'})\Delta n_{\theta'} \qquad (2.5.3)$$

where θ_{solid} is the angle measured from the center of the dish to the perimeter of the solid metal circle (Figure 2.7). This value is related to horizontal radius, r:

$$r = \frac{-1 + \sqrt{1 + \tan^2 \theta_{solid}}}{\tan \theta_{solid} / 2F} \qquad (2.5.4)$$

F is the focal length, which is equal to 3.81 m for Antenna 7. Figure 2.8 is a plot of the predicted noise reduction as the reflector is covered with solid metal starting from the center.

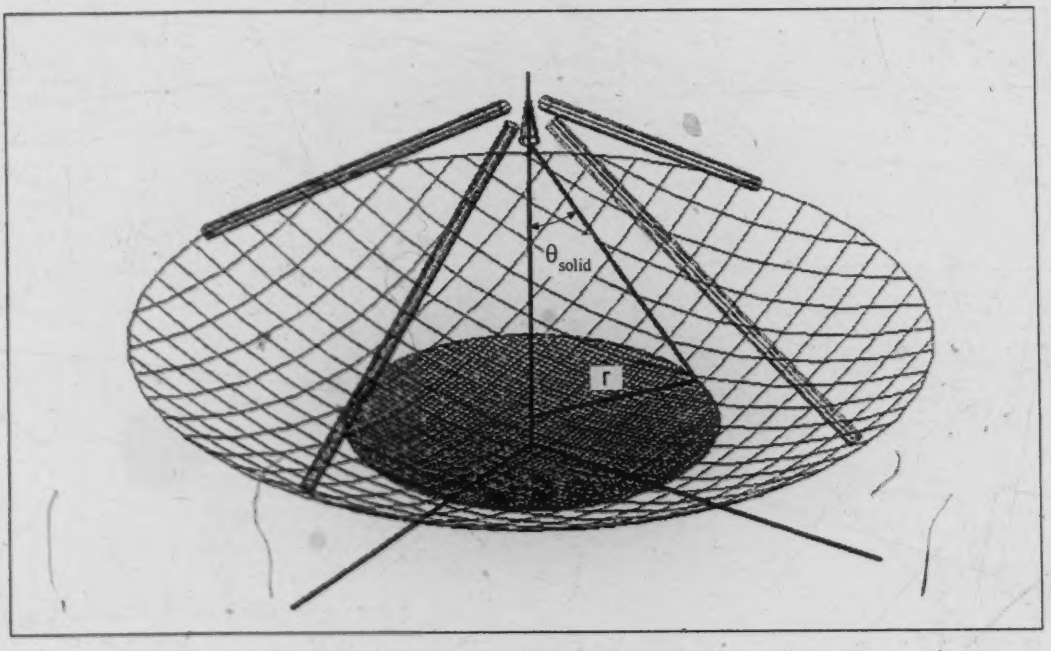

Figure 2.7 Geometry of the reflector with the central portion covered.

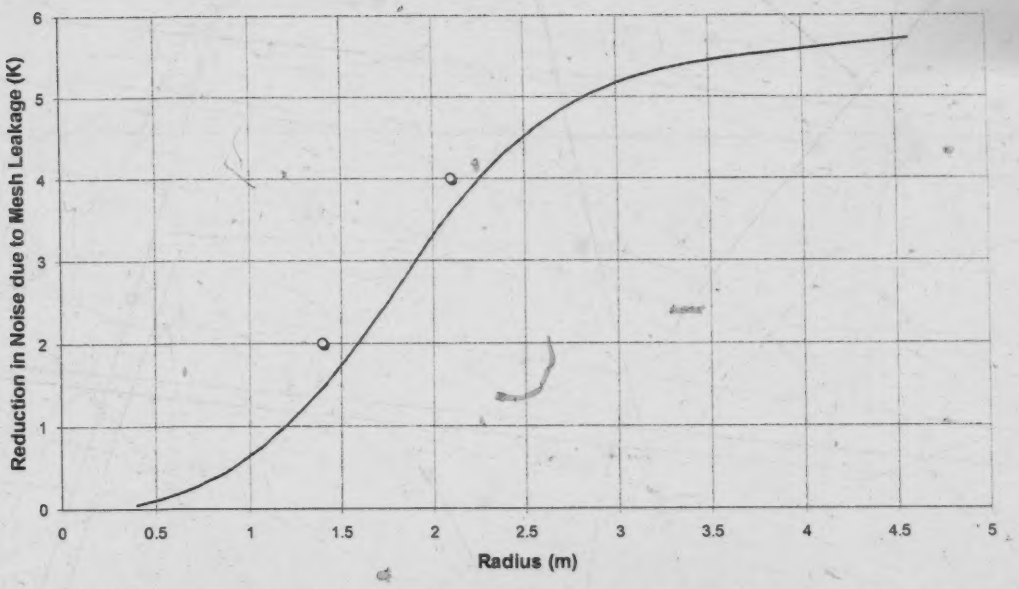

Figure 2.8 Reduction in noise from mesh leakage resulting from covering the central area of the reflector to radius r meters with solid metal. The circles shows experimentally determined values.

The relation between the radius and noise reduction is not linear because of the tapering of the feed pattern. Noise reduction increases exponentially at small radius, but levels off at larger radius, around 3 m. Therefore, it is sufficient to cover a radius of 2.5 m. Covering a larger radius will require a lot of material, yet the noise reduction will not be significant. If a radius of 2.5 m of the reflector is covered with the aluminum tape, a noise reduction of 4.5 K is expected. Then, the contribution to antenna temperature due to mesh leakage will reduce to 1.21 K.

2.5.2 Experimental results

Experiments were conducted to reduce the leakage through the mesh by covering the central portion of the reflector of Antenna 7 with 3M aluminum auto-body tape. The Synthesis Telescope repeats seven 12-hour observations in a four-day cycle. Within each cycle, approximately eight hours are reserved for maintenance. The aluminum tape was put on the reflector during this period. Therefore, the same seven observations were completed between each of the experiments. During the time of the experiment, four out of the seven observations were tracking objects at similar declinations (66° to 68°) and

starting hour angles (13h to 15h). The noise temperature data from these four observations were averaged to reduce the effects of fluctuations and instability in the data collecting mechanisms. Before the experiment, the pointing zenith angle for the four sets of Antenna 7 observations were computed using the C program **Time.c** (written by the author). These data were then averaged and plotted versus zenith angle (gray line in Figure 2.9). The same procedure was repeated after each experiment. In the first experiment, a circle of 1.4 m radius in the center of the reflector was covered. The noise temperature was reduced by 2 K (thin black line in Figure 2.9). These results are indicated on Figure 2.8 for comparison with theory. Then after covering 2.1 m radius of a 9-meter reflector, the noise temperature was successfully reduced by 4 K across all altitudes (thick black line in Figure 2.9). Figure 2.10 shows a picture of Antenna 7 after a circle of 2.1 m radius was covered with aluminum tape.

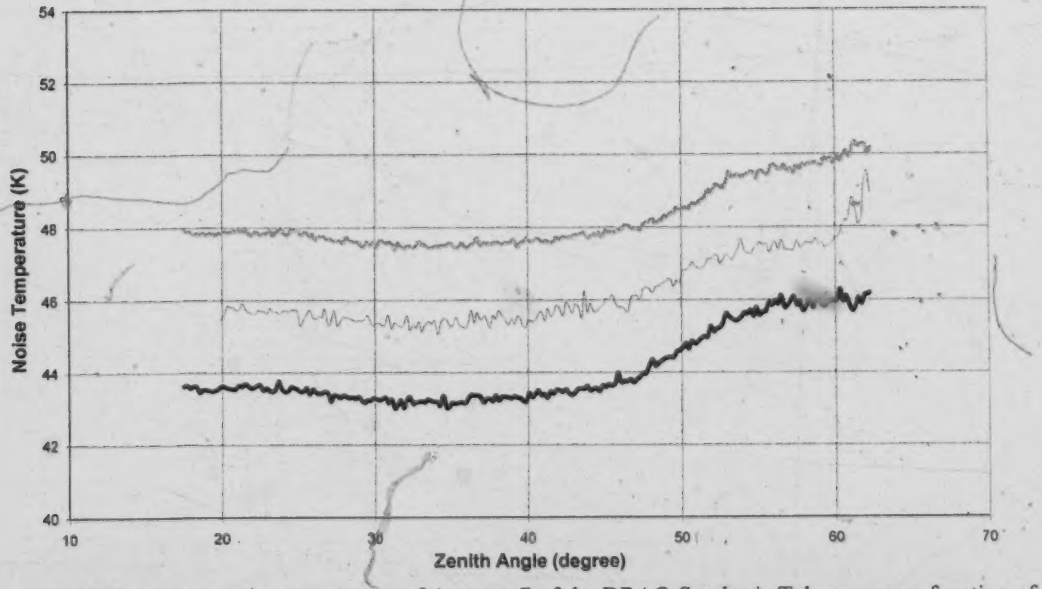

Figure 2.9 The system noise temperature of Antenna 7 of the DRAO Synthesis Telescope as a function of altitude. The gray line shows the noise temperature measured before the reflector was shielded. The thinner black line shows the noise temperature measured after a 1.4 m radius of a 9-m reflector was covered with aluminum tape. The thicker black line shows the noise temperature measured after 2.1 m radius was covered

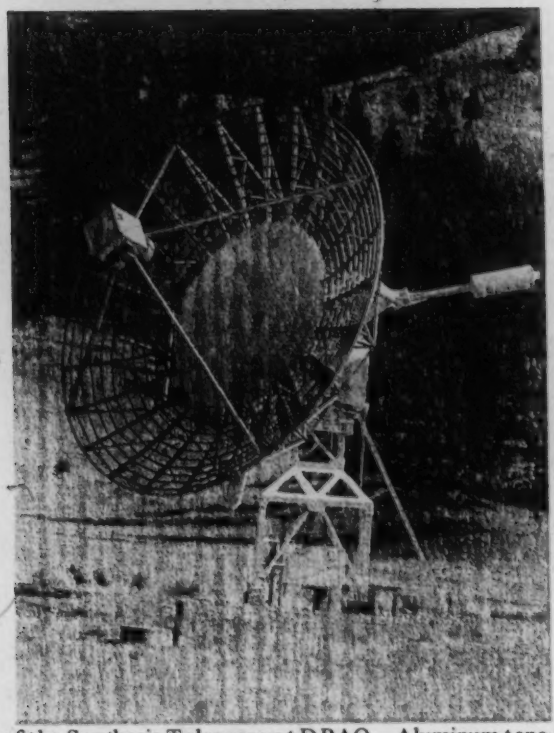

Figure 2.10 Antenna 7 of the Synthesis Telescope at DRAO. Aluminum tape covers the central 2.1 m radius of the reflector.

The results from both of these experiments agree well with the expected noise reduction calculated in section 2.4.1. Mesh leakage noise reductions of 1.5 K and 3.5 K were predicted when 1.4 m and 2.1 m radius of the reflector is shielded. The experimental result is a little better than the predicted value. An explanation could be the theoretical computation did not take into account the gaps between the panels on the reflector. Antenna 7 is constructed from 24 triangular sectors forming a parabolic shape. The gaps between the sectors are wider than the holes in the mesh and run from the center to the edge of the reflector. Thus, leakage through these gaps also adds to the noise temperature. As a result, sealing the mesh and the panel gaps yielded a larger noise reduction than the prediction.

2.6 Spillover

Spillover is the largest contributor to antenna noise. To understand the noise contribution due to spillover, consider the receiver at the focus of the antenna being replaced by a transmitter that radiates towards the reflector. The reflector does not intercept all the power radiated by the feed. The portion of radiation that is not intercepted by the reflector is called spillover. Similarly, when the radio telescope observes, the receiver will receive radiation from the spillover region. Since the radio telescope points to the sky, much of the spillover will fall on the ground which can be approximated as a blackbody radiating at approximately 300 K (see also section 2.6.1).

Geometric optics (GO) is assumed when calculating antenna noise due to spillover. GO uses ray methods without considering diffraction and other wave properties. Noise due to spillover can be calculated by integrating the antenna temperature equation (2.2.7) from the edge of the reflector to the horizon.

$$T_{spillover}(a,A) = \frac{1}{\Omega_F}\int_{0^\circ}^{360^\circ}\int_{60^\circ}^{horizon} T(\theta',\phi')\,g(\theta',\phi')\sin\theta'\,d\theta'\,d\phi' \qquad (2.6.1)$$

Where

Ω_F = feed solid angle = 1.20 Sr.

horizon = $180^\circ - a$ (a is the antenna pointing altitude)

$T(\theta', \phi')$ = the effective temperature of the ground

$g(\theta', \phi')$ = the normalized feed pattern

θ', ϕ' = angles in the feed spherical coordinate system as defined in Section 2.5

When the antenna is pointing at the zenith, the spillover region ranges from $\theta' = 60^\circ$ to 90° (Figure 2.11). However, the θ' range for the spillover region becomes larger ($\theta' = 60^\circ$ to 180°-a) when the antenna is tipped to a lower altitude. At DRAO, the nearby mountains rise above the nominal horizon to as much as 10° in certain directions as seen from the antennas. Radiation from ground above the nominal horizon has been ignored in this study since its contribution is very small. The contribution to spillover noise at different antenna pointing altitudes and azimuths was calculated using a C program, **Spillover.c**, written by the author.

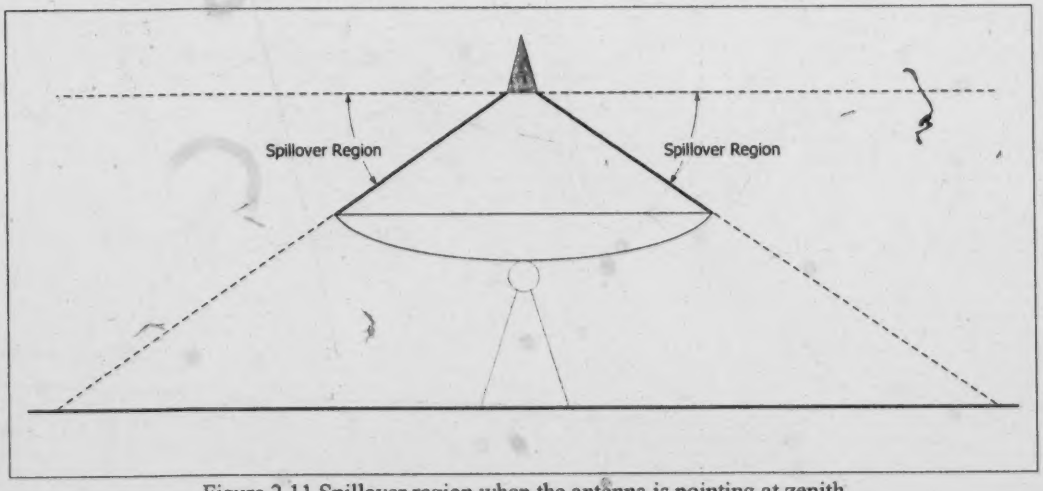

Figure 2.11 Spillover region when the antenna is pointing at zenith

The contribution to antenna temperature by spillover can be lowered by preventing the feed radiation from striking the ground. Reduction of spillover noise by attaching a shroud extending forward from the edge of the reflector was examined previously by Anderson [1989]. The shroud prevents ground radiation from entering the feed and thus lowers the antenna noise. However, it also raises the sidelobe level in the

front hemisphere, reduces antenna gain, and increases the level of cross polarization near the main beam. An experiment showed that when a cylindrical shroud of length l = 0.91 m was attached to the rim of one of the DRAO Synthesis Telescope antennas (d = 8.53 m), parallel to the antenna axis (Figure 2.12), the antenna temperature at 1420 MHz was reduced by approximately 8 K. At the same time, the antenna gain was decreased by about 4% [Anderson, 1989].

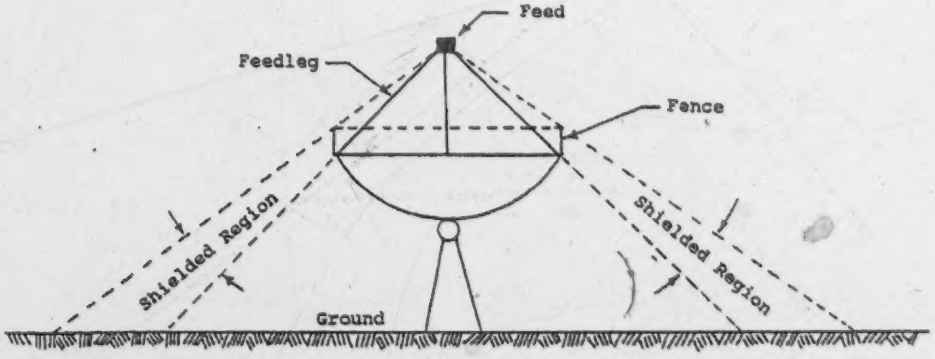

Figure 2.12 Reducing spillover noise by attaching cylindrical fence (shroud) to the rim of the antenna [Anderson, 1989]

The ground mesh method reduces spillover noise by putting mesh on the ground or building mesh fences around the antenna and avoids the risk of degrading the antenna performance. The effect of ground mesh can be understood by simple ray tracing. Consider an antenna pointing at the zenith and in the transmitting mode; a ray directed from the feed at angles beyond the reflector edge will strike the ground in the absence of any mesh on the ground. When mesh is placed on the ground, the ray will be reflected towards the cool sky (Figure 2.13). Since these rays are reflected away from the antenna, spillover reduction using ground mesh will not degrade the antenna performance. On the other hand, a vertical mesh fence will shield a greater amount of ground, but it will reflect radiation back towards the hot ground. Therefore, a mesh fence with a slanting angle θ_s is considered (Figure 2.13). Here, θ_s must be carefully calculated to avoid reflections towards the ground direction or back to the feed or antenna structure. The wire mesh used to build the fence has mesh sizes 3/4" x 3/4" with 19 BWG wires (0.042" in

diameter). Using the Mumford [1961] nomograph, the transmission power of this mesh is -15 dB at 21 cm. This mesh is available in rolls of 36" by 100'.

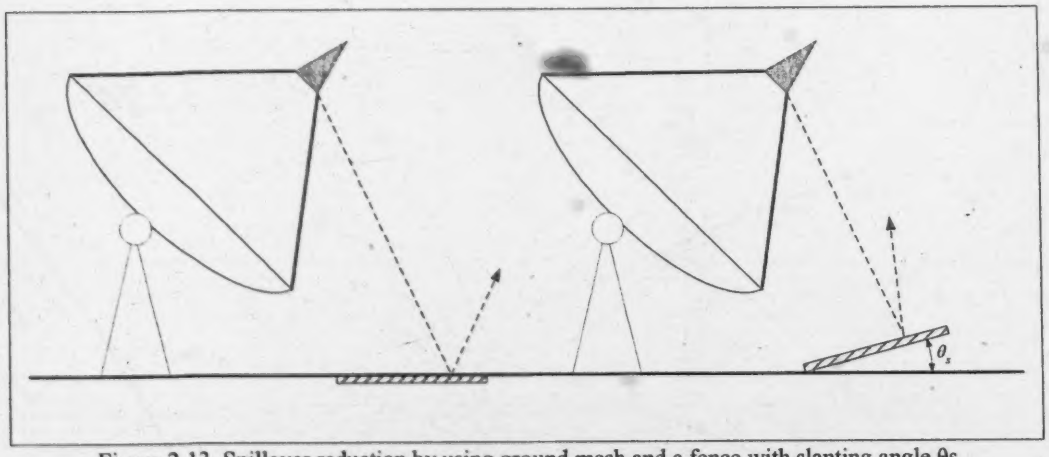

Figure 2.13 Spillover reduction by using ground mesh and a fence with slanting angle θs

In the following sections, noise contribution due to spillover when the antenna is pointing at different zenith and azimuth angles was calculated theoretically using geometric optics. In addition, the amount of noise reduction achieved by laying ground mesh and building mesh fences around the antenna was computed. Finally, experiments to reduce the spillover noise for Antenna 6, Antenna 1 and Antenna 7 of the DRAO Synthesis Telescope were performed based on these theoretical computations. The theoretical and experimental results were compared to evaluate the correctness of the computations and the effectiveness of the ground mesh method. Optimized mesh fence designs for Antenna 5 and the movable antennas (Antennas 2, 3 and 4) were also suggested for future plans to reduce spillover noise.

2.6.1 Theoretical Calculation

Noise due to spillover at different antenna pointing angles was calculated by a C program **Spillover.c**. This program also took into consideration the effect of ground mesh and slanted mesh fences on the brightness temperature seen by the antenna. It

computed the spillover noise temperature within an altitude (a) range of 10° to 90° (set by Synthesis Telescope observation limits) and an azimuth (A) range of 0° to 360°. For each antenna pointing, the spillover noise $T_{Spillover}(a, A)$ was calculated through ray tracing which determines the ground properties and the temperature seen by the feed at each θ' and ϕ' angle. θ' and ϕ' are defined in Figure 2.6. The spillover noise equation (2.6.1) was integrated numerically.

$$T_{Spillover}(a, A) = \frac{1}{\Omega_F} \sum_{n_{\phi'}=0^\circ}^{360^\circ} \sum_{n_{\theta'}=60^\circ}^{horizon} T(n_{\theta'}, n_{\phi'}) g(n_{\theta'}, n_{\phi'}) \sin(n_{\theta'}) \Delta n_{\theta'} \Delta n_{\phi'} \tag{2.6.2}$$

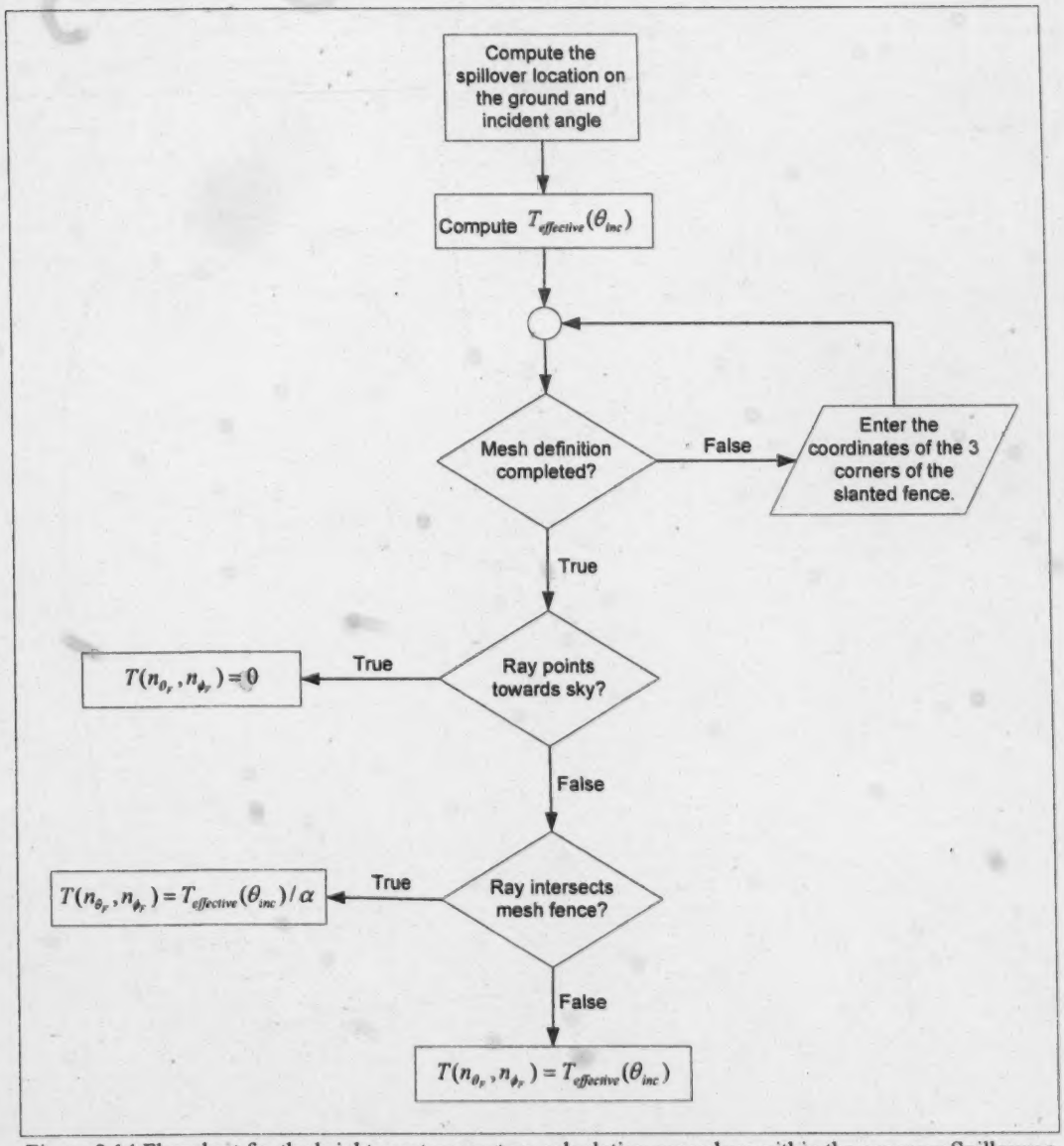

Figure 2.14 Flowchart for the brightness temperature calculation procedure within the program Spillover.c

The effective ground temperature is a function of the incident angle at which the radiation strikes the ground and is dependent on the frequency of the radiation and the ground properties (i.e. dielectric constant and conductivity). The relationship between the effective ground temperature at 1420 MHz at DRAO and the angle of incidence was measured experimentally [Anderson, 1989]. He showed that this relationship can be approximated by a piece-wise function (Figure 2.15). By writing the two linear

equations, the effective temperature of the ground can be estimated using the following equation.

$$T_{effective}(\theta_{inc}) = \begin{cases} 4.75\theta_{inc} + 155.02 & 0^o < \theta_{inc} \le 20^o \\ -0.18\theta_{inc} + 253.57 & 20^o < \theta_{inc} \le 90^o \end{cases} \qquad (2.6.3)$$

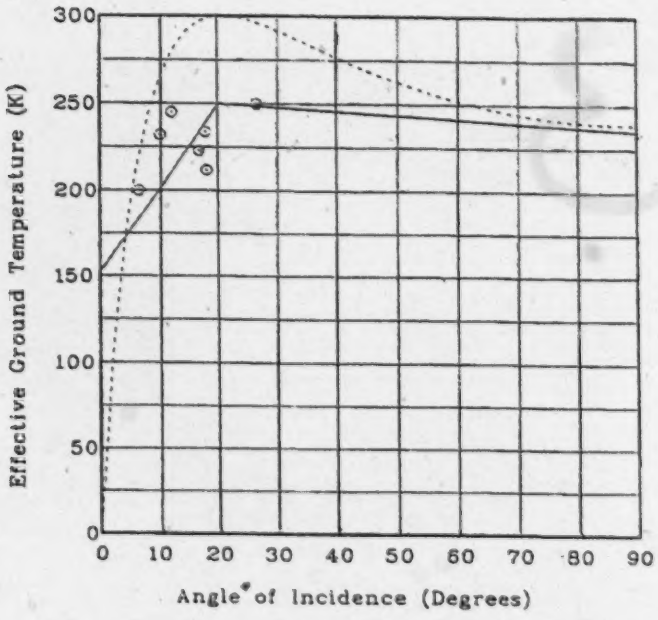

Figure 2.15 The effective temperature of the ground at 1420 MHz as a function of angle of incidence. [Anderson, 1989]

To calculate the incident angle, the location where the spillover radiation strikes the ground must be known. Using geometric optics, this location can be defined by extending a ray from the feed at an angle within the spillover region ($\theta' = 60^o$ to the horizon) to the ground. Figure 2.16 shows the three required coordinate systems, B, B' and P, to calculate the location of spillover on the ground (g). Coordinate system B' is the translated version of coordinate system B. Their z-axes point toward the zenith, x-axes point to the North and y-axes point to the East. Coordinate system B is located on the base of the antenna and the coordinate system B' is located at the feed of the antenna. The z-axis of coordinate system P is in the same direction as the antenna pointing, towards the source. When the antenna is pointing at the zenith, all three coordinate

systems have the same orientation. However, difficulties occur when the antenna is not observing at the zenith. Coordinate system P is rotated with respect to coordinate systems B and B'.

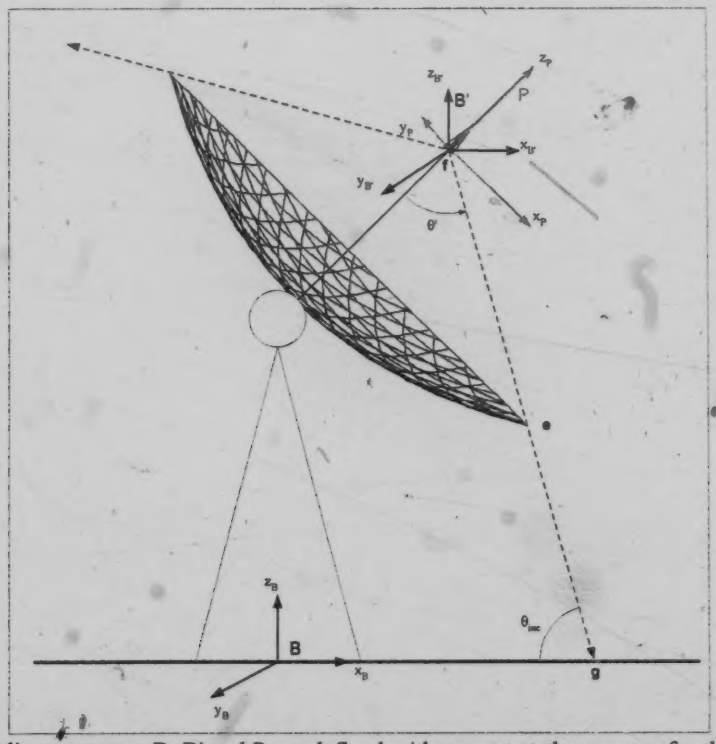

Figure 2.16 Coordinate systems B, B' and P are defined with respect to the antenna for the computation of spillover lobe on the ground. Also shown is the location of spillover on the ground using ray tracing.

To find the location of spillover on the ground, consider a ray from the feed at an angle ($\theta' = 60^{o}$) just beyond the edge of the reflector. The Cartesian coordinates of the feed (point f) and the reflector edge (point e) must be defined in terms of the coordinate system B, then a line equation connecting these two points is used to solve for the coordinates of point g where the ray intersects the ground (Figure 2.16). Since the vertex of the reflector (5.5 m above the base of the antenna) remains stationary and the line joining the feed and the vertex of the reflector is in the direction of the antenna pointing, the feed location (x_{fB}[2], y_{fB} and z_{fB}) in coordinate system B is:

[2] The notation x_{aB} refers to the x coordinate of the point a with respect to the coordinate system B.

$$x_{fB} = F\sin(90^\circ - a)\cos A \tag{2.6.4}$$

$$y_{fB} = F\sin(90^\circ - a)\sin A \tag{2.6.5}$$

$$z_{fB} = F\cos(90^\circ - a) + H \tag{2.6.6}$$

where F is the focal length of the antenna and H is the height of the vertex above the base of the antenna. Coordinate system P rotates with the antenna; the coordinates of the reflector edge in this coordinate system (r_{eP}, θ_{eP} and ϕ_{eP}) remain unchanged. The Cartesian coordinates of the edge with respect to B (x_{eB}, y_{eB} and z_{eB}) were written by first defining it in terms of the coordinate system B' ($R_{eB'}$, $\theta_{eB'}$ and $\phi_{eB'}$). Since coordinate system B' is the rotated version of the P system, $R_{eB'}$, $\theta_{eB'}$ and $\phi_{eB'}$ were solved using the computations for coordinate rotation as illustrated in Appendix A. The rotation between the two coordinate systems was defined by three parameters, $\theta_{B'P}$, $\phi_{B'P}$, and $\psi_{B'P}$ (see Appendix A for the calculation of coordinate system rotation).

$$\theta_{FP} = 90^\circ - a \tag{2.6.7}$$

$$\phi_{FP} = A \tag{2.6.8}$$

$$\psi_{FP} = 0^\circ \tag{2.6.9}$$

When the edge coordinates were computed with respect to system B', they were written in Cartesian form and then point e was mapped onto the coordinate system B by vector translation (i.e. $\bar{x}_{eB} = \bar{x}_{eB'} + \bar{x}_{fB}$). The location of spillover on the ground (x_{gB}, y_{gB} and z_{gB}) was computed by intersecting the line that joins point e and point f with the plane z = 0 (the ground). The spillover radiation hits the ground only if $z_{fB} > z_{eB}$, otherwise the ray is directed towards the sky and the computation for x_{gB} and y_{gB} is invalid. In this case, the temperature seen by the ray (θ', ϕ') was assumed to be zero since the ray is directed towards the cool sky. For the ray that strikes the ground, $T(\theta', \phi')$ was determined by both the angle of incidence at which the ray strikes the ground and the ground properties (i.e. if the ray strikes the ground or intersects the reflective mesh). The

angle of incidence was calculated using the feed and the ground spillover locations with respect to the antenna base.

$$\theta_{inc} = \tan^{-1} \frac{z_{fB}}{\sqrt{(x_{fB} - x_{gB})^2 + (y_{fB} - y_{gB})^2}} \tag{2.6.10}$$

The next step was to check whether the radiation intersects the mesh fence or not. The program allows the definition of rectangular shaped mesh fences by specifying the coordinates of three of four corners on the mesh. The location of the fence is defined with respect to coordinate system B. These three points define the vector equation of the mesh fence plane and the boundaries of the mesh fence. If the ray intersects the fence plane and is within the fence boundary, it is partially reflected towards the sky. Thus, the brightness temperature is reduced by the attenuation factor of the mesh or 15 dB. With the knowledge of the brightness temperature and the actual feed pattern as defined in **linearfeedpattern4.cut**, the spillover noise temperature was calculated using equation (2.5.2).

Spillover.c generates an output file with three columns, zenith angle, azimuth and noise temperature respectively. Then, the spillover noise temperature as a function of zenith angle (90° - altitude) and azimuth was plotted on a contour graph in polar form using Matlab. Figure 2.17 shows a plot of the spillover noise temperature for the case when no mesh fence or ground mesh was installed around the antenna. Increasing zenith angles are plotted radially outward with 0°, the antenna pointing at the zenith, in the center of the polar plot and 80° at the perimeter. Increasing azimuth angle is plotted clockwise around the circle. North is at $A = 0°$ and East is at $A = 90°$.

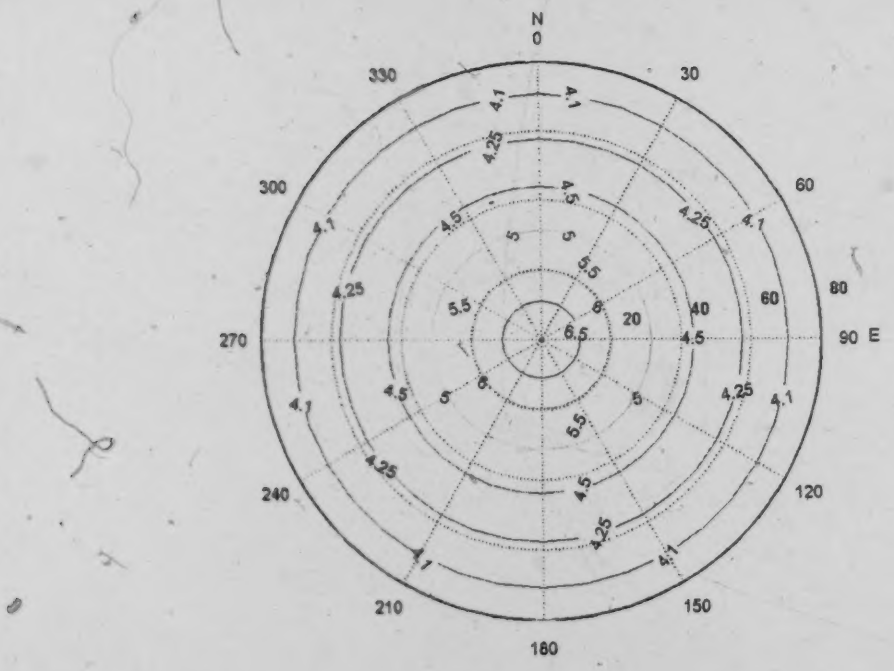

Figure 2.17 Calculated spillover noise as a function of antenna pointing, expressed as zenith angle (0° at the center of the plot) and azimuth.

In this case, the spillover noise temperature is constant with azimuth angle, but increases with decreasing zenith angle. The azimuthal symmetry observed in Figure 2.17 is the result of the symmetries in the radiation pattern and the uniformities in the ground properties around the antenna. When the antenna is pointing at the zenith, all the rays in the spillover region are directed towards the hot ground resulting in a higher spillover level. For an antenna pointed at a larger zenith angle, the integration range for the spillover noise is larger than when it is pointing at the zenith. However, some of the rays will be directed towards the sky where the brightness temperature is assumed to be zero. In addition, the feed pattern $g(\theta', \phi')$ is weak at large θ' angle and thus contribution to noise temperature in the extended spillover region ($\theta' > 90^\circ$) is small. Therefore, spillover noise is expected to be smaller at larger zenith angles, as observed in the theoretical plot above.

2.6.2 Considerations for Mesh Fence Design

The purpose of building mesh fences around the antenna is to reduce spillover noise. These designs must not degrade the performance of the antenna and should be as effective as possible, where "effective" means using a minimum amount of mesh fence to achieve the most spillover noise reduction.

1. Observation limits

The DRAO Synthesis Telescope is capable of observing sources down to an elevation of 12°. Full hour angle coverage or 12 hour observations are possible only for declinations of greater than +18° [Landecker et al., 2000]. Figure 2.18 shows a plot of antenna pointing zenith angle and azimuth of the Synthesis Telescope (latitude = 49°) for observation declinations equal to 90°, 80°, 70°, 60°, 50°, 40°, 30°, and 18° on a polar grid. When designing mesh fences, one should concentrate on reducing spillover noise for pointing altitude and azimuth North of the 18° declination curve. The antenna points mostly towards the North side. From the plot, a general conclusion can be made that it is more effective to build mesh on the north side of the antenna than on the south side.

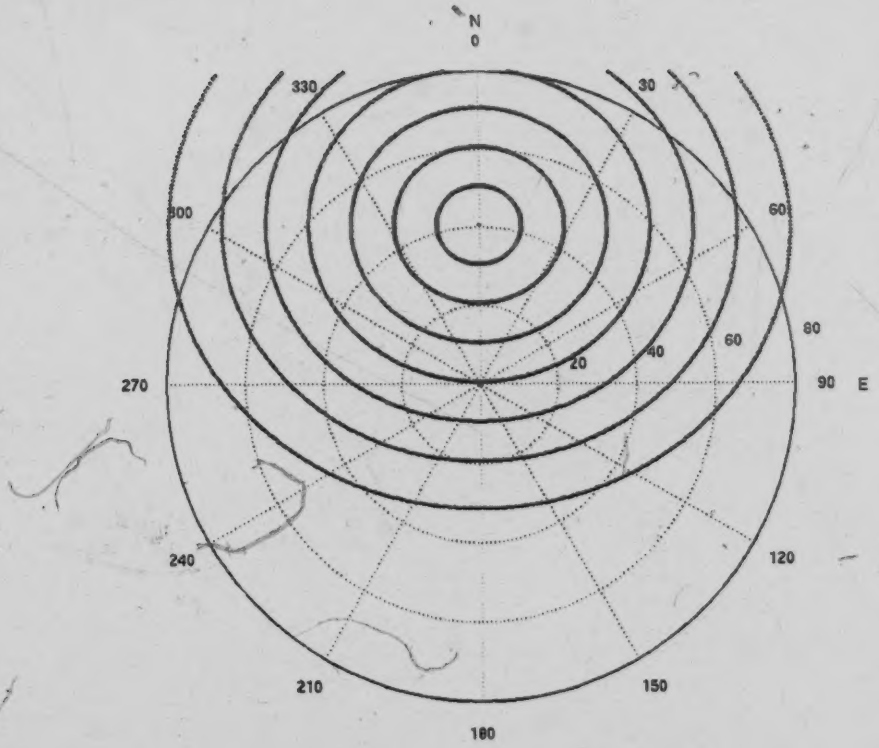

Figure 2.18 Antenna pointing zenith angle and azimuth for declination equals to 90° (dot at zenith angle = 41°) 80°, 70°, 60°, 50°, 40°, 30°, and 18° (largest curve).

2. Aperture blocking

Consider a fence surrounding the antenna which is taller than the feed of the antenna. Then no spillover radiation would strike the ground beyond the fence boundaries. However, if the antenna is tipped to a low altitude angle, this fence will block the reflector and reduce the effective aperture of the antenna. The maximum allowed height of the fence is calculated using simple ray tracing and geometries for cases when the antenna is tipped to the lower observation limit.

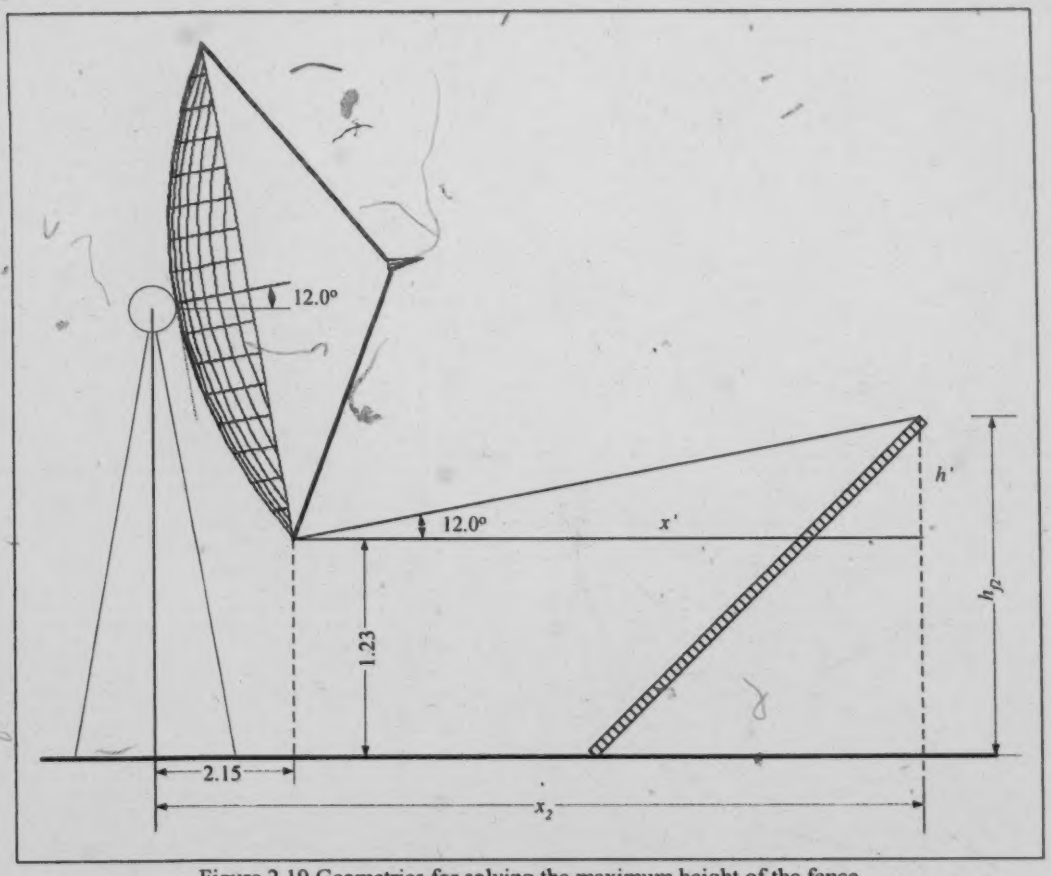

Figure 2.19 Geometries for solving the maximum height of the fence.

Consider a cylinder extending from the rim of the reflector; the mesh fence must not block any part of this cylinder. Figure 2.19 shows a reflector (diameter d = 9.144 m and focal length f = 3.810 m) observing at an altitude of 12° (observation limit of the Synthesis Telescope antenna). The cylinder, parallel to the reflector vertex-focus axis, is extended to a distance x' away from the edge of the reflector at a height h' above the edge. The maximum height of the fence h_{f2} allowed at a distance x_2 from the base of the antenna is

$$h_{f2} = (x_2 - 2.15)\tan 12^\circ + 1.23 \qquad (2.6.11)$$

To shield spillover noise, fences are built so that they slant away from the antenna. Thus the highest point of the mesh is at x_2, the mesh boundary furthest away

from the antenna (x_1 is the inner mesh boundary). The aperture blocking consideration sets an upper limit on the height of the fence for a given distance.

3. Reflection back towards the ground

Using the same amount of mesh, a fence with a larger slant angle will shield a greater amount of radiation. However, some of the radiation will be reflected back towards the hot ground if the slant angle of the mesh fence is too large. For a ray to reflect up towards the sky, it must strike the fence at an angle less than 90°. The maximum angle of incidence occurs when a ray intersects the fence at a distance closest to the antenna. Again, using ray tracing and geometry (Figure 2.20), the maximum slanting angle θ_s can be determined.

$$\theta_s < 90 - \theta_{inc} \tag{2.6.12}$$

where

$$\theta_{inc} = \max_{\beta}\left\{\tan^{-1}\frac{5.5 - h_{f1} + 3.81\sin a}{x_1 - 3.81\cos a}\right\} \tag{2.6.13}$$

In (2.6.13), x_1 is the distance between the antenna base and the inner edge of the fence, h_{f1} is the height of the mesh fence at x_1 and a is the observing altitude.

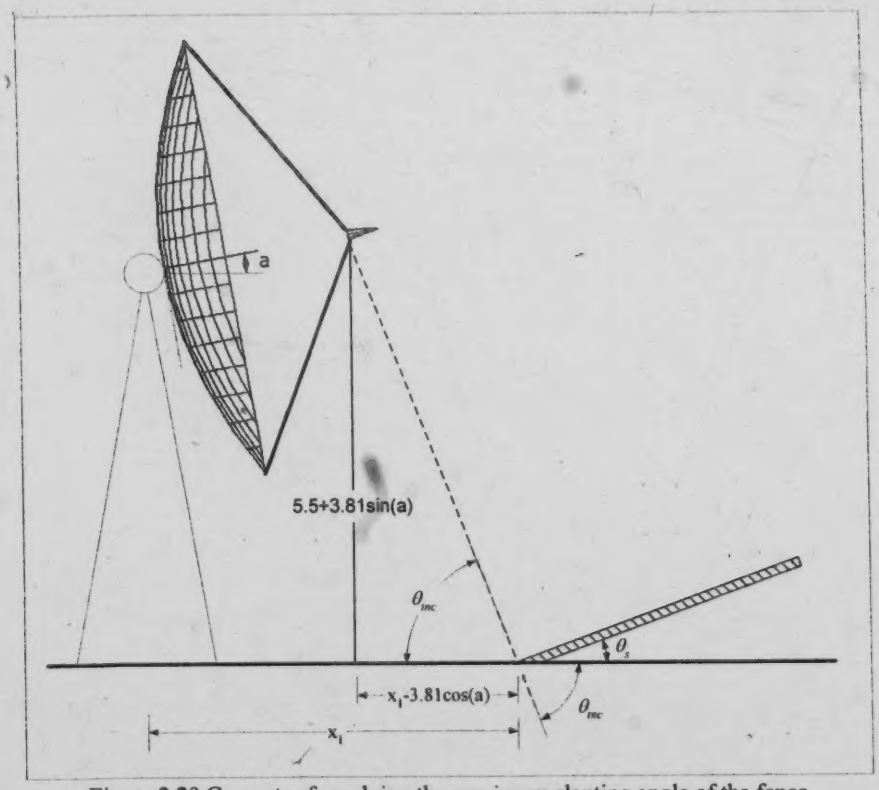

Figure 2.20 Geometry for solving the maximum slanting angle of the fence.

4. The relationship between mesh size and the amount of noise reduction

The first step in the design of the mesh fence is to have the knowledge of the attainable spillover noise reduction by a certain size of mesh for various values of antenna pointing altitude or zenith angle. **Spillover.c** was used to calculate the spillover noise temperature versus zenith angle plot for azimuth angle of 0^o when various sizes of square mesh are installed on the ground around the antenna. Assuming the antenna is located in the center of the mesh area, the resultant spillover noise when square mesh with sides of 4 m, 6 m, 10 m, 20 m, 30 m, 40 m, and 50 m are laid on the ground around the antenna is shown in Figure 2.21.

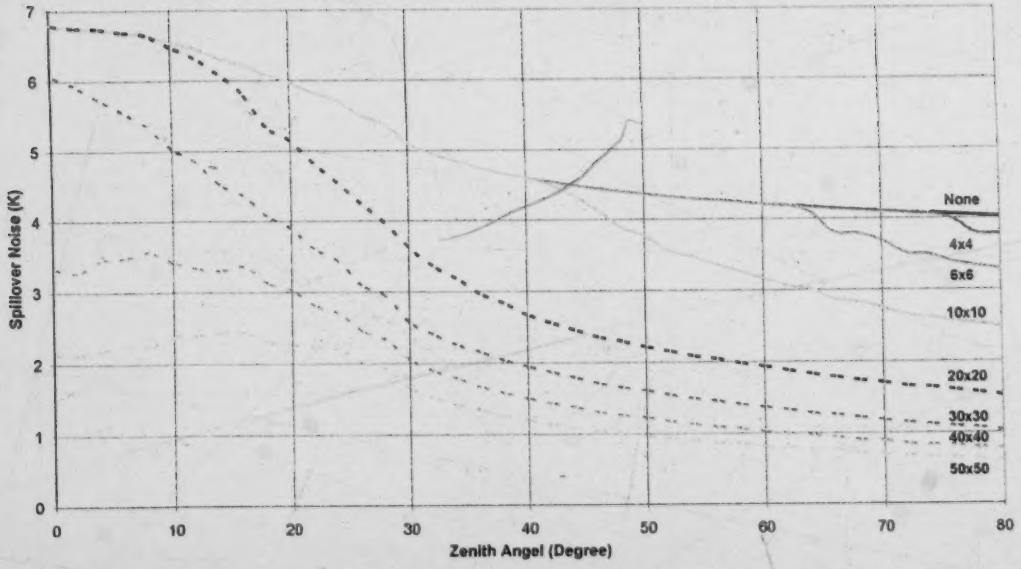

Figure 2.21 Square areas of mesh with side s (s = 4 m, 6 m, 10 m, 20 m, 30 m, 40 m, and 50 m) are placed on the ground around the antenna. The antenna is located in the center of the mesh area. The resultant spillover noise is plotted versus the antenna zenith angle.

This plot illustrates the approximate mesh size needed to achieve an optimum amount of noise reduction at a certain zenith angle. When the mesh area is small (s = 4 m, 6 m, and 10 m), reduction in noise is only observed for large antenna zenith angles. There is a sharp drop in spillover noise for ground mesh of s = 40 m compared to s = 30 m at low zenith angles. The rate of noise reduction diminishes for mesh areas greater than 40m x 40m. Therefore, the optimum mesh fence should have an effective radial shielding distance of 20 m from the antenna. Also, it is not necessary to install mesh within 3 m of the antenna.

2.6.3 Using Ground Mesh to Reduce Spillover Noise of Antenna 6

Antenna 6 of the Synthesis Telescope is located beside the parking lot in front of the new office building. During the construction of the new DRAO building, the existing asphalt road to the South of Antenna 6 was repaved and extended to become a parking lot. The new parking lot was originally a lawn. A possibility of placing mesh underneath the pavement to make the section of the parking lot look reflective at 1420 MHz was

examined. Tom Landecker conducted a simple experiment to measure the properties of asphalt at 1.4 GHz. A small piece of asphalt was inserted inside two waveguide-to-coaxial transitions which were connected back to back. Using the HP 8753 Network Analyzer, the attenuation was measured to be 1.4 dB and return loss was 6 dB. Conclusions can be drawn that most of the loss is due to reflection and that asphalt is not very lossy. The high return loss is expected, because even a good dielectric will be very reflective when placed inside a small area like the waveguide. Therefore, this experiment suggested that it is feasible to lay mesh underneath the pavement and to expect that the ground will still appear reflective at 1.42 GHz.

Mesh was placed on top of the original asphalt road and also underneath the new pavement on the edge of the new parking lot and in the area between the two machine shops. Figure 2.22 shows the location of the ground mesh around the antenna. The expected spillover noise reduction was calculated using **Spillover.c** (Figure 2.23). The Synthesis Telescope was completing different observation sets before and after the mesh was installed. Two sets of noise temperature data collected during observations at similar declinations were compared to examine the effect of the ground mesh. Also shown on this plot are the paths of antenna pointing for the observations at 42°, 43°, 68° and 69° declinations. These observations were used to compare the change in antenna temperature before and after placing the mesh underneath the pavement. The predicted noise reduction for these observations can be obtained by reading the contour lines along the path. For an observation at 43° or 42° declination, the spillover noise reduction was expected to be approximately 0.5 K when observing at negative azimuth angle and 1.0 to 2.0 K at positive azimuth angle. When observing a source at around 69° declination, the predicted noise reduction is approximately 1.25 K at all pointing angles.

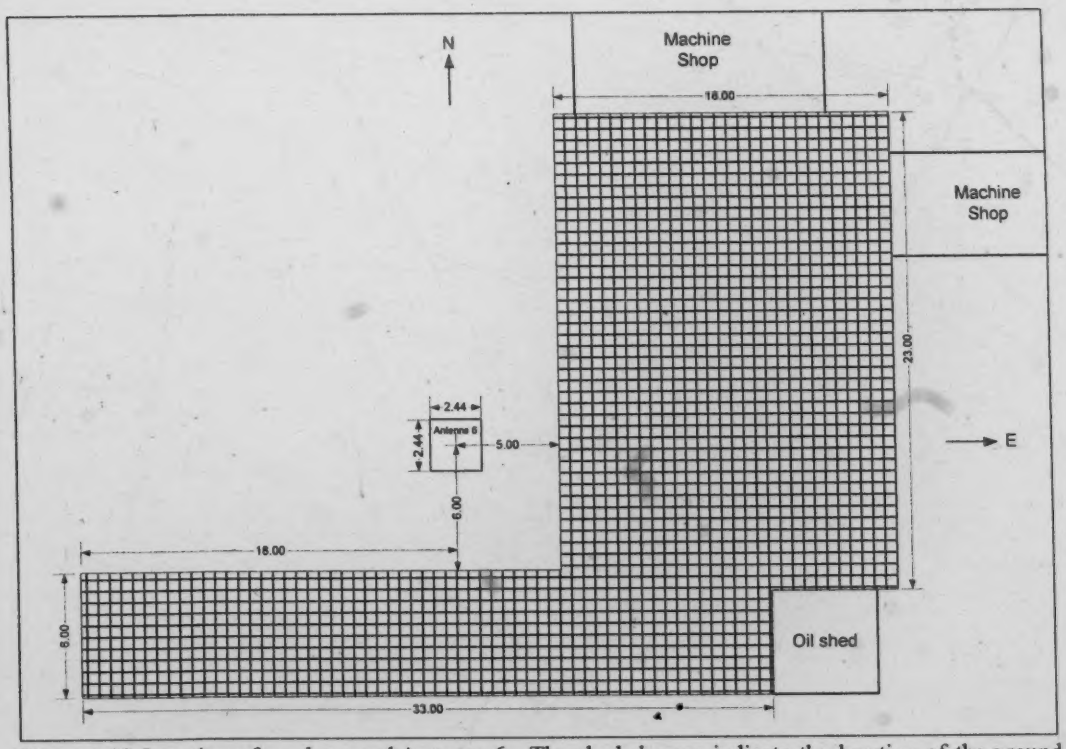

Figure 2.22 Location of mesh around Antenna 6. The shaded areas indicate the location of the ground screen.

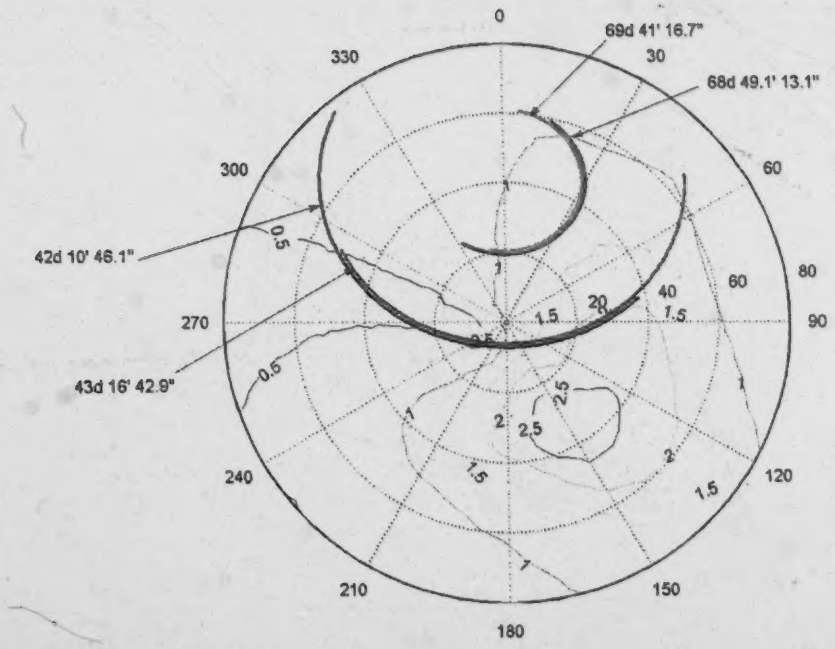

Figure 2.23 Expected spillover noise reduction. The four darker curves on the plot indicate the path of antenna pointing for the four observations (pointing declinations are indicated on the plot) used to compare the change in antenna temperature after the installation of the ground mesh.

The system temperature values stored in the T_{sys} files were processed by **Time.c** and then plotted against zenith angle. Figure 2.24 shows a comparison between the antenna temperature collected before (observation declination 43° 16' 42.9") and after (declination 42° 10' 46.1") the installation of the ground mesh. When pointing at positive (A = 0° to 180°) azimuth angle, the presence of the ground mesh reduces the antenna temperature by 0.5 to 1.0 K, approximately half of the predicted value. However, at negative (A = 180° to 360°) azimuth angle, a slight increase in antenna temperature of about 0.5 K was detected. The drop in noise temperature was less than the prediction and the increase in antenna temperature was unexpected. An explanation would be that the ground mesh did make part of the ground appear more reflective (noise reduction), but the new parking lot contributes more ground noise than the previous grass area. Since grass contains more moisture than the asphalt road, it is more reflective and has a lower effective brightness temperature. Thus, when the antenna is pointing towards the extended asphalt area in the Southwest or negative azimuth angle, the antenna temperature is higher than before the parking lot was paved. When the antenna is

pointing at positive azimuth angle and the spillover lobes fall on the area where the landscape did not change but mesh was placed underneath asphalt, the resultant antenna temperature was lower than before.

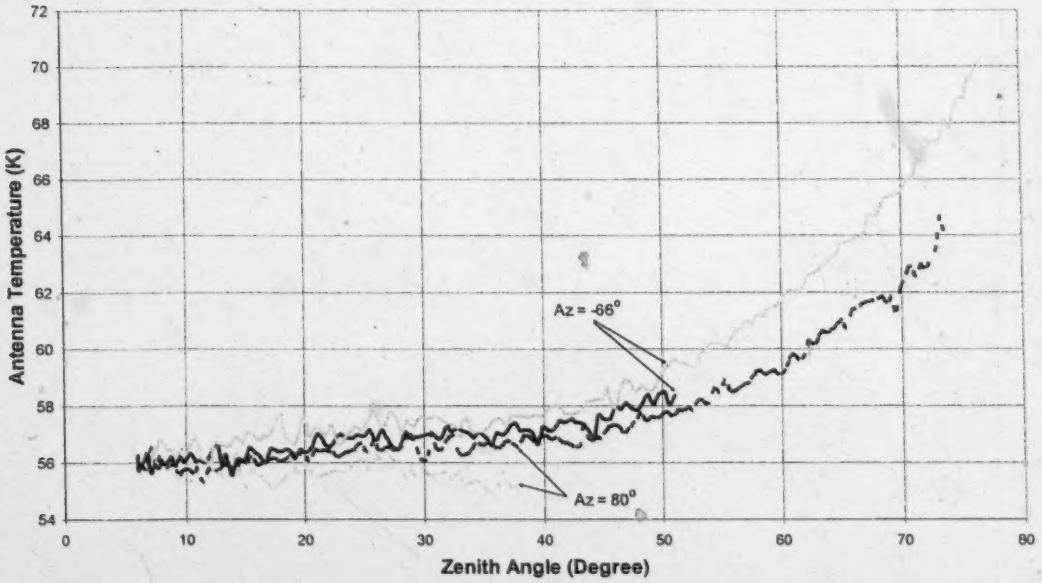

Figure 2.24 Antenna noise comparison. Dotted line indicates positive azimuth angles and solid line indicates negative azimuth angles. The black line is the average antenna temperature for observations at declination 43° 16' 42.9", collected before the installation of the ground mesh. The gray line shows the antenna temperature (observing at declination 42° 10' 46.1") when the ground mesh was present.

Antenna noise temperatures collected during observations at a different declination (69°) were also compared. Figure 2.25 illustrates that antenna noise decreased by 0.5 K to 1.25 K which agrees with the prediction. Maximum noise reduction is achieved when observing at zenith angle of 45° and azimuth angle of 30°. When the antenna was pointing at this direction, some of the spillover lobes see the reflective meshed pavement, but fall far from the new parking lot. Noise reduction was less than the prediction when the antenna is pointed at a small zenith angle. Using the method of ray tracing, it is clear that when the antenna is pointing near the zenith some of the spillover radiation will fall on the new parking lot which was originally covered with grass. This evidence, agrees with the previous comparison, and shows that the new parking lot is a larger contributor of noise temperature than the previous grass area, and also that the ground mesh is effective in reflecting spillover radiation towards the sky.

This experiment also demonstrated that placing mesh around the antenna can reduce spillover noise.

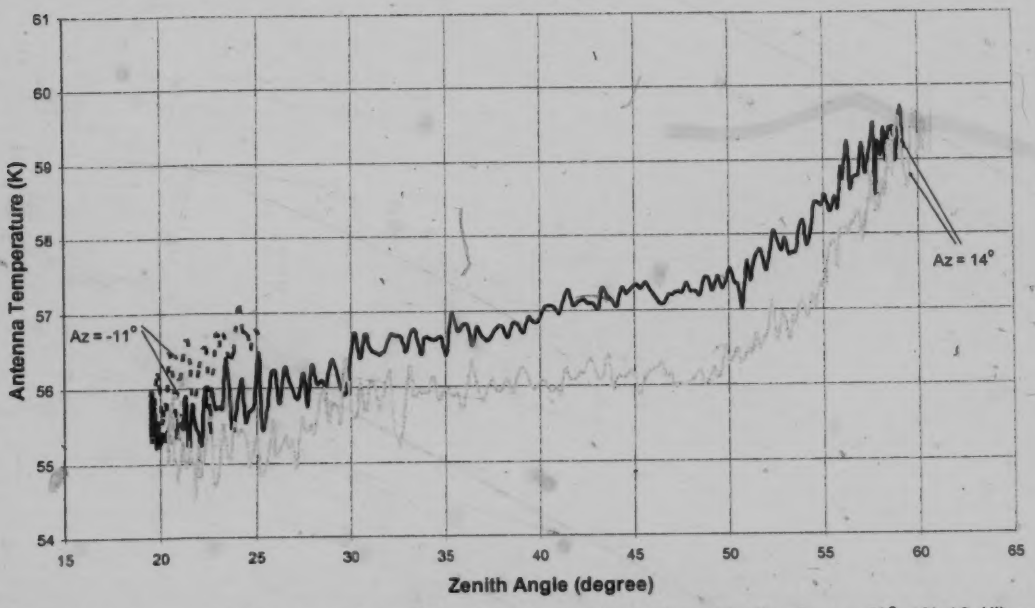

Figure 2.25 Antenna noise comparison. The data for the black line (declination = 68° 49' 13.1") was collected before the installation of the mesh and the data for the gray line (declination = 69° 41' 16.7") was collected after.

2.6.4 Modification of Antenna 1 to Reduce Spillover Noise

Antenna 1 of the Synthesis Telescope is located on the West end of the array. There is a small hill about 3 m high to the West side of this antenna. On its East side is the rail track for the movable antennas. Mesh fences were built around this antenna to reduce the spillover noise. Antenna 1 is one of the stationary antennas and this is the main reason why it was chosen for this experiment. Since spillover noise is dependent on ground properties, it would be difficult to conduct a controlled experiment if the antenna is moved with respect to the mesh fence as it is completing an observation set (twelve 12-hour observations which produce a complete sampling of the available baselines). The location, size and slope of the mesh fence were determined based on the results from the theoretical calculations produced by **Spillover.c** and based on the cost.

2.6.4.1 Design

Restrictions set on the design of the mesh fence around Antenna 1 included the landscape around the antenna and the budget allowed for the experiment. The hill to its West side, 3 m high with a slope of approximately 15°, set a lower limit on the height of the fence. The rail track located to its East obviously makes it not feasible to build a fence on this side. In addition, a driveway and a parking space are needed to allow the maintenance truck to drive to the antenna for servicing. The possible locations for mesh fences are on the West, South and North side of the antenna. The budget for this experiment allows a total fence area of approximately 250 m^2.

First consider building a fence on either the North or the South side of the antenna. Since the Synthesis Telescope is only able to obtain full hour-angle coverage for declinations north of 18°, the antenna points mostly towards the North. Thus, a fence to the North of the antenna is preferable and would achieve a greater noise reduction within the observation limit than a fence on the South side. A driveway 8 m wide measured from the edge of the track to the North of the antenna must be reserved to allow the maintenance truck to drive through. The edge of the track is 3.2 m from the center point of the antenna base. Therefore, the north fence was designed to be 11 m from the antenna base. The mesh used to build the fence is 36" or 0.9144 m wide. The width of the fence should be multiples of the mesh width for construction purposes.

Consider building a fence 25 m long and five-mesh or 4.57 m wide extending from the foot of the West hill, parallel to the track, at a distance of 11 m North of the antenna with a slanting angle of 26.6° (Figure 2.26). Equation (2.6.11) was used to check if the height of this fence exceeded the aperture-blocking requirement. With a slant angle of 26.6°, the highest point of this fence is 2 m at a distance 15 m from the antenna base. The maximum height allowed at this distance is 4.0 m. In addition, at a distance of 11 m, a maximum fence slant angle of 45.5° is allowed. Therefore, this fence satisfies both the maximum height and fence slant angle criteria. Figure 2.27 illustrates the predicted noise reduction calculated by **Spillover.c** on a polar grid. The calculated noise reduction is about 1 K when pointing at a small zenith angle and decreases to 0.2 K when tipped to a

larger zenith angle. Also drawn on the contour plot is the antenna pointing path when observing at 18° declination (the thick curve line).

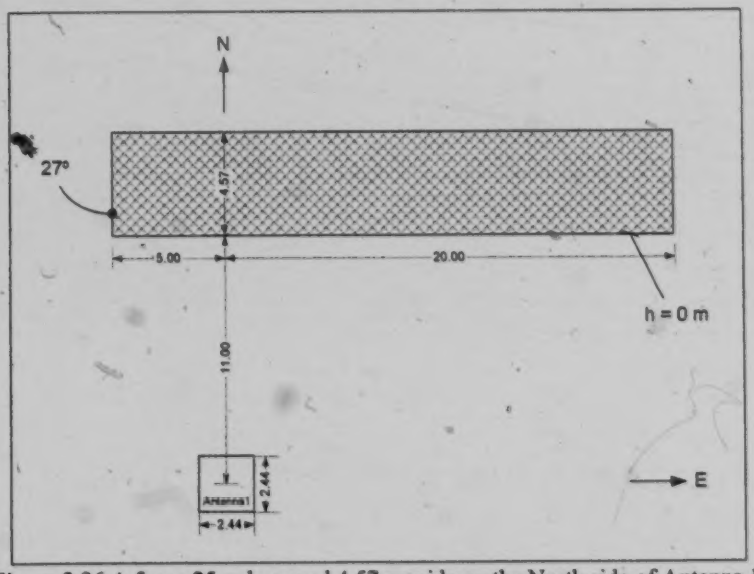

Figure 2.26 A fence 25 m long and 4.57 m wide on the North side of Antenna 1.

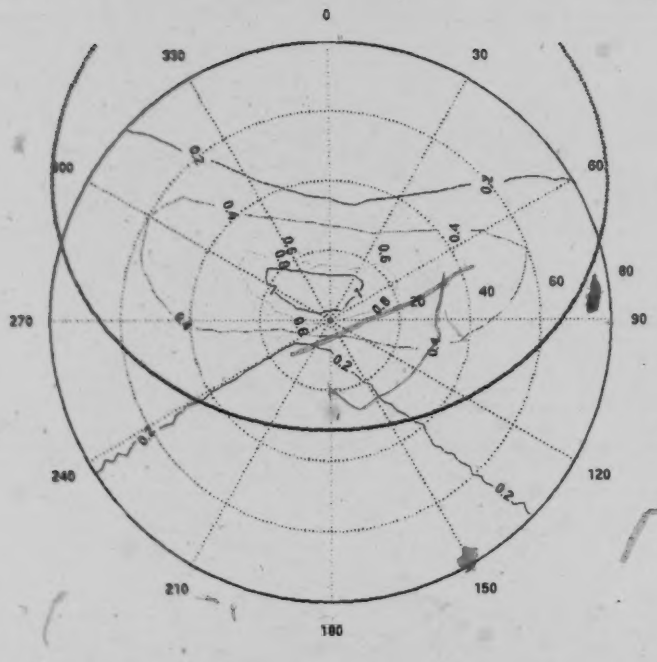

Figure 2.27 The predicted spillover noise reduction for a fence built to the North of the antenna. The thicker curve, the pointing path for 18° declination, indicates the observation limit of the Synthesis Telescope. The telescope is only used to observe sources with pointings above this curve.

Next, a 25 m long mesh fence was designed to stretch along the hill on the West side at a distance 5 m from the base of the antenna (Figure 2.28). Due to the slope of the hill, the lower edge of this mesh is 1.5 m up from the ground level. The length of this fence extends 15 m from the antenna on the North and 10 m on the South side. Using equations 2.5.11 and 2.5.12, the maximum slant angle of the fence was calculated to be 15° which is about the same steepness as the hill. The fence was designed to be 5.49 m wide. Equation 2.5.10 verified that this design is within the maximum height limit. Figure 2.29 shows the calculated reduction in spillover noise of this design.

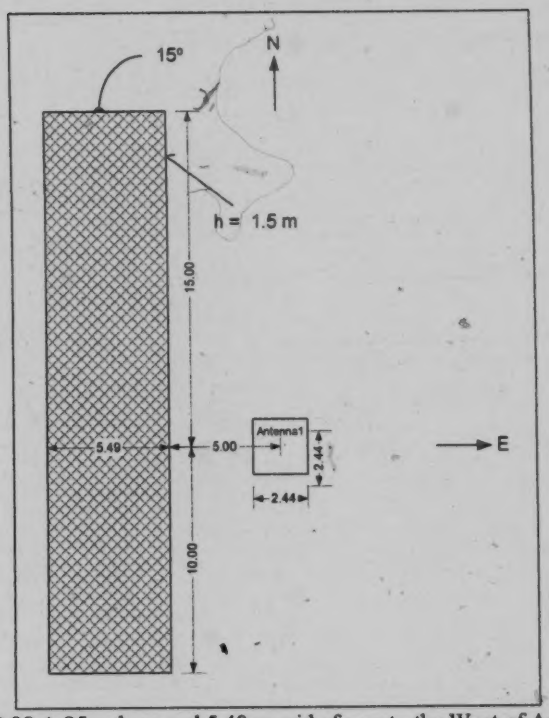

Figure 2.28 A 25 m long and 5.49 m wide fence to the West of Antenna 1.

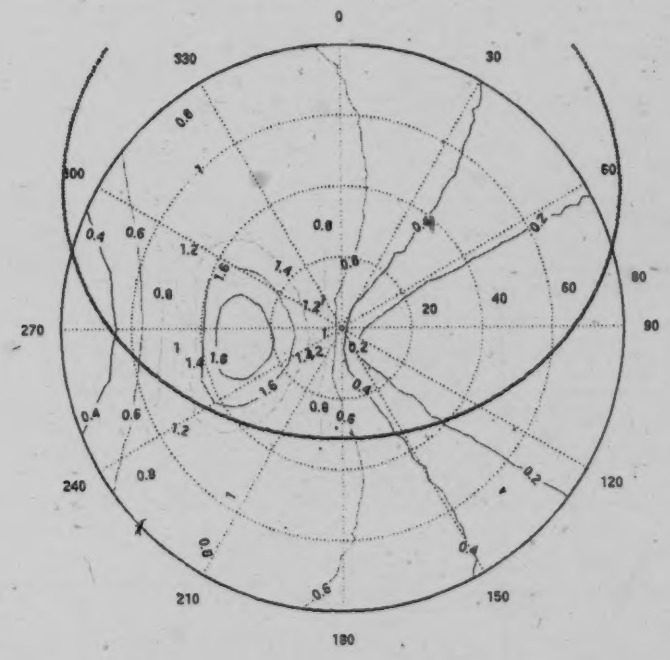

Figure 2.29 The expected spillover noise reduction after building the West fence

Upon examining the area around Antenna 1, the section of the fence directly North of the antenna must be pushed back by 2 m to allow the maintenance truck to park by the antenna during service. This part of the fence would have a larger slant angle but the same height as the rest of the fence on the North side. For this design (Figure 2.30), the total amount of mesh needed to build a fence on the West side and the North side is 237.63 m^2 which met the budget. The resultant noise reduction when these two fences are built is predicted in Figure 2.31.

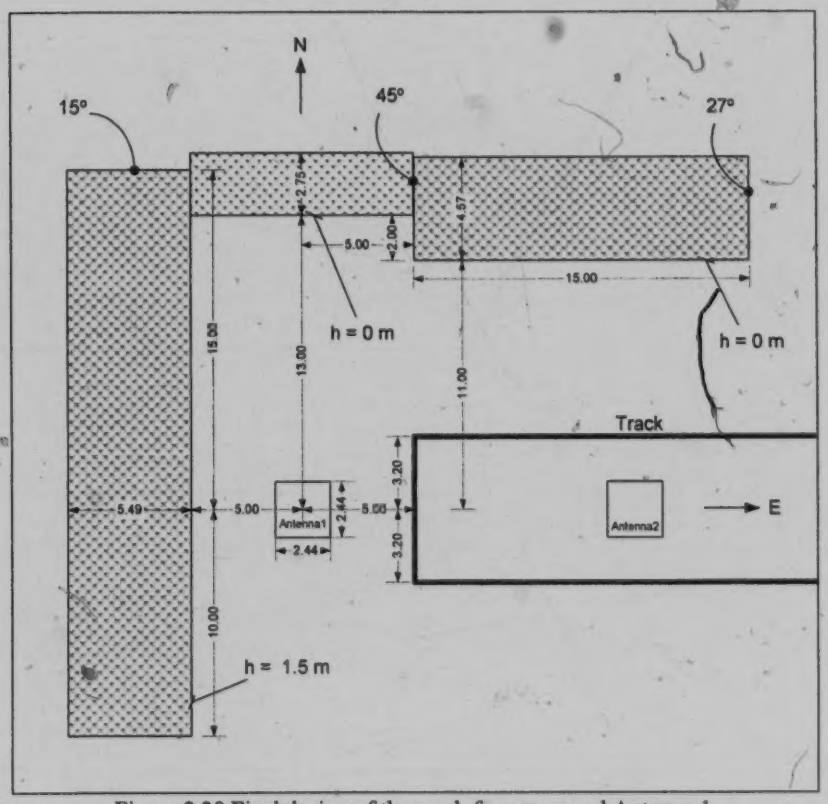

Figure 2.30 Final design of the mesh fences around Antenna 1.

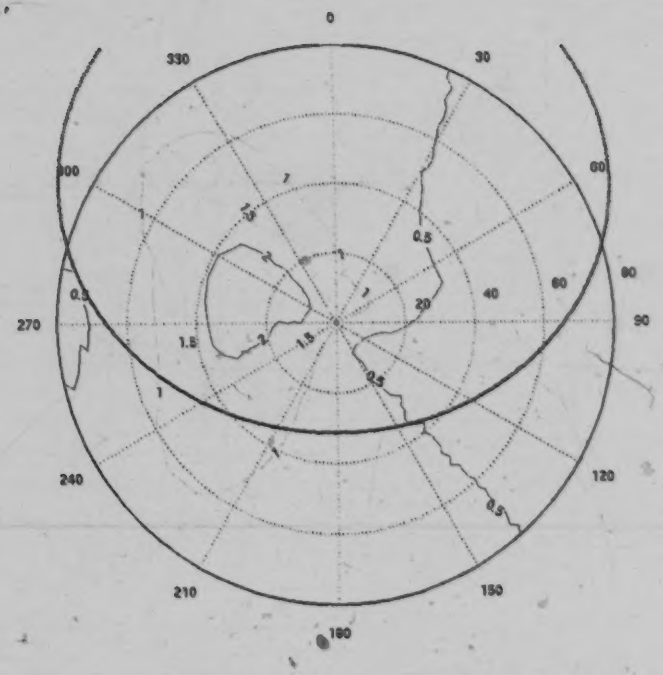

Figure 2.31 Antenna 1: predicted spillover noise reduction with both fences

2.5.3.2 Result

The slanted mesh fences based on the designs above were built around Antenna 1 (Figure 2.32). The dimensions of the actual mesh fence are illustrated in Figure 2.33. The west fence and north fence were built at different times. Antenna noise temperatures measured by the autocorrelator before the construction of the fence, after the implementation of the west fence and after the completion of both fences were compared.

Figure 2.32 Mesh fences built around Antenna 1 to reduce spillover noise.

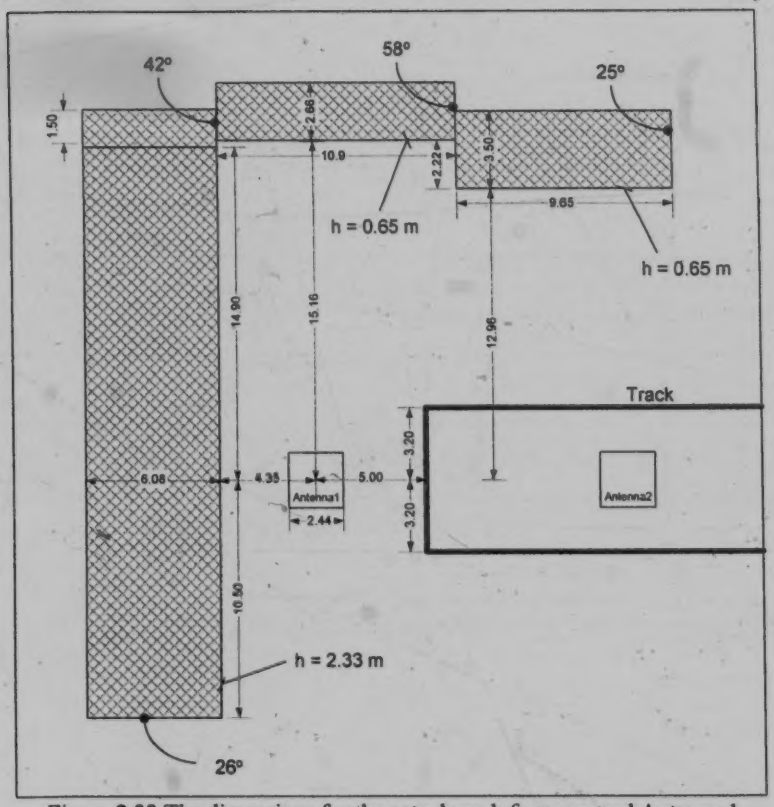

Figure 2.33 The dimensions for the actual mesh fence around Antenna 1

The theoretically calculated spillover noise reductions for implementing the west fence and for the entire design are shown in Figure 2.34 and Figure 2.35. The lower and upper curves indicate the 12-hour antenna-pointing path for declination 38° and 67°. Antenna temperature readings collected during these observations were used to measure the spillover noise reduction after building the mesh fences.

Figure 2.36 shows a comparison plot of the measured data when the antenna is observing at 38° declination. After building the west fence, a noise drop of 2 K to 3.5 K was detected when the antenna was pointing at negative azimuth angles towards the fence. A lower noise reduction, approximately 1 K, was detected when the antenna was pointing away from the fence. This trend agrees with the prediction. However, the actual noise reduction was much higher than that calculated by **Spillover.c**. This is especially evident when the antenna is observing at low altitude towards the West. At 70° zenith

angle and -53° azimuth angle, the predicted spillover noise reduction was 0.5 K, but the actual reduction measured was 3.5 K. With the addition of the fence on the North side, the antenna temperature was further reduced by 0.5 K to 1.0 K when observing at negative azimuth, but no noise reduction was measured when the antenna is pointing at low altitude toward the west. When pointing to the East, however (Az = 71°), the antenna temperature was reduced by a further 1 K.

Observations at another declination, 67°, were also compared (Figure 2.37). Spillover noise was reduced by approximately 1.0 to 2.0 K after the implementation of the west fence. Greater reduction was measured when the antenna was pointing at negative zenith angle or towards the fence. An additional noise reduction of less than 0.5 K was measured after the completion of the north fence. The predicted noise reduction ranges from 0.5 K for larger zenith angle and positive azimuth angle to 1.5 K for smaller zenith angle and negative azimuth angle. Although the measured noise reduction is larger than expected, this measurement does not exceed the theoretical calculation as much as the observation at 38° declination.

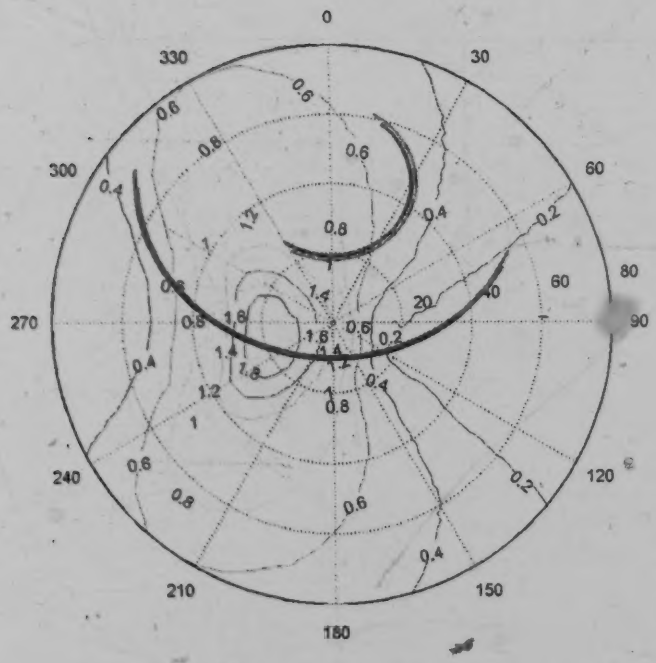

Figure 2.34 The expected spillover noise reduction when the west fence was built.

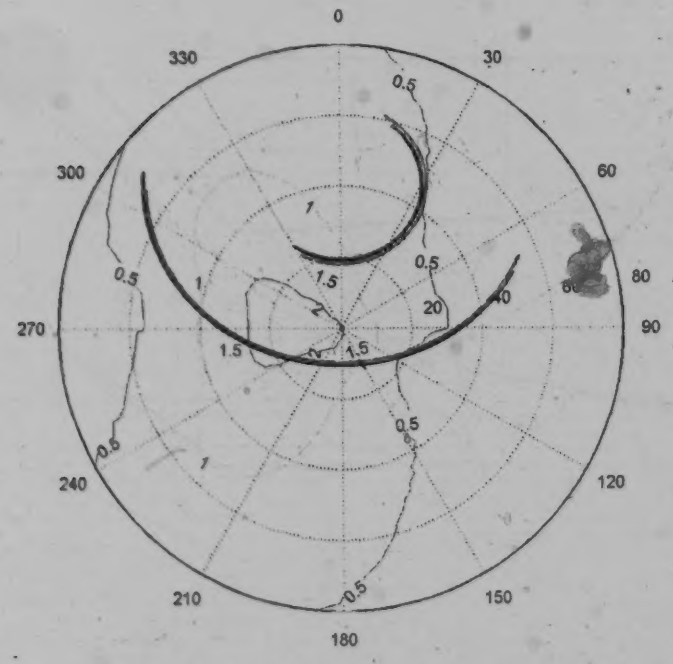

Figure 2.35 The expected spillover noise reduction upon the completion of the entire fence design.

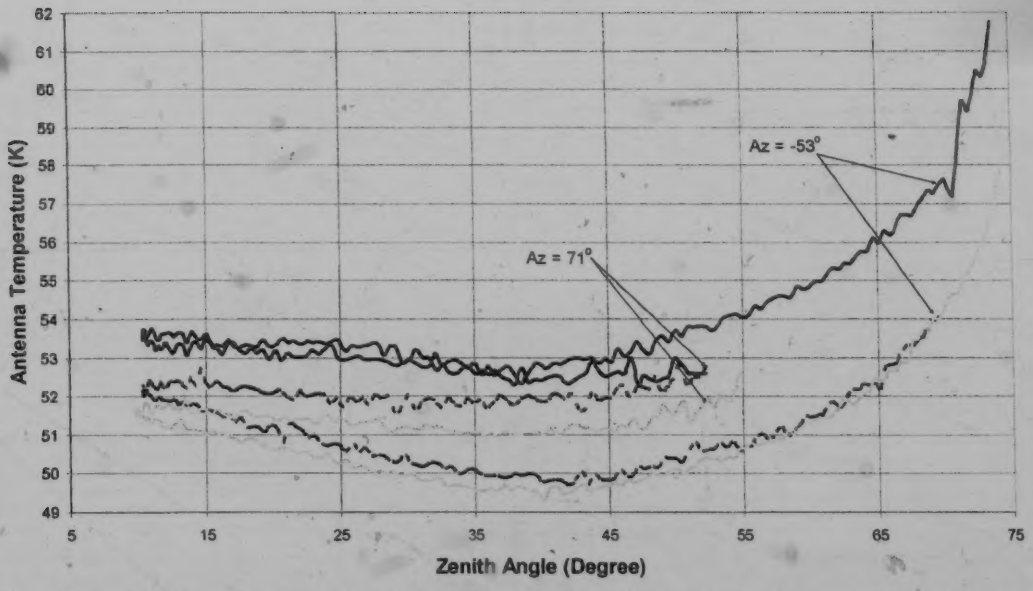

Figure 2.36 The measured antenna temperature for Antenna 1 when observing a source at 38° declination. The black line indicates the measured antenna temperature before any fence was built around the antenna; the dotted black line is temperature after the west fence was built; and the gray line is the antenna temperature when the entire fence was completed.

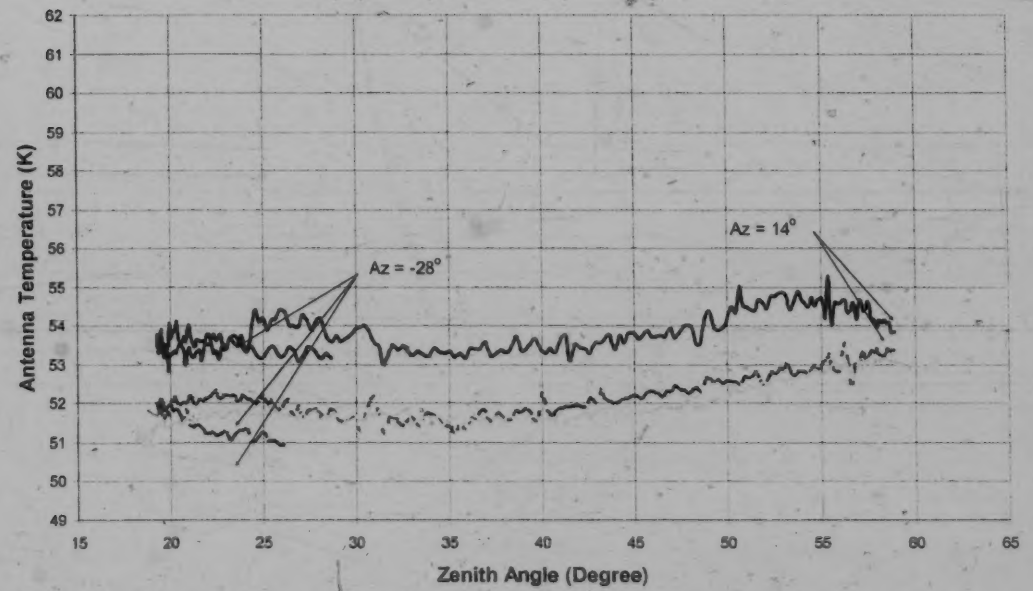

Figure 2.37 The measured antenna temperature for Antenna 1 when observing a source at 67° declination. Noise reduction comparisons for no mesh fence (black line), the west fence (dotted black line) and the entire design (gray line)

These two measurements demonstrated that the west fence, which was built closer to the antenna, is much more effective than the north fence, which was further away. The higher than expected noise reduction suggested that the fences not only reflect the direct spillover towards the cool sky, they also shield noise due to strut scattering and mesh leakage. Figure 2.38 illustrates the expected spillover plus strut scattering noise reduction achievable by the actual mesh fence built around Antenna 1. Comparing Figure 2.38 with Figure 2.36 and Figure 2.37, much better agreement between the predicted and the measured values was obtained when strut scattering was considered. A more detailed study of strut scatter will be presented in the following section. Since the mesh fence shields both direct spillover and strut scattering noise, the theoretically calculated noise reduction will consider both factors in the following mesh fence designs.

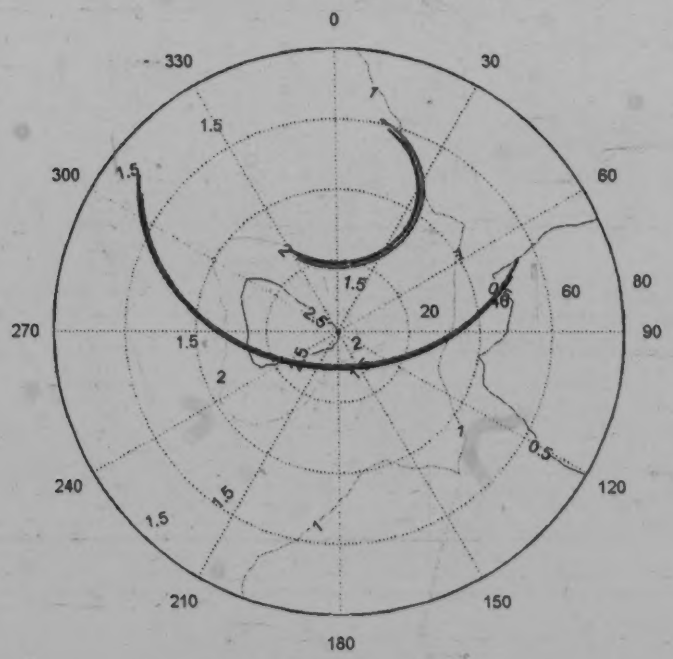

Figure 2.38 The calculated spillover and strut scattering noise reduction for the actual fence design.

The measured noise reduction is still greater than the prediction when the antenna is pointing at low altitude towards the West. This extra noise reduction can be explained by the West fence, being close enough to the antenna, shielding the mesh leakage when the antenna is tilted down. A conclusion drawn from this experiment is that a fence built

relatively close to the antenna is more effective than one built further away because it is more capable of shielding strut scattering and mesh leakage noise in addition to the direct spillover noise. Thus in the following designs, mesh fences and ground screens will be designed to be close to the antenna (the ideal distance for the inner boundaries would be 3 m from the antenna).

2.6.5 Modification of Antenna 7 to Reduce Spillover Noise

Antenna 7, the furthest antenna on the East side of the array, is situated in a big open area. Thus, there is a great deal of freedom in the design of this mesh fence.

2.6.5.1 Design

The only restriction on the fence design for this antenna is that the fence must have an opening of at least 4 m to allow the maintenance truck to drive through and a parking spot, on the North side of the antenna, for the truck during antenna servicing. This area must be at least 18 m long measured northward from the antenna and 8 m wide on the West side of the antenna. The previous experiment on Antenna 1 demonstrated that a mesh fence built closer to the antenna is more effective in reducing spillover, strut scattering and perhaps also mesh leakage noise. However, it is not possible to build fences within 8 m West and 18 m North of the antenna. Therefore, this design will combine the use of ground mesh (like the Antenna 6 experiment) and mesh fence (Antenna 1 experiment). The ground mesh will be laid directly on top of the sandy ground and then covered with a layer of pebbles and sand to allow the snowplow to shovel snow during winter.

The first step of the design procedure was to determine the inner boundary of the mesh area. Figure 2.21 shows that placing mesh within 3 m of the antenna will only reduce a small amount of spillover noise but mesh located relatively close to the antenna will reduce the spillover noise for low altitude observations as shown in the experiment on Antenna 1. The antenna tracks down to an elevation of 12° in the North, but the

minimum altitude angle allowed for the south side is 30°. Thus, the inner boundary of the mesh was set to be 3 m from the North, West and East of the antenna and 8 m from the South. The area north and west of the antenna is reserved as the driveway and parking space for the truck. Ground mesh rather than fences built above the ground was used in these areas. To simplify the design, ground mesh was also laid on the East side stretching from 3 m to 8 m from the antenna (Figure 2.39).

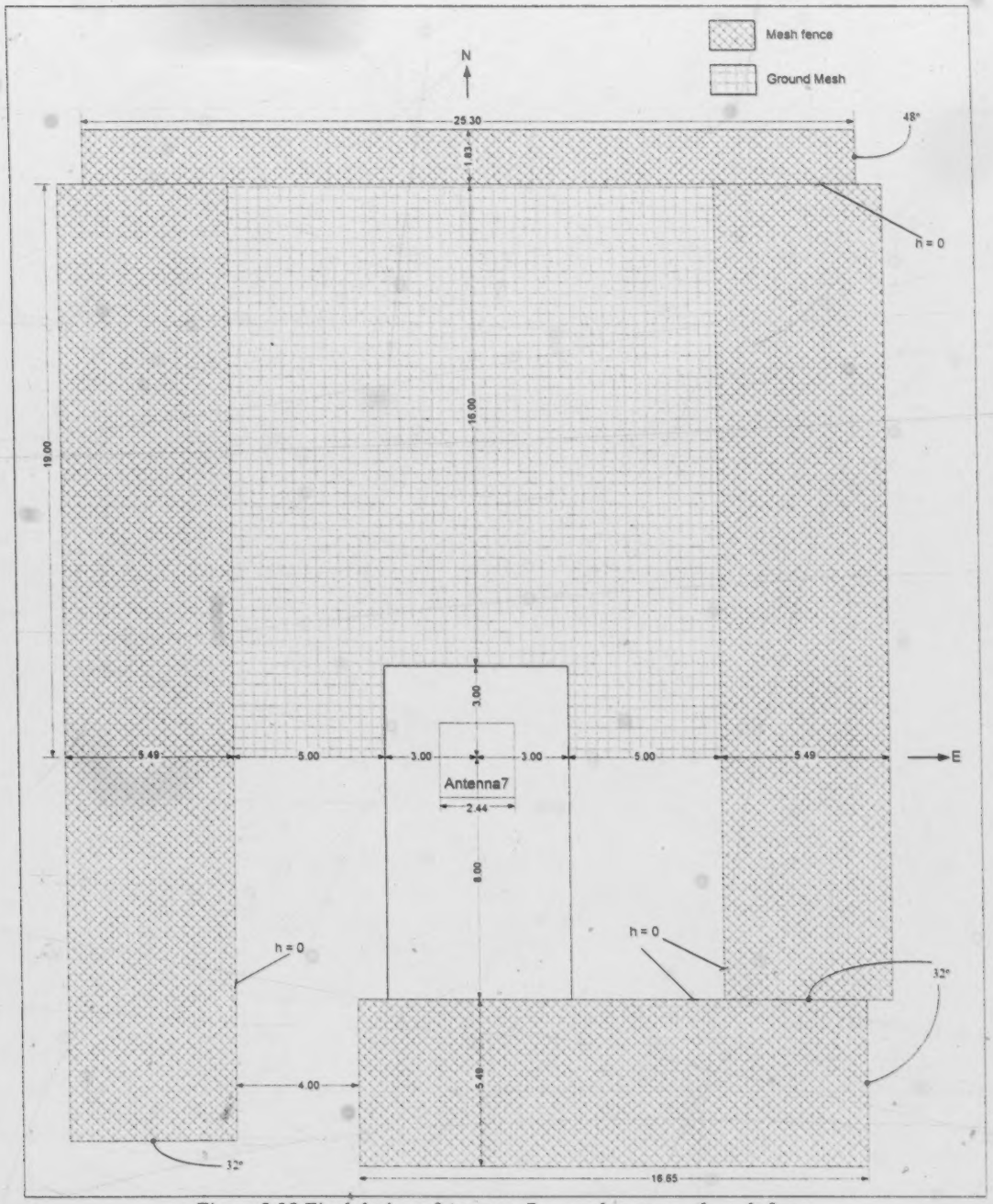

Figure 2.39 Final design of Antenna 7 ground screen and mesh fence

Slanted fences were designed around Antenna 7 starting from the south boundary and just beyond the ground mesh on the north, east and west side. A 4 m gap located between the west and the south fence was left open to allow the truck to drive to the

antenna. At a distance of 8 m from the antenna, a maximum fence-slant angle of 32.4° is allowed. This fence was designed to be 5.49 m wide slanting at a 32° angle. The maximum height of this fence is 2.91 m at a distance 12.65 m from the antenna. This met the height limit set to avoid blocking the aperture. Since the fence on the North side is further back from the antenna, a steeper slanting angle is allowed. The benefit of having a fence with a steeper slope is that it has a larger effective shielding area than a lower fence with the same amount of material. A 1.829 m wide fence with an angle of 48° was proposed to build at a distance 19 m North of the antenna. As shown in Figure 2.21, mesh beyond 20 m of the antenna only shields a small amount of spillover noise. Thus the North fence does not need to be any wider than 1.829 m as in the design.

The ground around the antenna is not level; it begins to slope down just beyond the designed ground mesh area. This will not create a problem in the above fence design. The base of the fence can be built above the ground at the same level as the antenna base. Figure 2.39 shows the final design of the ground screen and mesh fence around Antenna 7. The spillover and strut scattering noise reduction achievable by this design is illustrated in Figure 2.40. Noise reduction of 5 to 5.5 K is predicted for this design.

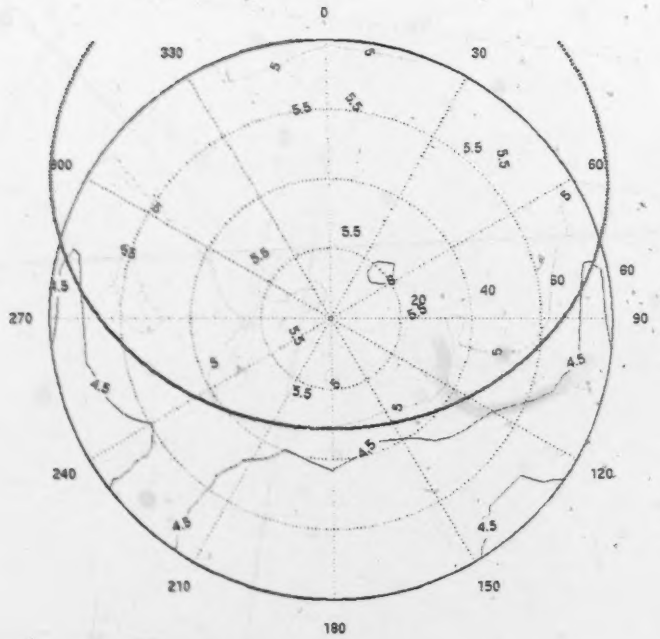

Figure 2.40 Plot of predicted direct spillover and strut scattering noise reduction for Antenna 7. The thick curves is the pointing path for 18° declination, the observation limit.

2.6.5.2 Result

The fence around Antenna 7 was built as designed (Figure 2.41) and the change in antenna temperature was analyzed. Figure 2.42 is a comparison of measured antenna temperature before and after the mesh fence was built. The temperature reduction was lowered by approximately 3 K when the antenna is pointing at zenith angles of 50° to 70°. A smaller reduction was detected when antenna is pointing close to the zenith.

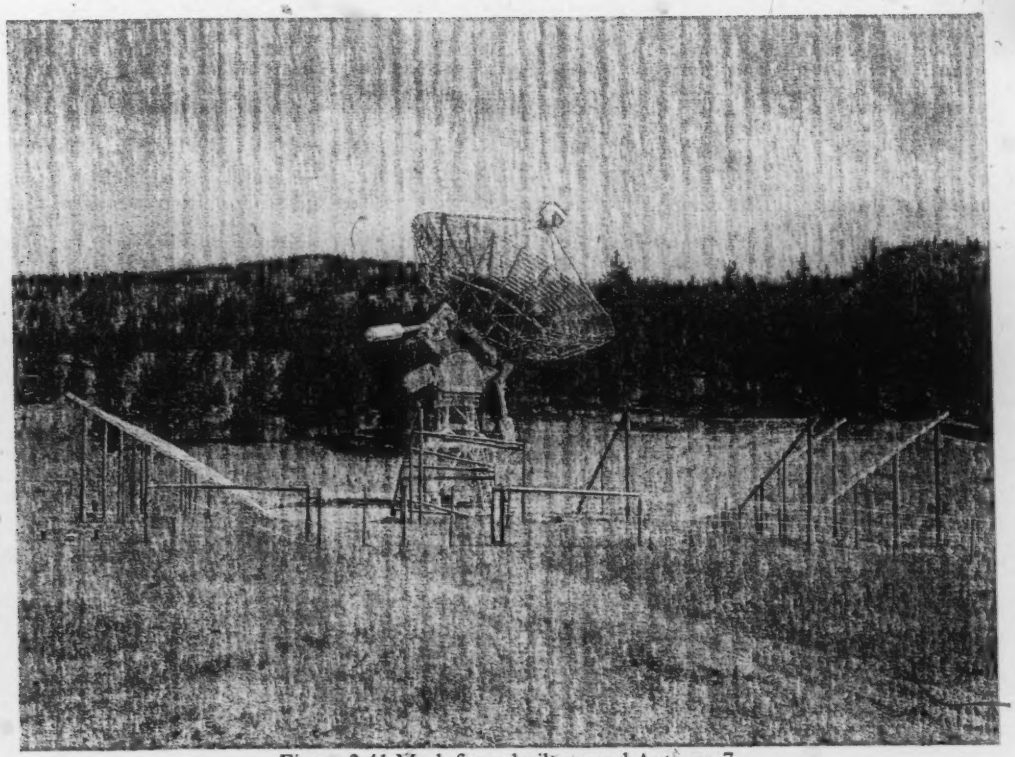

Figure 2.41 Mesh fence built around Antenna 7.

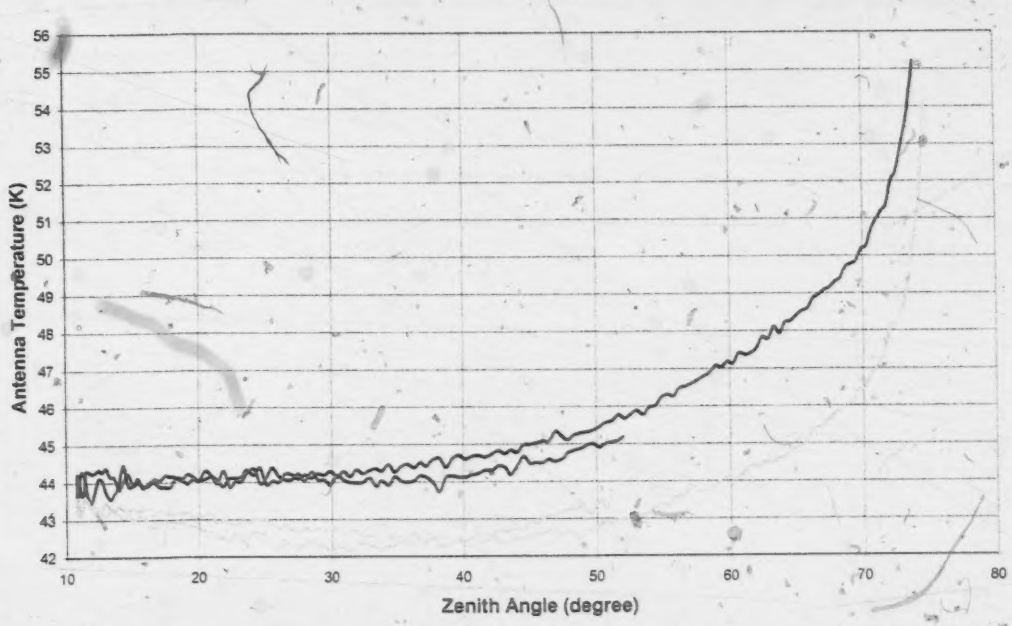

Figure 2.42 The measured antenna temperature for Antenna 7 when observing at 38° declination. Black line is the system temperature without the mesh fence and gray line is with the mesh fence.

The change in antenna temperature was lower than the prediction which expected a 5 to 6 K decrease. The less than expected temperature reduction can be explained by the difference in weather conditions between the before and after measurements. Since the fence was quite big, it took two weeks to construct. Over this period weather changed from wet and cool to dry and hot. The first set of data was collected before the mesh fence was built when the average air temperature was around 12°C. The air temperature after the completion of the mesh was 20°C. Thus, the ground temperature should also increase. In addition, the water content in the ground was lower when the second set of data was collected, thus the ground is less reflective. As a result, the ground appears to be a blackbody at a higher temperature. This reasoning was verified by comparing the measured antenna temperature for Antenna 1 over the same period of time. A temperature increase of approximately 2 K was measured across all zenith angles. Combining the 3 K temperature reduction as a result of the fence shielding and the 2 K increase due to the change in weather, a 5 K antenna temperature decrease was achieved as predicted in the theoretical calculation.

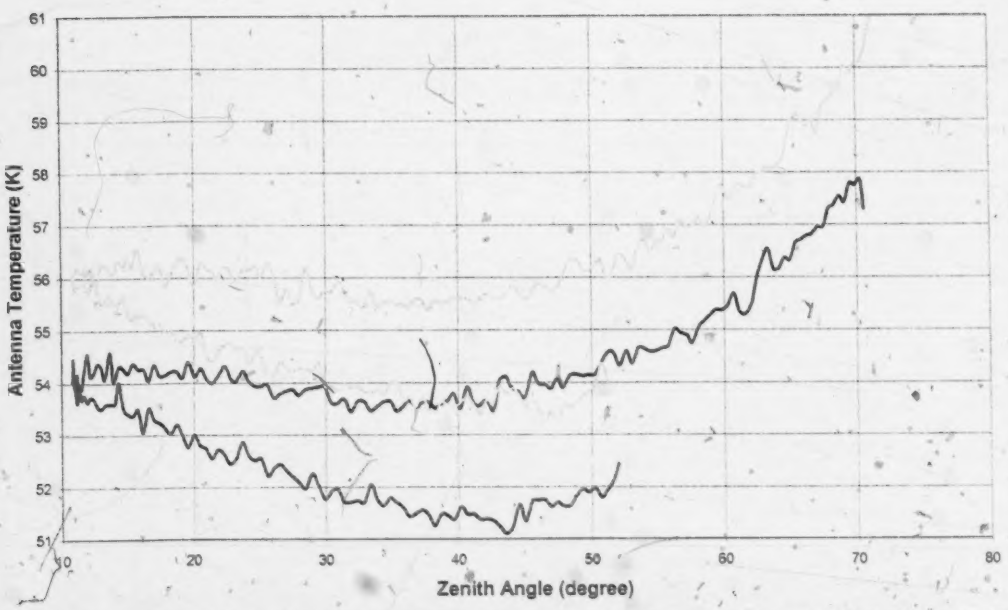

Figure 2.43 The measured antenna temperature for Antenna 1 when observing at 38° declination. The black line and the gray line show the antenna temperature before and after construction of the Antenna 7 fence, respectively. The 2 K increase is due to the change in the ground temperature.

2.6.6 Proposed Fence design for Antenna 5

Antenna 5 is the stationary antenna on the East end of the rail track. The mesh fence design for this antenna is very much limited by the building, the track and the road structure around it. The receiver building (Block House) is located on its North side at a distance of 14 m from the antenna. On either side of the track is the 8 m driveway and East of the track is the entrance to this driveway. To the Southeast side of the track is the main road to the observatory. Therefore, the only possible locations for the shielding fence would be on the North and South sides of the antenna beyond the driveway extending westward. Ground mesh, like that designed for Antenna 7, can also be placed on the rail track and on the driveway beside the rail track.

Figure 2.21 shows that a square mesh of 40 m by 40 m surrounding the antenna is the most effective mesh size. It is able to shield much of the spillover noise even when the antenna is observing at high altitude. Mesh sizes larger than this will give a decreasing return. Thus, the western boundary of the fence was chosen to be 20 m from the antenna. First consider covering the rail track with ground screen. The mesh can be placed along the track and then covered with a layer of sand. Since very little noise reduction will be achieved if mesh is located within 3 m of the antenna, this ground screen will extend from 3 m to 20 m on the West and from 3 m to the edge of the track which is 8 m from the antenna on the East. Ground mesh was also designed on the driveway to the north of the antenna. Like the ground mesh around Antenna 7, mesh will be laid on the ground and then covered with a layer of pebbles and sand to allow the snowplow to shovel snow during winter. This ground mesh will extend from the edge of the track to a distance 11 m North of the antenna. The length of the ground mesh will be 28 m, extending from the western fence boundary to the end of the track.

Next consider placing a mesh fence on the North side of the antenna just beyond the ground mesh. The mesh fence was designed to be 11 m from the antenna just beyond the ground screen. At this distance, a maximum slanting fence angle of 45.4° is allowed. This fence was designed to be 3.66 m wide at an angle of 45°. A wider fence will not provide much more improvement in spillover noise reduction than this design. The

height of this fence is within the maximum height limit. This fence is 24 m long extending westward from the Block House. The final design for the ground mesh and mesh fence around Antenna 5 is shown in Figure 2.44. Figure 2.45 shows the predicted spillover and strut scattering noise reduction. The total amount of mesh needed for this design is 375 m^2.

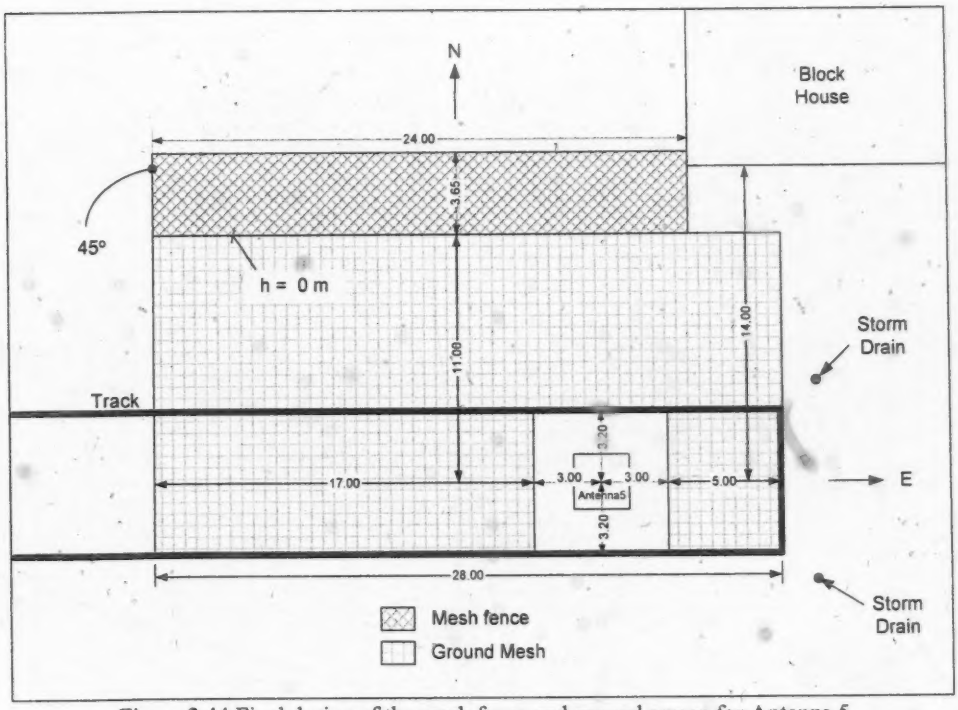

Figure 2.44 Final design of the mesh fence and ground screen for Antenna 5

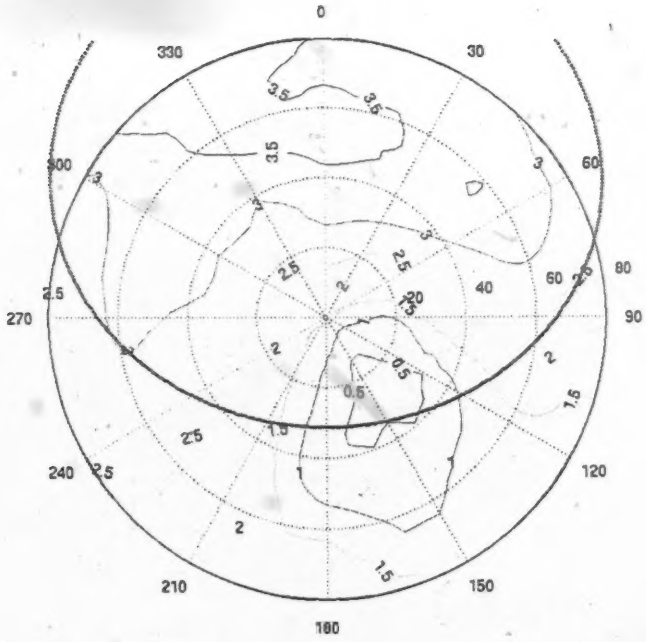

Figure 2.45 The expected spillover and strut scattering noise reduction for Antenna 5.

2.6.7 Proposed Fence Design for the Moveable Antennas

The three moveable antennas (Antennas 2, 3 and 4) are mounted on motorized platforms that ride on a 300 m machined track. Complete coverage of baseline for an observation set is obtained with 12 different settings of the movable antennas. The antennas are moved so that the spacing between Antennas 2, 3 and 4 are fixed at $12L$ (L = 4.286 m) while the separation between antennas 1 and 2 ranges from $3L$ to $14L$ during the observation set. Therefore, only the western 163 m part of the track is used and the design of the shielding fence does not need to cover the full track length; it extends only 183 m from the West end of the track.

The fence and ground screen design is very similar to that around Antenna 5. The mesh boundary would be from the west end of the track to 20 m beyond the eastern utilized track limit. Within this boundary, ground mesh will be placed on the track and to the north side of the track. A 3.66 m wide mesh fence will be built parallel to the track

11 m North of the antenna. This fence connects to the fence built previously for Antenna 1. However, to avoid creating large sidelobes which might catch the sun and contribute to the antenna noise, there will be a slight variation in the slant angle between the panels of mesh fence. The fence is designed to be divided into sections of 10 m with alternating slant angles of 45° and 35° (Figure 2.46).

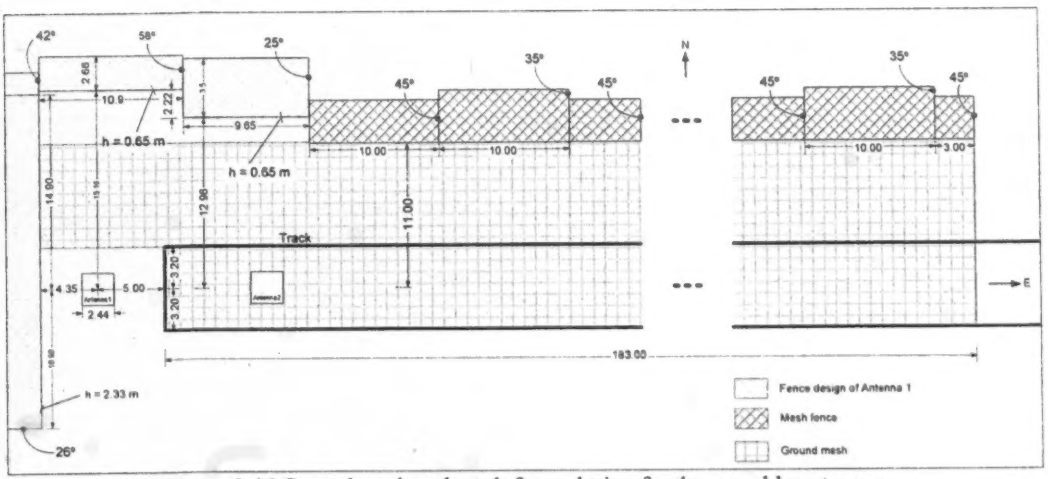

Figure 2.46 Ground mesh and mesh fence design for the movable antennas.

The resultant spillover and strut scattering noise reduction is dependent on the antenna's location relative to the fence. To simplify the calculation of the predicted noise reduction using **Spillover.c** and **ScatterCone.c** (see Section 2.7.2), the slanting angle was assumed to be 40° for the entire fence. Maximum noise reduction is achieved when the antenna is located in the middle of the fence length (Figure 2.47). Antenna 3 has triangular feed legs, so that its strut scattered noise is lower than Antennas 2 and 4 which have circular feed legs (see section 2.7.2). The maximum noise reduction for Antenna 3 (Figure 2.48) is therefore expected to be slightly less than that depicted in Figure 2.47 for an antenna with circular struts. The amount of noise reduction will be smaller when an antenna is moved further west, away from the center of the fence. When the separation between Antennas 1 and 2 is small, the fences designed for Antenna 1 also shield the spillover noise of Antenna 2. Similarly, fence design for the movable antennas is located close enough to Antenna 1 that it also helps to reduce spillover noise of Antenna 1.

Figure 2.49 illustrates the expected noise reduction for Antenna 1 when the proposed fence design is combined with the present fence design around Antenna 1.

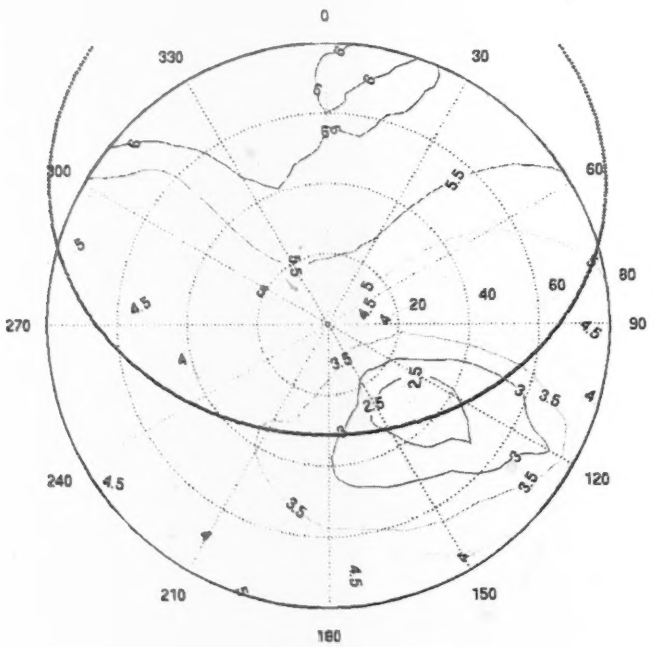

Figure 2.47 Expected spillover and strut scattering noise reduction for an antenna with three circular feedlegs (Antennas 2 and 4).

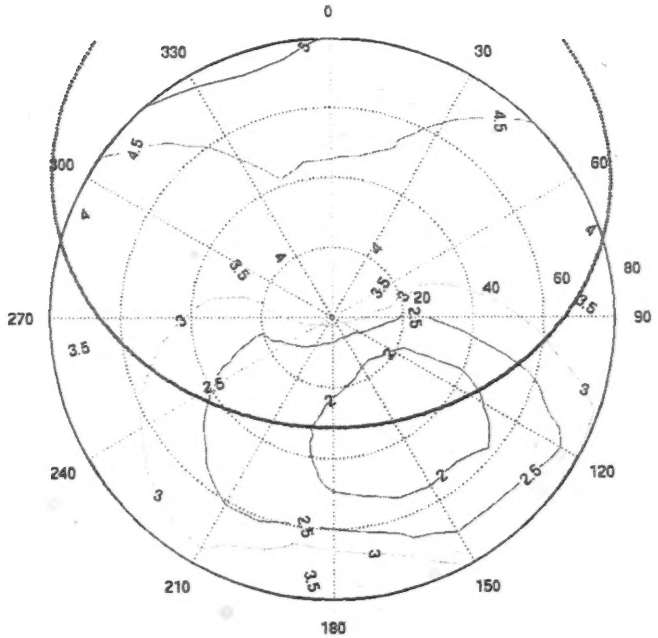

Figure 2.48 Expected spillover and strut scattering noise reduction of an antenna with three triangular struts (Antenna 3).

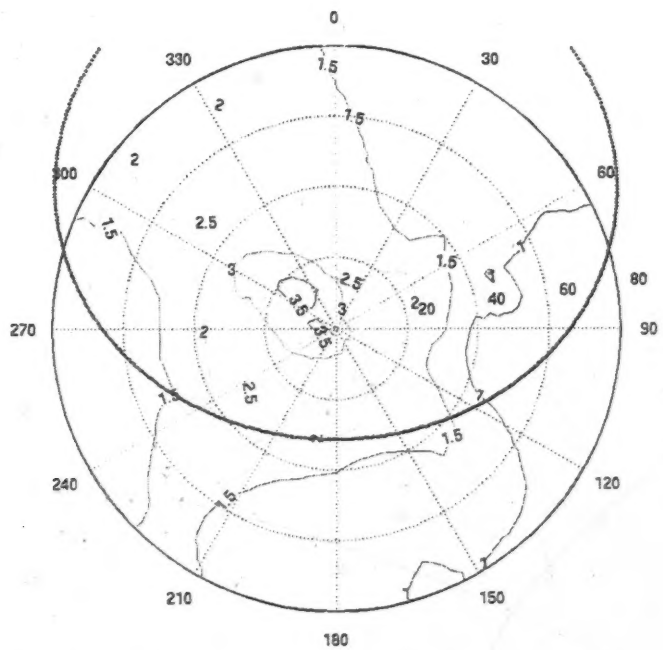

Figure 2.49 Expected spillover and strut scattering noise reduction of Antenna 1 (Compare with Figure 2.38)

2.7 Strut Scattering

A disadvantage of the symmetrical reflector antenna is that the aperture is partially obstructed by the feed and its supporting struts. This blockage causes a reduction of antenna gain, an increase in sidelobe and cross polarization levels and an increase in antenna noise temperature. The study of antenna noise due to strut scattering is simplified by invoking the reciprocity between a receiving and a transmitting antenna and by considering the antenna as a transmitter. Radiation scattered by the struts originates from two sources: a plane wave from the reflector and a spherical wave from the feed. The struts scatter the plane wave that leaves the reflector and produce large conical sidelobes or scatter cones (illustrated in Figure 2.59). Depending on the antenna orientation, part of these scattering cones may illuminate the relatively warm ground, which results in a rise in antenna temperature. However, if the struts are fixed close to the center of the reflector, the spherical wave radiated by the feed is also scattered by the struts and part of the reflector is shadowed by the struts. The spherical wave shadow starts at the base of the strut and broadens out to the edge of the aperture. Since the DRAO Synthesis Telescope antenna has struts that are attached to the reflector rim, only plane wave scattering will be considered in this section.

The intensity of energy scattered by a strut is dependent on its cross-sectional shape, size and the conductivity of the strut. By changing the strut cross sectional shape, antenna noise reduction can be achieved by reducing the intensity of the field scattered by the strut and by redirecting energy in the scatter cones into the forward direction to prevent the cones from striking the ground. The induced field ratio, a parameter that describes the effective blockage of the strut, and the scattering characteristics of struts with different cross-sectional shape were computed with the aid of **Micro-Stripes** [Flomerics Inc]. The noise contributions due to strut scattering were also calculated using the method of ray tracing for circular and triangular struts, based on the energy method derived by Landecker et al [1991]. Finally, an experiment to modify the cross sectional shape of the struts on antenna was conducted to reduce the strut scattering noise for Antenna 7 of the DRAO Synthesis Telescope.

2.7.1 Induced Field Ratio and Scattering Pattern

The scattering from an obstacle, such as a feed-support strut, is characterized by its induced field ratio (*IFR*) and its scattering pattern. *IFR* is the ratio of the effective blockage of an obstacle to its physical cross section. When an infinite cylinder is immersed in an incident plane wave, *IFR* is defined as the ratio of the forward scattered field from the obstacle when illuminated by a uniform plane wave ($E_{scatter}$), to the hypothetical field radiated in the forward direction by the plane wave in the reference aperture of width equal to the shadow of the geometrical cross section of the obstacle on the incident wavefront ($E_{geometry}$) [Rusch, 1976]. The subscripts *scatter* and *geometry* denote the actual field scattered by the obstacle and the hypothetical field radiated by a plane wave in an aperture of the same width as the geometrical shadow of the obstacle respectively. *IFR* is a complex, dimensionless parameter and is a function of the polarization of the incident wave. IFR_E and IFR_H are used when the electric field of the incident plane wave is polarized parallel or perpendicular to the cylinder axis, respectively. For a cylinder aligned along the z-axis and a plane wave propagating in the x direction (Figure 2.51 and Figure 2.52):

$$IFR_E = \frac{E_{z,scatter}}{E_{geometry}} \tag{2.7.1}$$

$$IFR_H = \frac{E_{y,scatter}}{E_{geometry}} \tag{2.7.2}$$

IFR_E is larger in magnitude than IFR_H and has a positive phase angle compared to a negative phase angle for the *H*-polarization. For a perfectly conducting obstacle such as an infinitely long metal cylinder, *IFR* will approach -1+j0 as the radius increases to infinity. *IFR* of -1+j0 corresponds to a purely geometrical blockage with the obstacle casting a geometrical shadow. The negative sign indicates that the forward scattered field cancels the incident field.

2.7.1.1 Micro-Stripes simulation

A commercial software package (**Micro-Stripes**) was used to aid the computation of *IFR* and scattering pattern of cylinders with different cross-sectional shape. **Micro-Stripes** is a three-dimensional electromagnetic simulator, which uses the numerical technique called transmission line matrix method (TLM). Chapter 1 has a brief explanation of the TLM method.

Micro-Stripes was used to calculate the field scattered by a cylinder when it is immersed in an incident plane wave. Cylinders with different diameters and cross-sectional shapes such as circular, triangular and teardrop shape (Figure 2.50) were examined. The simulation was carried out by constructing the cylinder along the z-axis and launching a plane wave from the negative x-axis. This plane wave was polarized parallel to the z-axis for E-field scattering (Figure 2.51) and parallel to the y-axis for H-field scattering (Figure 2.52).

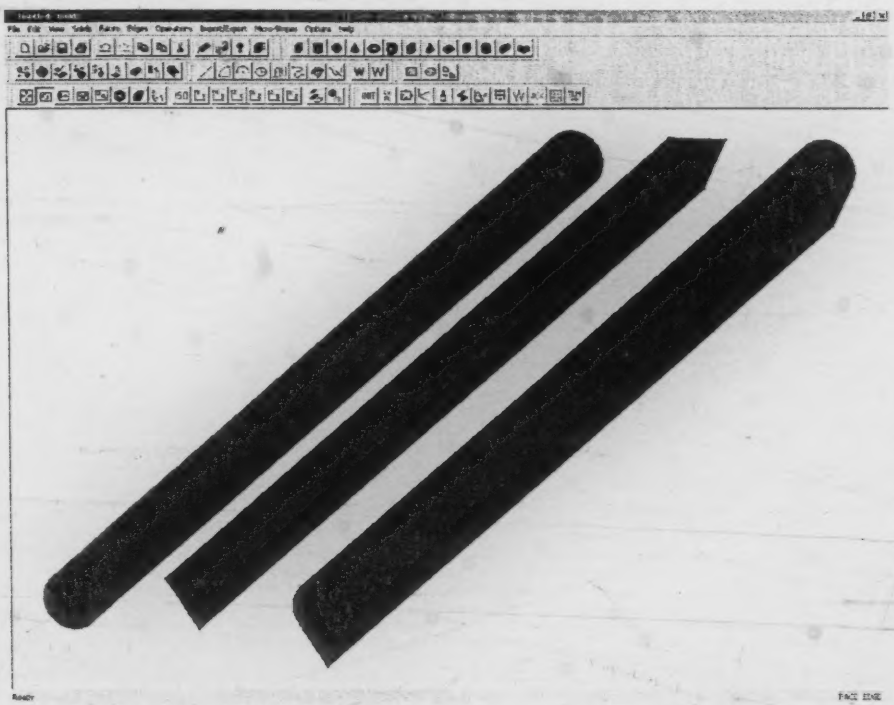

Figure 2.50 The three types of cylinder considered in the *IFR* calculation

The output of the Micro-Stripes simulation displays the far-field scattering pattern, and directivity and total power of the scattered field at a specified frequency (Figure 2.53). Using this information, IFR_E and IFR_H for various strut cross sections and diameters were calculated. In addition, the far-field scattering patterns for different struts were compared.

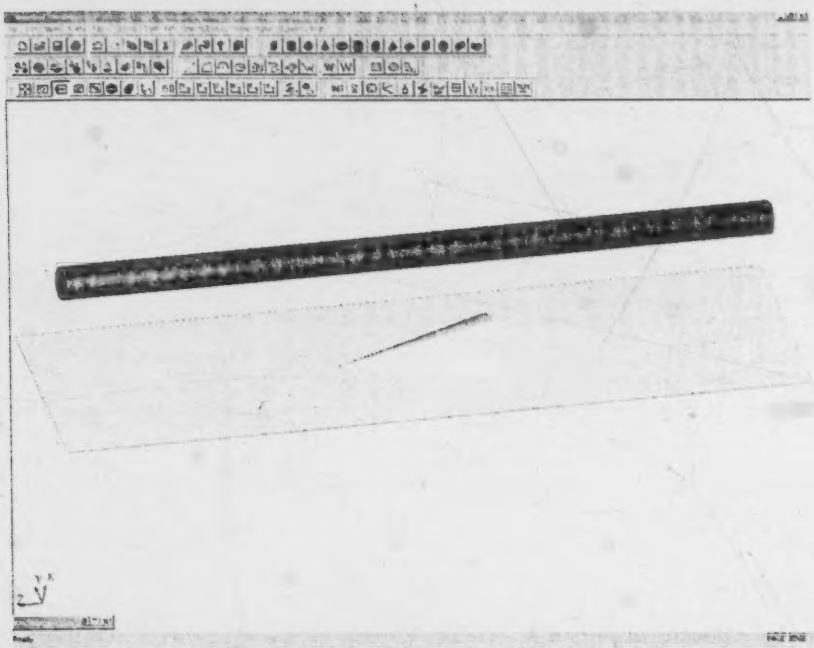

Figure 2.51 Micro-Stripes simulation for IFR_E calculation. The gray planar structure represents a plane wave which is propagating upwards (in the x direction) towards the cylinder. The cone shaped structure indicates the polarization of the wave. The plane wave is polarized parallel to the cylinder axis.

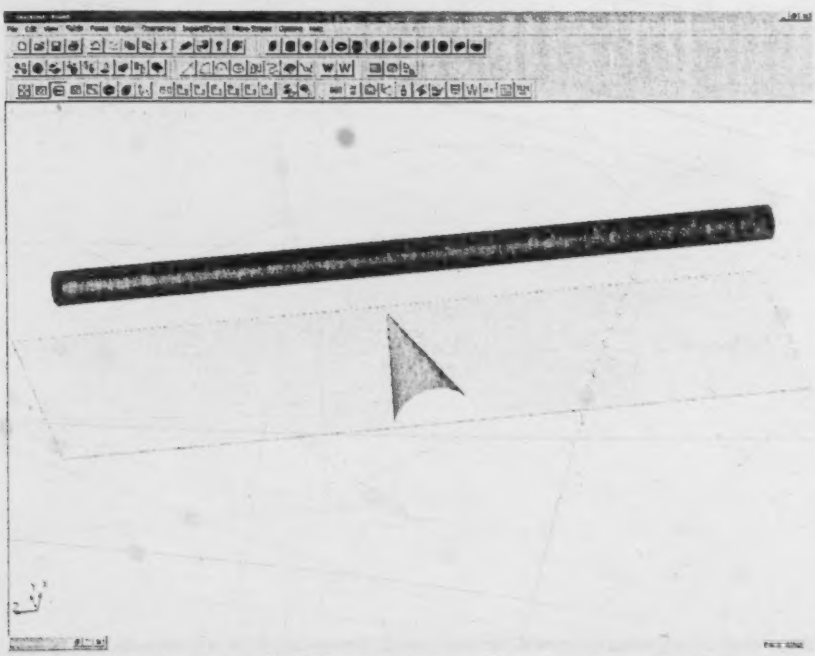

Figure 2.52 Micro-Stripes simulation for IFR_H calculation. The plane wave is polarized perpendicular to the cylinder axis.

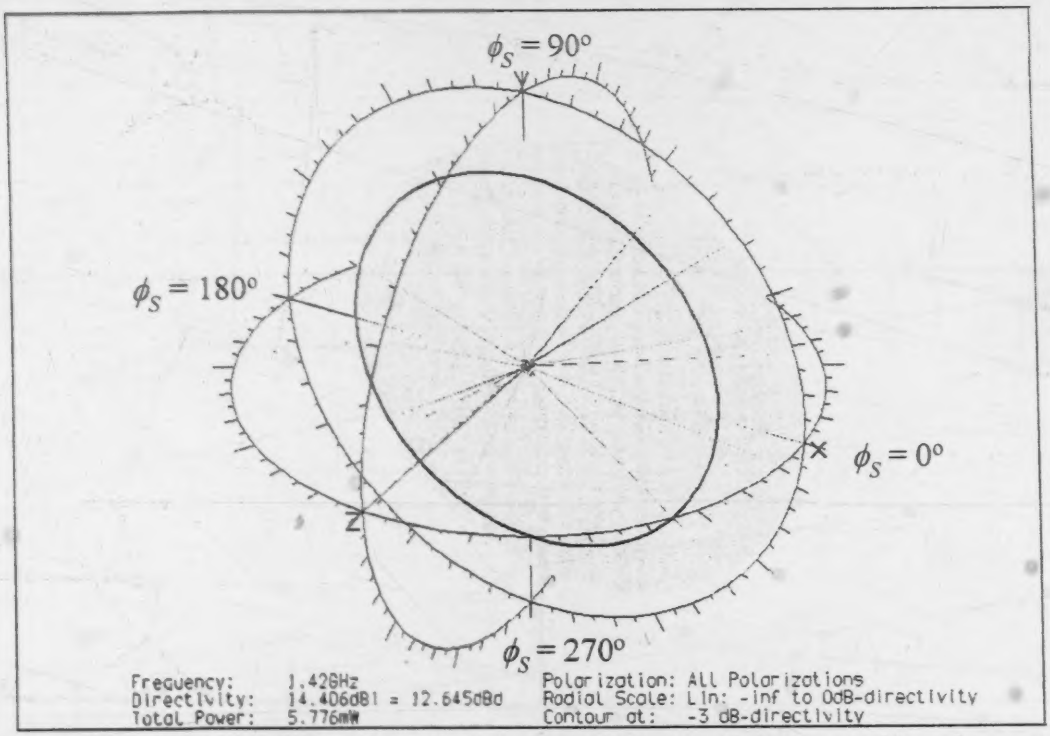

Figure 2.53 Output of the Micro-Stripes simulation for a 1" circular cylinder immersed in a plane wave polarized parallel to the cylinder axis. The frequency, directivity and total scattered power of the scattered field are shown at the foot of the plot on the left. The black line on the plot is the -3 dB contour. f s is the angle around the scattering pattern with f s = 0 o pointing towards the forward direction.

2.7.1.2 *IFR* calculation

The magnitude of *IFR* was calculated using equations (2.7.1) and (2.7.2) and the scattered field directivity and total power given in the Micro-Stripes simulation. Forward directivity ($D_{forward}$) is a ratio of the forward radiated power ($U(0,0)$) to the average radiation intensity (U_{avg}). $\phi_s = 0°$

$$D_{forward} = \frac{U(0,0)}{U_{avg}} \tag{2.7.3}$$

and

$$U_{avg} = \frac{U_{tot}}{4\pi} \tag{2.7.4}$$

therefore

$$U(0,0) = \frac{U_{tot}}{4\pi} D_{forward} \tag{2.7.5}$$

IFR magnitude is the ratio of forward scattered field to the forward hypothetical field and the electric field is proportional to the square root of power.

$$|IFR| = \frac{E_{scatter}}{E_{geometry}} = \frac{\sqrt{U_{scatter}(0,0)}}{\sqrt{U_{geometry}(0,0)}} \tag{2.7.6}$$

Inserting equation (2.7.5) into equation (2.7.6)

$$|IFR| = \sqrt{\frac{D_{scatter} U_{scatter}}{D_{geometry} U_{geometry}}} \tag{2.7.7}$$

In the above equation, both $D_{scatter}$ and $D_{geometry}$ represent directivity in the forward direction. $U_{scatter}$ and $U_{geometry}$ are values of total scattered power.

Directivity and the total power can be read from the Micro-Stripes simulation outputs. The directivity and the radiation intensity of the hypothetical aperture having a constant field over its cross section and cross sectional area equal to the geometrical shadow of the scatterer were then calculated. The hypothetical field has a maximum in the forward direction. Thus directivity in the forward direction is equal to the maximum directivity.

$$D_{geometry} = \frac{4\pi A_{geometry}}{\lambda^2} \tag{2.7.8}$$

where

$A_{geometry}$ = area of the geometrical shadow of the scatterer

λ = wavelength

The total radiation intensity is proportional to the product of the power per unit area or Poynting vector (S) and the geometrical shadow cross section area ($A_{geometry}$):

$$U_{geometry} = SA \tag{2.7.9}$$

and

$$S = \frac{1}{2}\frac{E^2}{Z_o} \tag{2.7.10}$$

where

1/2 is the peak to rms conversion

E = electric field over the aperture

Z_o = intrinsic impedance of free space = 376.7 Ω

Therefore

$$U_{geometry} = \frac{1}{2}\frac{E^2}{Z_o}A \tag{2.7.11}$$

To validate the computation of $|IFR|$ using **Micro-Stripes** simulations and the equations derived above, the $|IFR_E|$ and $|IFR_H|$ calculated using equations (2.7.7), (2.7.8) and (2.7.11) for circular cylinders were compared with the results calculated by Rusch [1978] using the method of moments (Figure 2.54). As shown in the plot, the two methods give very similar results, validating the derivation of *IFR* with Micro-Stripes. In addition, by increasing the strut length and decreasing the grid size, a closer match to the literature results can be obtained. However, this also increases the simulation time exponentially. The strut length of 30 m and the grid size used to compute the $|IFR|$ in Figure 2.54 is a sufficiently good approximation. This computation configuration was also used to calculate $|IFR|$ for cylinders with triangular and teardrop shaped cross-sections.

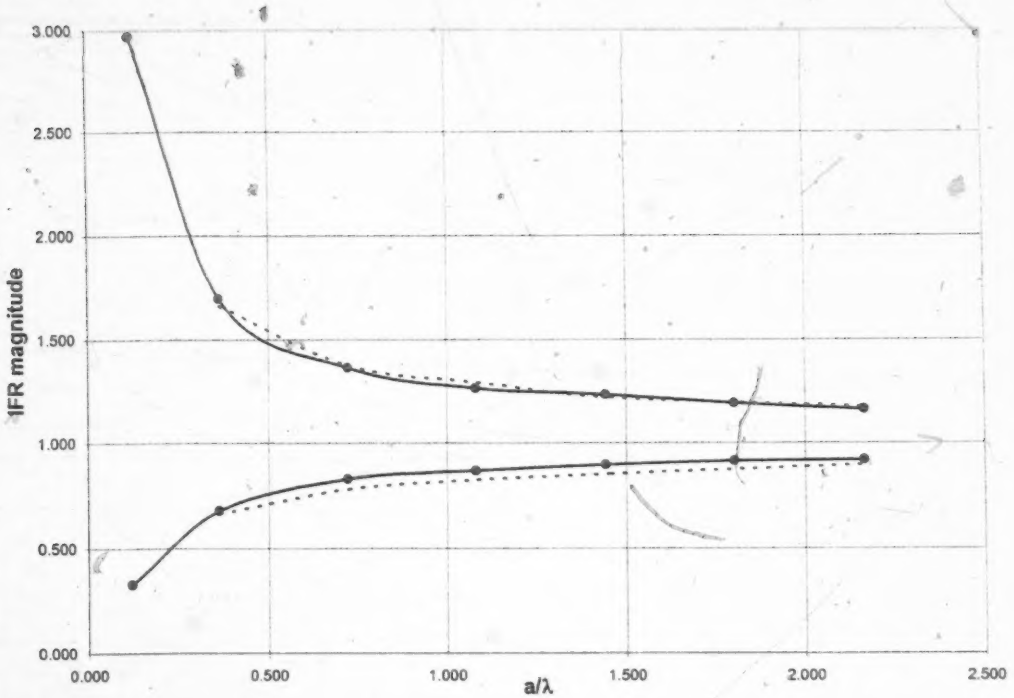

Figure 2.54 Comparison of $|IFR|$ for circular cylinders calculated using the Micro-Strips simulation (black lines) and the method of moments (dotted lines) [Rusch, 1978].

Next, $|IFR_E|$ and $|IFR_H|$ for cylinders of various widths and cross-sections were calculated. The results are plotted in the graph shown in Figure 2.55. The *IFR* of a triangular cylinder approaches the ideal limit of geometrical blockage much faster than circular and teardrop shaped cylinders. When the width of the cylinder is small compared to the wavelength, $|IFR_E|$ for the teardrop shaped cylinder is greater than that of the circular cylinder and $|IFR_H|$ is smaller. However, the two *IFR* magnitudes are very similar when the width of the cylinder is of the order of one wavelength.

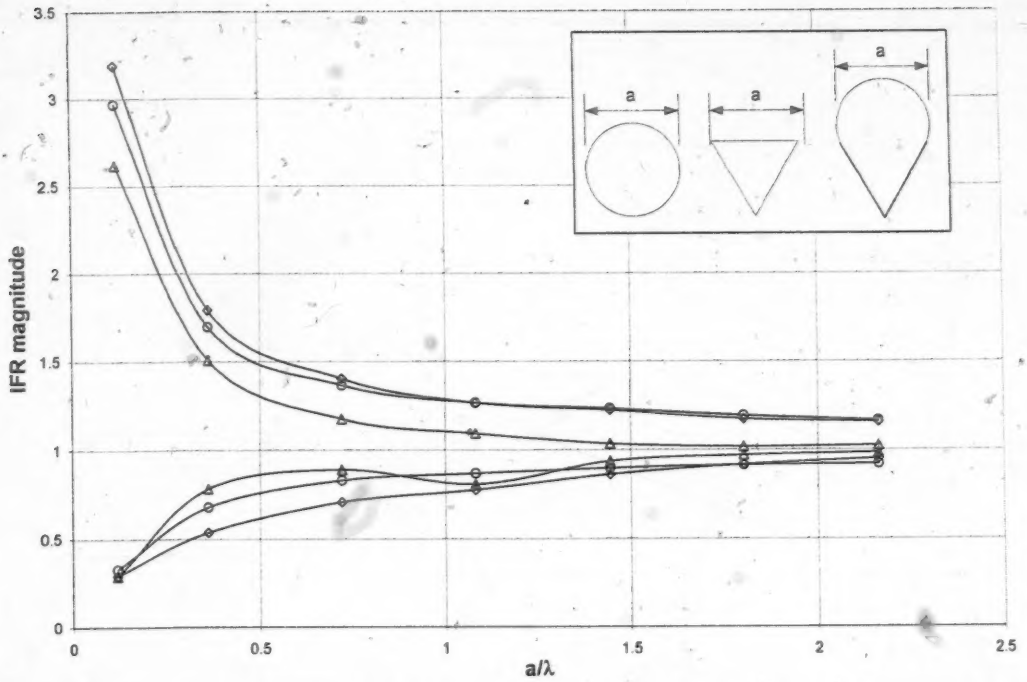

Figure 2.55 *IFR* magnitude for circular (circle marker), triangular (triangle marker) and teardrop shaped (diamond marker) cylinders. $|IFR_E|$ is greater than 1.0 and $|IFR_H|$ is less than 1.0.

The ripples in the triangular $|IFR_H|$ line suggest resonance. The wave diffracted off the front corner is added to the diffraction from the two back corners. When the triangular cross section has sides equal to odd multiples of 0.5λ, the two waves are added destructively to give a smaller $|IFR_H|$ or less blockage. However, when the sides are even multiples of 0.5λ, the two waves are in phase. The two in-phase diffracted waves are added constructively giving the triangular cylinder a worse blockage performance than a circular cylinder of the same width. The teardrop shaped cylinder has only one sharp diffracting corner in the front. There is no cancellation of scattering as a result of destructive combination of waves diffracted from the front and back corners, as seen in the triangular strut case. Therefore, from the blockage point of view, triangular struts would have the best performance among the three types of struts while teardrop shaped struts would have the worst.

Two of the Synthesis Telescope antennas have struts made of fiberglass. The magnitude of IFR_H and IFR_E for circular fiberglass cylinders of various diameters was

calculated using the procedure described above. The results are plotted in Figure 2.56. As shown in the plot, unlike metal cylinders, both $|IFR_E|$ and $|IFR_H|$ are very small for a dielectric cylinder thinner than half a wavelength meaning it is almost invisible to the incident plane wave. However, the strut becomes more visible as its diameter becomes larger.

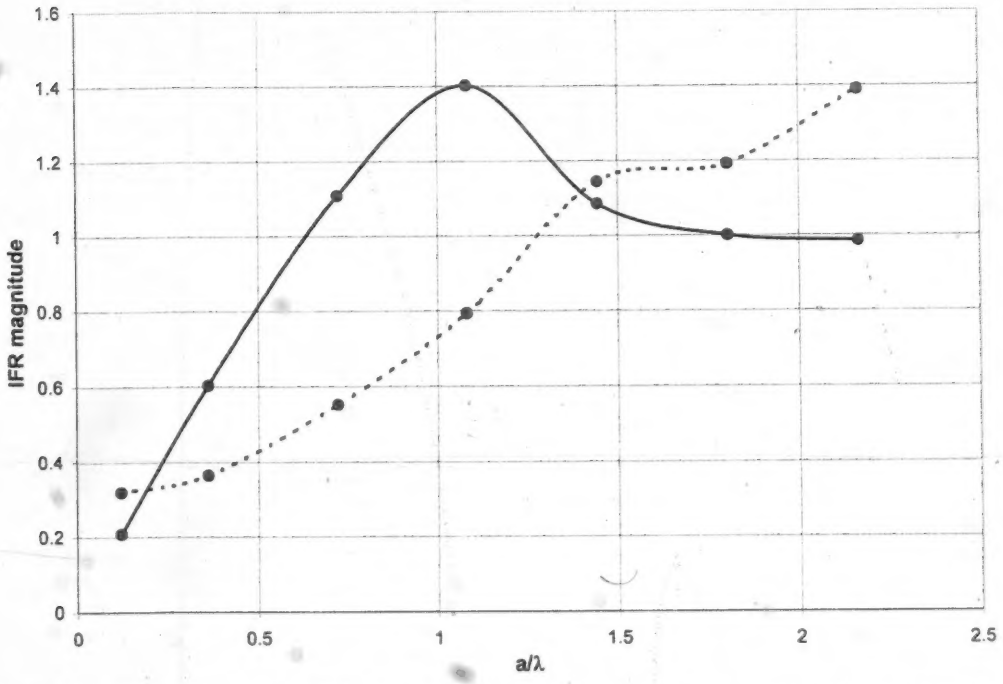

Figure 2.56 *IFR* magnitude for a dielectric, circular cylinder. Black line represents IFR_E and dotted line represents IFR_H.

For the case of random polarization, such as thermal ground radiation, the effective blockage is best described as the average of the two polarizations, $|IFR_M|$.

$$|IFR_M| = (|IFR_E| + |IFR_H|)/2 \tag{2.7.12}$$

The value of $|IFR_M|$ increases for smaller cylinder cross-section which means that the effective size of the strut exceeds its physical size. It can be seen from Figure 2.55 that $|IFR_M|$ for triangular struts approaches 1 more quickly than $|IFR_M|$ for circular and teardrop struts.

2.7.1.3 Scattering Pattern

The distribution of scattered radiation around the scatter cone will determine the ground noise contribution. Since the cylinders modeled in the simulations are long with respect to the simulation wavelength, their far-field patterns are flat disks oriented perpendicular to the cylinder axis (an example of the scattering pattern is shown in Figure 2.53). The shape of the disk determines the scattering pattern. There is a strong lobe in the forward direction (ϕ_S = 0° in Figure 2.53) of the scattering pattern. This lobe represents the shadow of the strut and the fields are in antiphase with the incident plane wave. When the incident field and the scattered field are added vectorially, a null is formed in the forward direction.

Scattering patterns for the case when the plane wave is polarized parallel and perpendicular to the cylinder axis were generated by **Micro-Stripes**. The patterns were stored in **Excel** files each containing 9 columns. The first 3 columns denote the direction of radiation in Cartesian coordinates. The last 6 columns describe the real and imaginary components of the electric field in the specified direction. The Cartesian directions were converted to spherical coordinates with angle ϕ_S as defined in Figure 2.53 and the power densities of the scattering patterns were calculated.

$$S = \frac{|E|^2}{\eta} \tag{2.7.13}$$

where

$$|E| = \sqrt{\mathrm{Re}^2\{E_x\} + \mathrm{Im}^2\{E_x\} + \mathrm{Re}^2\{E_y\} + \mathrm{Im}^2\{E_y\} + \mathrm{Re}^2\{E_z\} + \mathrm{Im}^2\{E_z\}} \tag{2.7.14}$$

η = intrinsic impedance of space= 376.7 Ω

Since thermal radiation from the ground is randomly polarized, a scattering pattern that averages power density of the E-field and H-field incident is most appropriate. Figure 2.57 and Figure 2.58 show the average scattering pattern of 3" and 6" struts with circular, triangular and teardrop cross-sectional shape.

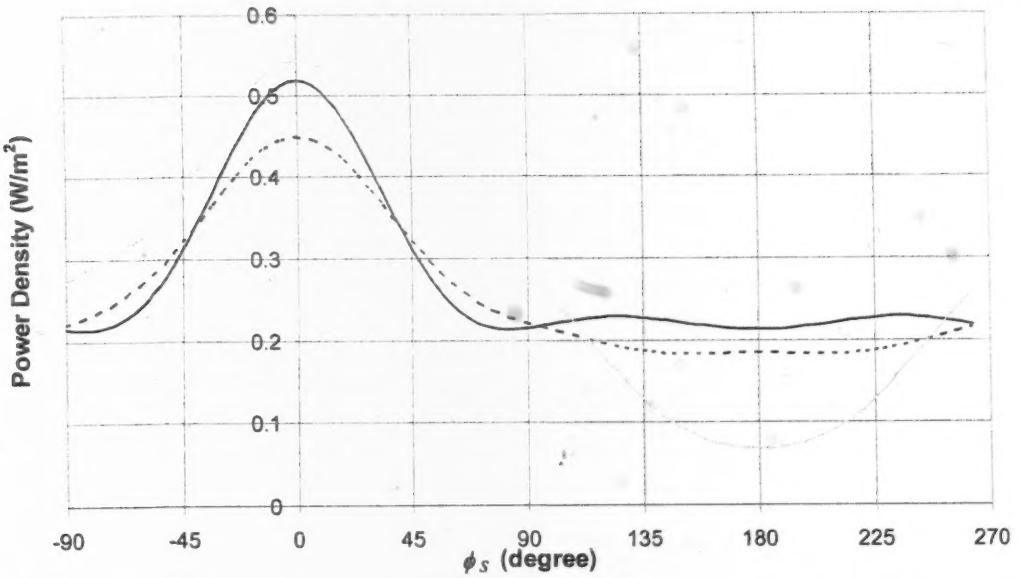

Figure 2.57 Scattering pattern of 3" struts with circular (black), triangular (dotted black) and teardrop shape (gray) cross sections at 1.42 GHz

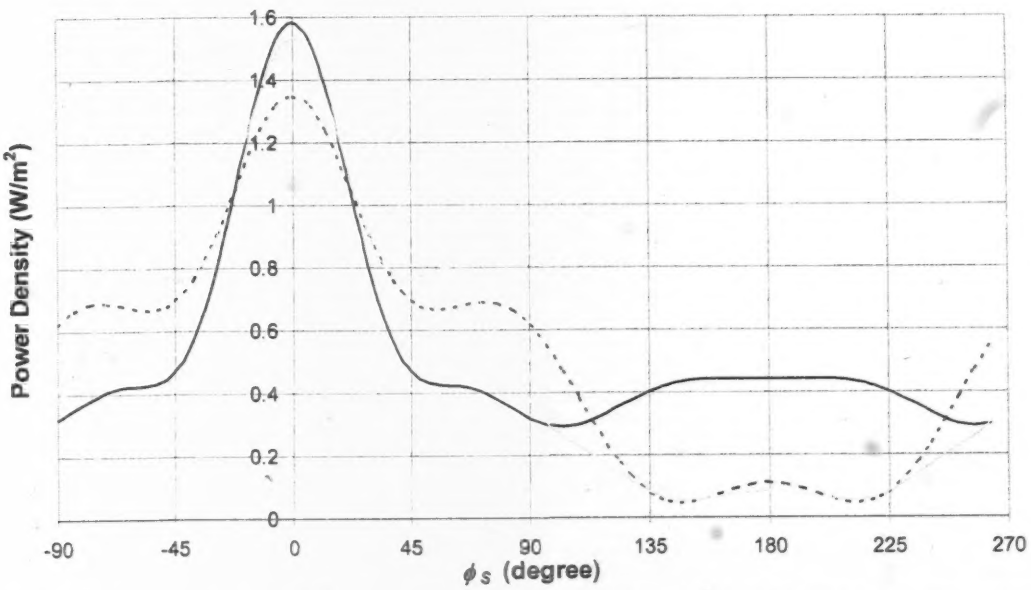

Figure 2.58 Scattering pattern of 6" struts with circular (black), triangular (dotted black) and teardrop shape (gray) cross sections at 1.42 GHz

The back-scattering region, which may illuminate the ground, ranges approximately from $\phi_S = 90^\circ$ to 270°. A low power density in this region is desired to

reduce strut scattering noise. When the strut cross section is small with respect to the wavelength (Figure 2.57), the back-scattering patterns for triangular and circular cylinders are very similar. However, a triangular strut has a smaller $|IFR_M|$ value at this cross-sectional size than a circular strut, and a triangular strut has a better antenna noise performance than circular struts. A teardrop shaped strut has a considerably lower back-scattering level than the other two struts. For a larger strut cross section (Figure 2.58), the scattering pattern for a circular strut remains relatively uniform in the back region. The improved back-scattering levels over circular struts are evident for triangular and teardrop shaped struts. In both cases, the teardrop shape is the best strut cross-section for redirecting scattered energy toward the forward direction.

2.7.2 Calculation of Antenna Noise due to Strut Scattering

The program **ScatterCone.c** (written by the author) performs the calculation of strut scattering noise. It is based on **Spillover.c** which calculates spillover noise using the method of ray tracing. In **ScatterCone.c**, rays originate from scatter cones located in the middle of each strut. The power patterns of the scatter cones were approximated using energy considerations.

The plane wave scattering can be understood by considering the energy scattered by an infinitely long cylinder when it is illuminated by an incident plane wave. Landecker et al. [1991] derived expressions that describe the size of the scatter cones and the strength of the scattered radiation using energy considerations. The struts approximately behave like linear antennas carrying induced currents and the scattered energy is concentrated into a cone with an opening angle 2γ, where γ is the angle between the strut and the boresight direction (Figure 2.59). The half-power width of the cone β is determined by the length of the strut, L, projected onto the aperture.

$$\beta = \frac{1}{(L\sin\gamma)/\lambda} \tag{2.7.15}$$

$$\beta = \frac{2\lambda}{D} \tag{2.7.16}$$

The second relation is valid if the struts are attached to the rim of the reflector with diameter D since $L\sin\gamma = D/2$. To simplify the strut scattering noise temperature, the energy distribution across the half-power width β of the scatter cone is assumed to be uniform with scattered energy zero outside the half-power width.

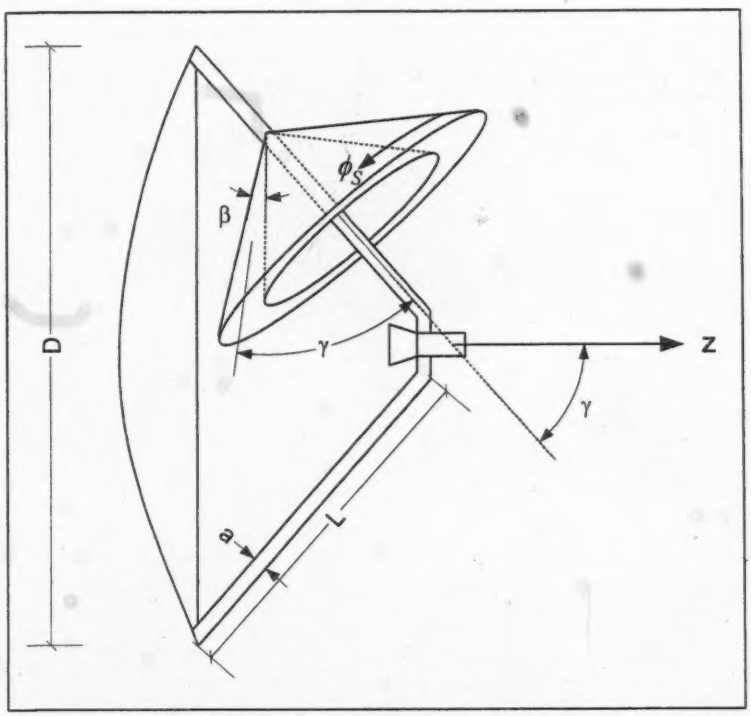

Figure 2.59 Geometry of the scatter cone of a feed support strut in a symmetrical paraboloidal antenna.

The fraction of transmitted power f scattered by the struts and reradiated into the scatter cones is equal to the fraction of the aperture area that is blocked by the struts multiplied by the effective blockage factor of the struts. *IFR* is a measure of how strongly the obstacle will block the incident field. For the calculation of strut scattering noise $|IFR_M|^2$ was considered since noise is randomly polarized and f is the fraction of scattered power rather than scattered field. Assuming uniform aperture illumination, the fractional aperture blockage is

$$f = \frac{2Na}{\pi D}\left|IFR_M\right|^2 \tag{2.7.17}$$

where N is the number of struts and a is the width of the strut projected onto the aperture. The solid angle in the scatter cones is

$$\Omega_s = N\beta 2\pi \sin\gamma \tag{2.7.18}$$

The level Q of radiation in the scatter cones relative to the main beam was calculated by comparing the power density in the scatter cones with the power density in the main beam. The power density in the main beam is P/Ω, where P is the total radiated power and Ω is the antenna solid angle. The power radiated in the scatter cones is dependent on the factor f. The power in the scatter cones is Pf and the power density is Pf/Ω_s.

With most antennas, aperture illumination is not uniform. As the feed distribution tapers, the aperture efficiency decreases and the power density in the main beam is reduced by the illumination efficiency, η_I. However, the effective fractional blockage by the struts increases. The energy in the scatter cones relative to the main beam increases because a greater fraction of the aperture is blocked near the center where the illumination is high. Landecker et al. [1991] found that the effective blockage f will increase by $\eta_I^{-0.5}$. Therefore, combining the effects of effective strut blockage and illumination tapering, the ratio of power density in the scatter cones to the power density in the main beam is:

$$Q = \frac{f\Omega_A}{\Omega_s}\eta_I^{-1.5} \tag{2.7.19}$$

The cross sectional shape of the strut not only determines the effective blockage as described by IFR, but also controls the energy distribution within the scatter cone. In communication antenna applications, it is important to reduce the peak level of sidelobes

since these sidelobes may cause interference between radio links. Methods have been studied to suppress the sidelobe levels by attaching metallic saw-tooth shaped plates at the reflecting surfaces of the struts [Satoh et al., 1984] and by using struts that bend outwards [Thielen et al., 1985]. Both methods redistribute the energy scattered by the strut over a larger solid angle and generate a higher backscattering level. From the point of view of antenna noise reduction, directing energy away from the ground towards the forward direction is preferable. Thus, neither of these strut modifications are suitable for the application of minimizing strut scatting noise.

In the paper by Landecker et al. [1991], struts with circular and triangular cross sections were examined. A strut with circular cross-section produces a scatter cone that can be approximated by a uniform energy distribution around the cone and within the half-power beam width β. A triangular strut, with its apex pointing down at the reflector, has two flat surfaces which are capable of concentrating scattered energy in the forward hemisphere. The energy distribution around the isosceles triangular strut's scatter cone can be approximated using two Gaussian functions centered at the two specular reflection directions θ_{sp}.

$$C(\phi_S) = \left(e^{-(\phi_S - \theta_{sp})^2 / 2\sigma^2} + e^{-(\phi_S + \theta_{sp})^2 / 2\sigma^2} \right) / MaxC \qquad (2.7.20)$$

where

ϕ_S = angle around the scatter cone as defined in Figure 2.59

θ_{sp} = direction of specular reflection

σ = standard deviation

$MaxC$ = normalization factor

Let the cross section of the strut be an isosceles triangle with an angle α at the apex; specular reflection would be α from the forward direction from either side of the strut (Figure 2.60). The standard deviation determines the width of the Gaussian function and can be calculated using the full width half maximum (*FWHM*) which is inversely proportional to the length of the triangular cross section side orthogonal to the incident plane wave.

$$\sigma = \frac{FWHM/2}{\sqrt{2\ln 2}} \tag{2.7.21}$$

where

$$FWHM = \frac{\lambda}{s\sin(\alpha/2)} \tag{2.7.22}$$

The FWHM of the Gaussian function is larger for thinner struts. The energy distribution around the scatter cone approaches uniform as the dimension of the cross section decreases. Thus, there is little difference between the behaviors of circular and triangular struts if the cross sectional width is small relative to the wavelength. This agrees with the scattering patterns simulated using **Micro-Stripes**. The back scattering patterns for 0.36λ circular and triangular cylinders are very similar (Figure 2.57). However, as the dimension of the triangular strut cross section increases, the scattering pattern will concentrate in the two specular reflection directions and a lower back scattering level will result.

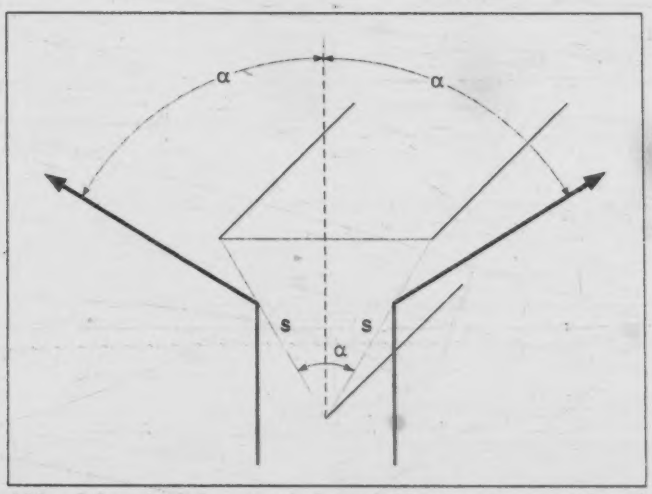

Figure 2.60 If the width of the triangular strut is large with respect to wavelength, scattered energy is concentrated in the two directions determined by specular reflection from the sides of the strut.

With the knowledge of the amount of radiation energy and the energy distribution in the scatter cones, the antenna noise due to strut scattering can be computed by integrating the antenna temperature equation (2.7.7) numerically.

$$T_{strut}(a,A) = \frac{D_C Q}{\Omega_A} \sum_{N=1}^{\#struts} \sum_{n_{\phi S}=0^\circ}^{360^\circ} \sum_{n_{\theta S}=62^\circ}^{horizon} T(n_{\theta_S}, n_{\phi_S}) C_N(n_{\theta_S}, n_{\phi_S}) \sin(n_{\theta_S}) \Delta n_{\theta_S} \Delta n_{\phi_S} \qquad (2.7.23)$$

where

Q = level of radiation in the scatter cone relative to the main beam

Ω_A = antenna solid angle = $4\pi/10000$ Sr.

D_C = directivity of the scatter cone pattern = $\dfrac{2\pi}{\int_{-\pi}^{\pi} C(\phi_S) d\phi_S}$

$T(n_{\theta_S}, n_{\phi_S})$ = effective brightness temperature of the ground

$C_N(n_{\theta_S}, n_{\phi_S})$ = power pattern of the Nth scatter cone

θ_S, ϕ_S are spherical angles in coordinate system S

Since the scattering pattern generated by the triangular strut is tapered in the back region (ϕ_S = 90° to 270°), the scaling factor D_C is needed to normalize for the amount of energy in the scatter cone. The circular strut has a uniform scattering pattern; the directivity of its scatter cone is 1. D_C for the triangular strut is greater than or equal to one depending on the width of the strut. The total strut scattering noise is the scalar summation of the noise contributions from all scatter cones. Since the struts scatter energy towards the ground and lead to an increase in antenna temperature, **ScatterCone.c** was also used to examine the use of mesh fences to reduce strut scattering noise.

The first step in the calculation of antenna temperature is to determine the location where a scatter cone strikes the ground and the angle of incidence using ray tracing. The function for ray tracing in **ScatterCone.c** is similar to that in **Spillover.c**. Rays were extended from each scatter cone, originating in the middle of each strut. Since the struts rotate with the antenna as it observes, five coordinate systems, B, B', P, P_N' and S_N

(Figure 2.61), are needed to solve for the line equation of the rays in each scatter cone with respect to coordinate system B. N is the scatter cone label. The scatter cones are labeled from 1 through the number of struts (3 or 4), starting from the East and counting clockwise when the antenna is pointing at the zenith. Coordinate systems B, B' and P are identical to that defined in Figure 2.16 for the calculation of spillover noise. Coordinate system P_N', located at the apex of the scatter cone in the middle of each strut, is the translated version of P. Coordinate system S_N has the same origin as P_N'. It is a right-hand system with z-axis aligned with the strut axis and x-axis pointing in the forward direction of the scattering pattern or away from the center of the reflector.

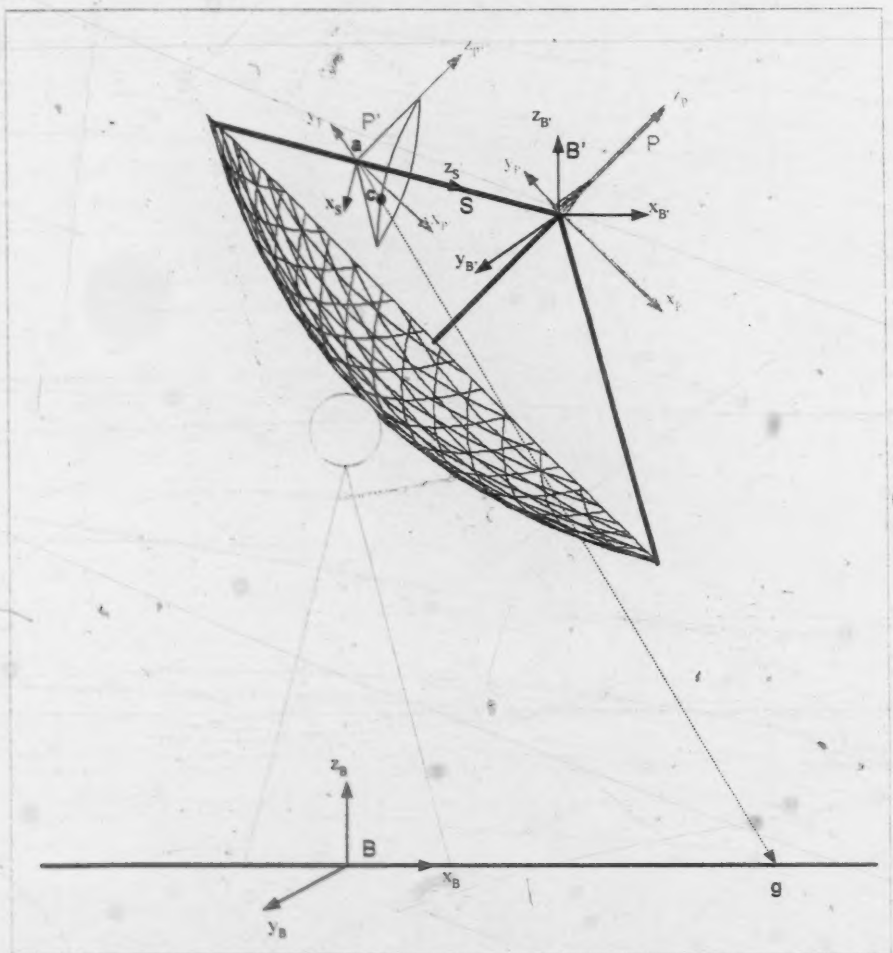

Figure 2.61 Coordinate systems B, B', P, P' and S are defined with respect to the antenna for the computation of scatter cone sidelobes on the ground.

Since the coordinate system S rotates with respect to P, which is rotated with respect to B, to write line equations for these rays in the system B, two coordinate system rotations and two vector translations are required. The two known points in these line equations are the cone apex (a) and the edge of the cone (c). The scatter cone apex (point a) is located in the middle of the strut and its coordinates with respect to system P can be determined by solving simple geometries. Point c, assumed to be 1 m from the apex, has coordinates $r_{cS} = 1$, $\theta_{cS} = \gamma - \beta/2$ to $\gamma + \beta/2$ and $\phi_{cS} = 0^\circ$ to 360°. Given the coordinates of point c in S_N, its coordinates in P_N' (r_{cP}, θ_{cP} and ϕ_{cP}) can be calculated using the rotation formulas stated in Appendix A. The rotation between coordinate systems S_N and P_N' is defined by $\theta_{SP'}$, $\phi_{SP'}$, and $\psi_{SP'}$ (see also Appendix A).

$$\theta_{SP'} = \sin^{-1}\frac{D/2}{L} \tag{2.7.24}$$

$$\phi_{SP'} = \begin{cases} 90^\circ + 120^\circ N & for 3 struts \\ -180^\circ + 90^\circ N & for 4 struts \end{cases} \tag{2.7.25}$$

$$\psi_{SP'} = \begin{cases} -90^\circ + 120^\circ N & for 3 struts \\ 90^\circ N & for 4 struts \end{cases} \tag{2.7.26}$$

where D is the diameter of the reflector, L is the strut length and N is a number representing each scatter cone. The coordinates of point c with respect to coordinate system P (x_{cP}, y_{cP}, and z_{cP}) were calculated by vector translation. Up to this point, both points a and c were defined in coordinate system P. The procedures used to compute their coordinates with respect to coordinate system B, the location where the ray strikes the ground, and the angle of incidence are identical to those used in the program **Spillover.c**. Using the calculated angle of incidence, the effective brightness temperature $T(n_{\theta_s}, n_{\phi_s})$ can be determined using equation 2.6.3.

Strut scattering increases the antenna temperature by illuminating the ground. Thus, fences used to shield direct spillover noise can also be used to reduce noise due to strut scattering. The function that checks whether the radiation intersects the mesh fence

was also implemented in **ScatterCone.c**. If the ray intersects the fence, it is partially reflected towards the sky. The effective temperature is then reduced by the transparency factor of the mesh. The sky is assumed to have zero brightness temperature.

The output of **ScatterCone.c** was a file with three columns, zenith angle, azimuth and noise temperature respectively. The strut scattering noise temperature was plotted on a polar grid in contour form using **Matlab**. The calculation of strut scattering noise was based on the two different antenna designs of the Synthesis Telescope. Antennas 1 and 7 have four 3" struts with circular cross section. The other antennas have three 6" struts with circular or triangular cross sections. With the exception of the struts of antennas 2 and 4 which are made of fiberglass, the other struts are made of metal. Strut scattering noise as a function of zenith angle and azimuth for these antennas is plotted below.

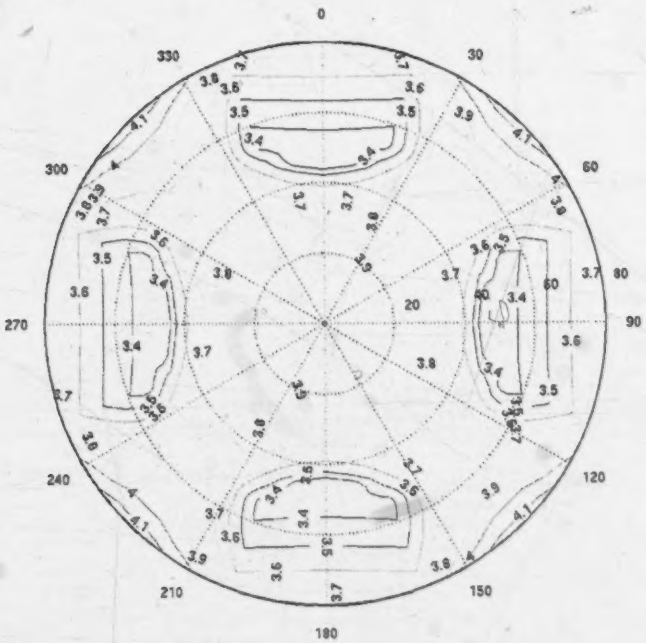

Figure 2.62 Predicted strut scattering noise for an antenna with four 3" circular metal struts

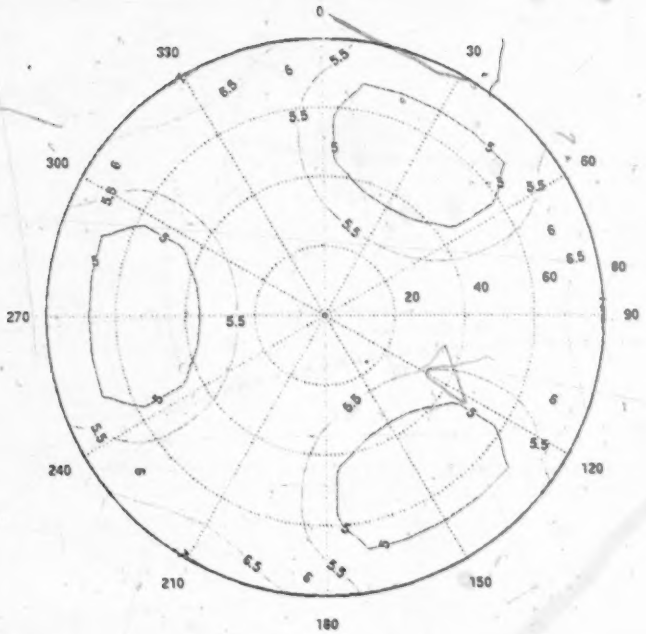

Figure 2.63 Predicted strut scattering noise for an antenna with three 6" circular metal struts

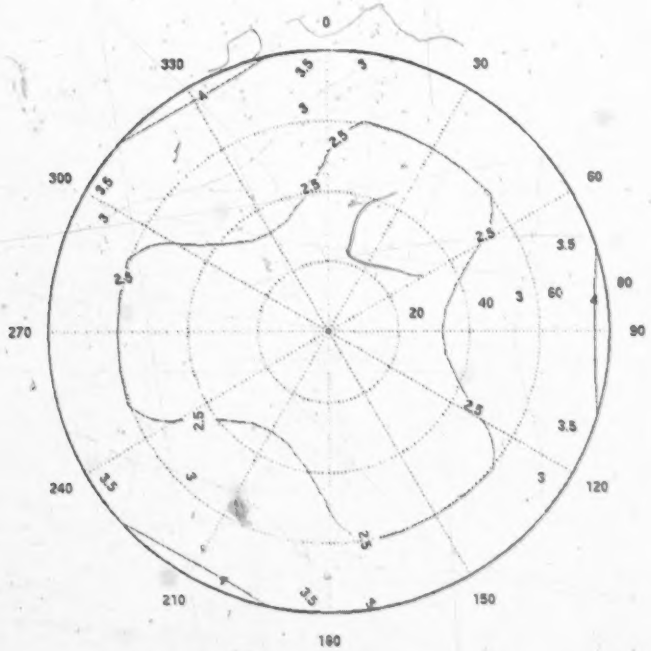

Figure 2.64 Predicted strut scattering noise for antenna with three 6" triangular metal struts

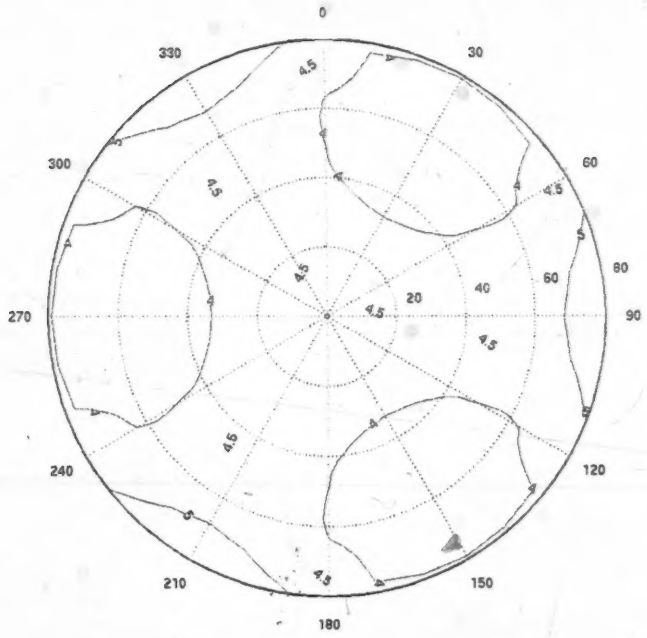

Figure 2.65 Predicted strut scattering noise for antenna with three 6" circular dielectric struts

The strut scattering noise for an antenna is relatively low when it is pointing towards the zenith. If the antenna is observing at a lower altitude, a larger portion of the strut scatter cone attached to the strut on the reflector upper half will strike the ground. As a result, the antenna temperature is highest when it is tipped at low altitude in the direction opposite from the strut locations.

Of all the Synthesis Telescope antennas, Antenna 3 which has three 6" circular metal struts is most contaminated by strut scattering noise. The strut diameters are large enough to create a significant blockage to the plane wave leaving the reflector. Also, the scatter cone generated by the circular struts has uniform energy distribution around the cone and a substantial amount of power density is directed towards the ground. The strut scattering noise of an antenna with three 6" triangular feedlegs is approximately 3 K below a similar antenna with circular struts. The noise reduction is greater when the antenna is pointing at the zenith and it is lower when the antenna is observing at a lower altitude.

A previous experiment was conducted on Antenna 3 by attaching metal plates onto the existing struts to convert their cross-section from circular to teardrop shape [Robitaille, 1997]. Noise improvement of 2 K was recorded when the antenna was pointing at the zenith (Figure 2.66). *IFR* for teardrop-shaped struts is larger than *IFR* for triangular struts (Figure 2.55), thus a teardrop-shaped strut would scatter a greater amount of energy than a triangular strut would. Therefore it is reasonable that the measured noise reduction was less than that predicted for an antenna with triangular struts as shown in Figure 2.63 and Figure 2.64. This experiment shows that teardrop-shaped struts are able to redirect scattered energy in the forward direction away from the ground. In addition, it also validates the calculation of strut scattering noise using energy considerations.

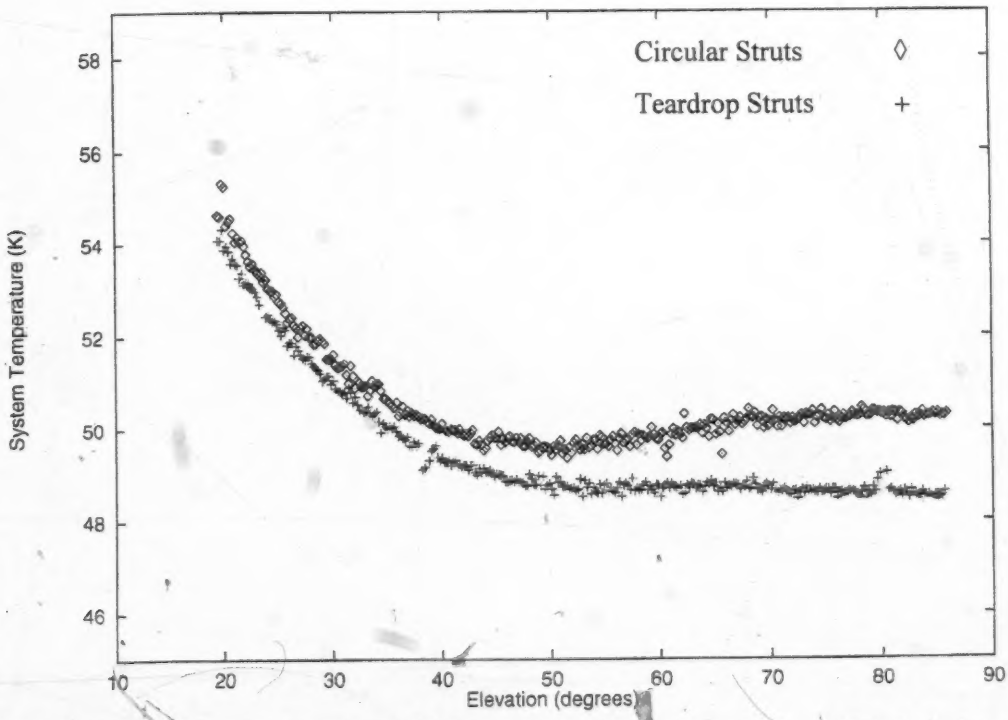

Figure 2.66 Antenna temperature measured before and after the strut cross sections of Antenna 3 were changed from circular to teardrop shape [Robitaille, 1997].

The scattering pattern generated by **Micro-Stripes** also shows that teardrop-shaped struts have a lower back-scattering level than triangular or circular struts. The existing strut cross-section can be modified into a teardrop shape by adding a V-shaped

metal strip onto the strut. Another advantage of teardrop shaped struts is that they can be constructed from the existing circular struts without creating larger geometrical shadows, as in the case of triangular struts. From the above evidence, it would be beneficial to modify the cross sectional shape of the existing Antenna 3 struts to teardrop shape.

Antennas 2 and 4 have circular fiberglass struts. Since fiberglass struts have a smaller $|IFR_M|$ than metal struts, they are less visible to the incident plane wave. The resultant strut scattering noise by these struts is less than that generated by metal struts of the same cross sectional size and shape. However, for the circular strut the energy distribution around the scatter cone is uniform, and still a large portion of the energy illuminates the ground. These two antennas have worse noise performance than an antenna with three 6" triangular, metal struts.

2.7.3 Modification of Strut Cross Sectional Shape

A previous experiment [Robitaille, 1997] measured the noise reduction when the cross sections of the metal 6" struts were changed from circular to teardrop shape. An experiment will now be described to examine the noise reduction achievable by changing the cross sections of the 3" struts on Antenna 7 from circular to teardrop shape. Aluminum sheets 6" wide and 4' long were bent in the mid-point along the length into V-shape strips with an angle of 60°. These strips were fastened onto the feedlegs using metal clamps. The apex of the V was adjusted to point down toward the reflector.

Both the teardrop shape struts and the triangular struts have flat surfaces that concentrate energy. The strut scattering noise of an antenna having four struts with 3" triangular cross sections, computed using **ScatterCone.c**, was used to predict the result of this experiment (Figure 2.67). Noise reduction of approximately 1.5 K across all altitudes was predicted if the strut cross-sections were converted from circular to triangular shape. A **Micro-Stripes** simulation showed that at this strut width, a teardrop shape strut has a lower back-scattering level than triangular struts (Figure 2.57). Therefore, a larger strut scattering noise reduction than the triangular strut prediction was

anticipated. During the experiment, the actual strut diameters were measured to be less than 3". The aluminum strips needed to be reshaped to a smaller opening angle of approximately 45°. Nevertheless, the experiment was carried out as planned and Figure 2.68 shows the antenna temperature measured by the Synthesis Telescope before and after the experiment.

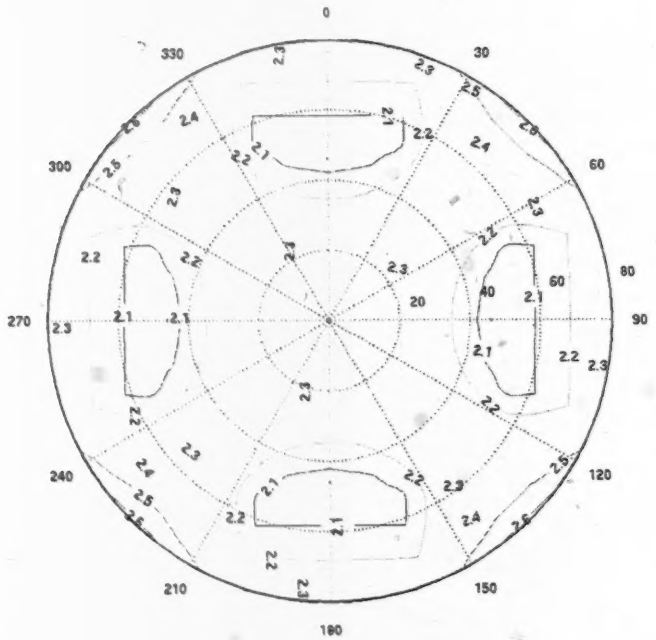

Figure 2.67 Predicted strut scattering noise for an antenna with four 3" triangular struts. (Compare to Figure 2.62)

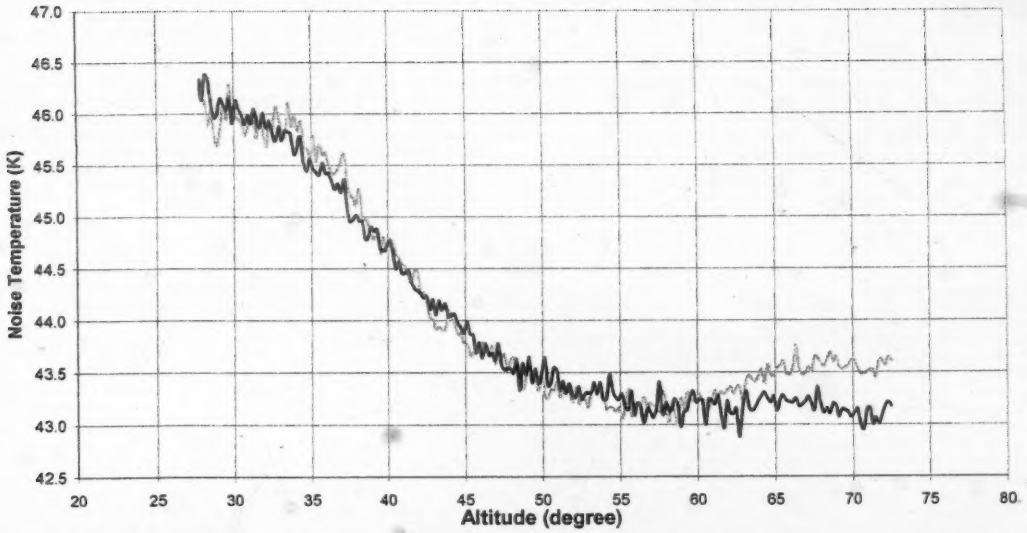

Figure 2.68 The system noise temperature of Antenna 7 of the DRAO Synthesis Telescope as a function of altitude. The gray line shows the noise temperature measured when the feed-support struts have circular cross sections. The black line shows the noise temperature measured after the struts were modified to have triangular cross sections.

A strut scattering noise reduction of approximately 0.5 K was achieved when the antenna was pointing at an altitude of 70°. The noise reduction decreased as the antenna was pointed at lower altitude. When observing at an altitude less than 60°, the antenna temperature was the same as before the strut modification. The measured noise reduction was therefore much lower than the prediction. The reason for this small change in antenna noise is the small strut diameter (0.36λ). If the dimension of the strut is small relative to the wavelength, there will be little difference between the energy distributions in the scatter cone for different cross sections. In addition, the opening angle of the V-shape strips was made smaller (60° to 45°) to fit onto the feedlegs. The FWHM of the cone pattern Gaussian functions is dependent on the width of the triangle side projected onto the aperture. With an opening angle of 45°, the projected width is 0.14λ and the calculated FWHM is 7.24 rad. Summing the Gaussian functions centered at the two specular reflection directions, the resultant energy distribution therefore departs very little from a uniform pattern. Therefore, a small noise reduction as measured is justified.

2.8 Diffraction around Rim

The smallest contribution to antenna temperature is ground noise entering the feed after being diffracted around the reflector rim. Diffraction is the bending of radio waves around obstacles. Anderson [1989] computed the diffracted noise by assuming the rim of the reflector is an infinite semi-plane placed between a receiver (the feed) and the transmitter (the ground at 300 K).

Consider a uniform plane wave incident on a conducting half-plane with a sharp, straight edge. The resultant diffraction pattern S_{av} behind the half-plane can be solved using physical optics. The power density ratio (S_{av}/S_o) as a function of κa is shown in Figure 2.69. The variable S_o is the power density of the incident plane wave, κ is a constant and a is the distance from the edge of the plane. When κa = ? , the power density at this point is zero, corresponding to complete obscuration of the plane wave by the conductive plane. At a transverse distance far from the half-plane or κa = -? , the power density is the same as that of the incident wave. However, the power density ratio does not rise from zero to one abruptly at the point below the edge of the plane; rather, the power density rises gradually and then oscillates. The oscillations damp out at large, negative κa.

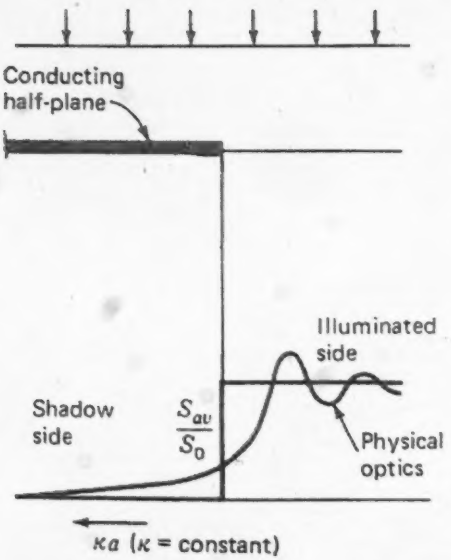

Figure 2.69 A plane wave illuminating a conducting half-plane from above and the resultant power density pattern below the plane. [Kraus, 1984]

Anderson [1989] computed the amplitude of the energy diffracted by the reflector rim using the function illustrated in Figure 2.69 and the noise contribution is given by Anderson [1989]

$$T_A = \int_{0^\circ}^{60^\circ} \frac{2\pi \sin\theta'}{\Omega_F} 300 A(\theta') f(60^\circ) d\theta' \qquad (2.8.1)$$

Where

Ω_F = solid angle of the feed pattern

$A(\theta')$ = amplitude of the power diffracted by the rim

$f(60^o)$ = power pattern of the feed evaluated at the rim

θ' is the angle in spherical coordinates as shown in Figure 2.6. The ground temperature was assumed to be 300 K. The antenna temperature due to diffraction around the rim was found to be 0.6 K for the Synthesis Telescope antennas. Since this noise contribution is very small compared to mesh leakage, direct spillover and strut scattering, modification of the Synthesis Telescope antennas to reduce edge diffraction noise was not considered

in this project. However, a brief discussion of methods to reduce diffraction noise will be included below.

Several techniques to modify the geometry of the reflector edge to reduce diffraction noise have been discussed in the literature. Bucci et al. [1982] suggested adding a flange to reduce the back scattering. The best performance is obtained by using a flange forming a right angle with the reflector surface (Figure 2.70). A significant reduction in backward scattering was obtained without affecting the field in the forward hemisphere since the flange is shadowed by the reflector surface. Bucci et al [1985] also showed that a lower backward scattering pattern can be obtained by corrugating the flange with the corrugations parallel to the reflector edge. E and H plane radiation patterns of a parabolic dish with a corrugated right-angled flange and without a flange are illustrated in Figure 2.71. The level of back scattering was lower in both E- and H-planes.

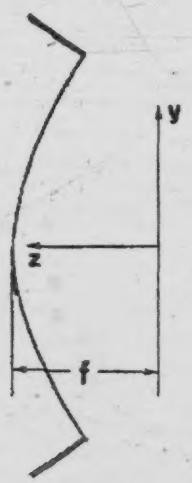

Figure 2.70 A flanged parabolic reflector. The flange forms a right angle with the reflector surface [Bucci et al., 1985].

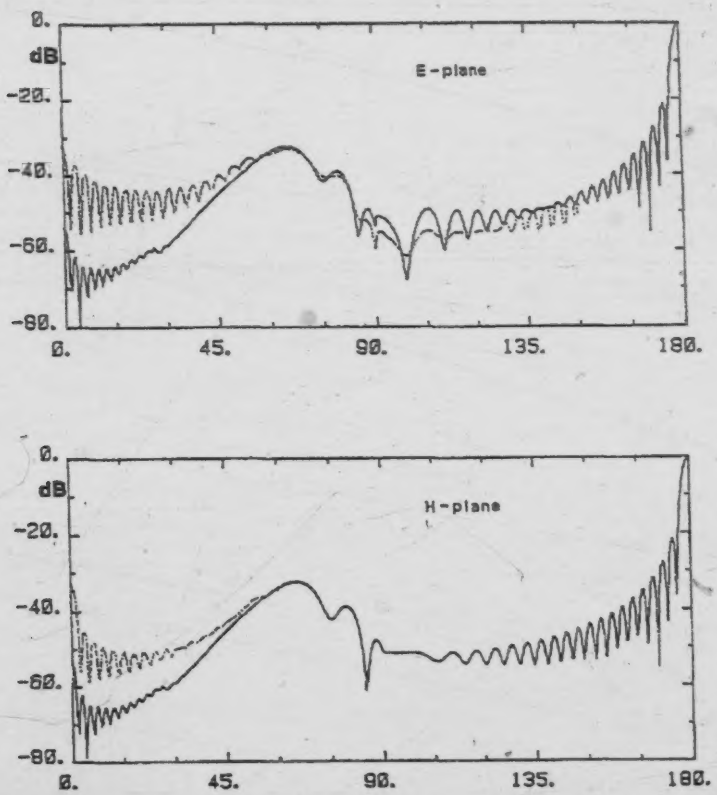

Figure 2.71 Radiation pattern of a parabolic dish with corrugated right-angled flange (solid lines) and unflanged (dotted lines) [Bucci et al., 1985]. Angle 180 is in the direction of the antenna bore sight and angle 0 behind the reflector.

Another method to minimize edge diffraction is to attach an optimized curved surface or rolled edge to the rim of the reflector to reduce the surface discontinuities. The elliptical rolled rim generates a diffracted field at the junction between the reflector and the attached edge due to the discontinuity in the radius of curvature. Gupta et al. [1990] defined an optimum blended rolled edge that blends an elliptical rolled edge with an extension of the parabola (Figure 2.72) to minimize the surface discontinuity. It is important to note that the minimum radius of curvature of the rolled edge must be at least a quarter of a wavelength.

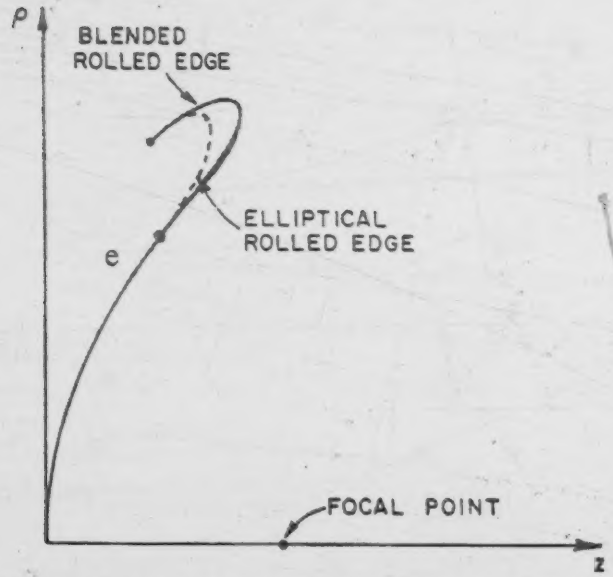

Figure 2.72 Side view of a paraboloidal reflector. This figure shows the elliptical edge (dotted line) and the blended rolled edge (solid line). Point e is the junction of the reflector and the rolled edge [Gupta et al., 1990].

2.9 Conclusion

In this chapter, the sources of antenna noise temperature and methods to reduce ground noise were examined in detail. The four contributors to ground noise are mesh leakage, direct spillover, strut scattering and diffraction at the rim. Through theoretical calculations and experimental modifications of the antennas, optimum methods to reduce each of the ground noise contributions were found.

Mesh leakage can be reduced by shielding the center portion of the reflector with solid metal. Among the seven Synthesis Telescope antennas, there are two types of mesh used for the reflector. Antennas 1, 2 and 7 have coarse mesh while the other antennas have finer mesh. The noise contributions for the two types of mesh surfaces are 5.71 K and 1.43 K. In the experiment on Antenna 7, a circle of 2.1 m radius measured from the vertex of the reflector was covered with autobody aluminum tape. This experiment successfully reduced the antenna temperature by 4 K across all altitudes. Therefore, it is recommended to also shield the reflectors of Antennas 1 and 2. It is suggested that the

coverage be extended to 2.5 m radius. This radius coincides with one of the ribs on the reflector surface; this provides better adhesion for the edge of the tape. In addition, by increasing the shielding area, a larger mesh leakage noise reduction can be achieved. Theoretical calculation shows that 4.5 K of the noise temperature can be eliminated with this shielding. The only problem encountered with this method is the durability of the tape. After being applied on Antenna 7 for one year, some of the metal tape has begun to detach from the reflector. Techniques to make the tape more permanent and more adhesive still need to be found.

The ground mesh and mesh fence experiments on Antennas 6, 1 and 7 demonstrated that these fences reduce noise temperature by reflecting radiation that strikes the fence towards the cool sky. Noise reductions of 1.0 K, 2.0 K and 5.0 K when the antennas are pointing at the zenith were achieved in these experiments. Since both direct spillover and strut scattering radiation falls on the ground, these fences are capable of reducing both direct spillover and strut scattering noise. Proposed fence designs for Antenna 5 and the three movable antennas on the track were discussed in section 2.7. Predicted noise reduction is 1.5 K for the Antenna 5 design. If the strut cross-sections for the three movable antennas were converted to metallic teardrop shape, the proposed fence design would decrease the antenna temperature of these antennas by 3.25 K.

Previous DRAO experiments by Robitaille [1997] and theoretical calculations showed that triangular struts are able to redirect the scattered energy towards the forward hemisphere away from the hot ground to reduce the strut scattering noise. Using the software package **Micro-Stripes**, it was further shown in this thesis that a teardrop shaped strut has a lower back scattering pattern than a triangular strut. Thus, the strut cross-section of Antennas 1 and 3 should be changed from circular to teardrop shape. After modifying the 6" circular struts to teardrop cross-section, the strut scattering noise of Antenna 3 will reduce from 5.9 K to 2.3 K when pointing at the zenith. The struts on Antenna 1 are identical to the Antenna 7 struts, four 3" struts with circular cross section. The expected decrease in noise temperature after converting the cross section to teardrop shape would be 1 K as demonstrated by the experiment on Antenna 7. Also, the noise

contribution by circular dielectric struts is larger than that by triangular metal struts. The dielectric circular struts of Antennas 2 and 4 should also be modified to become metal teardrop-shaped struts. This can be accomplished by wrapping the struts with metal tape and then adding a V-shaped strip onto each strut. The strut scattering noise for these two antennas will drop from 4.5 K to 2.3 K when pointing towards the zenith.

The ground noise levels for each of the Synthesis Telescope antennas before any modifications were computed theoretically and listed in Table 2.3. Table 2.4 shows the expected noise level for each antenna after shielding the reflector, modifying the strut cross-sectional shape and building mesh fences around the antenna as recommended above. The values in both tables reflect the noise temperature when the antenna is pointing at the zenith. The ground noise level of the Synthesis Telescope, calculated by taking the geometric mean of the seven antennas, successfully reduces from 14.3 K to 8.1 K. The goal of this project to cut down the contribution of ground noise to 8 K was achieved.

Antenna	Mesh Leakage (K)	Direct Spillover (K)	Strut Scattering (K)	Diffraction at rim (K)	Total (K)
1	5.7	6.8	4.0	0.60	17.1
2	5.7	6.8	4.5	0.60	17.6
3	1.4	6.8	5.9	0.60	14.7
4	1.4	6.8	4.5	0.60	13.3
5	1.4	6.8	2.3	0.60	11.1
6	1.4	6.8	2.3	0.60	11.1
7	5.7	6.8	4.0	0.60	17.2

Table 2.3 Initial noise contribution attributable to radiation from the ground.

Antenna	Mesh Leakage (K)	Direct Spillover (K)	Strut Scattering (K)	Diffraction at rim (K)	Total (K)
1	1.2	3.3	3.0	0.60	8.1
2	1.2	3.6	2.3	0.60	7.6
3	1.4	3.6	2.3	0.60	7.9
4	1.4	3.6	2.3	0.60	7.6
5	1.4	5.3	2.3	0.60	9.6
6	1.4	5.8	2.3	0.60	10.1
7	1.2	1.8	3.0	0.60	6.55

Table 2.4 Predicted noise levels after antenna modification as suggested above.

Chapter 3 Instrumental Polarization

3.1 Introduction

The radio emission from the Galaxy, observed by the Synthesis Telescope, is mostly randomly polarized with a small linearly polarized component. The linearly polarized component comes from synchrotron emission (see Section 1.6) and is generated by the interaction of fast electrons with magnetic fields. Polarization measurements can be used to study the magnetic field distribution within a radio source, and the distribution of thermal electrons and magnetic fields in the interstellar medium (ISM) via their impact on linearly polarized signals as they propagate through it.

For precise polarization imaging, observations must be corrected for instrumental polarization across the field of view. Instrumental polarization results from non-ideal properties of the radio telescope and causes unpolarized sources to appear polarized. An equatorially mounted telescope, like the Synthesis Telescope at DRAO, has a disadvantage, in that a difficulty occurs in the separation of the instrumental polarization from the source polarization [Smegal et al., 1997]. With an equatorial mount, the feed does not rotate relative to the sky, so that the beam pattern always has a fixed orientation on the sky. Further, the feed cannot be rotated mechanically. Therefore, the telescope must be calibrated by observing randomly polarized radio sources which have a large flux density (e.g. 3C147 and 3C295). Since the source is unpolarized, any polarization must be caused by instrumental imperfection. It is known that instrumental polarization worsens radially across the beam, from 0.2% (of Stokes I) in the center of the field to 3% at a radius of 1° [Smegal et al. 1997]. These measurements are obtained by observing unpolarized sources at many positions in the field. However, to obtain accurate instrumental polarization measurements with this procedure is very time consuming. Until now, experimental results have been used to correct observations within 75' of the field center [Peracaula, 1999]. Therefore, it is beneficial to analyze the instrumental polarization numerically.

The instrumental polarization was investigated using an antenna analysis software package **GRASP8** [TICRA Engineering Consultants]. Outputs from the program were further processed to calculate antenna performance in terms of Stokes parameters using software written by the author. The first exploration of the use of **GRASP8** for this purpose was carried out by Cazzolato [2000]. This thesis refines and greatly extends this work by investigating the roles of various antenna properties on instrumental polarization. The antenna components that have significant effects on instrumental polarization were investigated:

(1) Reflector curvature
(2) Cross polarization in the feed pattern
(3) Surface roughness
(4) Different strut configurations
(5) Different strut diameters
(6) Different strut cross-sectional shapes

An assessment of the role of each component of the antenna geometry in creating cross-polarization is presented in this chapter. A thorough understanding of the instrumental polarization can be gained by analyzing each of the above aspects separately. Using this knowledge, an antenna structure that generates the least instrumental polarization can be found and possible modifications to the Synthesis Telescope can be studied. This understanding will also assist in the design of other telescopes. In addition, the theoretical model constructed using this simulation procedure can possibly be used for the correction of instrumental polarization.

3.2 Stokes Parameters

The Stokes parameter representation for polarization is ideal for quantifying partially polarized waves. The four Stokes parameters I, Q, U and V fully describe the polarization state of an arbitrarily polarized wave, even a partially polarized wave. I is the total intensity of the radiation. Q and U characterize the difference in power intensity measured with orthogonal linear polarizations. Q represents the difference between horizontal and vertical polarization and U represents the difference between polarizations

at ?45°. These two parameters together specify the intensity and angle of any linear polarization. V is a measure of the sense and intensity of circular polarization. Consider a partially polarized wave with co-polar (E_x) and cross-polar (E_y) linear components propagating in the z-direction:

$$\vec{E} = E_x\hat{x} + E_y\hat{y} \tag{3.2.1}$$

where

$$E_x = e_x(t)\sin[\omega t - \delta_x(t)] \tag{3.2.2}$$

$$E_y = e_y(t)\sin[\omega t - \delta_y(t)] \tag{3.2.3}$$

The Stokes parameters are related to the amplitude and phase of the electric field components E_x and E_y.

$$I = \langle e_x^2 \rangle + \langle e_y^2 \rangle \tag{3.2.4}$$

$$Q = \langle e_x^2 \rangle - \langle e_y^2 \rangle \tag{3.2.5}$$

$$U = 2\langle e_x e_y \cos(\delta_x - \delta_y) \rangle \tag{3.2.6}$$

$$V = 2\langle e_x e_y \sin(\delta_x - \delta_y) \rangle \tag{3.2.7}$$

The angular brackets < > denote the time average. Averaging is necessary because a telescope measures radiation over a finite bandwidth so that the net polarization is the result of averaging many monochromatic components with independent polarization properties. Therefore, only the average polarization properties can be measured. The International Astronomical Union (IAU) has defined a conventional coordinate system (Figure 3.1) with the x and y axes in the plane of the sky pointing toward North and East respectively, and the positive z-axis along the line of sight toward the observer. Positive angle is measured counter clockwise from the North towards the East. With this definition, it follows that positive Q is along the x-axis while the positive U is in position angle 45°. The IAU also defined that the position angle of the electric vector of a right-

handed circularly polarized wave increases with time and thus V is positive for right-handed circular polarization [Hamaker et al. 1996].

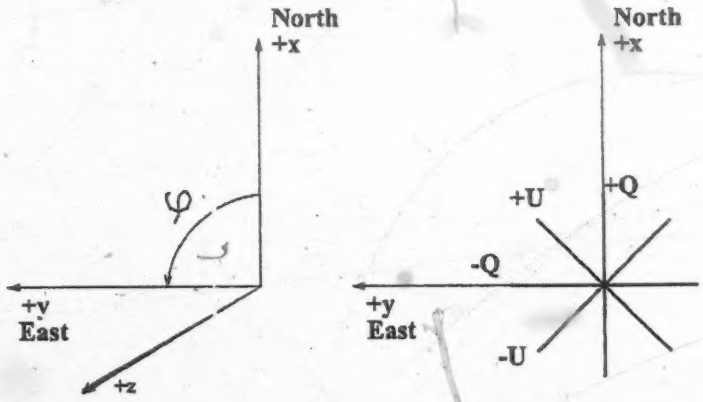

Figure 3.1 The IAU coordinate system with the z-axis pointing out of the page [Hamaker et al. 1996].

3.3 Simulation Procedures

The instrumental polarization was computed using a three-step simulation procedure. First, **GRASP8**, a commercial software package for general reflector antenna modeling and analysis, was used to compute the far-field radiation pattern of an antenna system excited with a linearly polarized feed. To simulate a randomly polarized source, four computations with the feed radiating in four different orientations of position angle ϕ were needed. Four scattering pattern files were generated in this step. Next, a C program, **SumField_daf.c**, took the scattering patterns computed in the first step and calculated the Stokes parameters I, Q, U and V. The last step was to plot the contours of the Q/I, U/I and V/I ratios across the antenna beam using the DRAO software packages **MADR** and **PLOT**. Figure 3.2 illustrates this three-step procedure graphically.

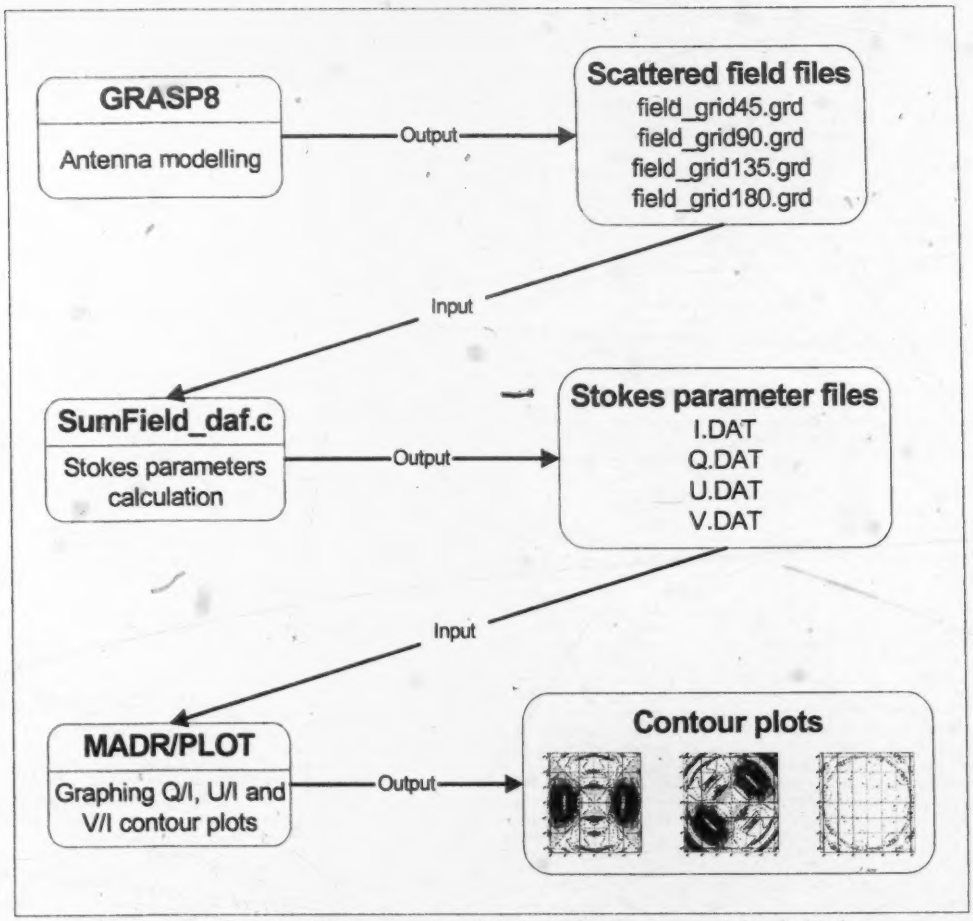

Figure 3.2 The simulation procedure for the study of instrumental polarization

First a prototype antenna based on the physical geometry of Antenna 3 of the DRAO Synthesis Telescope was defined. The Q/I and U/I plots for the prototype antenna were compared to experimental data to verify the accuracy of the simulation procedure. Then, this simulation procedure was used to demonstrate the contribution by each component of antenna structure to the instrumental polarization. Various aspects of the prototype antenna geometry were modified to analyze their effects on the polarization properties of the antenna. These modifications included correcting the feed polarization, adding surface roughness, relocating the struts and changing the size and cross-sectional shape of the struts.

3.3.1 GRASP8

The radio telescope is a receiving antenna. However, applying the reciprocity theorem, a transmitting antenna rather than a receiving antenna was considered in the **GRASP8** simulation. The reciprocity theorem indicates that the radiation pattern of the antenna will be identical in transmitting and receiving situations. **GRASP8** calculates the electromagnetic radiation from an antenna system consisting of feed, reflector, struts and other scatterers. It performs the scattering analysis in three steps. First, the surface current induced on the scatterer by an incident field is computed using Physical Optics (PO) supplemented with the Physical Theory of Diffraction (PTD) (see chapter 1). The second step is to compute the scattered field produced by these surface currents using a two-dimensional numerical integration over the entire surface of the scatterer. For a perfectly conducting surface B, the scattered field in the far-field region is defined by [Pontoppidan, 2000]

$$\vec{E}_{far} = -\frac{j\xi}{4\pi}\iint_B (\vec{J}^e - (\vec{J}^e \cdot \hat{r})\hat{r}) e^{jk\vec{r}'\cdot\hat{r}} k^2 ds' \tag{3.3.1}$$

where

ξ = free-space impedance $\xi = \sqrt{\mu/\varepsilon}$

$\vec{J}^e$ = induced electric current

$\hat{r}$ = far-field direction

$\vec{r}'$ = point on the integrating surface

k = wave number $k = 2\pi/\lambda$

ds' = infinitesimal surface area

Finally, the incident fields and the scattered fields are added vectorially to obtain the total field.

3.3.1.1 Antenna modeling

GRASP8 uses the object-oriented programming technique. Each antenna element is defined by pointing to several objects belonging to different classes that describe either the geometrical or electrical property of the element. For example, a parabolic reflector is defined by an object in the rim class that describes the shape and size of its rim and an object in the paraboloid class that identifies the curvature of its surface. The prototype antenna modeled in the simulation was Antenna 3 of the Synthesis Telescope at DRAO. It is a prime-focus paraboloidal antenna. Physical and electrical characteristics of Antenna 3 are summarized in Table 3.1. Objects describing the antenna geometry, feed properties, PO and PTD calculations, and file storages were defined in the object repository (.tor) file Antenna.tor.

Operating frequency	1420 MHz
Reflector diameter (d)	8.534 m
Focal length (f)	3.658 m
Number of struts (N)	3
Strut diameter (a)	6 inches
Strut length (L)	4.90 m
Strut cross-section	Circular
Feed pattern	Tabulated

Table 3.1 Physical characteristics of Antenna 3

The three struts are attached to the focus box support ring and to the edge of the reflector. Their end point coordinates relative to the antenna coordinate system at the vertex of the reflector were determined geometrically. In the model, the struts do not actually touch the reflector surface, but this is necessary for the purpose of computation. If a strut intersects the reflector surface, **GRASP8** will generate a calculation error when computing the induced currents on the reflector due to the current on the strut. To solve this problem, a small gap of one tenth of a wavelength was inserted between the strut and reflector. Although this is not a true representation of the geometry, a gap of one tenth of a wavelength is small relative to the length of the strut, and its impact will be negligible.

After defining the reflector dimensions, focal length and strut locations, the description of the physical characteristics for the prototype antenna was completed. The geometrical plot of this model antenna is shown in Figure 3.3.

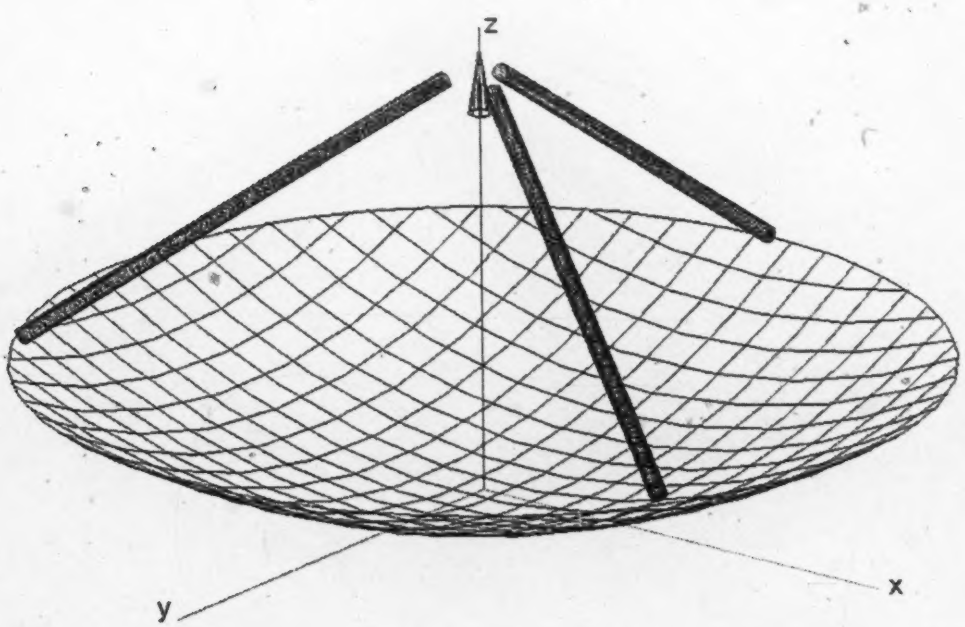

Figure 3.3 Geometrical plot of Antenna 3 with the antenna coordinate system

Next the tabulated feed was defined. The feed pattern for the model was described in the file **linearfeedpattern4.cut**. This file, computed by a commercial software program **MICRO-STRIPES** [Flomerics Inc.], is based on the actual feed horn structure and electrical properties. It is arranged in four columns describing the real and imaginary components of the co-polar and cross-polar pattern, $\mathrm{Re}\{E_x\}$, $\mathrm{Im}\{E_x\}$, $\mathrm{Re}\{E_y\}$ and $\mathrm{Im}\{E_y\}$ respectively. The magnitude of the co- and cross-polar patterns of the tabulated feed in the E-, D- and H-plane are plotted in Figure 3.4. The E-plane is parallel to the electric vector of the (linearly polarized) field excitation; the H-plane is orthogonal. Cross polarization is zero in the E- and H- planes, and peaks at 45° to both planes (the D-plane).

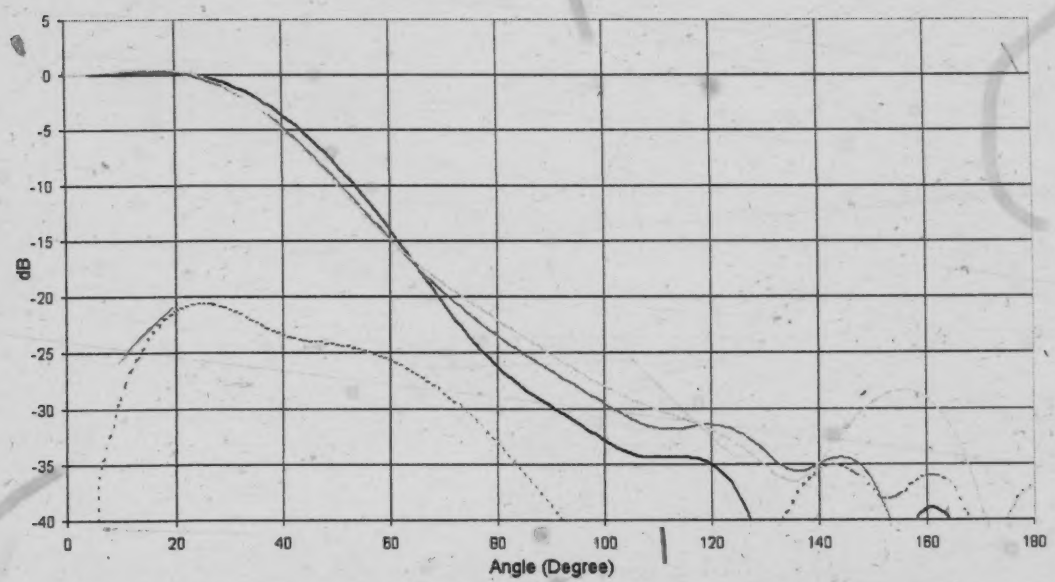

Figure 3.4 The feed radiation pattern in the E- (black), D- (gray) and H- (light gray) planes. The co-polar pattern is plotted with solid lines and the cross-polar pattern in the D-plane is plotted with a dotted line.

3.3.1.2 Simulation

GRASP8 calculates the field pattern by first finding the induced current on a scatterer when it is illuminated by a source, then the scattered fields are computed and summed. **GRASP8** is unable to determine an integration grid for the physical optics computations (equations 3.3.1 and 3.3.2) automatically. In order to calculate the induced current on a scatterer, the integration grid must be defined by specifying the number of grid points *po1* and *po2*. Too small values of *po1* and *po2* will produce an inaccurate result. Large values, on the other hand, will take more computation time than necessary. The integration grid on the reflector and on the struts must be specified separately. For a focused reflector with circular rim, the PO integral will converge under the following conditions:

$$po1 = \mathrm{int}(\frac{z}{2.4}) \tag{3.3.2}$$

$$po2 = \mathrm{int}(z) \tag{3.3.3}$$

where

$$z = 1.09 \cdot \pi \frac{d}{\lambda} \sin\theta_o + 10 \tag{3.3.4}$$

The function *int* gives the nearest integer, d is the reflector diameter, and θ_o is the maximum angle from the beam center at which the integration should converge. Using the above equations, *po1* and *po2* for the prototype reflector were found to be 12 and 27 respectively.

The circular_struts_po object specifies how the PO current should be calculated on circular struts. It requires an input of the integration grid, N_l and N_ϕ, and the approach of analyses (simple PO approach or canonical solution). The number of grid points necessary for convergence can be calculated by:

$$N_l = \frac{3L}{\lambda} \tag{3.3.5}$$

$$N_\phi = \frac{16a}{\lambda} + 4 \tag{3.3.6}$$

where L is the strut length, and a is the diameter of the strut. For the 6" struts in the prototype antenna, N_l and N_ϕ were calculated to be 70 and 16 respectively. There are two types of analysis for circular struts: the simple PO approach and the canonical solution. The simple PO approach uses equation (1.4.2) and is only suitable for circular struts that are large in terms of wavelength. The canonical solution, a much better prediction of the current on the strut with diameter in the order of a wavelength, was used in the simulation. The scattered field from a plane wave incident on an infinite circular cylinder, which has a solution in series form, is used to obtain the current distribution along the circumference of the strut. This method gives an exact solution for the scattered field if the numerical integration of the induced current converges. For the case of spherical wave incidence, the canonical solution also gives a good approximation to the induced current on the strut. The incident E and H fields and the propagation constant are calculated at a specific point on the cylinder. The induced current at this point is

assumed to be the same as the current on an infinite cylinder illuminated by a plane wave with the same direction of propagation, amplitude and phase.

In order to store the scattered field values generated by the induced surface current in an output file, a field storage object in the spherical_field_grid class was defined. It specifies the field points in a two-dimensional grid on a sphere where the far-field scattering field will be calculated. This object definition identifies the size of the two-dimensional grid, the number of data points in the grid, the type of grid and the name of the output file where the field data are to be stored. A 6.5° x 6.5° grid with 75 x 75 data points in the uv plane (see section 3.3.4) was defined for the model.

The next step was to specify a simulation sequence that describes how the sources and the scatterers interact. In this simulation, spherical wave scattering was used. First, the feed illuminated the struts. The currents on the reflector were calculated by treating both the strut currents and the feed as the source. The reflector then in turn illuminated the struts. Finally, the currents on the struts and reflector were integrated (3.3.1) and summed to calculate the total scattered field. Figure 3.5 illustrates the spherical wave scattering process. The simulation sequence was stored in the command input file (.tci), **Antenna-Strut.tci**.

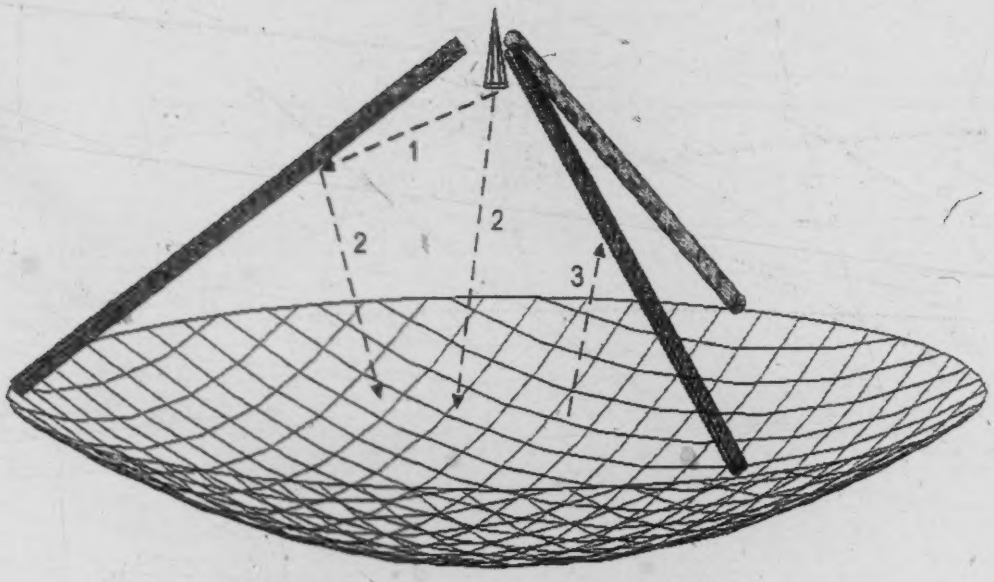

Figure 3.5 Spherical wave scattering: 1) feed illuminates the struts, 2) the feed and the induced current on the struts illuminate the reflector and 3) current induced on the reflector in turn illuminates the struts

Using the reciprocity theorem, a transmitting antenna rather than a receiving antenna was considered in the **GRASP8** simulation. The antenna was excited by applying a linearly polarized signal to the actual feed. In order to simulate an unpolarized source, the linear feed must appear to radiate in all possible angles on its plane of polarization by rotating it 180° about the axis perpendicular to the plane. It was found that averaging the scattering field resulting from four feed orientations ($\phi = 45^{\circ}, 90^{\circ}, 135^{\circ}, 180^{\circ}$ relative to the z-axis of the antenna coordinates) was sufficient to approximate a randomly polarized source [Cazzolato, 2000]. Since the radiation patterns of the four feed orientations were averaged, any polarization seen must be instrumental polarization. Thus, the spherical wave scattering process was repeated four times as the feed was rotated while the other antenna components remained stationary. To simplify the simulation process, the command input file **Antenna-Strut.tci** was designed to model all four feed positions in a single run. The four feed-coordinate-system objects (feed_coor45, feed_coor90, feed_coor135, feed_coor180) rotated the feed to the four ϕ angles. Then, the four linear feeds with the same tabulated feed pattern (Feed45, Feed90, Feed135 and Feed180) were defined with respect to these feed coordinate systems. The

four spherical-field-grid objects (Spherical_grid45, Spherical_grid90, Spherical_grid135, and Spherical_grid180) allowed the field data to be stored in four separate files. At this point, the prototype antenna model and simulation using **GRASP8** was completed. The next steps were to process the **GRASP8** output files to determine and plot the Stokes parameters.

3.3.2 Stokes Parameter Computation

The **GRASP8** simulation generated four ASCII files containing the radiation patterns for the four feed orientations. Each file contained the real and imaginary components of the co- and cross-polar electric fields, $\mathrm{Re}\{E_x\}$, $\mathrm{Im}\{E_x\}$, $\mathrm{Re}\{E_y\}$, and $\mathrm{Im}\{E_y\}$ respectively. A C program, **SumField_daf.c**, was written by the author to compute the Stokes parameters. It takes the four **GRASP8** output files as input and calculates the four Stokes parameters I, Q, U and V, for random polarization. However, equations 3.2.4 to 3.2.7 are not suitable for calculating Stokes parameters in this case. Those relations are for partially polarized waves. The scattering patterns generated in the **GRASP8** simulation contain only completely polarized electric fields. The Stokes parameters I, Q, U and V were calculated point-by-point for each feed orientation using the following equations:

$$I = E_x^{\,2} + E_y^{\,2} \tag{3.3.7}$$

$$Q = E_x^{\,2} - E_y^{\,2} \tag{3.3.8}$$

$$U = 2E_xE_y\cos(\delta_x - \delta_y) \tag{3.3.9}$$

$$V = 2E_xE_y\sin(\delta_x - \delta_y) \tag{3.3.10}$$

where

$$E_x = \sqrt{(\mathrm{Re}\{E_x\})^2 + (\mathrm{Im}\{E_x\})^2} \tag{3.3.11}$$

$$E_y = \sqrt{(\mathrm{Re}\{E_y\})^2 + (\mathrm{Im}\{E_y\})^2} \tag{3.3.12}$$

$$\delta_x = \tan^{-1}\frac{\mathrm{Im}\{E_x\}}{\mathrm{Re}\{E_x\}} \tag{3.3.13}$$

$$\delta_y = \tan^{-1}\frac{\mathrm{Im}\{E_y\}}{\mathrm{Re}\{E_y\}} \tag{3.3.14}$$

Since I, Q, U and V are power, their combined contributions representing the case of random polarization can be calculated by taking the average (e.g. $I_{random} = (I_{45^\circ} + I_{90^\circ} + I_{135^\circ} + I_{180^\circ})/4$). **SumField_daf.c** saved the average I, Q, U and V patterns in four separate direct-access files which can be read by **MADR** and **PLOT** to generate contour plots.

3.3.3 Plotting with MADR and PLOT

The four direct-access files created by the C program were read by the DRAO software packages **MADR** and **PLOT** to generate contour plots. The Stokes parameters Q, U and V were normalized against the total intensity I. The "manipulate" function in **MADR** computed the ratio Q/I, U/I and V/I. **PLOT** generated the contour plots in POSTSCRIPT files.

3.3.4 Verification of the Simulation Procedure

To verify the simulation procedure, the Q/I and U/I contour plots for the prototype antenna were compared to the experimental data. The orientation of the simulation plots is relative to the far-field pattern when looking from the ground up towards the sky. The Q/I (Figure 3.6) and U/I (Figure 3.7) contour plots were presented in a uv coordinate system where

$$u = \sin\theta\cos\phi \tag{3.3.15}$$

$$v = \sin\theta\sin\phi \tag{3.3.16}$$

Here θ and ϕ are angles in spherical polar coordinates (Figure 2.1). For small θ angles, the uv grid can be viewed as a rectangular plane on a sphere centered at the boresight of the antenna beam. Applying the small angle approximation, sin $\theta = \theta$, the uv plot is a plot of angle θ from the beam center. Since the maximum value of θ is 0.113 radians and the angle ϕ ranges from zero to 2π radians, both horizontal (u) and vertical (v) axes have a range from -6.5^{O} and 6.5^{O}. The contour lines represent positive values (0.0001 to 0.5) and shadings represent negative values (-0.5 to 0). Figure 3.8 shows the lines and shading patterns used to graph all the Stokes parameter contour plots in this chapter.

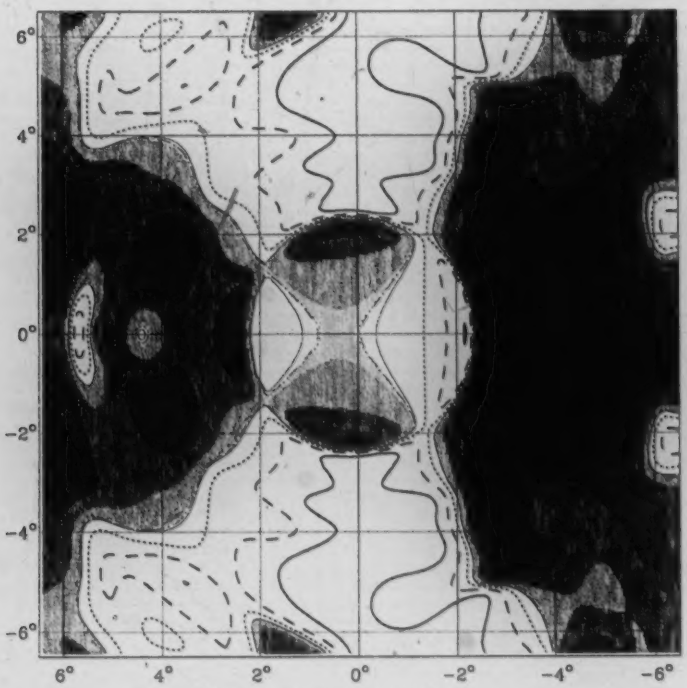

Figure 3.6 Q/I plot for the prototype antenna.

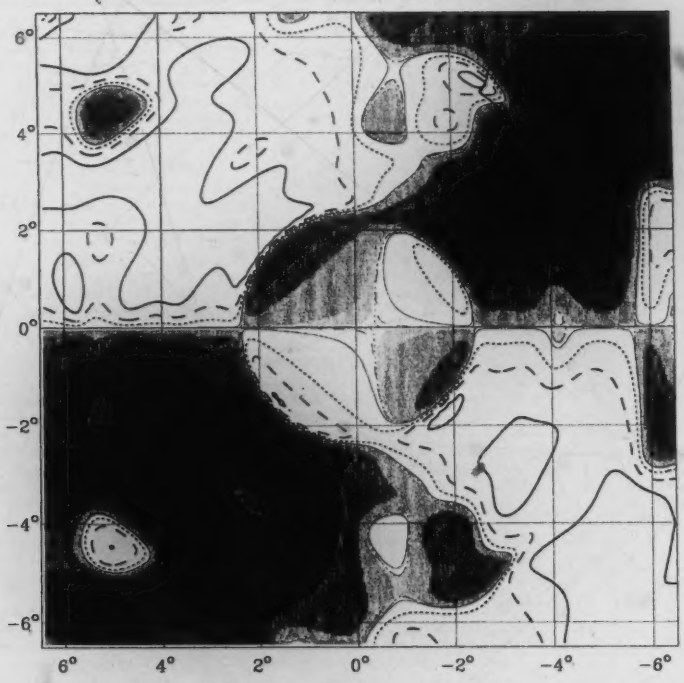

Figure 3.7 U/I plot for the prototype antenna.

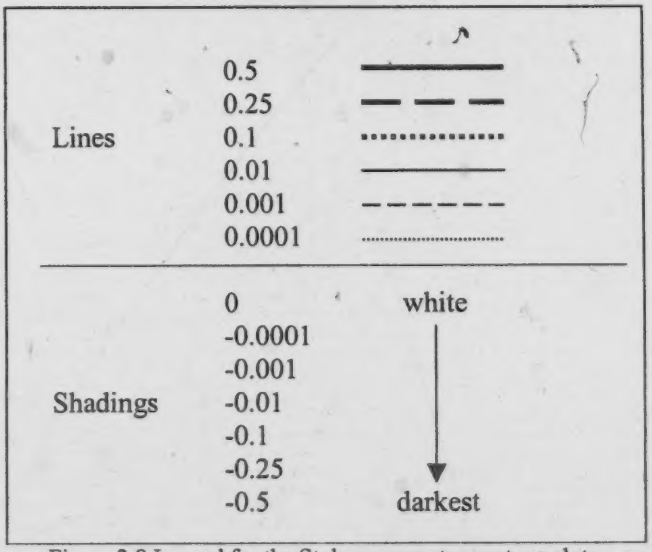

Figure 3.8 Legend for the Stokes parameter contour plots.

The instrumental polarization of the Synthesis Telescope was measured experimentally by observing polarized and unpolarized sources at different offsets from the field center in different directions [Peracaula 1999]. These data are applied to the

individual CGPS fields to correct for instrumental polarization. The Q/I (Figure 3.9) and U/I (Figure 3.10) experimental data are plotted in a uv grid with units in arcminutes. The contours cover the angular range –90 arcminutes to 90 arcminutes relative to the field center, well within the first null of the field pattern. The contour units of the experimental plots are in percent.

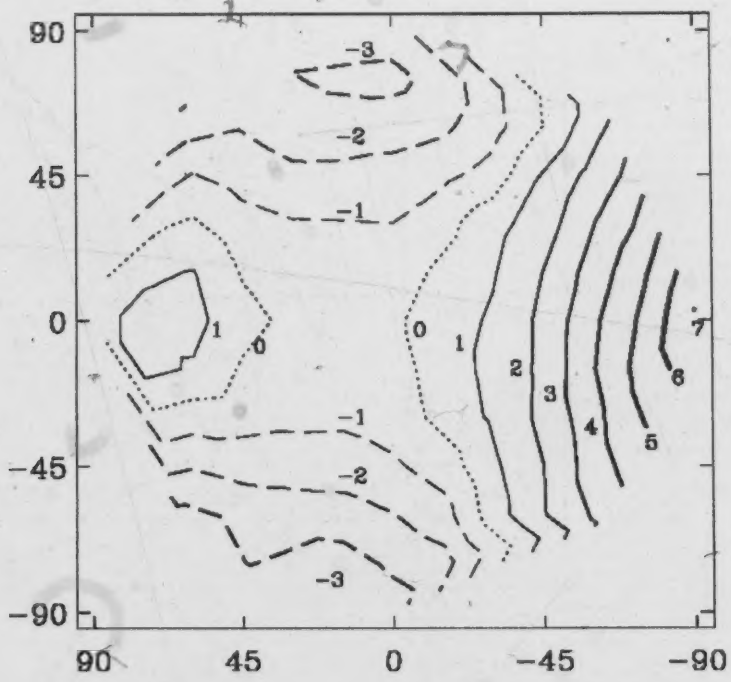

Figure 3.9 Q/I plot for the experimental data. [Peracaula, 1999]

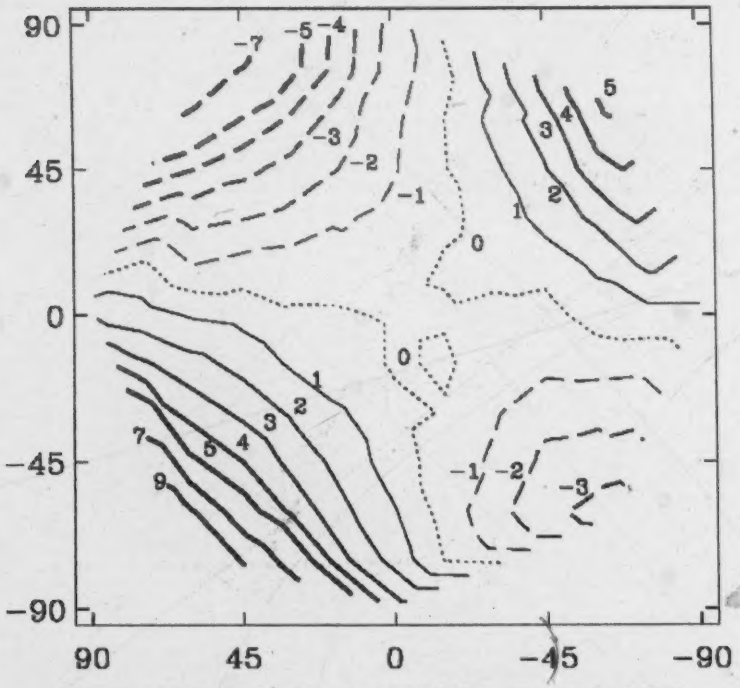

Figure 3.10 U/I plot for the experimental data. [Peracaula, 1999]

Although the seven antennas of the Synthesis Telescope are not identical in their physical structures, five of the antennas have the same reflector size and strut configuration as the prototype antenna. Therefore, the Q/I and U/I contour plots for the prototype antenna should reflect the actual instrumental polarization. V/I is not considered here because for the case of linear polarization, its contribution is negligible. Comparing the two sets of Stokes parameter plots, the general shapes and symmetries agree very well in the main beam. For the Q/I plot, the degree of polarization is zero in the center of the beam, and increases to less than 10% at 90 arcminutes from the center on the right side, but remains relatively low on the left side. Similarly, U/I is zero in the center, but the degree of polarization is greater on the left side than the right side. The same minima and maxima, symmetry and asymmetry patterns are observed in both the simulated graphs and the experimental data. This gives confidence that all components of the simulation procedure were designed correctly.

3.4 Study of Instrumental Polarization

After the prototype antenna system was defined, various aspects of this antenna were modified to examine the contribution to instrumental polarization due to curvature of the reflector, cross-polarization in the feed pattern, surface roughness, different strut arrangement, different circular strut diameter, and different strut cross-section.

3.4.1 Reflector curvature

To identify the contributions to instrumental polarization by the curvature and shape of the reflector, an antenna system consisting of a perfect feed with no cross polarization illuminating a reflector with no struts was simulated. The IEEE standard definition of cross polarization is "the polarization orthogonal to a reference polarization" [Ludwig, A. C., 1973]. This definition is adequate for circular polarization, but it does not have a well-defined reference direction for the cases of linear and elliptical polarizations. There are two explanations to this definition. Consider the case of linear polarization. (1) In a rectangular coordinate system, the direction of cross polarization is taken to be 90^{o} from the reference polarization on a plane perpendicular to the wave propagation. (2) A precise definition describes the reference and cross polarization pattern as the antenna patterns measured by a probe aligned parallel to and orthogonal to the polarization of the antenna. A "perfect" feed has a pattern which is "orthogonal to itself after a 90^{o} rotation" about the axis in the direction of propagation [Ludwig, 1973]. A pattern with zero cross polarization by both definitions satisfies this requirement.

The co- (reference) and cross- polarization components in the actual feed pattern are described in a rectangular coordinate system as in the first definition of cross polarization. A perfect feed was created by setting all the cross polarization components (E_y) of the actual feed pattern to zero. The model antenna system was simulated in **GRASP8** by first illuminating the reflector with the perfect feed, calculating the induced current on the reflector and then integrating the current on the reflector to give the scattered field by equation (3.3.1).

Figure 3.11 and Figure 3.12 are the Q/I and U/I plots for a perfect feed illuminating the reflector with no struts. The circular structure of radius 2.5° in the middle of the plot represents the first null of the radiation pattern and contains the main beam. The ring around the main beam, extending from ?2.5° to ?6.2°, is the first sidelobe. Polarization in the center of the main beam is zero, but the magnitudes of both normalized Q and normalized U increase radially outward. In addition, symmetry is observed in both plots. Adjacent quadrants have polarization in anti-phase forming a "cloverleaf" structure in the main beam. This form of polarization distortion, known as "Barrel distortion" [Christiansen and Högbom, 1985], is the result of the curved electric field lines generated by the curved reflector surface when illuminated by a linearly polarized feed (Figure 3.13). This distortion contains cross polarization which is strongest on the lines 45° from the feed polarization. When an unpolarized source illuminates the reflector, the curved field lines on the dish change the direction of the incident unpolarized electric vectors upon reflection. As a result, the Stokes parameters Q and U are non-zero and the received pattern appears polarized even when observing an unpolarized source.

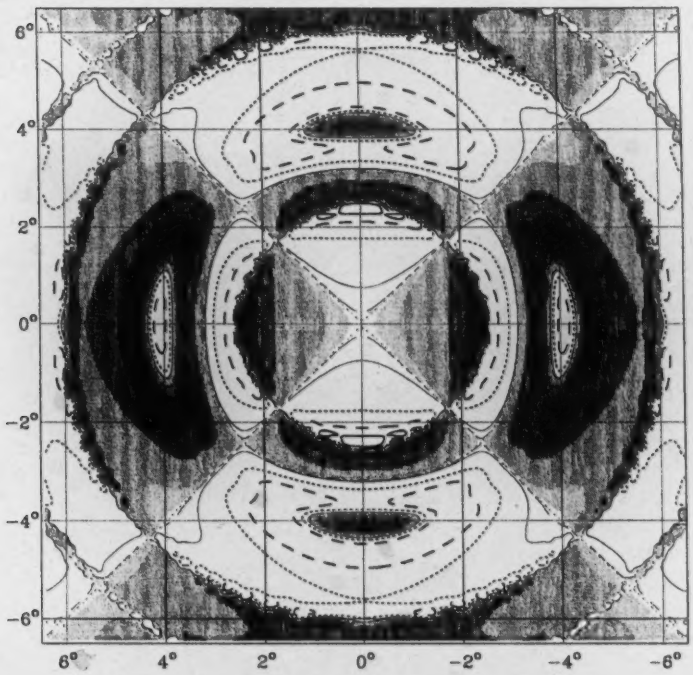

Figure 3.11 Q/I contour plot for a perfectly linear feed illuminating a paraboloidal reflector with no struts.

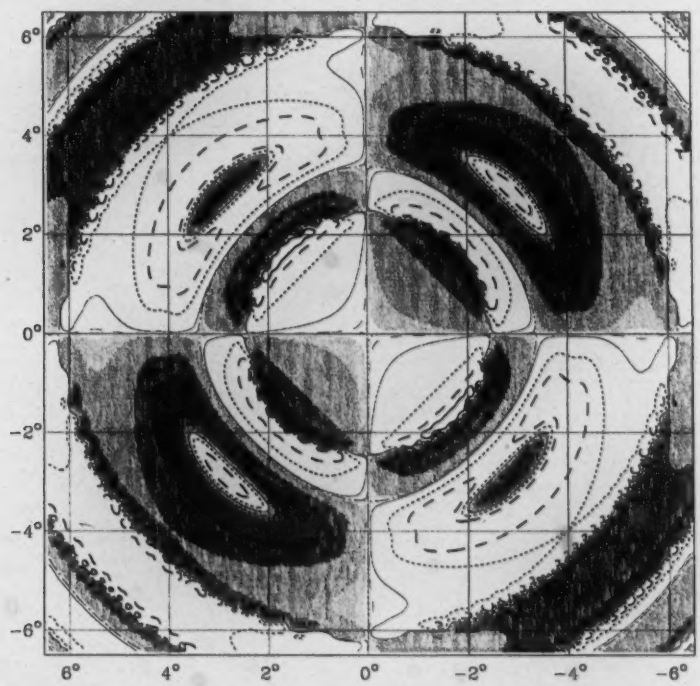

Figure 3.12 U/I contour plot for a perfectly linear feed illuminating a paraboloidal reflector with no struts.

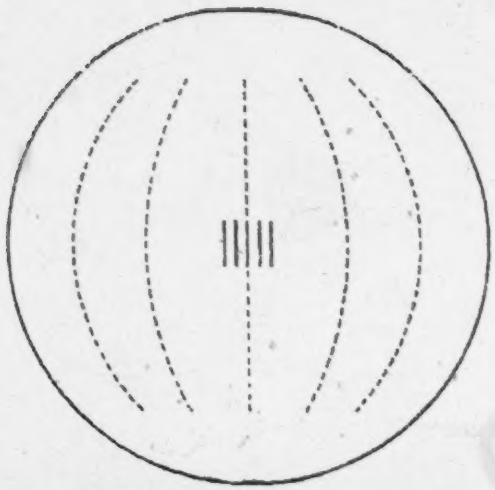

Figure 3.13 A feed with perfect linear polarization, after reflection, produces the field lines shown by the dashed lines. This distorted field contains cross-polarized components, strongest on lines at 45o to the feed polarization. [Christiansen and Högbom, 1985]

The Q/I and U/I plots show that the edge of the main beam and the first sidelobe are highly polarized. Figure 3.14 is a plot of the Stokes I and absolute value of Stokes Q on a logarithmic scale. The degree of polarization is highest near the first null since the value of I drops faster than Q. In addition, Figure 3.14 shows that cross polarization has a lower main beam to sidelobe ratio than the total intensity. Therefore, Q/I and U/I are expected to be higher in the sidelobe than in the main beam region as shown in the contour plots above.

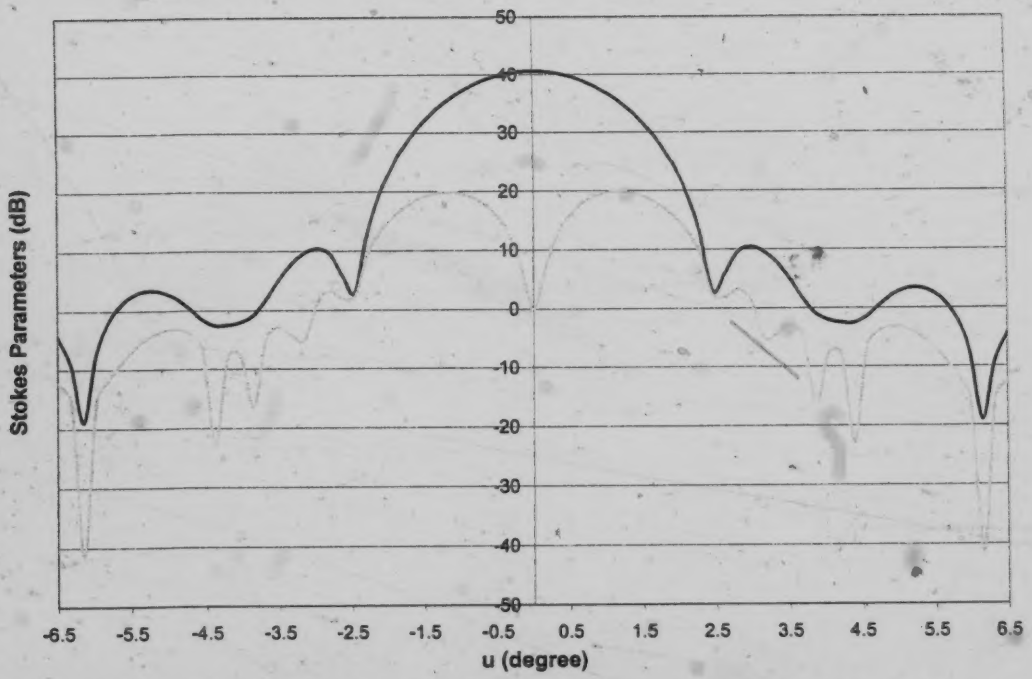

Figure 3.14 Plot of Stokes parameter I (black) and the absolute value of Q (gray) through the u-axis.

3.4.2 Feed Cross Polarization

The actual tabulated feed pattern (see Figure 3.4), which includes the cross polarized components, will now be used in the simulation (Figure 3.15 and Figure 3.16). These results will be compared with the Stokes parameter plots for the perfect feed case in section 3.4.1 to examine the effects of the feed cross polarization.

Polarization is still found to be zero in the center of the main beam and the symmetry is maintained throughout the radiation pattern. However, there is a sign inversion in the Q/I and the U/I plots between the perfect feed case and the actual feed case. Also, the degree of polarization is smaller at the edge of the main beam in the real feed case. Instrumental polarization due to the feed cross polarization acts in the opposite direction from the polarization due to the reflector shape. Therefore, the net polarization is reduced at the edge of the main beam. In addition, the first sidelobe is no longer clearly defined, and the degree of polarization is stronger and is in the same direction as

the perfect feed case beyond the first sidelobe. The conclusion can be drawn that the feed cross polarization has a larger effect on instrumental polarization than the reflector curvature.

The differences in the instrumental polarization response between a reflector illuminated with a "perfect" feed and with the actual feed show that the polarization characteristics of a feed affect the direction of currents induced on the reflector which in turn determine the polarization of the antenna pattern. The evidence that polarization due to reflector curvature is dominated by that produced by feed cross polarization suggests that there might be an "ideal" feed that gives zero cross-polarization. Koffman [1966] defined an "ideal" feed as one that induces parallel current flow on the surface of the reflector. For a prime-focus paraboloidal reflector, a pair of crossed electric and magnetic dipoles of equal intensity, also known as the Huygens source [Koffman, 1966], is the "ideal" feed. The far-field pattern of this antenna system is free of cross polarization. However, electric and magnetic dipoles are idealized point sources and cannot be realized perfectly. Another "ideal" feed defined by Ludwig [1973] is a physically circular feed with equal E- and H-plane amplitude and phase patterns. As shown in Figure 3.4 the actual feed pattern is very similar in the E- and the H-planes. The slight asymmetry or ellipticity in the feed pattern introduces cross polarization in the "perfect" and the actual feed cases.

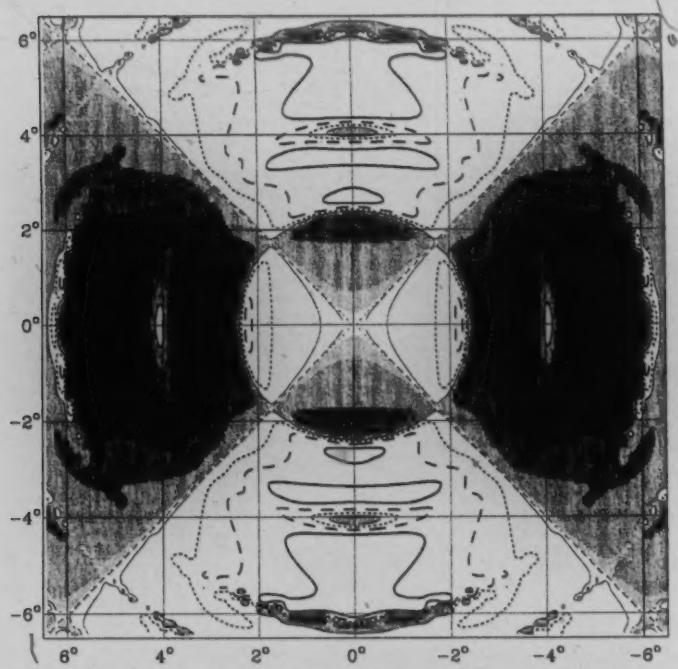

Figure 3.15 Q/I contour plot for the actual feed illuminating a paraboloidal reflector (no struts).

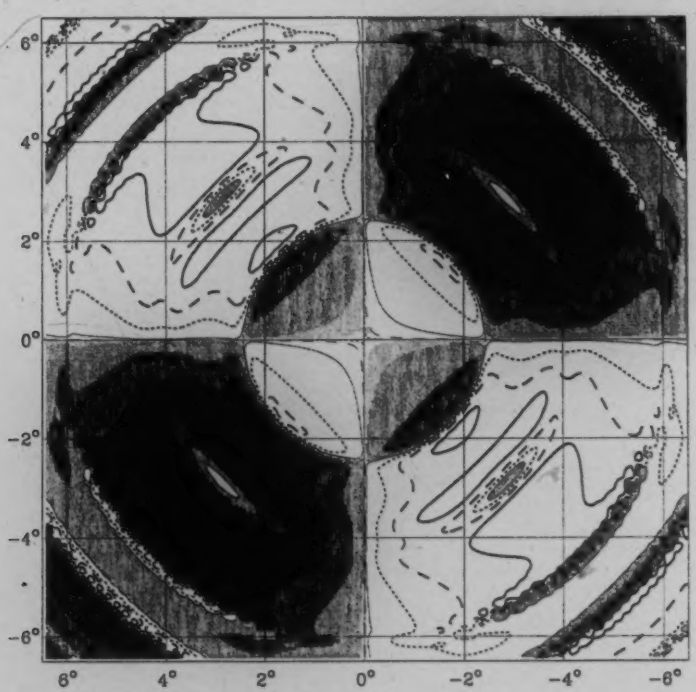

Figure 3.16 U/I contour plot for the actual feed illuminating a paraboloidal reflector (no struts)

3.4.3 Surface Roughness

Surface roughness was modeled by defining an object in the Random Surface class. **GRASP8** introduces a rectangular grid with spacings C_x and C_y both equal to the characteristic length of the surface errors: The heights of the grid nodes are random values between specified peak-to-peak limits with a mean of zero, which describes the roughness. A cubic interpolation function yields a smooth surface between the random values at the nodes.

When a surface roughness with a characteristic length of 0.5 m and rms value p of 0.005 m (a peak value of 0.0106 m) is introduced on the reflector surface, both the Q/I (Figure 3.1) and U/I (Figure 3.16) plots become randomly distorted (see Figure 3.17 and Figure 3.18). The effect of randomness caused by the surface roughness is more prominent outside and near the edge of the main beam where the energy level is lower. This is an indication that surface roughness introduces a uniform disturbance across the entire radiation pattern. The polarized fields caused by the random surface errors are randomly added constructively and destructively to the other instrumental polarization contributions. This results in a lower linear instrumental polarization or a depolarization effect. Therefore, with the addition of the surface roughness, the net degree of linear polarization becomes smaller than in the case of the actual feed illuminating a perfect reflector.

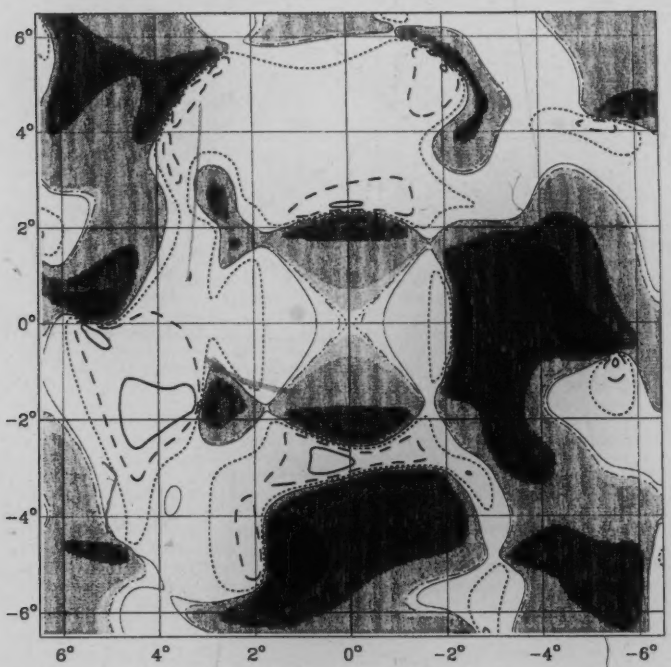

Figure 3.17 Q/I plot for the actual feed illuminating a reflector with surface roughness (no struts).

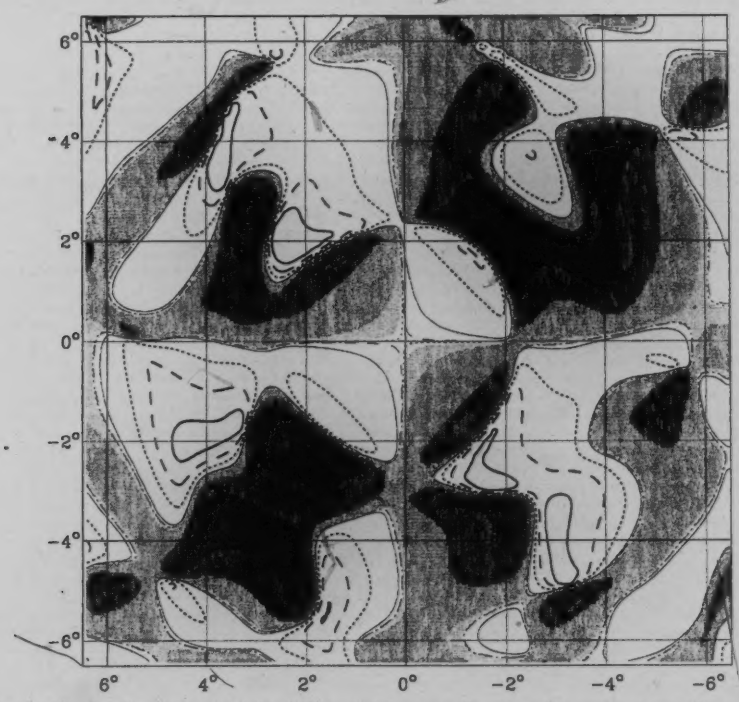

Figure 3.18 U/I plot for the actual feed illuminating a reflector with surface roughness (no struts).

On the other hand, though the cross polarization improves, the total intensity (Stokes I) in the main beam drops. The maximum total intensity for the case of the perfect reflector illuminated with the actual feed is 40.61 dBi, but when surface roughness of 0.005 m rms is introduced on the reflector, maximum I dropped by 0.32 dB. The surface gain-loss factor can also be calculated by considering the phase delay or advance of a plane wave after it is reflected from an irregular surface with surface deviation of δ'. If the separation between the irregularities (or characteristic length) is larger than a wavelength and the mean of the surface error is zero, the normalized surface gain-loss factor, k_g [Kraus, 1988] is

$$k_g = \cos^2\left(720^\circ \frac{\delta'}{\lambda}\right) \tag{3.4.1}$$

The gain-loss factor can also calculated using the Ruze relation

$$k_g = e^{-(4\pi\delta'/\lambda)^2} \tag{3.4.2}$$

where δ' is the rms roughness of the surface.

The calculated gain-loss factors are compared with the drop in maximum intensity computed by **GRASP8**. Figure 3.19 shows a plot of gain-loss factor as a function of rms surface roughness. The **GRASP8** results agree with the Ruze relation very well. This validated the accuracy of **GRASP8** in the computation of the antenna response for an antenna system with surface roughness. The energy lost from the main beam is redirected towards the sidelobes. Thus, a drop in the maximum intensity and a rise in the sidelobe level are observed as the surface roughness becomes more severe (Figure 3.20)

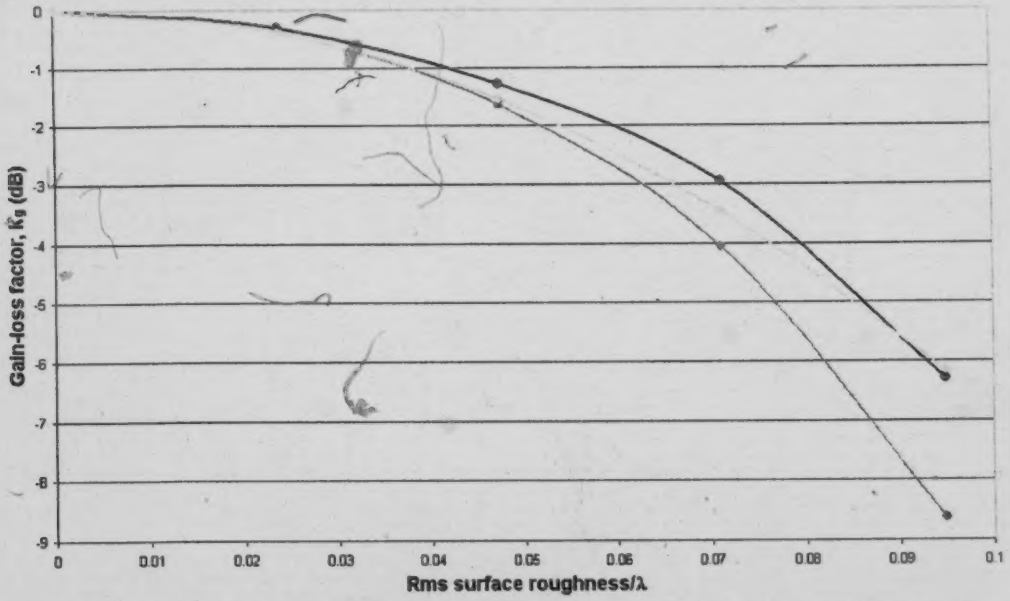

Figure 3.19 Gain-loss factor as a function of surface roughness as calculated by GRASP8 (black), and using equation 3.4.1 (gray) and the Ruze relation (light gray).

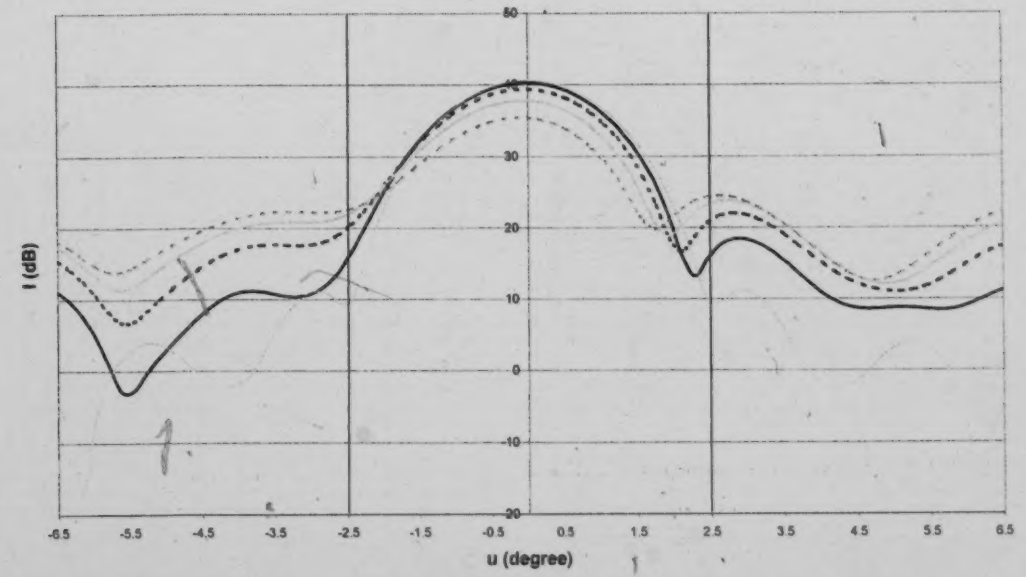

Figure 3.20 Stokes I through u-axis for the case of a perfect reflector (no struts) with no surface roughness (thin gray) is compared with an imperfect reflector having rms roughness of p (black), 2p (dotted black), 3p (gray) and 4p (dotted gray). p = 0.005 m. The vertical lines indicate the extent of the main beam

In addition, the surface roughness introduces circular polarization. There is an increase in the degree of circular polarization V/I (Figure 3.21) compared to the perfect

reflector case (Figure 3.22). To understand this phenomenon, consider a circularly polarized wave. The feed is excited by a linear signal; a linearly polarized wave can be decomposed into two equal magnitude, circularly polarized waves rotating in opposite senses. When a circularly polarized wave is reflected from the antenna dish, it remains circularly polarized, but in opposite rotating sense and with a phase shift. In the perfect reflector case with no feed struts, the phase shift is entirely due to the reflector curvature and is identical to the rotation of linearly polarized wave on the aperture. (The bending of electric vectors for the case of a perfect feed illuminating a smooth reflector is shown in Figure 3.13). This phase shift is in opposite direction for orthogonal, linearly polarized incident waves. Thus, in the case of random polarization, the phase shifts in the radiation pattern which result from feed orientations that are at 90° cancel to produce a negligible V/I ratio.

However, plane waves reflected from the irregular surface will be advanced or delayed with respect to waves reflected from a perfect surface. As a result, the two circularly polarized waves no longer cancel completely and a non-zero V is produced. V/I is positive on the top part of the main beam (above the u-axis) and negative on the bottom (below the u-axis). This beam squinting is a feature of an offset antenna. With the offset antenna, the phase shift due to a pair of orthogonal, linearly polarized incident waves does not cancel. Chu [1973], in a paper explaining the polarization characteristics of an offset antenna, stated that "beam displacement occurs because of variation in phase shift across the reflector." The similarity in circular polarization properties between a focused feed illuminating a rough reflector and an offset antenna property suggests that the best fit line of the rough reflector departs from a symmetrical paraboloid. Thus, the feed appears to be off center, as in an offset reflector. For the same reasoning as the Q/I and the U/I ratios, the degree of circular polarization is stronger outside the main beam and is randomly distributed.

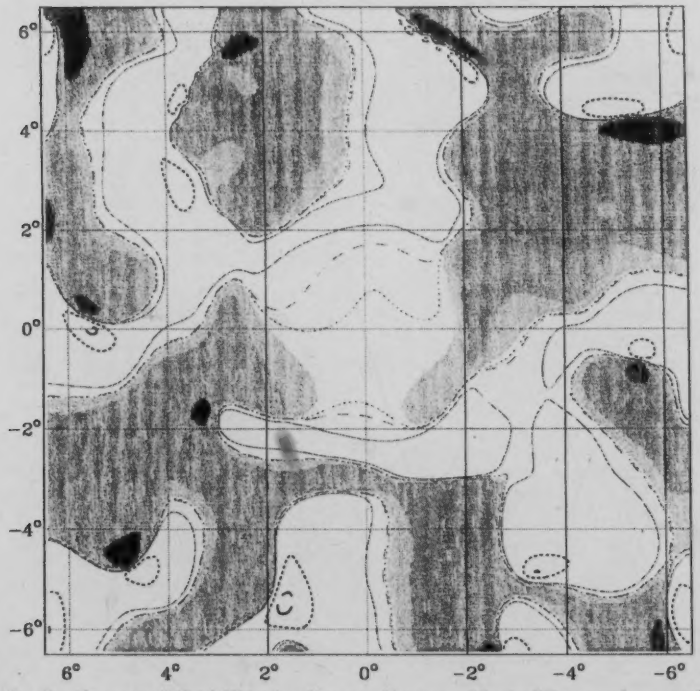

Figure 3.21 V/I plot for the actual feed illuminating a reflector with surface roughness of 0.005 m rms (no struts).

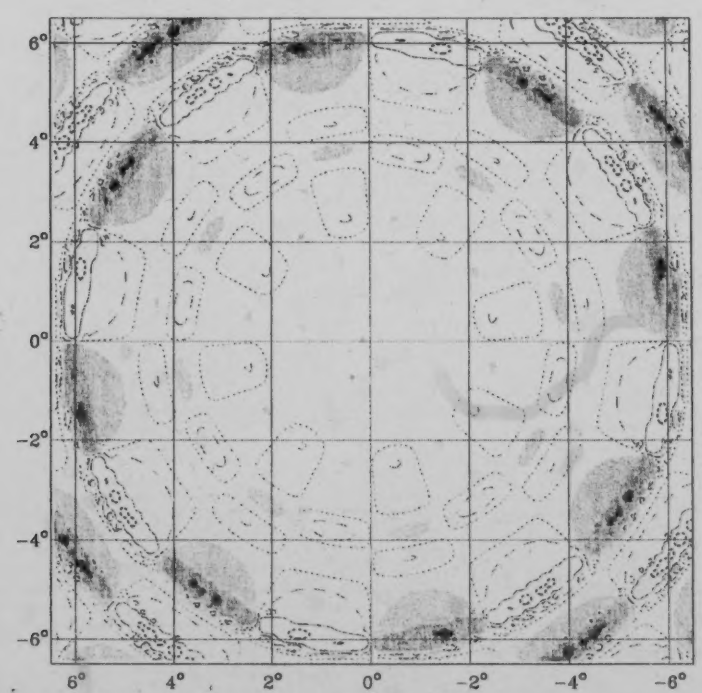

Figure 3.22 V/I plot for the actual feed illuminating a reflector with no surface roughness (no struts).

The effect of surface roughness on circular polarization was further examined by varying the rms value of the roughness (Figure 3.23). In the center of the main beam, the magnitude of V/I increases for increasing surface roughness. However, on the edge of the main beam and in the sidelobe region, the magnitude of V/I is lower for a rougher surface. As seen in Figure 3.20, sidelobe level in Stokes I increases as roughness increases. This is the reason for the drop in |V/I| outside the main beam as the rms roughness increases. The amount of circular polarization increases throughout the field of view for larger surface error due to the increase in phase errors.

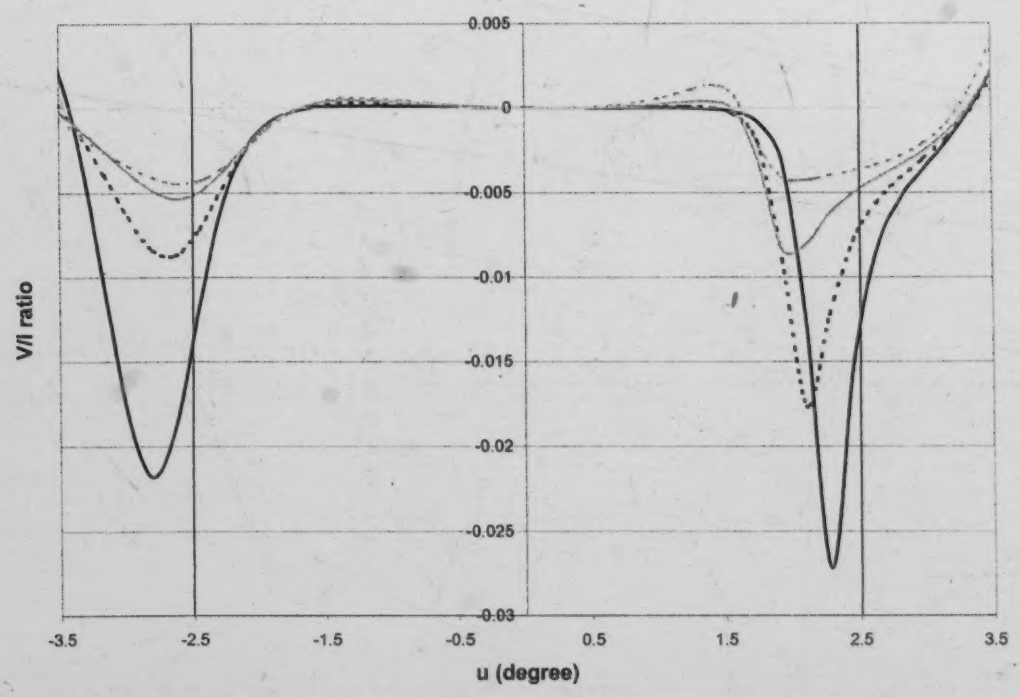

Figure 3.23 V/I plot through u-axis for rms surface error of p = 0.005 m (black), 2p (dotted black), 3p (gray) and 4p (dotted gray). The two vertical lines indicate the extent of the main beam.

3.4.4 Different Strut Configurations

The seven antennas of the Synthesis Telescope have either three or four feed-support struts attached to the rim of the reflector. The effects of strut arrangements were examined by comparing an antenna system with three struts (i.e. the prototype antenna)

and one with four struts. Figure 3.24 shows the position of the struts with respect to the polarization plots. Both the three-strut and the four-strut models were excited by the actual feed. The spherical scattering simulation sequence as described in section 3.3.1.2 was used to compute the scattering pattern.

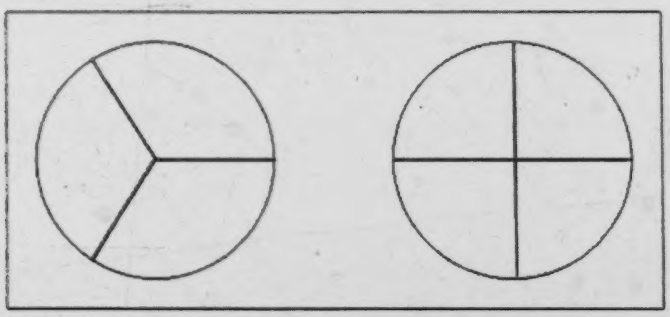

Figure 3.24 Strut positions for the three-strut configuration (left) and four-strut configuration (right). Both diagrams are positioned relative to the Stokes parameter contour plots.

Different feed support strut arrangements have a great impact on the symmetries of the polarization pattern. In the three-strut configuration, all the polarization patterns (Figure 3.25, Figure 3.26 and Figure 3.27) are symmetrical about the x-axis, but not about the y-axis. In the four-strut arrangement, pairs of struts are located symmetrically opposite each other. Symmetries in the Stokes parameter plots (Figure 3.28, Figure 3.29 and Figure 3.30) are observed about both axes. The Q/I and the U/I contour plots for this configuration resemble those for the no-strut model more than the three-strut configuration. In addition, the degree of linear polarization is higher on the edge of the main beam in the three-strut arrangement. From the above evidence, symmetries in the strut arrangement create a cancellation effect in the linear polarization pattern. However, the degree of circular polarization (V/I) is very similar for the two strut configurations.

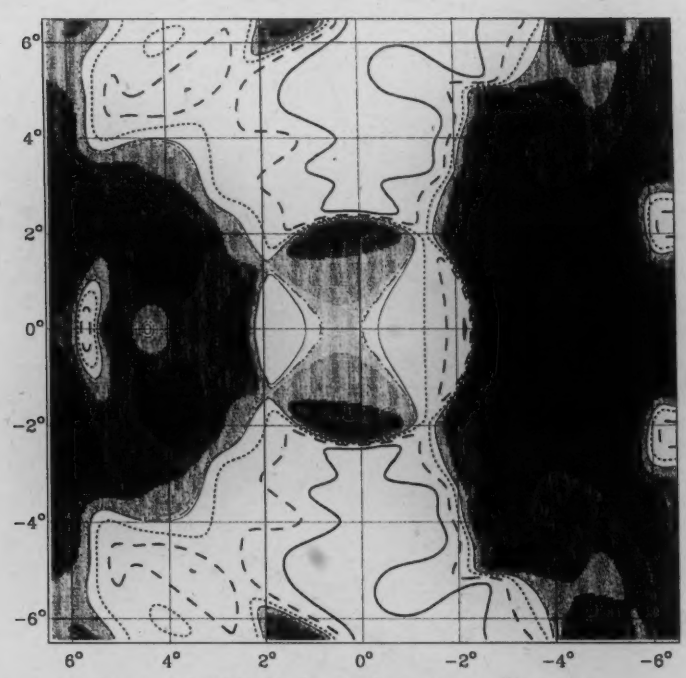

Figure 3.25 Q/I plot for the three-strut configuration

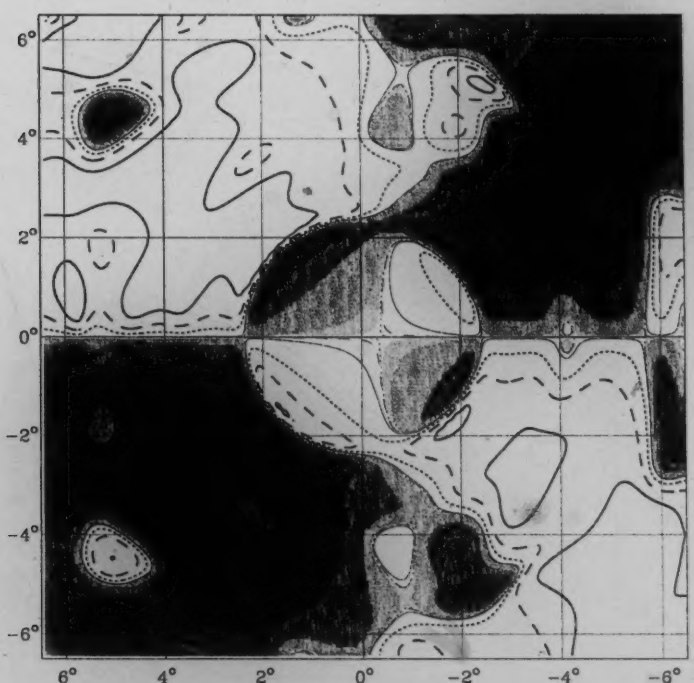

Figure 3.26 U/I plot for the three-strut configuration

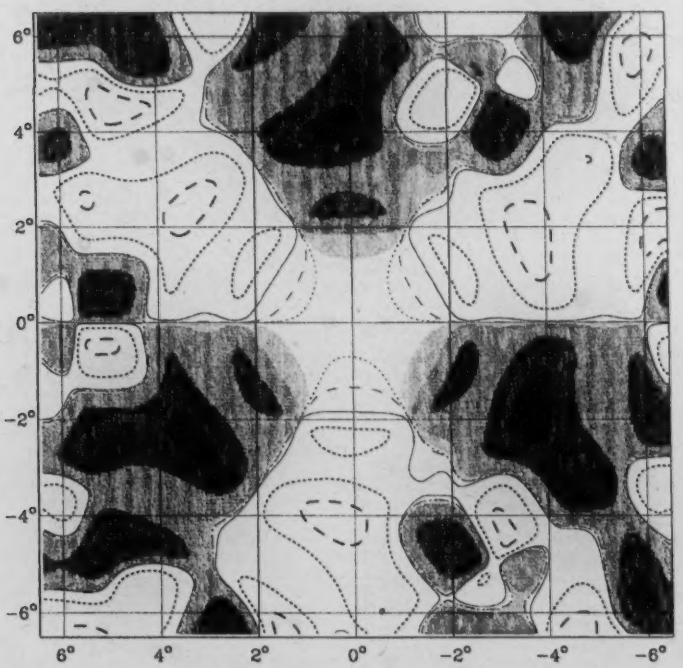

Figure 3.27 V/I plot for the three-strut configuration

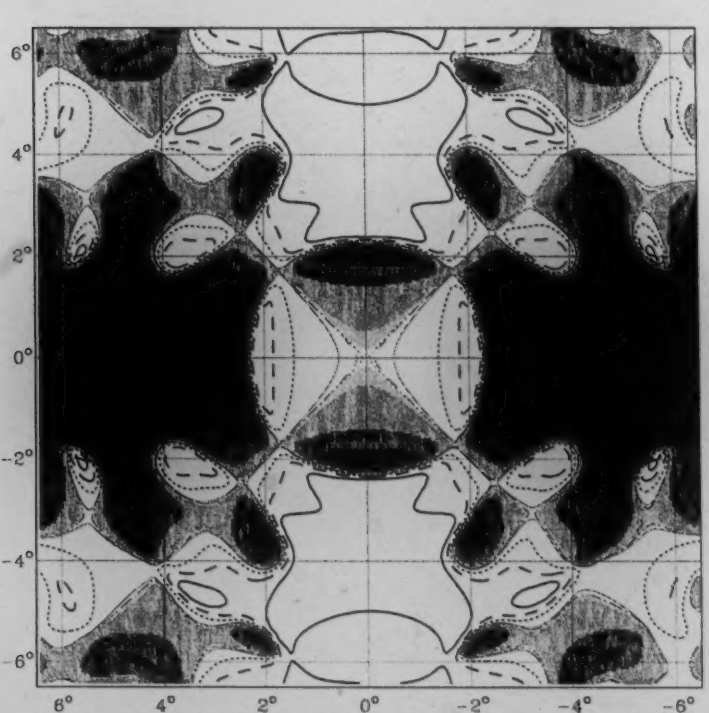

Figure 3.28 Q/I plot for the four-strut configuration

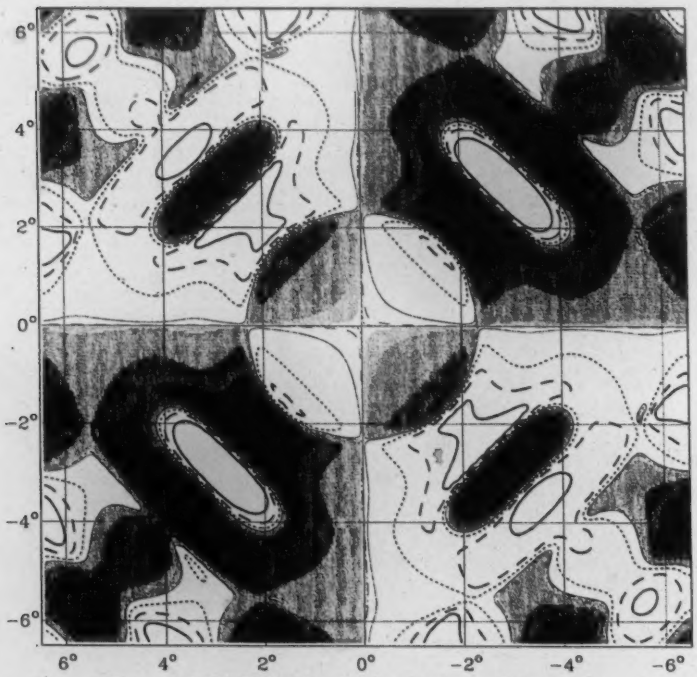

Figure 3.29 U/I plot for the four-strut configuration

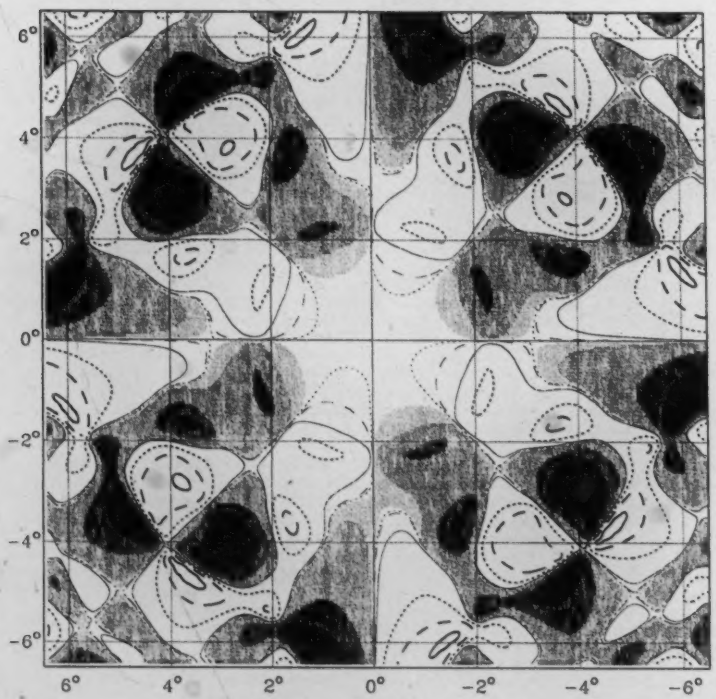

Figure 3.30 V/I plot for the four-strut configuration

These observations agree with the study of cross polarization using induced field ratio (*IFR*) [Kildal et al., 1988]. Section 2.7.1 gives a thorough definition of *IFR*. Kildal et al. concluded that the cross-polar field is largest if the strut makes angles of 45^{O} with the feed polarization. When the struts are oriented parallel or orthogonal to the feed polarization, the cross polarization becomes zero for all θ. In the four-strut configuration, the cross polarization introduced by a linearly polarized source is equal to the co-polarization component due to the struts introduced by a linearly polarized source that is oriented orthogonal to the first source. Therefore, in the case of random polarization, the cross polarization introduced by an orthogonal pair of linear polarized sources cancel. This cancellation effect is not found in the three-strut configuration. This is why instrumental polarization introduced by three struts is asymmetrical and is more severe than that introduced by four struts.

Another effect of struts on instrumental polarization is the increase in the Stokes V/I ratio. The reason for this increase is similar to the introduction of circular polarization when the feed illuminates a rough reflector. The wave diffracted off the strut is advanced or delayed with respect to the wave reflected from the reflector. When the two waves are added, destructive cancellation of circular polarization is not complete and thus V/I becomes non-zero. Superimposing the strut position diagrams (Figure 3.24) onto the V/I plots for both the 3-strut and 4-strut configuration, a sign change along the length of the strut is observed. This suggests that diffraction from either side of the strut is opposite in phase and the two circular polarized beams are offset in opposite directions.

3.4.5 Different Strut Diameters

The effect on the instrumental polarization of circular strut size was examined by varying the strut radius in the Circular Strut class. It is obvious that thicker struts would produce polarization patterns that depart farther from the no-strut model than thin struts would (Figure 3.31). In addition, thicker struts also create a greater degree of asymmetry in the three-strut configuration. However, the degree of polarization is not directly proportional to the width of the struts. The cross polarization magnitude is proportional

to both the diameter, a, of the struts and the IFR_D, half the difference between the magnitudes of the IFR_E and the IFR_H [Kildal et al., 1988]. IFR is a function of the polarization of the incident wave. IFR_E is defined for the E-vector parallel to the cylinder axis and IFR_H is defined for the H-vector parallel to the cylinder axis. The IFR_E and IFR_H magnitudes for circular struts of various sizes are shown in Figure 2.55 in section 2.7. From the graph, both $|IFR_E|$ and $|IFR_H|$ approach 1.0 as the diameter of the strut increases, but $|IFR_E|$ approaches the limit from above while $|IFR_H|$ approaches the limit from below. Thus, IFR_D is smaller for bigger struts. For strut diameters in the order of a wavelength, as the strut diameter increases, the two factors a and IFR_D counteract each other. Therefore, the Q/I curves for the 6-inch and 9-inch circular struts are quite similar in the main beam region.

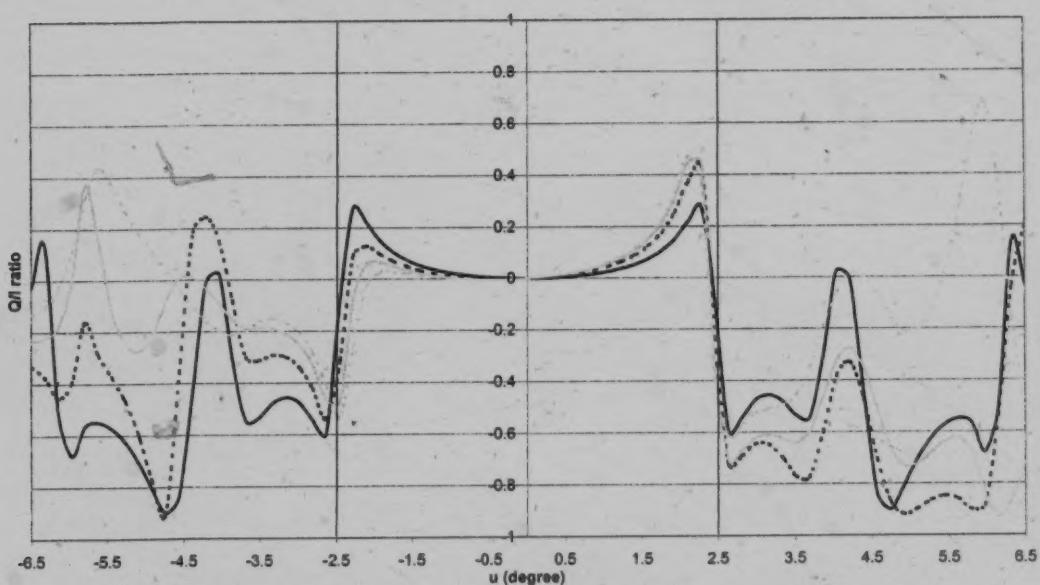

Figure 3.31 Q/I plot through u-axis. Solid black line represents no struts, dotted black line - 3" struts, solid gray line - 6" struts, dotted gray line - 9" struts (strut diameter is used in each case). The vertical lines indicate the extent of the main beam.

3.4.6 Different Strut Cross-sectional Shapes

Different strut cross-sectional shapes were defined using the Polygonal Strut class by specifying the coordinates of the polygon corners in the plane perpendicular to the

axis of the strut. The computational approach for polygonal struts is based on a combination of PO and PTD. The standard PO method is used to estimate the scattering from struts whose cross section sides are large in terms of wavelength. The diffraction by the edges of smaller struts is better modeled using PTD. The PTD theory assumes the diffraction from a specific edge of the strut to be the same as the diffraction from an infinite canonical wedge with the same angle as the edge when illuminated with a plane wave. This approximation is valid for strut diameters on the order of a wavelength. In the **GRASP8** manual, the performance of the PO plus PTD approach for struts smaller than a wavelength was examined by comparing the resultant scattered field with one calculated using the method of moments (MoM). MoM is a theoretically exact method used in electromagnetic scattering analysis. A square cylinder with sides $s = 0.89\lambda$ was illuminated with a plane wave polarized perpendicular to the strut axis. Figure 3.32 shows a comparison plot of the scattered field calculated using PO, PO+PTD and an integral equation solved by the MoM. The plot shows that **GRASP8** computes an accurate scattered field even for polygonal struts with sides smaller than a wavelength.

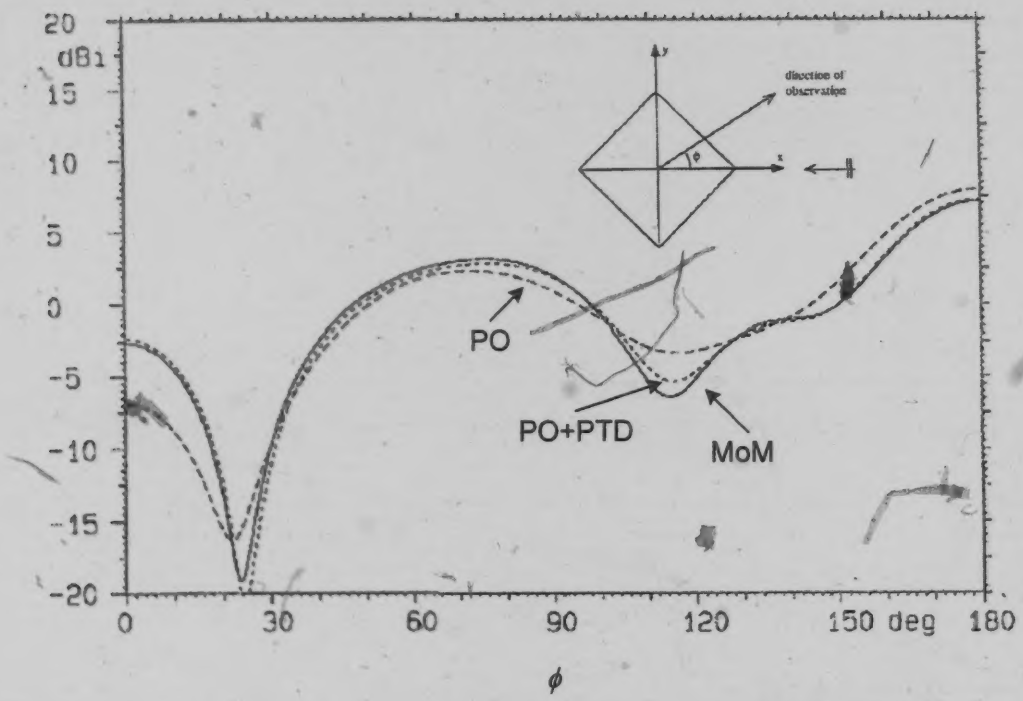

Figure 3.32 Scattered field from a square cylinder with sides s = 0.89λ calculated by MoM, PO+PTD and PO [Pontoppidan, 2000]

Struts with circular and triangular cross-section of the same widths will now be compared in a reflector antenna having three feed-support struts. In the triangular strut model, the apex of the struts points towards the center of the reflector. The struts have an equilateral triangular cross-section with sides of 0.722λ, similar in size to the **GRASP8** example. The triangular strut (Figure 3.33 and Figure 3.34) cross-section has much better linear polarization performance than the circular cross-section (Figure 3.25 and Figure 3.26). There is a smaller degree of asymmetry observed in both Q/I and U/I plots. The main beam of the U/I and Q/I plots for the reflector with triangular struts resembles the plots for the reflector with no struts (Figure 3.15 and Figure 3.16) more than the three circular strut model. Comparison between the two sets of Q/I and U/I plots shows that the triangular struts contribute less to linear instrumental polarization than circular struts. This result agrees with the conclusion made by Kildal et al. that cross polarization is proportional to IFR_D. According to the $|IFR|$ graph in Figure 2.55, a triangular cylinder has a much lower IFR_D than a circular cylinder.

However, the cost of good linear polarization performance is the degradation of circular polarization performance. In the triangular strut model, the degree of circular polarization in the main beam is higher than the circular strut model. The cause of the increase in circular polarization was not clearly understood. In an attempt to explain this phenomenon, the V/I ratio of an antenna system having three teardrop shaped struts was examined. The degree of circular polarization introduced by the teardrop strut is similar to Figure 3.35. This shows that diffractions from the two sharp corners on the backside of the triangular struts are not responsible for the increase in circular polarization.

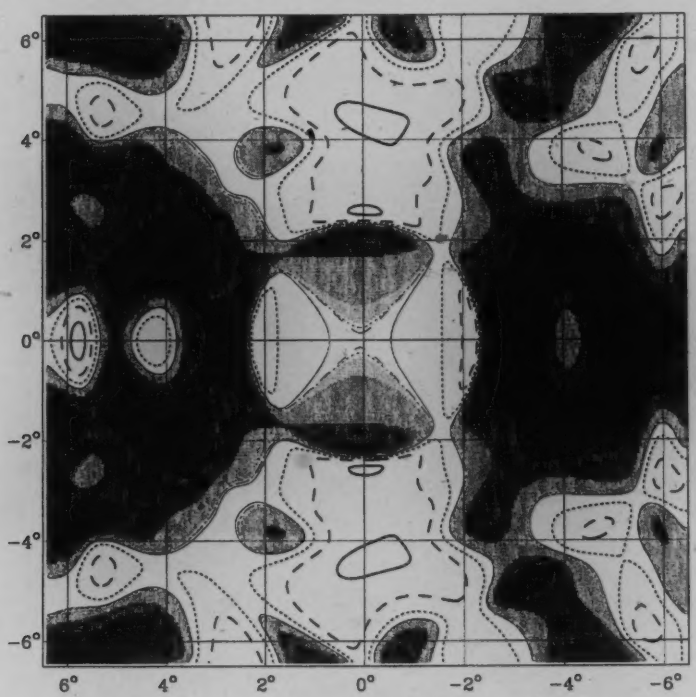

Figure 3.33 Q/I plot for an antenna with three triangular struts

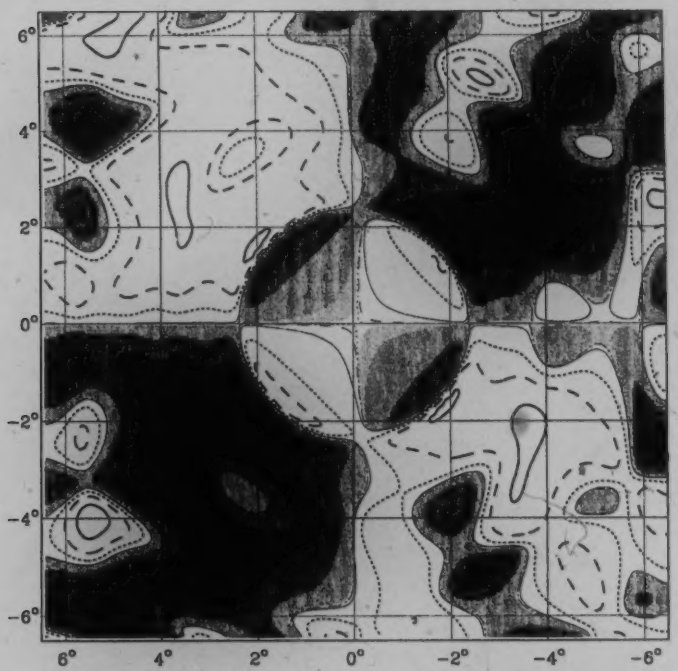

Figure 3.34 U/I plot for an antenna with three triangular struts

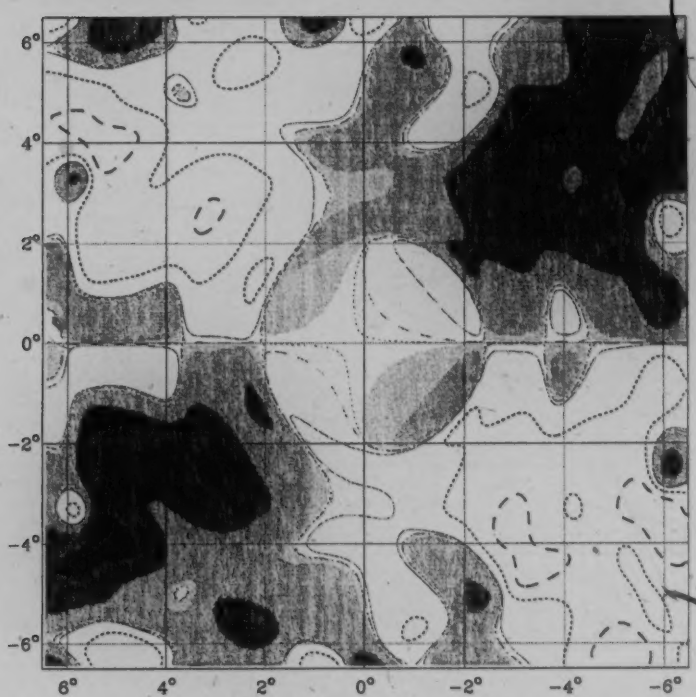

Figure 3.35 V/I plot for an antenna with three triangular struts

A possible explanation would be that V is produced by the flat surfaces of the triangular strut. The sense of circular polarization changes when the wave is reflected off the flat side of the triangular strut. The reflected wave and plane wave leaving the reflector rotate in opposite sense. When the scattered radiations are added vectorially with the plane wave leaving the reflector, a large offset between the two circularly polarized beams is created which leads to an increase in the V/I ratio. Despite the increase in V/I ratio, triangle is still a better choice for strut cross-section than circle for a radio telescope that is mainly used to detect Galactic emission that is mostly unpolarized with a small degree of linearly polarized component.

3.5 Stokes Parameter Plots for the Synthesis Telescope

Antennas 2, 3 and 4 of the DRAO Synthesis Telescope have reflector diameter of 8.534 m and focal length of 3.81 m. The imperfection of the reflector can be described as random roughness of 0.005 m rms and characteristic length of 0.5 m. The three feed-support struts are 6" in diameter and have circular cross sections. The antenna is illuminated by a prime focal feed with a pattern as described in **linearfeedpattern4.cut**. Stokes parameter contour plots that reflect these three Synthesis Telescope antennas are shown in Figure 3.36, Figure 3.37 and Figure 3.38.

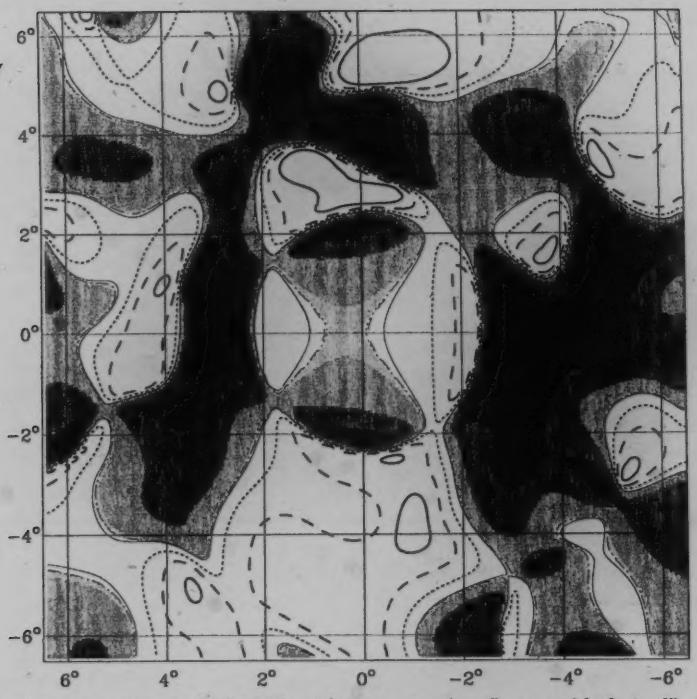

Figure 3.36 Q/I plot for the actual feed illuminating a rough reflector with three 6" circular struts

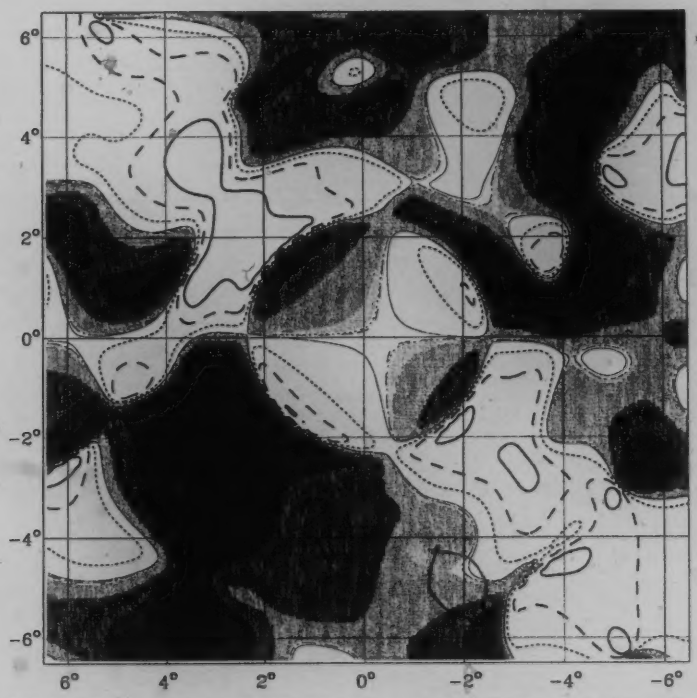

Figure 3.37 U/I plot for the actual feed illuminating a rough reflector with three 6" circular struts

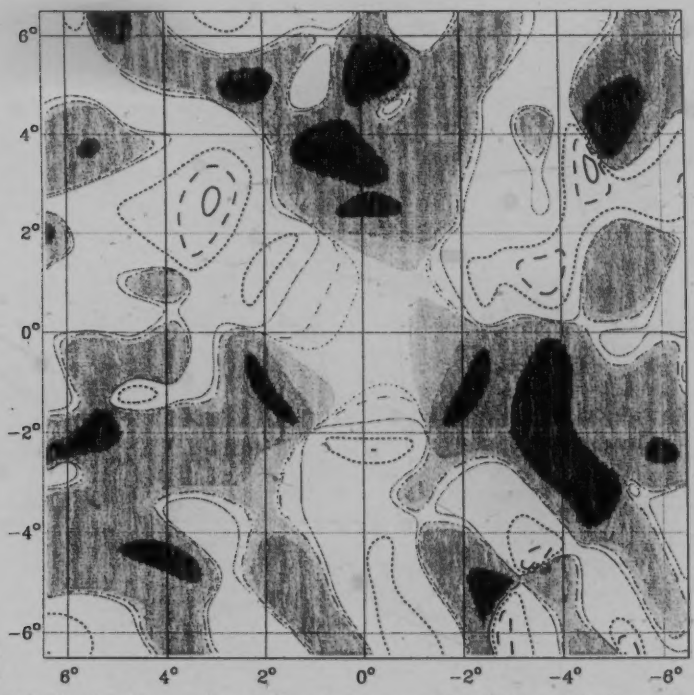

Figure 3.38 V/I plot for the actual feed illuminating a rough reflector with three 6" circular struts

These three Stokes parameter plots resemble those for the three-strut configuration (Figure 3.25, Figure 3.26 and Figure 3.27). However, the degree of linear polarization, Q/I and U/I, is reduced due to the introduction of random reflector surface roughness. Circular polarization, on the other hand, is larger in this case than in an antenna system without surface roughness. Phase errors generated by surface roughness and strut blockage are added, leading to a higher degree of circular polarization.

3.6 Conclusion

The sources of instrumental polarization for a prime focal paraboloidal reflector antenna were considered. The reflector curvature, feed cross polarization, reflector surface roughness, and strut arrangement and cross-section shape all contribute to the instrumental polarization in different degrees. Feed cross polarization causes the greatest degree of instrumental polarization. Reflector curvature, which bends the electric field lines along the reflector, also contributes significantly to the instrumental polarization.

Surface roughness generates random error in the polarization plots and causes a depolarization effect. Its contribution is significant only outside the main beam area. Among the 7 Synthesis Telescope antennas, the reflector rib structures are of two types. Although there are similarities in the reflector construction, it is not likely that the surface error of any two antennas would be identical. In the case of aperture synthesis where signals are received by several antennas, the surface errors on each antenna are slightly different and the combined effect of surface roughness will be reduced. The instrumental polarization of the pair will be smaller than for either antenna alone. Different strut arrangements and cross sections have considerably different effects on the polarization pattern. Four triangular struts attached to the edge of the reflector give the best polarization performance. In conclusion the contributions to instrumental polarization listed from the most significant to the least are:

1. feed cross polarization
2 (a) strut configuration (3-strut or 4-strut)
   (b) strut cross-section (circular or triangular)
3. reflector curvature
4. surface roughness

Under contribution 2, maximum linear instrumental polarization is obtained with circular struts in a 3-strut configuration, and minimum linear polarization is obtained with triangular struts in a 4-strut configuration. Therefore, the antenna system that generates the least Q/I and U/I instrumental polarization is a system with 4 triangular struts attached to a reflector with random surface errors.

Chapter 4 Conclusion

This thesis investigated two topics, both of which aimed to improve the performance of the Synthesis Telescope. The first topic was concerned with methods to reduce ground noise. By reducing the ground noise and receiver noise (a thesis project in working progress), the total system noise when detecting 21 cm continuum emissions will be halved and the telescope sensitivity will be doubled. The second part of the thesis discussed the sources of instrumental polarization which result from non-ideal properties of a radio telescope. Based on this study, an antenna system that generates the least instrumental polarization was deduced.

The antenna noise level when the antenna is pointing at the zenith was previously predicted by Dr. T. Landecker to be 20.2 K at 1420 MHz [private communication]. This includes 5.7 K sky noise and 14.5 K ground noise. The sources of ground noise are mesh leakage, spillover, strut scattering and diffraction at the rim. By considering each of the ground noise contributions separately and using the computation techniques developed in this thesis, the average ground noise (obtained by taking the geometric mean of the seven ground noise values in Table 2.1) was computed to be 14.3 K. The theoretical calculation agrees very well with the previous prediction. This demonstrates that the computation techniques can determine the individual contributions to ground noise accurately.

Methods to reduce each source of ground noise were studied and antenna modifications were suggested. Noise due to mesh leakage can be minimized by covering the reflector with aluminum tape. Experiment showed that a 4.0 K improvement in antenna temperature could be realized by shielding the center portion (a circle of 2.1 m radius) of the reflector. Building mesh fences around the antenna reflects the radiation that strikes the fence towards the sky and hence reduces spillover noise. This method is capable of reducing both direct spillover and strut scattering noise. Noise reduction of 1.0 K to 5.0 K when the antenna was observing the zenith was achieved by implementing different mesh fence designs. The strut cross section determines the amount of radiation scattered and the distribution of the scattered radiation. Computations showed that by

converting the cross-sections of the struts from circular to teardrop shape, strut scattering noise was lowered by redirecting the scattered energy away from the ground. Experiment showed that antenna noise reduced by 1 K and 2 K when 3" and 6" circular struts were changed to teardrop shape. Combining the results from the experiments performed and the suggested antenna modifications, ground noise can be reduced from 14.3 K to 8 K.

In the second section of the thesis, the instrumental polarization was computed numerically using **GRASP8** and the author's program **SumField_daf.c** and then verified against a set of measured data within the mainbeam. The simulation procedure was capable of extending the angular range of our knowledge of the Stokes parameters to include the mainbeam and the first sidelobe. This study showed that feed cross polarization is the biggest contributor to instrumental polarization. The second largest contributor is the struts; the severity of the strut effect depends on the strut arrangement, cross-section shape and size. In general, a 4-strut configuration has better polarization performance than 3-strut due to the cancellation effects which result from symmetry. Although triangular struts introduce less linear polarization than circular struts, they generate a much higher degree of circular polarization. The reflector creates cross polarization by rotating electric field vectors. An interesting effect is that instrumental polarization due to feed cross polarization and reflector curvature oppose and cancel each other to some extent. The least significant source of polarization is surface roughness. Surface roughness introduces random phase errors in reflected plane waves which lead to a depolarization effect in the Q/I and U/I ratio. However, circular polarization is also produced by the phase errors. In random polarization, the two circularly polarized waves no longer cancel perfectly. Based on the simulated results, the antenna system that generates the least linear instrumental polarization is a system with 4 triangular struts attached to a reflector with random surface errors. Since only Stokes Q and U images are measured with the Synthesis Telescope, this antenna system is ideal for the DRAO Synthesis Telescope.

Appendix A. Defining the Coordinates of a Point in a Rotated Coordinate System

To fully define the rotation of a new coordinate system with respect to a reference coordinate system, three parameters, θ_{NR}, ϕ_{NR}, ψ_{NR}, are needed. The subscripts N and R denote the new and the reference coordinate system, respectively. θ_{NR} is the θ location of the reference z-axis with respect to the new coordinate system, ϕ_{NR} is the ϕ location of the reference z-axis in the new coordinate system (θ and ϕ are the same as that defined in Figure 2.1), and ψ_{NR} is the rotation about the z-axis of the new coordinate system. Figure A.1 shows a point P in the reference coordinate system (R_{pR}, θ_{pR}, ϕ_{pR}) and a new coordinate system that has the same origin as the reference but is rotated. Since the origins of the two coordinate systems coincide, R_{pR} and R_{pN} are equal and assumed to be one. The coordinates (θ_{pN} and ϕ_{pN}) of this point in the new coordinate system can be calculated using spherical trigonometry.

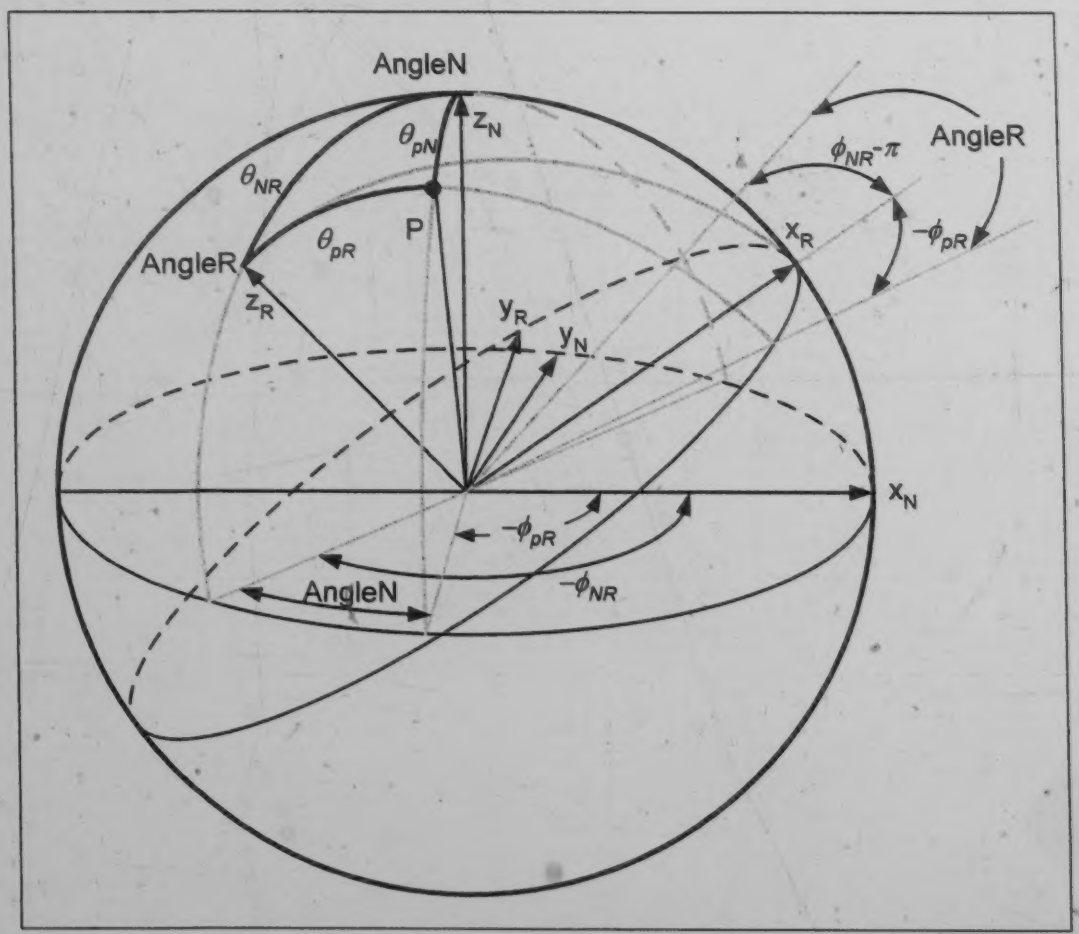

Figure A.1 The reference z-axis, new z-axis and the point P form a spherical triangle on the surface of a sphere. The geometries for solving AngleN and AngleR are shown. This diagram assumes ψNR = 0.

First, let $\psi_{NR} = 0$; a spherical triangle is constructed by connecting the z-axes of the reference and the new coordinate system and the point P on a sphere with radius $R = R_{pN} = R_{pR} = 1$. The side arc lengths of the spherical triangle are θ_{NR}, θ_{pR} and θ_{pN}. To solve for the unknown θ_{pN}, the spherical triangle cosine law requires the knowledge of the angle oppsite of the side θ_{pN}. This angle, denoted as *AngleR*, can be solved geometrically as shown on the left side of Figure A.1.

$$AngleR = \phi_{NR} - \phi_{pR} - \pi \tag{A.1}$$

$$\cos\theta_{pN} = \cos\theta_{NR}\cos\theta_{pR} + \sin\theta_{NR}\sin\theta_{pR}\cos AngleR \tag{A.2}$$

To solve for the second unknown ϕ_{pN}, the angle opposite to θ_{pN} is denoted as *AngleN*. Again this angle is solved geometrically (right diagram of Figure A.1). *AngleN* is solved using both the sphercical triangle cosine law and sine law to give the angle in the correct quadrant.

$$\cos\theta_{pR} = \cos\theta_{NR}\cos\theta_{pN} + \sin\theta_{NR}\sin\theta_{pN}\cos AngleN \tag{A.3}$$

$$\frac{\sin AngleN}{\sin\theta_{pR}} = \frac{\sin AngleR}{\sin\theta_{pN}} \tag{A.4}$$

$$AngleN = \tan^{-1}\frac{\sin AngleN}{\cos AngleN} \tag{A.5}$$

ϕ_{pN} can be calculated by adding ϕ_{NR} to AngleN.

However, the above formulation only considers the case when the new coordinate system has no rotation about the z-axis or $\psi_{NR} = 0$. Now, let the new coordinate be arbitrarily rotated about its z-axis and ψ_{NR} can be non-zero. In this case, ψ_{NR} must be subtracted from ϕ_{pN} to undo the rotation about the z-axis. *AngleR* is identical to the previous case, but *AngleN* is modified to become:

$$AngleN = \phi_{pN} - \phi_{NR} - \psi_{NR} \tag{A.6}$$

θ_{pN} and ϕ_{pN} are solved using the same technique as above.

Reference

Anderson, M. D., Reducing Antenna Noise in a Synthesis Telescope and an Observation of an HII Region, M.S. thesis, Univ. of Alberta, Edmonton, Alberta, Canada, 1989.

Anderson M. D., Landecker T. L., Routledge D., and Vaneldik J. F., The Far Sidelobes and Noise Temperature of a Small Paraboloidal Antenna Used for Radio Astronomy, Radio Science, 26, 353-361, 1991.

Bucci O. M., Gennarelli C., and Palumbo L., Flanged Parabolic Antennas, IEEE Trans. Antennas Propaga., 30, 6, 1081-1085, 1982.

Bucci O. M., Gennarelli C., and Palumbo L., Parabolic antennas with a Loaded Flange, IEEE Trans. Antennas Propaga., AP-33, 755-762, 1985.

Burke B. F., and Graham-Smith F, An Introduction to Radio Astronomy, Cambridge University Press, New York, 2002.

Cazzolato F., Modeling the Instrumental Polarization of the DRAO Synthesis Telescope using Antenna Theory, 2000. Proceedings of a Workshop held at Université de Montréal.

Christiansen W. N. and Högbom J. A., Radiotelescopes, Cambridge University Press, 1985.

Del Rizzo D., Calculation of Gain and System Temperature Values for the Synthesis Telescope, DRAO Technial Memorandum, 2003.

Fomalont E., and Wright M., Galactic and Extra-Galactic Radio Astronomy, 1st ed., eds. Verschuur G. L., and Kellerman K. I., Springer-Verlag, New York, 1974.

Garcia A., "Transistor Parameter Measurement and Low Noise Amplifier Design and Testing for the Synthesis Telescope Receivers at 1420 MHz", University of Alberta M.Sc. Research Project Proposal, 2002.

Gray A., "Radio Polarimetry", DRAO Summer Lecture Series, 1998.

Ghobrial S. I., Axial Cross Polarization in Reflector Antennas with Surface Imperfections, IEEE Trans. Antennas Propaga., 28, 610-616, 1980.

Gupta I. J., Ericksen K. P., and Burnside W. D., A Method to Design Blended Rolled Edges for Compact Range Reflectors, IEEE Trans. Antennas Propaga., 38, 6, 853-861, 1990.

Hamaker J. P.,and Bregman J. D., Understanding Radio Polarimetry. III. Interpreting the IAU/IEEE Definitions of the Stokes Parameters, A&AS, 117, 161-165, 1996.

Hamaker J. P., Bregman J. D. and Sault R. J., "Understanding Radio Polarimetry. I. Mathematical Fundations, A&AS, 117, 137-147, 1996.

Heiles C., All-Stokes Parameterization of the Main Beam and First Sidelobe for the Arecibo Radio Telescope, PASP, 113, 1247-1273, 2001.

Kildal P. S., Olsen E., and Aas J. A., Losses, Sidelobes, and Cross Polarization Caused by Feed-Support Struts in Reflector Antennas: Design Curves, IEEE Trans. Antennas Propaga., 86, 182-190, 1988.

Knee L. B. G., The Canadian Galactic Plane Survey, RevMexAA (Serie de Conferencias), 15, 301-301, 2003.

Koffman, I. Feed Polarization for Parallel Currents in Reflectors Generated by Conic Sections, IEEE Trans. Antennas Propag., 14, 37-40, 1966.

Kraus, J. D., Antennas, McGraw-Hill, Boston, 1988.

Kraus, J. D., Electromagnetics, McGraw-Hill Book Company, New York, 1984.

Kraus, J. D., Radio Astronomy, Cygnus-Quasar Books, Powell, 1986.

Landecker, T. L., Dewdney, P. E., Burgess, T. A., Gray, A. D., Higgs, L. A., Hoffmann, A. P., Hovey, G. J., Karpa, D. R., Lacey, J. D., Purton, C. R., Roger, C. R., Willis, A. G., Wyslouzil, W., Routledge, D., Vaneldik, J. F., The Synthesis Telescope at the Dominion Radio Astrophysical Observatory, A&AS, 509-524, 2000.

Landecker, T.L., Routledge, D., Smegal R. J., Trikha, P., Vaneldik J. F., Ground Radiation Scattered from Feed Support Struts: A Significant Source of Noise in Parabolodial Antennas, Radio Sci., 26, 363-373, 1991.

Landecker, T. L., Smegal, R. J. and McKinley, J. M., Cylindrical and Conical Shrouds for the Reduction of Ground Noise of Paraboloidal Antennas, Radio Sci., 32, 2139-2148, 1997.

Landecker, T. L. and Veidt B., "New Low-Noise Amplifiers for the Synthesis Telescope", DRAO report, 2001.

Lang, K. R., Astrophysical Formulae, Springer-Verlag, 1980.

Lawrence, C. R., Herbig, T., Readhead, A. C. S., Reduction of Ground Spillover in the Owens Valley 5.5-m Telescope, Proc. IEEE, 82, 763-767, 1994.

Ludwig A. C., The Definition of Cross Polarization, IEEE Trans. Antennas Propaga., 21, 116-119, 1973.

Milligan T. A., Modern Antenna Design, McGraw-Hill Book Company, New York, 1985.

Moreira F. J. S., Prata, A., and Thorburn, M. A., Minimization of the Plane-Wave Scattering Contribution of Inverted-Y Strut Tripods to the Noise Temperature of Reflector Antennas, IEEE Trans. Antennas Propaga., 44, 492-499, 1996.

Mumford W. W., Some Technical Aspects of Microwave Radiation Hazards, Proc. IRE, 49, 427-447, 1961.

Peracaula, M. Instrumental Polarization Corrections at 1420 MHz for the DRAO ST Field, DRAO Technical Memorandum, 1999.

Pontoppidan K., Technical Description of GRASP8, TICRA Engineering Consultants, Copenhagen, Denmark, 2000.

Robitaille, N., DRAO Technical Report, 1997.

Rohlfs K., and Wilson T. L., Tools of Radio Astronomy, Springer, New York, 2000.

Rusch W. V. T., Forward Scattering from Cylinders of Triangular Cross Section, IEEE Trans. Antennas Propaga., 26, 849-850, 1978.

Rusch W. V. T., Forward Scattering from Square Cylinders in the Resonance Region with Application to Aperture Blockage, IEEE Trans. Antenna Propaga., 24, 182-189, 1976.

Satoh T., Endo S., Matsunaka N., Betusdan S., Katagi T., and Ebisui T, "Sidelobe Level Reduction by Improvement of Strut Shape, IEEE Trans. Antenna Propaga., 32, 7, 698-705, 1984.

Simmons A. J., A Compact Broad-Band Microwave Quarter-Wave Plate, 1952. Proc. IRE , 40, 1089-1090.

Smegal R. J., Landecker T. L., Vandeldik J.F., Routledge D., and Dewdney P.E., Aperture Synthesis Polarimetry: Application to the Dominion Radio Astrophysical Observatory Synthesis Telescope, Radio Science, 32, 643-656, 1997.

Stewart J. V., Intermediate Electromagnetic Theory, World Scientific Publishing Co. Pte. Ltd., New Jersey, 2001.

Stutzman W. L., Polarization in Electromagnetic Systems, Artech House, Boston, 1993.

Stutzman W. L., and Thiele G. A., Antenna Theory and Design, John Wiley & Sons Inc., New York, 1998.

Thielen H., Reduction of the Strut Radiation of Reflector Antennas, Antennas and Propagation Society International Symposium, Vol. 19 , Jun 1981

Tinbergen J., Astronomical Polarimetry, Cambridge University Press, Cambridge, 1996.

Trikha P. K., Improvement of the Radiation Pattern of a 9m Radio Telescope antenna at 408 MHz, M.Sc. Thesis, Univ. of Alberta, Edmonton, Alberta, Canada, 1991.

Veidt B., Selecting 3D Electromagnetic Software, Microwave Journal, 44, 126-137, 1998.

Verschuur G. L., The Invisible Universe Revealed: The Story of Radio Astronomy, Springer-Verlag, New York, 1987.

Volakis J. L., Kempel L. C., Electromagnetics: Computational Methods and Considerations, IEEE Computational Science and Engineering, 2 42-57, 1995.

http://www.ras.ucalgary.ca/IGPS/